12-9-2004

Integrated Uv-Vis Multiangle-Multiwavelength Spectrometer For Characterization Of Micron And Sub-Micron Size Particles

Yong-Rae Kim
University of South Florida

Integrated Uv-Vis Multiangle-Multiwavelength Spectrometer

For Characterization Of Micron And Sub-Micron Size Particles

by

Yong-Rae Kim

A dissertation submitted in partial fulfillment
of the requirements for the degree of
Doctor of Philosophy
Department of Physics
College of Arts and Sciences
University of South Florida

Co-Major Professor: Luis Humbolt Garcia-Rubio , Ph.D.
Co-Major Professor: Myung Keun Kim, Ph.D.
Nicholas Djeu, Ph.D.
Pritish Mukherjee, Ph.D.
Maria Kallergi, Ph.D.

Date of Approval:
December 9, 2004

Keywords: light scattering, transmission, fluorescence, joint particle property distributions, particle shape and composition

Color illustrations are necessary for clear distinction of the intensities of UV-VIS Multiangle-Multiwavelength response surface plots. Color illustrations can be found as hard copy at the University of South Florida library or electronically found from the Electronic library.

DEDICATION

I dedicate this dissertation to my late father-in-law Jeong-Hoon Lee who missed his beloved youngest daughter until his last moment. To my mother-in-law Ki-Soon Han. To my father Myung-Soo Kim. To my mother Jeong-Hee Seo. To my beloved wife Kyung-Hee Lee. To my son Sun-Joong Kim. Without their love, patience, and sacrifice, this work would be impossible.

ACKNOWLEDGEMENTS

I would like to express my deepest appreciation to my advisors Dr. Myung Keun Kim and Dr. Luis H. Garcia-Rubio. Without Dr. Kim and Dr. Garcia-Rubio's valuable understanding, patience, and guidance, this research would not be successful. I would like to express my thanks to Dr. Nicholas Djeu, Dr. Maria Kallergi, and Dr. Pritish Mukherjee for their encouragement and serving on my dissertation committee. I would like to thank Dr. Robert Potter for chairing my defense examination. I would like to thank Dr. Debra Huffman, Dr. Akihisa Nonoyama, Dr. Vineet Shastry, Dr. Andres Cardenas, Dr. Michelle Cardenas, Dr. Christina Bacon, and Dr. Judy Fu, Tony Greco, Edward Zurek, Angela Brooke, Greta Klungness, Christie Stephans, and Tracy Berg for their help throughout the research and writing dissertation. I would like to thank Sue wolf, Evelyn Keeton Williams, Phil Bergeron, and the staffs of the machine shop in the college of Marine Sciences for their support. I would like to thank Berm-Jae Choi, Dr. David Austell, Mary Ellen Reilly, Dr. Hui Lee, Dr. Chul-Hwan Yoon for their friendship. I would like to express my thanks to my nephew Seong-Min Hong, sister-in-law Soon-Mi Lee, my wife Kyung-Hee Lee, and my son Sun-Joong Kim for their love and patience. Lastly, I would like to express my greatest thank to God who always helps and guides me and my family with his amazing grace.

TABLE OF CONTENTS

LIST OF TABLES

LIST OF FIGURES

Integrated UV-VIS Multiangle-Multiwavelength Spectrometer for Characterization of Micron and Submicron Size Particles

Yong-Rae Kim

ABSTRACT

Characterization of micron and sub-micron size particles requires the simultaneous measurement of the joint particle property distribution (JPPD). The JPPD is comprised of particle size, shape, orientation, composition, optical properties, and surface properties. Measurement of each of the particle properties independently is a difficult task and it has been only partially successful. To determine as many particle properties as possible using optical methods it is necessary to simultaneously measure all aspects of the interaction of the incident light with the particles of interest. This approach leads to the concept of multidimensional spectroscopy suggested by Prof. Garcia-Rubio. Dr. Bacon proved the proposition by developing and testing a prototype multiangle-multiwavelength (MAMW) spectrometer proposed by Prof. Garcia-Rubio. However, the prototype MAMW spectrometer has limitations in the amount of information it can obtain because of strong absorption of deep UV light and detector saturation due to the use of optical fibers and single integration time for the CCD detector.

The Integrated UV-VIS MAMW spectrometer has been developed to overcome the limitations of the prototype MAMW spectrometer. Improvements have become

possible through the use of UV lenses and integration time multiplexing (ITM). The Integrated UV-VIS MAMW spectrometer has the capabilities to perform low angle scattering measurements starting from 4^{o} with simultaneous detection of multi-wavelength light from 200 nm to 820 nm, UV-VIS transmission spectroscopy, and frequency domain fluorescence spectroscopy. Following the development, possible sources of errors were analyzed and data calibration procedures have been established to ensure the validity and reproducibility of the measurement results.

The capabilities of the Integrated UV-VIS MAMW spectrometer were tested by measuring UV-VIS MAMW spectra of polystyrene standards. The measured UV-VIS MAMW spectra clearly show differences due to particle size, shape, and compositional changes. Measurements of the UV-VIS MAMW spectra of sickled whole blood samples demonstrate that particle shape and compositional changes can be detected simultaneously. These results confirmed that the Integrated UV-VIS MAMW spectrometer could be a powerful tool for the characterization of micron and sub-micron size particles. Alternate approaches to enhance these capabilities further, i.e., the development of a new multidimensional MAMW spectrometer, are also described.

CHAPTER 1. INTRODUCTION

Micron and sub-micron size particle characterization is important for industry, environmental monitoring, biology, and medicine because of improved product quality, higher throughput and increased efficiency, reduced environmental pollution, compliance with regulatory requirements (FDA, EPA, OSHA), and as a new methodology for early detection of, especially, spreading diseases by non-invasive detection of microorganisms, etc.[46, 56] Methods of particle characterization include light-based methods, sedimentation, chromatography, sieves, acoustic, and gas adsorption, etc.[67] These methods exploit the joint particle property distribution (JPPD) to characterize particles. The JPPD is comprised of particle size or size distribution, shape, orientation, composition, structure, optical properties, and surface properties (area, charge, porosity, etc.).[2,10] The JPPD can serve as the spectroscopic fingerprint of particle. Fig. 1.1 shows some particles with different JPPD.[56] However, most of the particle characterization methods measure only one property and lead to inconsistencies in the results and errors in the estimation because micron and sub-micron size particle properties are interactive, interrelated and thus, they are dependent on each other.[18] Moreover, as particle homogeneity changes not only in space but also in time, serial JPPD measurement using different procedures can lead to

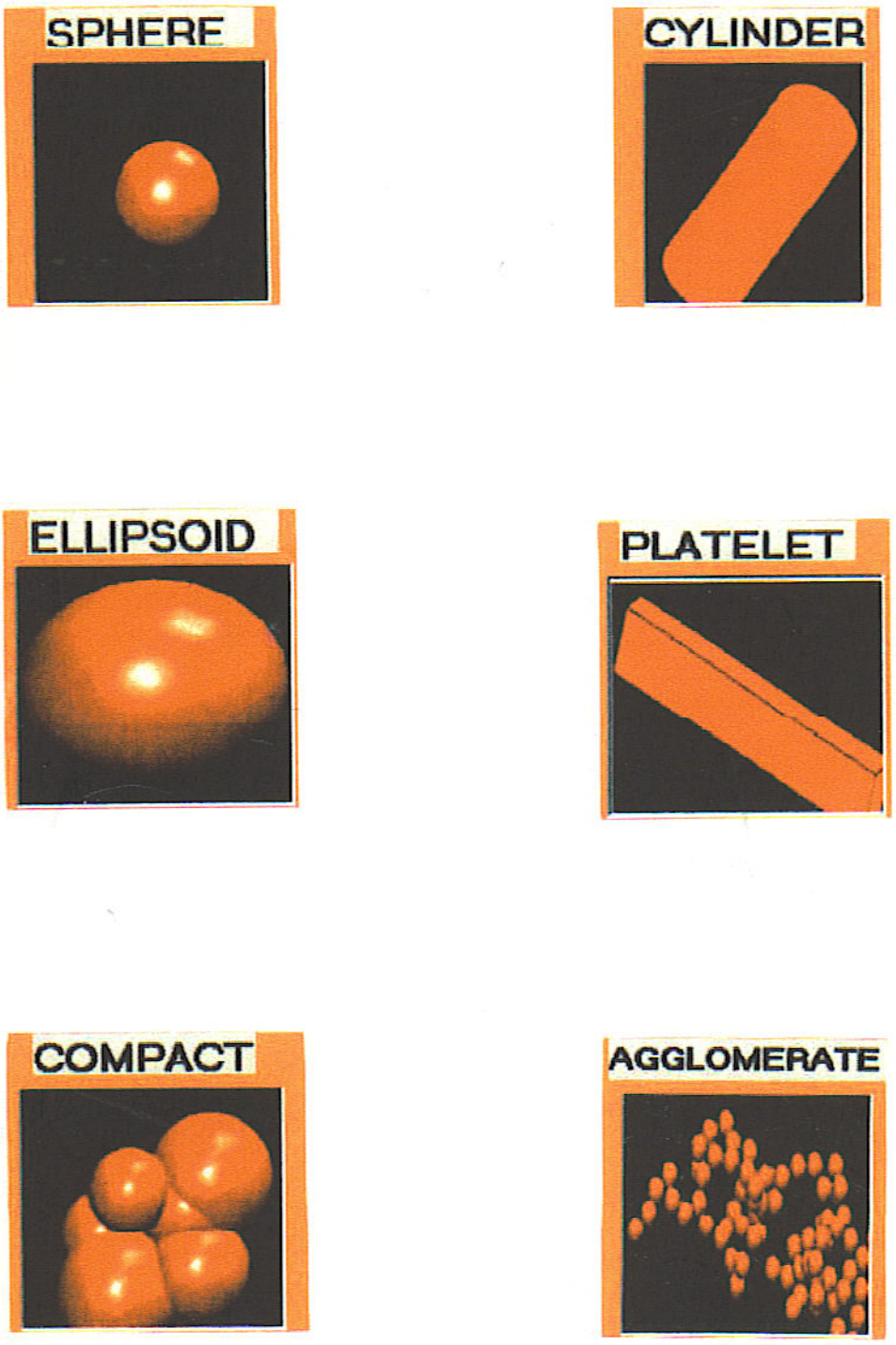

Figure 1.1. Particles with different joint particle property distribution (JPPD). Adapted from Reference 56.

the additional inaccuracy in the obtained results. To overcome the limitation of single particle property measurement, Prof. Garcia-Rubio has suggested the concept of multiangle-multiwavelength (MAMW) spectrometer that incorporated multiwavelength static light scattering and transmission spectroscopy.[2,3] By developing and testing a prototype MAMW spectrometer that employs a tungsten-halogen lamp as light source, optical fibers as light delivery tool, and a miniature CCD diode array spectrometer for detector, Dr. Bacon had proved that MAMW spectrometer would be a possible modality of detecting different JPPD (mainly size, shape, and composition) simultaneously.[2] Measured JPPD of different polystyrene and silica standards were consistent with results obtained by theoretical simulation.

On the other hand, in spite of these early accomplishments, there has been a necessity to develop a new MAMW spectrometer. The use of optical fibers as light delivery tool and single integration time for the CCD detector limited the capabilities of the prototype MAMW spectrometer. It utilized multiwavelength light scattering only within the spectral range of 400 nm ~ 800 nm and angular range of 30^{o} ~ 90^{o}, respectively.[2] In addition, incorporation of spectroscopic techniques other than scattering, like transmission, fluorescence, and polarization measurements were not possible. Consequently, information available from measurements or range of particles that could be characterized by the prototype MAMW spectrometer had limitations. Thus, the necessity of developing a new MAMW spectrometer that can overcome the limitations of the prototype and enhance the JPPD detection capability has drawn significant research interest. This gives motivation for this dissertation research, ‘Development of the

Integrated UV-VIS MAMW spectrometer for characterization of micron and sub-micron size particles.'

The limitations of the prototype MAMW spectrometer are overcome by the use of fused silica UV lenses as light delivery tool and integration time multiplexing (ITM), optimized use of the 2 x 10^8 dynamic range of Ocean Optics S2000 CCD diode array spectrometer.[43] The adoption of UV lenses enables the use of broadband UV light source, increases the intensity of the incident light to sample cell, and together with the use of narrow width slits and ITM, enhances the low angle scattering capability. The incorporation of ITM avoids detector saturation due to CCD linearity. By overcoming the limitations of the prototype MAMW spectrometer, detection of fluorescence, transmission, and low angle scattered light becomes possible. Because it can perform not only scattering but transmission and fluorescence spectroscopy, it is an integrated spectrometer. The Integrated UV-VIS MAMW spectrometer has the following capabilities to perform:

1. low angle scattering starting from 4^o with simultaneous detection of multiwavelength light from 200 nm to 820 nm,
2. UV-VIS transmission spectroscopy with wavelengths for analysis ranging from 200 nm to 820 nm and
3. frequency domain UV-VIS fluorescence spectroscopy.

The capability 1 is the unique characteristics of the Integrated UV-VIS MAMW spectrometer. As of Nov. 15, 2004, the INSPEC (physics reference search engine) search

results show no particle characterization reports using both multiangle and multiwavelength UV-VIS light scattering. In addition, it has room to adopt polarization optics to measure the Mueller matrix, dichroism in transmission spectroscopy and fluorescence anisotropy. Consequently, the capacity of the MAMW spectrometer has been enhanced considerably. The enhanced low angle scattering capability and the use of UV-VIS light source allow the characterization of polystyrene spheres ranging from 20 nm to 10 μm with further extension possibilities. Moreover, measured UV-VIS MAMW spectra clearly show differences due to particle shape or compositional changes. Besides, UV-VIS MAMW spectra of sickled whole blood samples confirmed that particle shape and compositional changes can be measured simultaneously with the Integrated UV-VIS MAMW spectrometer. All the results proved the possibility that the Integrated UV-VIS MAMW spectrometer could be a prospective modality that can characterize micron and sub-micron size particles by the simultaneous detection of the JPPD, specifically, size, shape, and composition. The Integrated UV-VIS MAMW spectrometer has potential to be applied to viral particle detection and nano-technology in addition to the characterization of microorganisms or micron and sub-micron size industrial particle characterization.

The capabilities of the Integrated UV-VIS MAMW spectrometer can be enhanced further. This can be accomplished by either upgrading the current prototype Integrated UV-VIS MAMW spectrometer or developing a new multidimensional MAMW spectrometer. The multidimensional MAMW spectrometer will perform multidimensional spectroscopy simultaneously and allow obtaining optimum information

necessary to characterize particles. Methods to implement upgrading of the Integrated UV-VIS MAMW spectrometer and developing a new multidimensional MAMW spectrometer are described in the later part of this dissertation.

The main contributions of this dissertation research are as follows.

1. Development of the Integrated UV-VIS MAMW spectrometer that can perform multiwavelength static light scattering, transmission, and frequency domain fluorescence spectroscopy using single light source and single detector.
2. Development of data correction procedures for the Integrated UV-VIS MAMW spectrometer.
3. Simultaneous JPPD (size, shape and composition) measurements of polystyrene and biological standards.
4. Suggestions of how to upgrade the Integrated UV-VIS MAMW spectrometer and to develop a new multidimensional MAMW spectrometer.

Dissertation Layout

This dissertation has seven chapters. The introductory chapter is followed by: CHAPTER 2. LITERATURE REVIEW - brief summary of references pertinent to particle characterization by the detection of the JPPD using light based spectroscopy, CHAPTER 3. THEORY – description of static light scattering, transmission, and frequency domain fluorescence spectroscopy theory that are indispensable to the

development of the Integrated UV-VIS MAMW spectrometer and the interpretation of the experimental results, CHAPTER 4. DEVELOPMENT – description of background information, specifications of the instrumentations, design criteria, and error analysis including reproducibility and the effect of the angle of acceptance, CHAPTER 5. MEASUREMENT – description of experimental methods and resulting data analysis including correction factors and calibration procedures, CHAPTER 6. RESULTS AND DISCUSSION – description of measurement results, the prospects of the Integrated UV-VIS MAMW spectrometer, and ways to upgrade the Integrated UV-VIS MAMW spectrometer and develop a new multidimensional MAMW spectrometer, and CHAPTER 7. SUMMARY – summary of this dissertation research activity, the results, and the lists of recommended work.

CHAPTER 2. LITERATURE REVIEW

The objective of this dissertation research is the development of the Integrated UV-VIS MAMW spectrometer for micron and sub-micron size particle characterization by the simultaneous measurement of the JPPD. It has been achieved by the incorporation of multiwavelength UV-VIS static light scattering, UV-VIS transmission, and frequency domain fluorescence spectroscopy in one instrument. Each of the above spectroscopic methodologies has its own strength in the detection of the individual particle property.[7, 19, 32] Considering the depth and breadth of spectroscopy and the amount of relevant publications, whole literature review is virtually impossible and unpractical. Thus, very brief review of literature and previous research activities directly related to the topic are described in this section.

2.1. Particle Characterization by Light Scattering

Light scattering has been widely used in particle characterization because it provides nondestructive and instantaneous way of measuring particle properties.[10] Particle size, size distribution, and simple geometrical shape information are primarily obtained by light scattering measurement.[7,10] Moreover, nowadays general technical

development and the improvement of computational capability lead to the investigation of other characteristics such as irregularity, structure, composition and refractive index.[30]

2.1.1. Particle Size or Size Distribution Measurement by Light Scattering

Angular light scattering provides a way of obtaining particle size information because scattering pattern relies on both the size parameter and the relative refractive index.[31] As particle size increases, the pattern becomes more and more complicated and sufficiently unique so that it can be used as a measure of particle size. In many instances, if refractive index of particle is known, the determination of particle size only requires the angular location of the maxima and minima in the scattering pattern.[31]

If particles are no longer of nearly the same size, it is necessary to obtain the particle size distribution (PSD) instead of extracting size information for characterization. In practice the PSD is widely used because ideal monodisperse systems of particles are very rare. The acquisition of the PSD can be done by determining a normalized distribution function p(a) that gives the fraction of particles with radii between a and a + Δa.[31]

Forward scattering is also an attractive method of particle sizing. Near the forward direction, scattering by large particles is dominated by diffraction that depends on particle area, regardless of its shape, and is independent of refractive index. Because of these advantages of refractive index independence and insensitivity to shape, forward scattering has been actively used to size non-spherical particles with unknown optical properties.[7]

Light scattering has been an important tool to investigate particle size or size distribution for various samples of importance in many different application areas due to its rapid and noninvasive measurement. The capacity of this technique will be enhanced further with the advances in available theory and instrument.[30]

2.1.2. Particle Shape Measurement by Light Scattering

Interests in the characterization of non-spherical particles by light scattering have increased significantly in recent years due to a wide variety of application areas. Unlike the homogeneous spherical particle characterization problem, the characterization of non-spherical particles becomes more complicated because it needs the particle orientation information in addition to the parameters required to describe shape.[12] To avoid the complexity, a tremendous amount of theoretical calculations have been made using Mie theory even if typical scattering particles are not always perfect spheres. This has been justified by two obvious and important reasons; I) many of the qualitative and even quantitative characteristics of particle scattering are satisfactorily described by area-equivalent spheres and II) Mie theory calculations have been easy to carry out even before the advent of current high speed computers.[21] However, uncritical use of Mie theory leads to imperfect and in some cases to spurious and misdirecting results in a number of applications of practical interests.

Mie theory provides exact solutions only to the cases of homogeneous sphere, layered sphere, homogeneous circular cylinder, layered circular cylinder, and ellipsoidal cylinder.[12] For the other cases, approximate methods, like Rayleigh, Rayleigh-Debye-

Gans (RDG), anomalous diffraction theory (ADT), Fraunhofer diffraction, coupled-dipole model and T-matrix, are available.[7,30,60]

For particles with sizes larger than the Rayleigh particles but close to the wavelength of the incident light, Rayleigh-Debye-Gans (RDG) approximation is available. Scattering by arbitrarily shaped particles can be treated using RDG approximation because this approximation incorporates the form factor.[31] Fairly accurate estimates of the light scattering can be acquired from RDG theory for suspension of randomly oriented, asymmetric particles of slightly irregular shape.

Van de Hulst formulated the anomalous diffraction theory. It is based on the assumptions that the refractive index of particle is different from that of the environment very slightly and the particle size parameter is large.[60] One of distinct advantages of the anomalous diffraction theory is that it is sufficiently general and applicable to bodies of different shapes directly.[55] As a result, scattering of large particles of arbitrary shape and orientation are investigated using this theory.[30, 31]

T-matrix is a method based on integral form of the scattering problem caused by particles of arbitrary shape and large volume. It is actively being used at present because numerical results can be obtained by this method.[7,38, 49] Consequently, T-matrix method or Waterman's extended boundary condition method (EBCM) becomes one of the most robust and efficient methods to investigate scattering by non-spherical particles.[49] Barber and Latimer applied RDG, ADT and EBCM to the scattering of the ellipsoids of revolution and found that EBCM substantially yielded reasonably accurate results in most cases studied.[33]

Coupled dipole model regards an arbitrary particle as an array of N polarizable subunits to calculate total scattering.[14] In spite of its relative simplicity, coupled dipole model was not popular because of the vast computer storage and central processing unit (CPU) time requirement necessary for modeling particles with large size parameters. However, an increasing number of people have begun to employ the coupled-dipole method recently due to the development of faster computers and more efficient programming techniques.[14]

Considerable amount of efforts have been made to extend the realm of light scattering theory beyond Mie theory. As a result, a diversity of theories has been developed to explain scattering by non-spherical particles. However, the acquisition of particle shape information by light scattering still remains as a big challenge.

2.1.3. Particle Characterization by Polarized Light Scattering

Polarized light scattering seems to be suitable for the characterization of non-spherical particles because particle shape and/or orientation significantly changes the polarization status of light.[36, 52] Therefore, polarized light scattering has been actively used in the characterization of particles with different orientation and shape because of its sensitivity. Smith et al. measured the cross correlation between the polarization status of scattered laser speckle as a function of scattering angle for a range of spherical and non-spherical particle suspensions and concluded that this measurement has the possibility of non-spherical particle detection and characterization.[52]

Biological particles provide a wide variety of geometrical shapes and internal structures that can be uniformly altered and regulated during light scattering experiments. Consequently, polarized light scattered from well-prepared biological particles such as bacteria, pollen, spores, and red and white blood cells in solution provides information particular to the biological condition of the particle.[6] W.S. Bickel et al. investigated biological scatterers by measuring the Mueller matrix and concluded that polarization effects in light scattering can yield a very sensitive tool to study the structural changes of cells during their life cycles.[5]

2.2. Particle Characterization by Multiwavelength Transmission Spectroscopy

Multiwavelength transmission spectra could be used to extract the particle size of nearly spherical particles by matching the measured features with those calculated from Mie theory. It is valid for monodisperse and sufficiently dilute system of particles.[15, 16, 19]

The optical density of particle dispersion (combined absorption and scattering characteristics) provides information that, in principle, can be employed to estimate the particle size distribution (PSD) and to identify the chemical composition of the suspended particles. The particle composition affects its optical properties, i.e., the complex refractive index of the particles that will result in absorption and scattering of light.[2] Absorption depends on the particle size in addition to the optical properties of the particles. Consequently, unique absorption spectral features of solutions for a very dilute system of particles can be used to identify particles or to determine the PSD.[2]

Multiwavelength transmission spectra can be obtained from the measured optical density spectra by eliminating scattering spectra using the mathematical deconvolution method.[35] The recovery of PSD from the measured multiwavelength transmission spectra requires to solve the Fredholm integral of the first kind that includes the particle size distribution, volume fraction, and scattering efficiencies Q_{sca}.[29] The scattering efficiencies can be calculated using classical scattering theories if wavelength, relative refractive index, and the particle diameter are given. Therefore, the acquisition of particle size distribution from the measured multiwavelength transmission spectra relies on (1) the proper inverse algorithm for a solution to Fredholm integral equation of the first kind and (2) the development of proper multiwavelength transmission spectra measurement methods.[29] The inverse solution of the measured multiwavelength transmission spectra can be obtained by either analytical inversion[64] or numerical inversion method.[15,16] The analytical inversion method has the advantage of yielding a fast solution to the inverse problem considered. On the other hand, this method needs the prior knowledge of the turbidity over the whole spectrum of wave numbers that is not practical. Therefore, a procedure of stabilizing or smoothing is required.[29] Using an analytical inversion algorithm, Wang and Hallett succeeded to recover the latex sphere size distribution.[64] Numerical inversion method that employs nonlinear least-squares algorithms and regularization techniques does not require the prior information of turbidity and thus, provides accurate recovery of the PSD with a reasonably fast computational time.[29] Elicabe and Garcia-Rubio successfully recovered the PSD of polystyrene lattices with range of 50 ~ 3950 nm using the numerical inversion technique in their simulated

studies.[15,16] Multiwavelength transmission spectroscopy using the numerical inversion technique has been applied to the quantitative interpretation of the measured human blood platelet spectra.[35]

2.3. Particle Characterization by Fluorescence Spectroscopy

Fluorescence has been well known for over 300 years and has proven to be a viable method in biology and chemistry due to the superb detection limits on material composition.[9] However, fluorescence spectroscopy has not been actively used for particle characterization other than organic or biological sample identification. This can be attributed to the fact that most intrinsic fluorephores, except rare earths, are organic aromatic molecules and fluorescence measurement requires complicated instruments.[32] On the other hand, application of fluorescence spectroscopy to medicine like biological particle identification and medical diagnostics has attracted keen research interests recently.[20, 44] For instance, Gray et al. showed that UV fluorescent spectra could be used to identify bacteria like E. coli, S. aures, and S. typhimurium.[20] Characterization of particles contained in human body fluids using fluorescence spectroscopy seems to be very realistic.

CHAPTER 3. THEORY

This chapter describes the basic aspects of static light scattering, transmission, and frequency domain fluorescence spectroscopy theory. Static light scattering theory treated in this chapter includes Rayleigh scattering theory, Mie theory and Fraunhoffer Diffraction. These are indispensable for the development of the Integrated UV-VIS MAMW spectrometer and for the interpretation of the experimental results. In describing transmission theory, priority is given to clarifying ambiguities existing in terms and definitions. Fundamental aspects of frequency domain fluorescence spectroscopy are briefly described as an introduction to fluorescence spectroscopy. In addition, optical constants that explain inherent optical properties of material as well as the fundamentals of polarization theory including the Mueller matrix are introduced.

3.1. Optical Constants

The optical properties of a particle are completely specified by frequency-dependent optical constants namely, the complex refractive index and the complex dielectric constant.[7] They are interdependent and either of them can be chosen depending on the application. The complex refractive index that is comprised of the real and the imaginary parts is a critical parameter in the light scattering theory. The difference in the

real part of the refractive index of the medium and that of the particle causes the scattering of light. The imaginary part of the particle's refractive index, i.e. absorption coefficient, decides the amount of light attenuation. Precise calculation of the complex refractive index is essential for the estimation of the absorption and scattering of light by the particle. The derivation of optical constants using Lorentz's simple classical harmonic oscillator model, brief investigation of the optical properties of dielectric material, and the description of the ways to evaluate the complex refractive index constitute this section.

3.1.1. Optical Constants and Dispersion

Optical constants describe the intrinsic optical properties of materials. There are two sets of commonly used optical constants, namely the complex refractive index, $N = n + ik$, and the complex dielectric constant, $\in = \in' + i \in''$. They are not independent and related to each other by expressions[7]

$$\in' = n^2 - k^2, \qquad \in'' = 2nk \tag{3.1}$$

$$n = \sqrt{\frac{\sqrt{\in'^2 + \in''^2} + \in'}{2}}, \qquad k = \sqrt{\frac{\sqrt{\in'^2 + \in''^2} - \in'}{2}} \tag{3.2}$$

The complex refractive index is preferred to describe wave propagation while the complex dielectric constant is favored to explain absorption and scattering by particles,

especially, small compared with the wavelength. These optical constants can be derived by Lorentz's simple harmonic oscillator model that describes the classical aspects of optical properties of material.[7] In this model, the electrons behave as though they are held by springs and are subjected to damping force and restoring force. The applied electromagnetic fields provide driving force to the electrons. The result is known as a dispersion equation[45]

$$n^2 = 1 + \frac{N_e e^2}{m_e \varepsilon_0} \sum_j \frac{f_j}{\omega_j^2 - \omega^2 - i\gamma_j \omega} \tag{3.3}$$

where N_e is the number of electrons, e is charge on an electron, m_e is the mass of an electron, ε_0 is the permittivity of free space, ω_j is the resonance frequency of material, ω is the angular frequency of the radiation, f_j is the oscillator strength for the resonance frequency ω_j, and γ_j is the damping constant of the electron (responsible for absorption).

Fig. 3.1.a shows the frequency dependence of the real and imaginary parts of the refractive index of a dielectric medium and Fig. 3.1.b exhibits that of the reflectance at normal incidence.[7] The refractive index n increases as frequency ω increases (normal dispersion) except the region where ω is close or equal to the resonance frequency ω_j (decreasing n, anomalous dispersion). The region of high absorption around the resonance frequency causes an associated region of high reflectance. Thus, a material

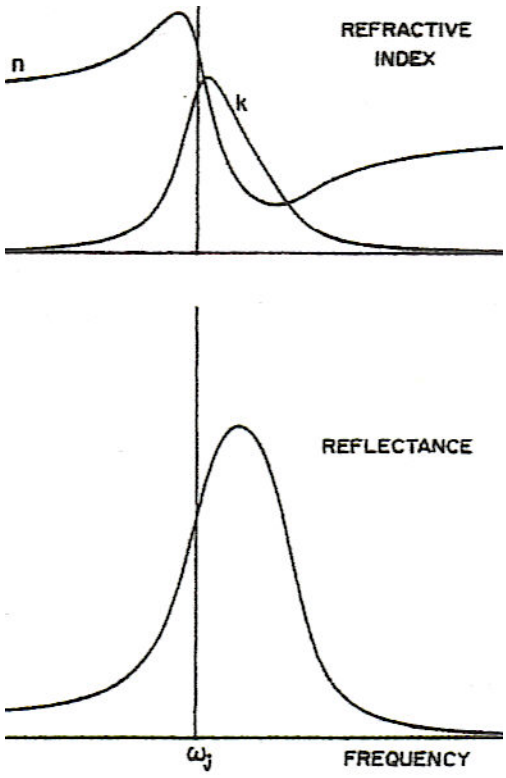

Figure 3.1. Optical property of a dielectric medium (a) the dispersion relation and (b) the corresponding reflectance at normal incidence. Adapted from Reference 7.

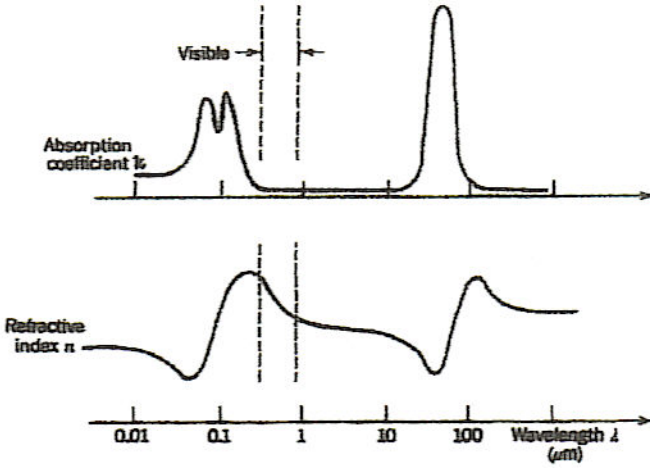

Figure 3.2 Wavelength dependent variation of the complex refractive index of a dielectric material. Adapted from Reference 50.

with $k >> 1$ is highly reflecting not highly absorbing and little light that gets into the material is rapidly attenuated.[7]

Fig.3.2 shows typical wavelength dependent profile of the complex refractive index of a dielectric material.[50] There is a strong absorption in the ultraviolet region because the photon energy corresponds to energy differences between filled and empty electron energy levels. The continuity of both empty and filled levels results in a broad region of high absorption. As wavelength increases, absorption index *k* becomes small and almost constant. Therefore, the material is transparent in the visible region. All visibly transparent materials have strong absorption in the UV region. The resonance absorption in the infrared region, can be attributed to the absorption caused by lattice vibration.[7]

3.1.2. Estimation of the Refractive Index

Eq. (3.3) is inconvenient to calculate the refractive index because it requires the information of atomic properties. Hence, simple approximation methods have been developed. The Cauchy dispersion equation, deduced from Eq. (3.3), is an empirical approximation formula relating the real part of the refractive index to the wavelength λ. It is given by

$$n = d_0 + \frac{d_1}{\lambda^2} + \frac{d_2}{\lambda^4} + ... \qquad (3.4)$$

The number of parameters d_n is determined by the required accuracy to fit the experimentally obtained data.[45]

The complex refractive index can be described as a harmonic complex number and thus, fulfills the Kramers-Kronig transform. As a result, the real part of the refractive index can be computed if the imaginary part of the refractive index is known or vice versa, using the transforms expressed by Eq. (3.5) and Eq. (3.6).

$$n(\omega) = 1 + \frac{2}{\pi} P \int_0^{\infty} \frac{\Omega\, k(\Omega)}{\Omega^2 - \omega^2}\, d\Omega \tag{3.5}$$

$$k(\omega) = \frac{-2\omega}{\pi} P \int_0^{\infty} \frac{n(\Omega)}{\Omega^2 - \omega^2}\, d\Omega \tag{3.6}$$

where Ω is the variable representing frequency in the integral, and P is the principal value of the integral.[7]

In addition to these approximation methods, the optical constants often can be obtained from experiment. However, both the real and imaginary parts of the complex refractive index cannot be measured directly. Therefore, they must be derived from measurable quantities using a proper theory.[7]

3.2. Polarization

In analytical spectroscopy, the polarization status of light, either incident or detected, provides valuable information that is indispensable for the study of the objectives under investigation. The Stokes vector and the Mueller-matrix approach for light scattering,

fluorescence anisotropy, and dichroisms (linear and circular) in absorption spectroscopy are examples of experimental methods that produce a wealth of information by taking the advantages of polarization.

Fundamentals of polarization theory are briefly reviewed in this section. Derivation of the polarization status of light, the Stokes vector approach to express polarization status as observable quantity, and the Mueller matrix concept required for complete characterization of the optical properties of material are explained in this section. This information is necessary for the description of light scattering and fluorescence theory that will be the subject of following sections.

3.2.1. Introduction to Polarization

The Maxwell equations in an infinite medium when there are no electric and magnetic sources are:[27]

$$\nabla \cdot \vec{E} = 0 \qquad \nabla \times \vec{E} + \frac{1}{c}\frac{\partial \vec{B}}{\partial t} = 0$$

$$\nabla \cdot \vec{B} = 0 \qquad \nabla \times \vec{B} - \frac{\mu\varepsilon}{c}\frac{\partial \vec{E}}{\partial t} = 0 \tag{3.7}$$

In Eq. (3.7) c is the speed of light in vacuum, ε is permittivity and μ is permeability. The simplest solution of these equations is general homogeneous plane wave propagating in the direction of $\vec{k} = k\vec{n}$

$$\vec{E}(\vec{x},t) = (\ \vec{\in}_1 E_1 + \vec{\in}_2 E_2\ ) e^{i\vec{k}\cdot\vec{x} - i\omega t} \qquad (3.8)$$

where $\vec{\in}_1$, $\vec{\in}_2$, and $\vec{n}$ are a set of real mutually orthogonal unit vectors, k is propagation number $(\omega\sqrt{\varepsilon\mu}\ )$, and E_1 and E_2 are amplitudes with complex numbers.[27]

The polarization status of $\vec{E}(\vec{x},t)$ is determined by the magnitude and the phase of E_1 and E_2. In case of linearly polarized wave, E_1 and E_2 have the same phase and the polarization vector making an angle $\theta_p = \tan^{-1}(E_2/E_1)$ with $\vec{\in}_1$ and a magnitude $E = \sqrt{E_1^{\ 2} + E_2^{\ 2}}$ as shown in Fig 3.3

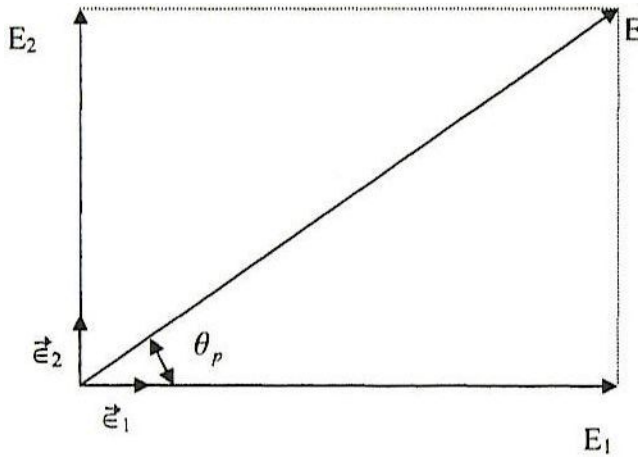

Figure 3.3. Electric field of a linearly polarized wave. Adapted from Reference 27.

The Eq. (3.8) expresses elliptically polarized wave if E_1 and E_2 have different phases. If E_1 and E_2 have the same magnitude, but differ in phase by 90^o, the Eq. (3.8) represents circularly polarized wave and becomes:

$$\vec{E}(\vec{x}, t) = E_0 (\vec{\epsilon}_1 \pm i\, \vec{\epsilon}_2)\, e^{i\vec{k}\cdot\vec{x} - i\omega t} \tag{3.9}$$

with the common real amplitude E_0.[27] Suppose that axes are selected so that the wave is propagating in the positive z direction, while $\vec{\epsilon}_1$ and $\vec{\epsilon}_2$ are in the x and y directions, respectively. Then the wave in case of $(\vec{\epsilon}_1 + i\, \vec{\epsilon}_2)$ is called left circularly polarized while the wave for $(\vec{\epsilon}_1 - i\, \vec{\epsilon}_2)$ is described as right circularly polarized.[27]

3.2.2. Stokes Vector and the Mueller Matrix

If a plane electromagnetic wave is expressed in the form of Eq. (3.8) with known coefficients (E_1 , E_2), the information of the polarization status of the wave can be acquired without much difficulty. However, in practice, it is indispensable to decide the polarization status by observing the beam and thus, Eq. (3.8) is not a convenient form to use for this purpose. To avoid this complication, each of the scalar coefficients in Eq. (3.8) can be defined as a magnitude times a phase factor:

$$E_1 = a_1 e^{i\delta_1}, \qquad E_2 = a_2 e^{i\delta_2} \tag{3.10}$$

where a_1, a_2 are the amplitudes and δ_1, δ_2 are the phases.[27] Let the subscripts 1 and 2 designate parallel and perpendicular direction respectively. Then electric fields can be rewritten as parallel and perpendicular to the plane of interest[60]

$$E_{//} = a_{//} e^{i\delta_{//}} e^{i\mathrm{k}z - i\omega t},$$
$$E_{\perp} = a_{\perp} e^{i\delta_{\perp}} e^{i\mathrm{k}z - i\omega t}. \tag{3.11}$$

The Stokes parameters I, Q, U, V, which completely describe the intensity and the polarization status of a light wave using directly observable quantities, are related to the electric field vector as follows:[60]

$$I = E_{//}E_{//}^{*} + E_{\perp}E_{\perp}^{*} = a_{//}^2 + a_{\perp}^2,$$
$$Q = E_{//}E_{//}^{*} - E_{\perp}E_{\perp}^{*} = a_{//}^2 - a_{\perp}^2,$$
$$U = E_{//}E_{\perp}^{*} + E_{\perp}E_{//}^{*} = 2\,a_{//}a_{\perp}\cos\delta, \tag{3.12}$$
$$V = i(E_{//}E_{\perp}^{*} - E_{\perp}E_{//}^{*}) = 2\,a_{//}a_{\perp}\sin\delta,$$

where δ is the phase difference $\delta_{//} - \delta_{\perp}$ and * represents the complex conjugate. The Stokes parameters have an obvious interpretation. For example, *I* is the total intensity, *Q* is parallel or perpendicular linear polarization to the scattering plane, *U* is linear polarization at ±45° to the scattering plane, and *V* is left or right circular polarization.[5]

The Stokes parameters for a quasi-monochromatic light are written as[4]

$$
\begin{aligned}
I &= < E_{//} E_{//}^{*} + E_{\perp} E_{\perp}^{*} >, \\
Q &= < E_{//} E_{//}^{*} - E_{\perp} E_{\perp}^{*} >, \\
U &= < E_{//} E_{\perp}^{*} + E_{\perp} E_{//}^{*} >, \\
V &= i < E_{//} E_{\perp}^{*} - E_{\perp} E_{//}^{*} >,
\end{aligned}
\tag{3.13}
$$

where the angular brackets indicate time averages over an interval longer than the period $\mathrm{T} = 1/f$, where f is the optical frequency (~10^{15}/s). There is a relationship among the Stokes parameters:[4]

$$
I^2 \geq Q^2 + U^2 + V^2 \tag{3.14}
$$

The equal sign holds for the totally polarized light while inequality represents the cases of partially polarized light and $Q = U = V = 0$ defines the natural or unpolarized light. The Stokes vector, a column vector, the four elements of which are the Stokes parameters can represent a beam of arbitrary polarization including partially polarized light.

When light interacts with optical components such as lenses, filters, polarizers, surfaces, scattering media, etc., the polarization status of light is changed in general.[25] This interaction of light with any optical elements or material can be described as a multiplication of the four-component Stokes vector with a 4 x 4 matrix. This sixteen-

element matrix is called the Mueller matrix or the scattering matrix if scattering is involved. The Mueller matrix $[S]$,

$$[S] = \begin{bmatrix} S_{11} & S_{12} & S_{13} & S_{14} \\ S_{21} & S_{22} & S_{23} & S_{24} \\ S_{31} & S_{32} & S_{33} & S_{34} \\ S_{41} & S_{42} & S_{43} & S_{44} \end{bmatrix} \tag{3.15}$$

completely characterizes the optical properties of any components or material.[4] Once an incident four-component Stokes vector $|\mathbf{V}_i|$ and a Mueller matrix $[S]$ are given, a final Stokes vector $|\mathbf{V}_f|$ is determined from the relation $|\mathbf{V}_f| = [S]|\mathbf{V}_i|$ or

$$\begin{vmatrix} I_f \\ Q_f \\ U_f \\ V_f \end{vmatrix} = \begin{bmatrix} S_{11} & S_{12} & S_{13} & S_{14} \\ S_{21} & S_{22} & S_{23} & S_{24} \\ S_{31} & S_{32} & S_{33} & S_{34} \\ S_{41} & S_{42} & S_{43} & S_{44} \end{bmatrix} \begin{vmatrix} I_i \\ Q_i \\ U_i \\ V_i \end{vmatrix} \tag{3.16}$$

Eq. (3.16) can be applied to a series of optical elements placed in a beam.[5] The final polarization status of the beam can be obtained by multiplying the corresponding Mueller matrix of each element.[4]

If incident light is perfectly polarized, Jones vector, another representation of polarized light that has the advantages of being applicable to coherent beams, provides

extremely concise representation. The details of Jones Vector and corresponding Jones Matrix approach can be found in Reference 50.

3.3. Light Scattering Theory

If an electromagnetic wave irradiates an object, the electric field of the incident wave forces electric charges in the object to begin oscillatory motion which results in the acceleration of electric charges. Scattering is the re-radiation of electromagnetic energy in all directions by these accelerated electric charges in the object.[7] If part of the incident electromagnetic energy is transformed into other forms, like thermal energy, by the excited elementary charges, it is called absorption. Scattering and absorption cannot be considered separately in general because the sum of the attenuation of incident radiation by both scattering and absorption accounts for the total extinction of the incident light.[7] In scattering, the incident radiation frequency is different from the natural frequency of molecules in the object.

The static light scattering theory for diluted particle system can be classified into rigorous theory and approximation.[30] For rigorous theory, parameters can be calculated to any desired accuracy by boundary condition method and integration method. The former, solution is figured out by applying the electromagnetic boundary conditions and the latter, solution is found from an integral over the volume of the scatterer.[30] Due to the complexity of the scattering problem, rigorous solutions require considerable amount of computer time and storage even for the simplest shapes and smallest particles. Therefore, a wide range of approximation theories has been developed. Each of them may be used

for certain ranges of size and refractive index only. However, they are easy to calculate and often provide much insight into the scattering process.[30]

In this research, Mie theory is adopted as the primary interpretation model because the exact solution explaining the scattering of light by a sphere that has size comparable to the wavelength of incident light can be obtained using it.[7] In addition, Mie theory can provide approximations for spheres with a wide range of sizes or non-spherical particles with simple geometrical shape. Besides Mie theory, Rayleigh approximation and diffraction theories are also described.

3.3.1. Introduction to Light Scattering Theory

If an infinite plane wave illuminates a single particle, the total scattered power by the particle P_{sca} is given

$$P_{sca} = C_{sca} I_i \tag{3.17}$$

where I_i is the incident light intensity and C_{sca} is the scattering cross section.[30] The total absorbed power P_{abs} is defined in the same way

$$P_{abs} = C_{abs} I_i \tag{3.18}$$

where C_{abs} is the absorption cross section.[30] The cross section, a quantity with

dimensions of area, is the energy taken away from the incident radiation. The scattering cross section C_{sca} is the energy removed by scattering and the absorption cross section C_{abs} corresponds to the energy pulled off by absorption. The combined effect of absorption and scattering is extinction and accounts for the total energy eliminated from the incident radiation.[7] The total power extinguished is

$$P_{ext} = C_{ext} I_i \tag{3.19}$$

The extinction cross section C_{ext} can be written as the sum of the absorption cross section C_{abs} and the scattering cross section C_{sca} because of the conservation of energy:[7]

$$C_{ext} = C_{abs} + C_{sca} \tag{3.20}$$

The Efficiencies for extinction, scattering, and absorption are defined by normalizing the corresponding cross section with the particle size:

$$Q_{ext} = \frac{C_{ext}}{G}, \qquad Q_{sca} = \frac{C_{sca}}{G}, \qquad Q_{abs} = \frac{C_{abs}}{G} \tag{3.21}$$

where *G* is the particle cross-sectional area projected onto a plane perpendicular to the incident beam.[7] The efficiencies for extinction, absorption, and scattering are related to each other by Eq. (3.22)

$$Q_{ext} = Q_{abs} + Q_{sca} \tag{3.22}$$

The efficiencies are merely dimensionless cross sections.

The scattered electric field at sufficiently large distances from the particle has the form of an outgoing spherical wave[7]

$$\vec{E}_{sca} = \frac{e^{ikr}}{-i\mathrm{k}r}\vec{A} \tag{3.23}$$

where $\vec{A}$ is the real vector field independent from time but depend on position. $\vec{E}_{sca}$ is transverse to the radial direction of propagation $\hat{r}$. Eq. (3.23) may be rewritten as

$$\vec{E}_{sca} = \frac{e^{i\mathrm{k}(r-z)}}{-i\mathrm{k}r}E\vec{F}(\theta,\phi) \tag{3.24}$$

$\vec{F}(\theta,\phi)$ is the dimensionless vector scattering amplitude, θ is the angle between the incident light and the scattered light, ϕ is the azimuthal angle, and z is the direction of the incident radiation.[7,30] The corresponding magnetic field is[7]

$$\vec{H}_{sca} = \frac{\mathrm{k}}{\omega\mu}(\hat{r} \times \vec{E}_{sca}) \tag{3.25}$$

The Poynting vector that specifies the electromagnetic energy flux is[7]

$$\vec{S} = \frac{1}{2}\mathrm{Re}(\vec{E} \times \vec{H}^{*}) \tag{3.26}$$

By substituting Eq. (3.24) and Eq. (3.25) into Eq. (3.26), we can find the Poynting vector for the scattered field[30]

$$\vec{S}_{sca} = \frac{I_i}{\mathrm{k}^2 r^2} \left| F(\theta, \phi) \right|^2 \hat{r} \tag{3.27}$$

The integration of $\vec{S}_{sca}$ over the surface of the spherical volume of the medium surrounding the scattering particle yields the scattering cross section[30]

$$C_{sca} = \frac{P_{sca}}{I_i} = \int_0^{2\pi} \int_0^{\pi} \frac{\left| F(\theta, \phi) \right|^2}{\mathrm{k}^2} \sin\theta \, d\theta \, d\phi = \int_{4\pi} \frac{\left| F(\theta, \phi) \right|^2}{\mathrm{k}^2} d\Omega \tag{3.28}$$

The term $\frac{\left| F(\theta, \phi) \right|^2}{\mathrm{k}^2}$ is named as the differential scattering cross section or "Rayleigh ratio" and often designated as $dC_{sca}/d\Omega$. Physically, the differential scattering cross section describes the angular distribution of the scattered light: the amount of light scattered into a unit solid angle (Ω) about a given direction.[7] The phase function p,

which expresses probability that during a scattering event a photon with initial direction ϕ is scattered in the direction θ, is defined by normalizing (3.28)[30]

$$p(\theta,\phi) = \frac{4\pi \left|F(\theta,\phi)\right|^2}{\mathrm{k}^2 C_{sca}} \tag{3.29}$$

and

$$\frac{1}{4\pi}\int_0^{2\pi}\int_0^{\pi} p(\theta,\phi)\sin\theta\, d\theta\, d\phi \;= 1 \tag{3.30}$$

The extinction cross section is obtained from the optical theorem[7]

$$C_{ext} = \frac{P_{ext}}{I_i} = \frac{4\pi}{\mathrm{k}^2}\mathrm{Re}\{(\hat{r}\cdot\vec{F})_{\theta=0}\} \tag{3.31}$$

It is convenient to relate incident and scattered electric fields through the matrix form[7]

$$\begin{pmatrix} E_{//sca} \\ E_{\perp sca} \end{pmatrix} = \frac{e^{i\mathrm{k}(r-z)}}{-i\mathrm{k}r}\begin{pmatrix} S_2 & S_3 \\ S_4 & S_1 \end{pmatrix}\begin{pmatrix} E_{//i} \\ E_{\perp i} \end{pmatrix} \tag{3.32}$$

where $E_{//}$ is the electric field component polarized parallel to and $E_{\perp}$ is that polarized perpendicular to the scattering plane. Eq. (3.32) defines the amplitude scattering matrix.

Its elements $S_j\ (\ j = 1, 2, 3, 4\ )$ depend in general on the scattering angle θ and the azimuthal angle ϕ.[7] The Muller matrix in Eq. (3.15) is called the scattering matrix if scattering is involved. Its 16 elements are given in terms of the amplitude scattering matrix elements S_1, S_2, S_3 and S_4. For example, S_{11}, which defines the angular distribution of the scattered light in case of unpolarized incident light, becomes[7]

$$S_{11} = \frac{1}{2}\left(|S_1|^2 + |S_2|^2 + |S_3|^2 + |S_4|^2\right) \tag{3.33}$$

Expressions for the other elements can be found in Reference 7. S_{11} is directly related to the ratio of scattered to incident intensity (I_{sca}/I_i)

$$\frac{I_{sca}}{I_i} = \frac{S_{11}}{\mathrm{k}^2 r^2} \tag{3.34}$$

where I_{sca} is the scattered light intensity.[7]

If particle shape is isotropic then S_3 and S_4 of the amplitude scattering matrix in Eq. (3.32) become nullified because no cross-polarization is introduced. For an infinite plane incident wave, the azimuthal angle at $\theta = 0^{\circ}$ can be ignored and it follows that $S_1(0) = S_2(0) = S(0)$. Substituting this into Eq. (3.31) leads to

the expression for the extinction cross section[7]

$$C_{ext} = \frac{4\pi}{\mathrm{k}^2}\mathrm{Re}\{S(0^\circ)\} \tag{3.35}$$

3.3.2. Rayleigh Scattering Theory

Rayleigh scattering occurs when the size of the scattering particle is much smaller than the wavelength of the light being scattered. In case of the Rayleigh scattering, the expressions for the amplitude scattering matrix elements S_1 and S_2 are[7]

$$S_1 = \frac{3}{2}\mathrm{a}_1, \qquad S_2 = \frac{3}{2}\mathrm{a}_1\cos\theta \tag{3.36}$$

where a_1 is a scattering coefficient

$$\mathrm{a}_1 = -i\frac{2x^3}{3}\frac{m^2-1}{m^2+2} \tag{3.37}$$

The size parameter x and the relative refractive index m are defined as

$$x = \mathrm{k}a = \frac{2\pi N\ a}{\lambda}, \qquad m = \frac{\mathrm{k}_1}{\mathrm{k}} = \frac{N_1}{N} \tag{3.38}$$

where N_1 and N are the complex refractive indices of particle and medium, respectively.[7] The resulting scattering matrix becomes[7]

$$\frac{9|a_1|^2}{4k^2 r^2}\begin{pmatrix} \frac{1}{2}(1+\cos^2\theta) & \frac{1}{2}(\cos^2\theta-1) & 0 & 0 \\ \frac{1}{2}(\cos^2\theta-1) & \frac{1}{2}(1+\cos^2\theta) & 0 & 0 \\ 0 & 0 & \cos\theta & 0 \\ 0 & 0 & 0 & \cos\theta \end{pmatrix} \tag{3.39}$$

The scattered light intensity I_{sca} for unpolarized incident light with intensity I_i is given[7]

$$I_{sca} = \frac{8\pi^4 N a^6}{\lambda^4 r^2}\left|\frac{m^2-1}{m^2+2}\right|^2 (1+\cos^2\theta) I_i \tag{3.40}$$

For a sphere, the scattering cross section and the absorption cross section are approximately[7]

$$C_{sca} = \frac{128\pi^5 a^6 N^4}{3\lambda^4}\left|\frac{m^2-1}{m^2+2}\right|^2, \tag{3.41}$$

$$C_{abs} = 4\pi x \,\mathrm{Im}\left\{\frac{a^3(m^2-1)}{(m^2+2)}\right\}$$

Dividing Eq. (3.41) by πa^2, we can find the scattering efficiency and the absorption efficiency[7]

$$Q_{sca} = \frac{8}{3}x^4\left|\frac{m^2-1}{m^2+2}\right|^2$$

$$Q_{abs} = 4x\,\mathrm{Im}\left\{\frac{m^2-1}{m^2+2}\right\} \tag{3.42}$$

For sufficiently small particles the absorption and the scattering efficiencies can be approximated[7]

$$Q_{abs} \propto \frac{1}{\lambda}, \qquad Q_{sca} \propto \frac{1}{\lambda^4} \tag{3.43}$$

The extinction spectrum varies as $1/\lambda$ if it is dominated by absorption and as $1/\lambda^4$ if it is dominated by scattering. In general shorter wavelengths are extinguished more than longer wavelengths and this accounts for blue sky or red sunset.

3.3.3. Mie Theory

Mie theory that is a thorough description of the interaction of an infinite plane wave with a dielectric sphere describes scattering if the particle size is similar to or larger than the wavelength of the incident light. To obtain an analytical solution, the fields need to be expanded in a proper coordinate system part of which is made on the particle surface. By adopting spherical coordinate system, Mie could find the exact solution for the scattering problem for a sphere.[7]

For a spherical particle, the two amplitude scattering matrix elements S_1 and S_2 are[7]

$$S_1(\theta) = \sum_{n=1}^{\infty} \frac{2n+1}{n(n+1)} \{a_n \pi_n(\cos\theta) + b_n \tau_n(\cos\theta)\}$$

and (3.44)

$$S_2(\theta) = \sum_{n=1}^{\infty} \frac{2n+1}{n(n+1)} \{b_n \pi_n(\cos\theta) + a_n \tau_n(\cos\theta)\}$$

where the angular functions π_n and τ_n , which decides the θ dependence of the fields, are[7]

$$\pi_n(\cos\theta) = \frac{1}{\sin\theta} P_n^1(\cos\theta) \quad , \qquad \tau_n(\cos\theta) = \frac{d}{d\theta} P_n^1(\cos\theta) \qquad (3.45)$$

Here, P_n^1 are the associated Legendre polynomials. Fig. 3.4 shows the polar plots of π_n and τ_n for n = 1-5.[7] As n grows, the forward-direction lobe becomes narrower. This behavior of π_n and τ_n explains the enhancement of forward scattering in case of large particle because the increased sphere size incorporates the higher order π_n and τ_n in the scattering diagram.[7]

The scattering coefficients a_n for the electric multipoles and b_n for the magnetic multipoles are given by[7]

$$a_n = \frac{m\,\psi_n(mx)\,\psi_n'(x) - \psi_n(x)\,\psi_n'(mx)}{m\,\psi_n(mx)\,\xi_n'(x) - \xi_n(x)\,\psi_n'(mx)}$$

and (3.46)

$$b_n = \frac{\psi_n(mx)\,\psi_n'(x) - m\,\psi_n(x)\,\psi_n'(mx)}{\psi_n(mx)\,\xi_n'(x) - m\,\xi_n(x)\,\psi_n'(mx)}$$

where

$$\psi_n(x) = \left(\frac{1}{2}\pi x\right)^{1/2} J_{n+1/2}(x) \quad , \qquad \xi_n(x) = \left(\frac{1}{2}\pi x\right)^{1/2} H_{n+1/2}(x) \quad (3.47)$$

are the Riccati-Bessel functions, and $J_{n+1/2}(x)$, $H_{n+1/2}(x)$ are spherical Bessel functions[7]

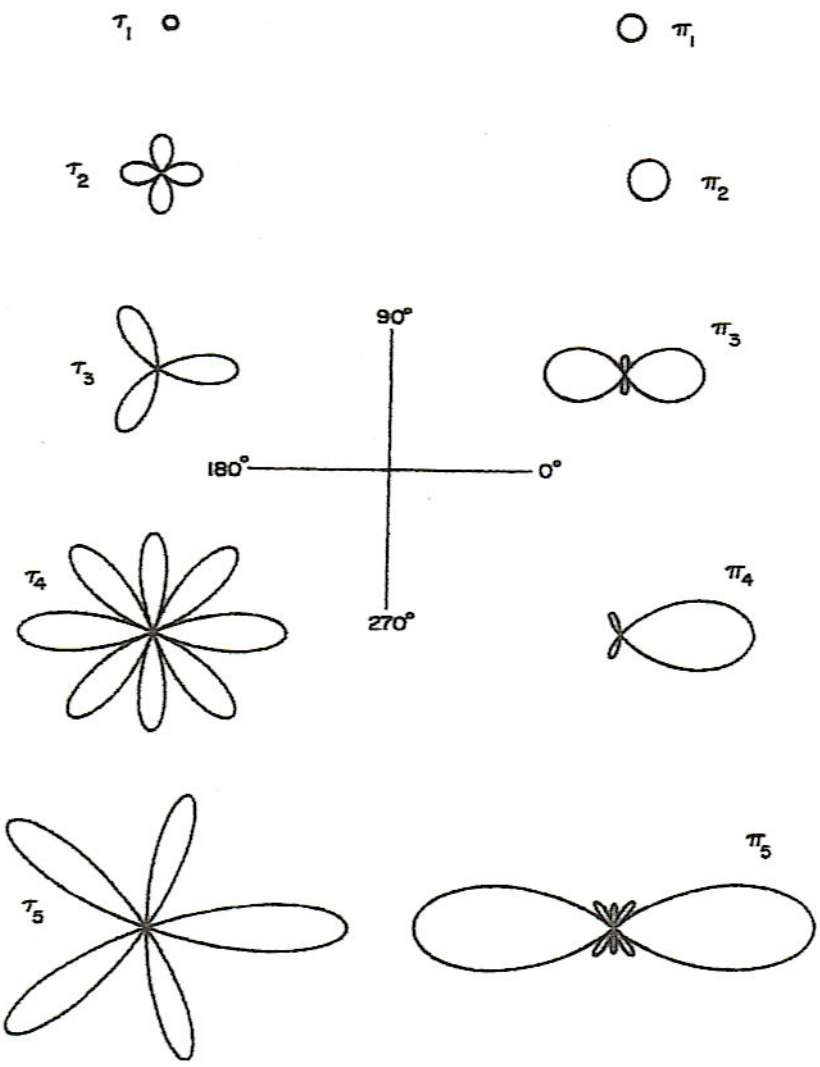

Figure 3.4. The polar plots of the angular functions π_n and τ_n . Cited from Reference 7.

The scattering coefficients a_n and b_n, which are functions of the size and optical properties of the particle and the nature of the surrounding medium in addition to the wavelength and the polarization status of the incident light, allow determining all the observable quantities associated with scattering and absorption like cross sections and the scattering matrix elements.

The cross sections for Mie scattering are given as follows[60]

$$C_{sca} = \frac{2\pi}{k^2}\sum_{n=1}^{\infty}(2n+1)(|a_n|^2 + |b_n|^2),$$

and (3.48)

$$C_{ext} = \frac{2\pi}{k^2}\sum_{n=1}^{\infty}(2n+1)\{\mathrm{Re}(a_n + b_n)\}$$

The efficiencies are

$$Q_{sca} = \frac{2}{ak^2}\sum_{n=1}^{\infty}(2n+1)(|a_n|^2 + |b_n|^2)$$

and (3.49)

$$Q_{ext} = \frac{2}{ak^2}\sum_{n=1}^{\infty}(2n+1)\{\mathrm{Re}(a_n + b_n)\}$$

3.3.4. The Fraunhofer Diffraction

Fraunhofer diffraction is valid if the incident light is unpolarized, particles are large, and scattering is close to the forward direction. For a large sphere of radius *a*, the scattering amplitude which is independent of the azimuthal angle ϕ is[7]

$$S(\theta) = x^2 \frac{(1+\cos\theta)}{2} \frac{J_1(x\sin\theta)}{x\sin\theta} \tag{3.50}$$

where J_1 is the Bessel function of the first kind.

The scattered light intensity is given[30]

$$I_{sca} = I_i \frac{\pi^2 a^4}{16\lambda^2} \left[\frac{2J_1(x\sin\theta)}{x\sin\theta} \right]^2 \frac{1}{2}\left(1+\cos^2\theta\right) \tag{3.51}$$

where the term inside the bracket defines the Airy function. The angular position of the first minimum in intensity can be found from the expression[30]

$$\sin\theta = \frac{1.22\lambda}{a} \tag{3.52}$$

If the refractive index of the particle is very low ($|m-1| << 1$), the particle transmits light almost without deflection. This transmitted light interferes with diffracted

light and results in the anomalous diffraction. The scattering efficiency for the anomalous diffraction is[60]

$$Q_{ext} = 2 - (\frac{4}{\rho})\sin\rho + (\frac{4}{\rho^2})(1 - \cos\rho) \tag{3.53}$$

where

$$\rho = 2x(m - 1) \tag{3.54}$$

3.4. Transmission

If a plane homogeneous wave traverses a medium, its intensity becomes exponentially attenuated by scattering and absorption as the wave crosses the medium. Transmission is the ratio of the intensities measured with and without the sample interposed between light source and detector.[7] Transmission measurement is indispensable for the estimation of the JPPD because the acquired spectra can be used to derive the chemical composition information in addition to the particle size distribution.

Transmission has been expressed in different forms depending on the knowledge that is sought from the material system under study. These include the Bouger-Lambert law, the turbidity, and the Beer-Lambert law.[19] The Bouger-Lambert law is the most general expression relating transmission to the attenuation of the incident radiation by sample material. It doesn't impose any restrictions on either the attenuation mechanism

or the material under investigation. The turbidity provides the basis for understanding physical phenomena of incident radiation extinction. On the other hand, the Beer-Lambert law allows the estimation of chemical composition or chromophore concentration. Because these are merely different expressions of the same phenomena, i.e., they have the same functional form, there is enough room for confusion about their derivation, interpretation and usage. Therefore, the description of transmission theory in this section is focused on the clarification of similarities and differences among the Bouger-Lambert law, the turbidity, and the Beer-Lambert law.

3.4.1 Transmission and Absorbance

If a plane wave traverses an absorbing medium of path length l, the intensity of the wave after crossing the medium is described by:[7]

$$I_{trs} = I_i e^{-\alpha l} \tag{3.55}$$

where I_i is the intensity of the wave before entering the medium and α is the absorption (also called attenuation or extinction) coefficient. The absorption coefficient α is a distinctive property of material. α can be derived from the Poynting vector of a plane wave and expressed as[7]

$$\alpha = \frac{4\pi k}{\lambda} \tag{3.56}$$

Here, the imaginary part of the complex refractive index k decides the rate at which electromagnetic energy is removed from the wave as it propagates through the medium. The transmission T is defined as the ratio of the intensities I_i and I_{trs} [7]

$$T = \frac{I_{trs}}{I_i} = e^{-\alpha l} \tag{3.57}$$

The logarithmic form of Eq. (3.57) is known as the Bouger & Lambert law[19]

$$\ln\left(\frac{I_{trs}}{I_i}\right) = -\alpha l \tag{3.58}$$

The Bouger-Lambert law specifies the absorption or the extinction of the incident radiation due to material. There is no restriction in the attenuation mechanism or material to apply the Bouger-Lambert law.

The absorbance A is a different way to relate the ratio of the intensities of the incident light and the transmitted light. It is defined as the log of the inverse of the transmission[59]

$$A = \log\frac{I_i}{I_{trs}} = -\log\frac{I_{trs}}{I_i} = -\log T \tag{3.59}$$

It is evident that the measurement of I_i and I_{trs} leads to the information of the absorption coefficient α and the imaginary part of the complex refractive index *k*. However, this kind of measurement should be done carefully to avoid or minimize unwanted effects like reflections from cuvette walls.[7]

3.4.2 Turbidity

When light passes through a particulate medium, it loses intensity due to absorption and scattering by particles in the medium. This loss of electromagnetic wave intensity defines extinction. If multiple scattering is negligible, the transmission Eq. (3.57) can be rewritten[7]

$$T = \frac{I_{trs}}{I_i} = \exp(-\alpha_{ext} l) \tag{3.60}$$

where the extinction coefficient α_{ext} is given by[7]

$$\alpha_{ext} = N_p C_{ext} = N_p (C_{abs} + C_{sca}) \tag{3.61}$$

In Eq. (3.61), N_p is the total number of particles per unit volume, C_{ext}, C_{abs}, and C_{sca} are the extinction, absorption and scattering cross sections, respectively.

Turbidity τ is defined as the logarithm of the ratio of transmitted to incident radiation if absorption and scattering are present. For diluted solutions, it has been shown that the turbidity is given by[19]

$$\tau = \ln I_i / I_{trs} = \alpha_{ext} l = N_p C_{ext} l \tag{3.62}$$

The turbidity $\tau(\lambda)$ measured at a given wavelength λ can be related to the number, size, and optical constants of suspended isotropic spherical particles through the Mie theory[19]

$$\tau(\lambda) = N_p (\frac{\pi}{4}) l \int_0^\infty Q_{ext}(m, x) D^2 f(D) dD \tag{3.63}$$

Where D is the particle diameter, and $f(D)$ is the normalized particle size distribution for spherical particles. The Mie extinction efficiency $Q_{ext}(m, x)$ is a function of the particle size parameter x and the complex refractive index ratio of the particle to the surrounding medium m.

Though it is not easy, turbidity Eq. (3.63) can be solved by inversion techniques, either analytical inversion or numerical inversion.[29] The resulting solution yields information regarding particle number, size distribution, or optical properties of material. Thus, it can be used in different ways depending on the information sought and the data available. For example, if the optical properties are known as functions of wavelength, Eq. (3.63) can be used to estimate the particle size distribution or vice versa.[35]

Measurement of extinction requires the exclusion of the forward-scattered light entering the detector. However, it is difficult to practice experimentally, especially for large particles because forward scattering is enhanced with increasing particle sizes.[7] Therefore, the term optical density (OD) that is defined as $\log\frac{1}{T}$, is frequently used to express the magnitude of the measured transmission[7,31] Taking this into account, optical density is preferably used to show the magnitude of the measured transmission in this dissertation following Bohren and Huffman.[7]

3.4.3 Beer-Lambert Law

If the attenuation of the incident wave is caused by the chromophores of the absorbing medium, transmission can be expressed using the molar absorption coefficient $\varepsilon(\lambda)$, the concentration of chromophores c, and the sample path-length *l*

$$T = \frac{I_{trs}}{I_i} = e^{-\varepsilon(\lambda)cl} \tag{3.64}$$

where

$$\varepsilon(\lambda) = \frac{4\pi k(\lambda)}{\lambda} \tag{3.65}$$

The molar absorption coefficient $\varepsilon(\lambda)$ is specific to the chromophores of substance and may be regarded as a subset of the absorption coefficient α defined in Eq. (3.56) that can be applicable to any absorbing material. Eq. (3.64) can be rewritten to obtain the Beer-Lambert law[19]

$$\ln I_{trs} / I_i = -\varepsilon(\lambda) \mathrm{c} l \tag{3.66}$$

The Beer-Lambert law expresses that the decreased incident light intensity is proportional to the molar absorption coefficient $\varepsilon(\lambda)$, the concentration of chromophores c, and the sample path-length *l*.

It is well known that the Beer-Lambert law is a special case of Mie theory. The turbidity expression τ becomes the Beer-Lambert law if there is no scattering due to small particle sizes, less than 10 nm for polystyrene, or the sample to medium refractive index ratio close to1.[19] If these requirements cannot be fulfilled, then scattering effects can be accounted for and removed from the measured extinction spectrum by deconvolution.[35]

3.5. Fluorescence Spectroscopy

If a molecule absorbs electromagnetic radiation, it can be stimulated to an electronically excited state. The molecule's inherent structure and the physiochemical characteristics of its local environment decide the molecule's pathway to the ground state. In some situations, it returns to the ground state by emitting electromagnetic

radiation. Fluorescence is the emission of light from the singlet excited states in which the electron has the opposite spin orientation as the ground-state electron.[32] Therefore, return to the ground state is spin-allowed and thus, end in the fast emission rates (10^8 s^{-1}). Typical fluorescence lifetime is about 10 ns.[32] Fluorescence has been known for more than 300 years and has proven to be an indispensable tool in biology, biochemistry, and chemistry because of its superb detection limits.[9] In this part of theory, the basic aspects of fluorescence spectroscopy and introduction to fluorescence anisotropy are described.

3.5.1. Characteristics of Fluorescence Spectrum

The energy level diagram illustrates absorption and emission of light by molecules as shown in Fig 3.5.[32] When the sample under investigation is irradiated, the molecules with the lowest vibrational energy primarily absorb the excitation energy. Electrons in the substance are generally excited to some higher vibrational levels of either S_1 or S_2 and then, with a few uncommon exceptions, promptly relax to the lowest vibrational level of S_1. This process is called internal conversion.[32] Because internal conversion usually occurs in 10^{-12} s, far shorter than fluorescence lifetime, it results in fluorescence emission from a thermally equilibrated excited state, i.e., the lowest-energy vibrational state of S_1.

If molecules in the S_1 state experience a spin conversion to the first triplet state T_1, this process is called intersystem crossing.[32] Phosphorescence is the emission of light from triplet states. It is forbidden transition and thus, results in the slow emission rates (10^3-10^0 s^{-1}).[32] The phosphorescence lifetimes are normally milliseconds to seconds.

The characteristics of fluorescence emission are I) Stokes' Shift - the wavelength of the emitted light is longer than that of the excited light, II) Kasha's Rule - the emission spectra are typically independent of the excitation wavelength, III) mirror image – in general, the emission is the mirror image of the $S_0 \rightarrow S_1$ absorption alone, not of the total absorption spectrum.[32]

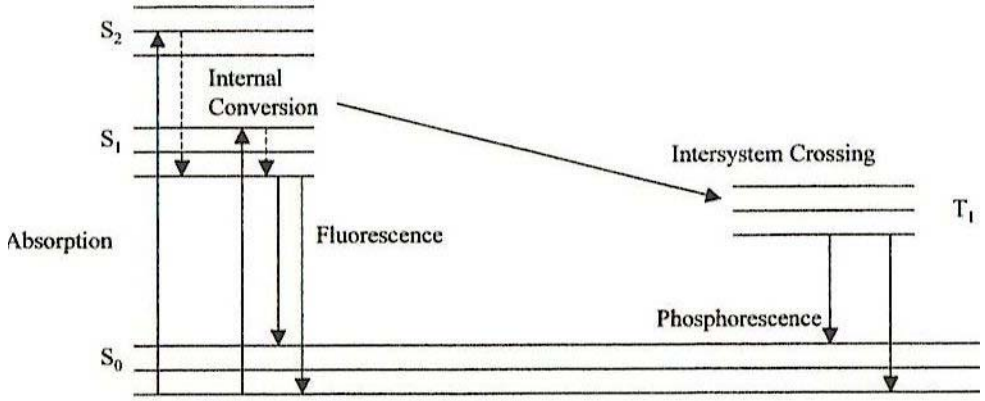

Figure 3.5 Energy level diagram illustrating absorption and emission of light by molecules. Adapted from Reference 32.

3.5.2. Fluorescence Lifetimes and Quantum Yields

The fluorescence quantum yield is defined by the ratio of the number of emitted photons to the number of absorbed photons and is expressed by[32]

$$\eta = \frac{\Gamma}{\Gamma + k_{nr}} \tag{3.67}$$

where Γ is the radiative rate constant and k_{nr} is the nonradiative rate constant. Both radiative and nonradiative processes depopulate the excited state as shown in the Fig. 3.6.[32]

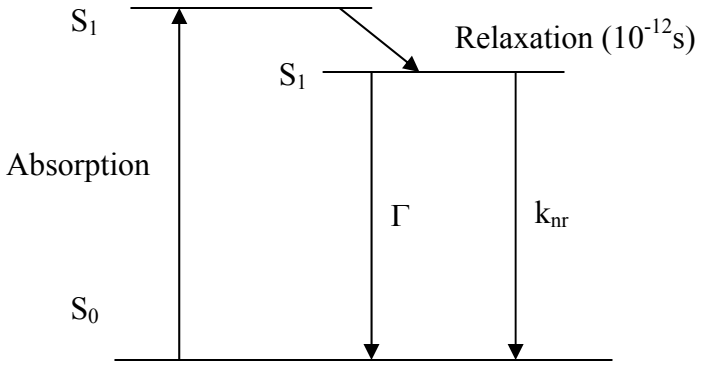

Figure. 3.6. Depopulation of the excited states by radiative and nonradiative decay. Adapted from Reference 32.

The fluorescence lifetime is the average time that the molecule spends in the excited state before its return to the ground state. Fluorescence lifetime is given by[32]

$$\tau_{fl} = \frac{1}{\Gamma + k_{nr}} \tag{3.68}$$

Because fluorescence emission is a random process, few molecules emit their photons at exactly $t = \tau_{fl}$. In case of a single exponential decay, 63% of the molecules have decayed

before $t = \tau_{fl}$ while 37 % decay after $t = \tau_{fl}$. Due to complexity, the determination of the lifetime from multiple exponential decays requires numerical analysis.[9,32]

3.5.3. Fluorescence Quenching

The decreases of fluorescence intensity by a wide variety of processes are called quenching.[32] For example, collisional quenching happens if the excited-state fluorophore is deactivated upon contact with some other molecule, the quencher, in solution. In case of static quenching, fluorophores form nonfluorescent complexes with quenchers and this process takes place in the ground state and does not depend on diffusion or molecular collisions. Quenching can also arise by numerous nonmolecular mechanisms like the attenuation of the incident light by the fluorophore itself or other absorbing species. Fluorescence quenching yields information necessary to understand the role of the excited-state lifetime to detect dynamic processes in solution or in macromolecules.[32]

3.5.4. Fluorescence Anisotropy

Anisotropy measurements are essential for the biochemical applications of fluorescence and yield information on the size and shape of proteins or the rigidity of various molecular environments.[32] Photoselective excitation of fluorophores by polarized light provides the grounds of anisotropy measurement because fluorophores favorably absorb photons of which electric vectors are aligned parallel to the transition moment of the fluorophore. The selective excitation follows a partially oriented population of

fluorophores (photoselection) and partially polarized fluorescence emission.[32] The fluorescence anisotropy r_{fl} and polarization P_{fl} are given by[9,32]

$$r_{fl} = \frac{I_{fl//} - I_{fl\perp}}{I_{fl//} + 2I_{fl\perp}} \quad , \qquad P_{fl} = \frac{I_{fl//} - I_{fl\perp}}{I_{fl//} + I_{fl\perp}} \tag{3.69}$$

where $I_{fl//}$ and $I_{fl\perp}$ represent the fluorescence intensities of the vertically (//) and horizontally ($\perp$) polarized emission if the sample is excited with the vertically polarized light. Anisotropy can be converted into polarization and vice versa using Eq. (3.70)[32]

$$P_{fl} = \frac{3r_{fl}}{2 + r_{fl}} \quad , \qquad r_{fl} = \frac{2P_{fl}}{3 - P_{fl}} \tag{3.70}$$

CHAPTER 4. DEVELOPMENT

This chapter provides information pertinent to the development of the Integrated UV-VIS MAMW spectrometer. For development background, the analysis of the research activities related to the prototype MAMW spectrometer that motivated the development of the Integrated UV-VIS MAMW spectrometer is described. The development became possible by observing and fully enabling the characteristics of each instrument that constitutes the Integrated UV-VIS MAMW spectrometer. Specifications of each instrument, the design criteria, and overall lay out of the Integrated UV-VIS MAMW spectrometer are described in this chapter. The credibility of the measured UV-VIS MAMW spectra depends on the reproducibility of the data and the angle of acceptance. Therefore, the last two sections of the chapter discuss procedures necessary to secure the reproducibility of the measured data and the analysis of the effect of the angle of acceptance.

4.1. Development Background

This section provides the development background of the Integrated UV-VIS MAMW spectrometer. It includes the description of the prototype MAMW spectrometer and the analysis of its limitation. Methods that overcome the shortfalls of the prototype

MAMW spectrometer and lead to the development of the Integrated UV-VIS MAMW spectrometer are described in detail.

4.1.1. Description of the Prototype MAMW Spectrometer

Dr. Bacon developed a MAMW spectrometer that has the capacity of measuring the scattered light from 30^o to 90^o within the wavelength range of 400 ~ 800nm.[2] Throughout this dissertation, we will designate it as the prototype MAMW spectrometer. It utilized Oriel Instruments model 6333 100-W tungsten-halogen lamp that was installed in Oriel 60020 convective lamp housing as light source, a 200 μm UV transparent optical fiber as incident light delivery tool, and an Ocean Optics S2000 production miniature CCD diode array spectrometer (S2000 production spectrometer) as detector. In addition, a fused silica lens with 13 mm diameter and 25 mm focal length was attached in front of the detector to collect scattered light. The schematic of the prototype MAMW spectrometer is shown in Fig.4.1.[2]

The prototype MAMW spectrometer had been tested by measuring the JPPD of the selected particle standards simultaneously and validated by comparing the measured results to the ones obtained by simulations. These standards include polystyrene spheres (500 nm, 1 μm, 10 μm, hollow 1μm, and red dyed 3 μm), silica (470 nm, 1 μm), and silver chloride cube (500 nm) in water and pure red blood cells in saline. Fig.4.2.a and Fig. 4.3.a show the MAMW response surface of polystyrene 1 μm standard in water measured by the prototype MAMW spectrometer and the contour plot, respectively.[2]

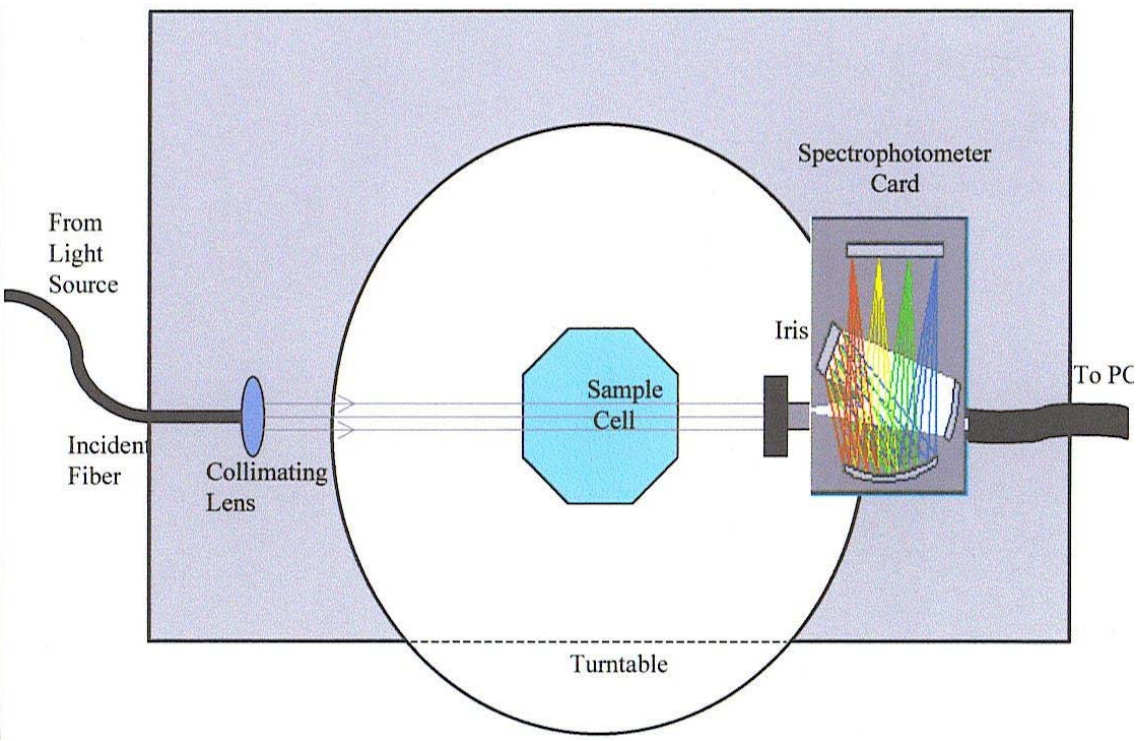

Figure.4.1. Schematic of the prototype MAMW spectrometer. Cited from Reference 2.

Fig.4.2.b and Fig. 4.3.b represent the simulated MAMW response surface of polystyrene 1 μm standard in water and its contour plot, respectively.[2] The fact that the measured MAMW responsive surfaces of polystyrene and silica standards are consistent with those obtained by simulation had proved the proposition that MAMW spectroscopy could be a modality of micron and sub-micron size particle characterization by the simultaneous detection of the JPPD.

4.1.2. Limitations of the Prototype MAMW Spectrometer

The prototype MAMW spectrometer has some limitations in both measurement ranges and applicable methodologies despite its success in proof of the particle characterization by the simultaneous JPPD measurement concept. These limitations are as listed:

1. Lack of the low-angle scattering measurement capability: the prototype MAMW spectrometer was unable to perform scattered light measurements at angles lower than 30^{o},
2. Inability to perform measurements in the UV range: measurements were done only in the visible to short NIR range of 400 ~ 800 nm and
3. Inability to adopt spectroscopic techniques other than light scattering: incorporation of transmission and fluorescence spectroscopy or polarization optics was not possible.

Measurement of the low-angle scattered light is crucial for the characterization of large size particles including biological particles such as bacteria or blood cells because

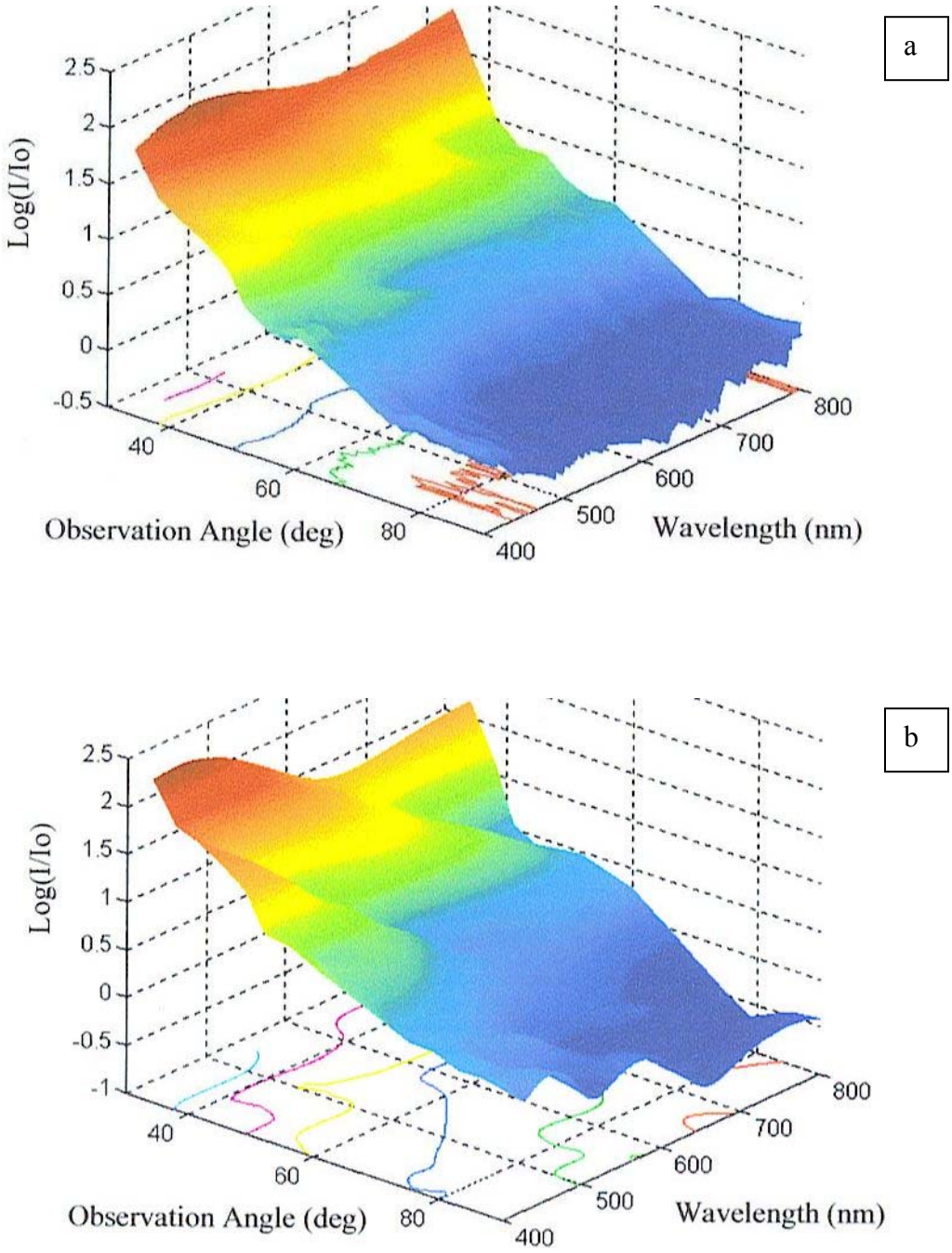

Figure 4.2. MAMW response surfaces of polystyrene 1 μm standard in water. a) MAMW response surface of polystyrene 1 μm standard in water measured by the prototype MAMW spectrometer. b) Simulated MAMW response surface of polystyrene 1 μm standard in water. Cited from Reference 2.

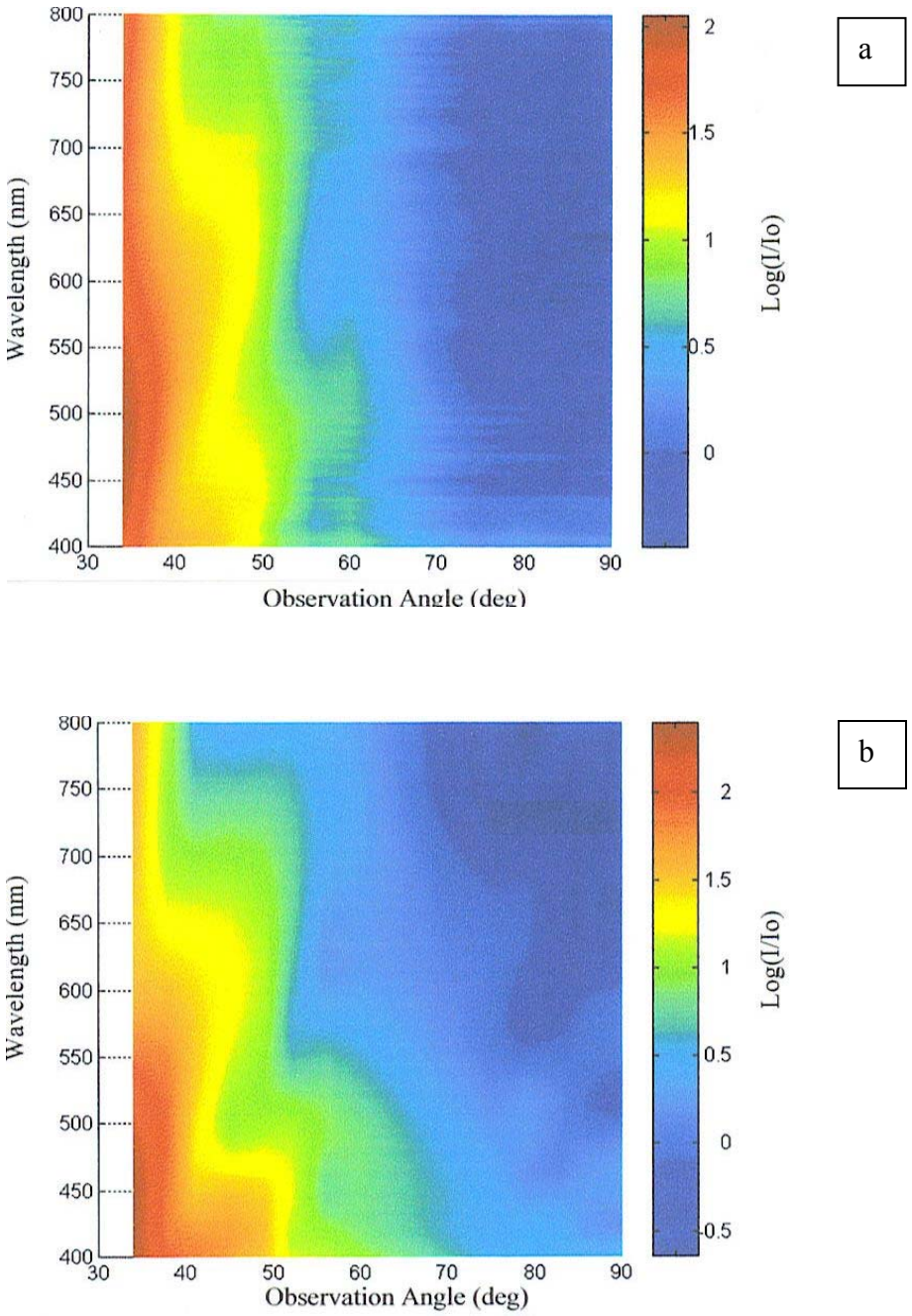

Figure. 4.3. Contour plots of MAMW response surfaces of polystyrene 1 μm standard in water. a) Contour plot of MAMW response surface of polystyrene 1 μm standard in water measured by the prototype MAMW spectrometer. b) Contour plot of the simulated MAMW responsive surface of polystyrene 1 μm standard in water. Cited from Reference 2.

increased particle size enhances forward scattering or diffraction as shown in Fig. 4.4, simulated Rayleigh ratios for particles with different sizes.[17]

The UV spectroscopy is important for biological particle characterization due to the absorption of UV light by DNA (260 nm) and protein (280 nm). Moreover, the use of UV light can reinforce the capability of small size particle characterization because the increased ratio of particle size to the wavelength of the incident light enhances the interference effects. Therefore, the adoption of UV light is desirable for the MAMW spectrometer. Besides, transmission and fluorescence spectroscopy will add additional dimensions to the particle characterization capabilities of the MAMW spectrometer because they are superb in the detection of particle composition. Taking all these into consideration, the necessity of developing a MAMW spectrometer that encompasses all the merits stated above has drawn significant research interests, especially for the characterization of biological particles.

4.1.3. Development of the Integrated UV-VIS MAMW Spectrometer

The limitations of the prototype MAMW spectrometer are attributed to:

1. the use of single integration time for the S2000 production spectrometer and
2. the adoption of optical fiber as the incident light delivery tool.

Firstly, considering the fact that the scattered light intensity varies several orders of magnitudes depending on particle sizes, ways to avoid the detector saturation should be devised. Typically, this can be done by the insertion of neutral density filter (NDF).[7]

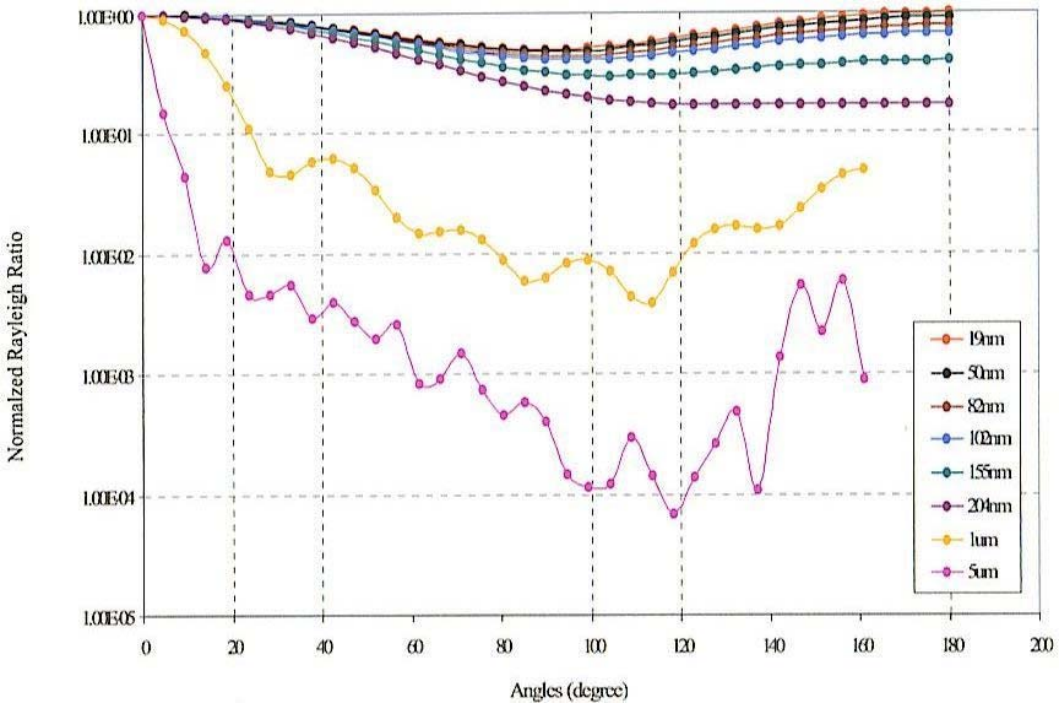

Figure 4.4 Simulated Rayleigh ratios for particles with different sizes. Cited from Reference 17.

However, there was no room for NDF in case of the prototype MAMW spectrometer because of the use of fiber. Another way to avoid the detector saturation is adjusting the signal intensity by manipulating integration time. In case of Ocean Optics S2000 spectrometer, this can be done by the OOIBase32 spectrometer operating software that is installed in the computer. The reason is unclear but single detector integration time of 2000 ms had been used for all the measurements done with the prototype MAMW spectrometer. Because this integration time was set for the measurement of the scattered light from 30^{o} to 90^{o}, which has several orders of magnitude weaker intensity compared to that of the low-angle scattered light, it is apparent that the detector saturation made the low-angle scattering and transmission measurements not possible.

Secondly, optical fiber strongly absorbs UV light and thus, resulted in the disparity in intensities between UV light and VIS light as shown in Fig.4.5.[2] As a result, UV light was not used in the prototype MAMW spectrometer. Moreover, optical fiber allows only small portion of light to be delivered to the sample cell due to its small cross section. Consequently, weak signal intensity made fluorescence measurement unfeasible.

Methods to overcome the limitations of the prototype MAMW spectrometer have been sought. These include:

1) use of UV-VIS fused silica lenses as light delivery tool,
2) adoption of a method of integration time multiplexing (ITM), optimized use of the dynamic range of Ocean Optics S2000 production spectrometer, to avoid detector saturation and

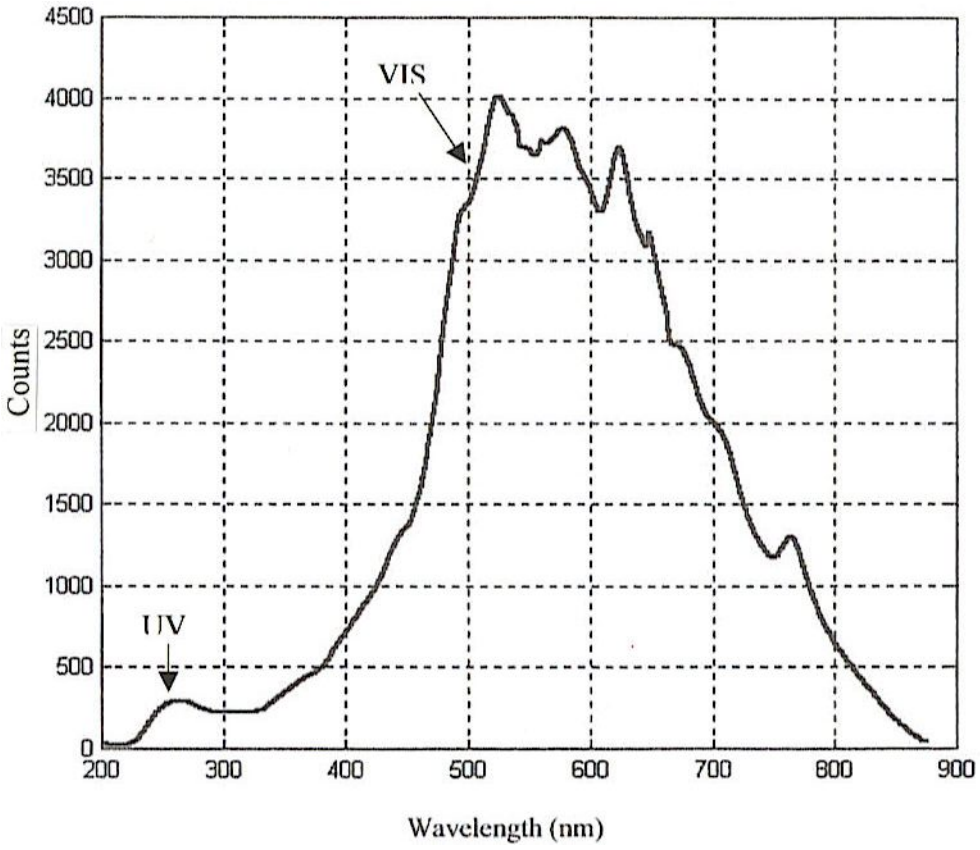

Figure 4.5. UV-VIS beam spectrum measured with the prototype MAMW spectrometer. Note the disparity in intensities between UV and visible beam due to the use of optical fiber as incident light delivery tool. Cited from Reference 2.

3) installation of a couple of narrow width slits before and after the sample cell (cuvette) to enhance the capability of the low-angle scattered light detection.

Typical uncoated fused silica UV lens is transparent from 190 nm to 2100 nm.[39] Therefore, very little UV light is absorbed by lens and thus, the disparity between the intensities of UV light and visible light becomes negligible with the adoption of lenses as shown in Fig. 4.6. Besides, lens has large cross section compared to the fiber. As a result, the intensity of light delivered via lens is far stronger than that delivered via fiber. Consequently, the measurement of the fluorescence spectra with the MAMW spectrometer becomes feasible with the adoption of lenses.

Ocean Optics S2000 spectrometer has 2 x 10^8 dynamic range that is determined by multiplying the ratio of the maximum to the minimum integration time (2 x 10^4 for 3 msec sec to 65 sec) by the ratio of the maximum to the minimum signal counts for single scan (2 x 10^3 for 2 to 4000 signal counts).[43] Therefore, if we choose the proper integration time, detector saturation can be avoided and the detection of transmitted or scattered light for a wide range of angles without the use of NDF becomes possible. Fig. 4.7 illustrates the UV-VIS beam spectra recorded with different integration times. It shows that the intensity of UV-VIS beam is proportional to the used integration time. For the Integrated UV-VIS MAMW spectrometer, integration time of 5,000 msec (1 x 10^3) has been used. Together with a single scan dynamic range, this yields dynamic range of $10^5 \sim 10^6$. The intensities of signals caught with different integration times must be corrected for the standard integration time and this can be accomplished by multiplying the proper integration time ratios.

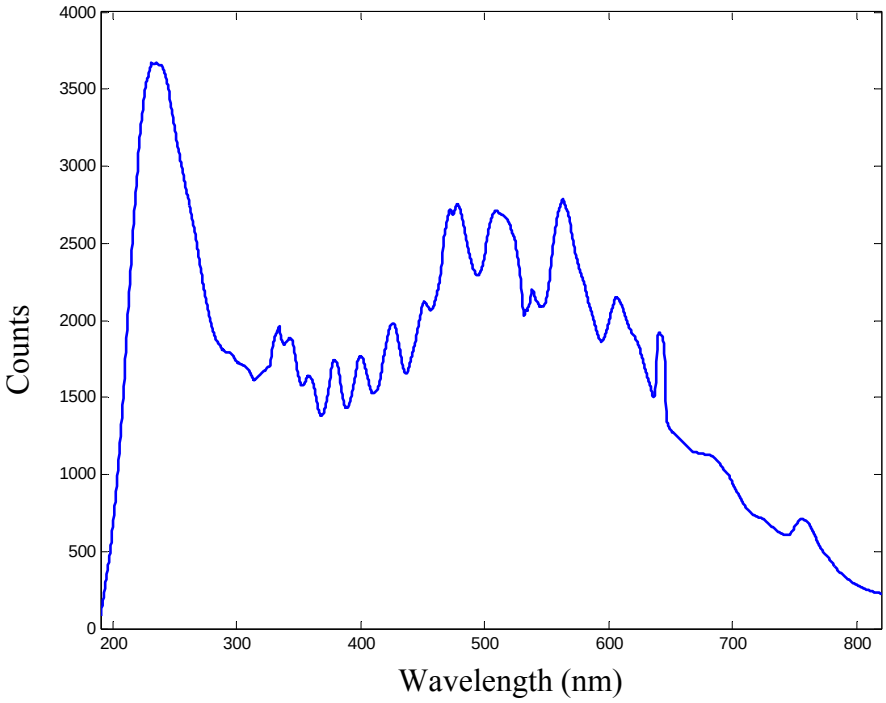

Figure 4.6. UV-VIS beam spectrum measured with the Integrated UV-VIS MAMW spectrometer. Disparity in intensities between UV beam and visible beam is negligible due to the use of lenses.

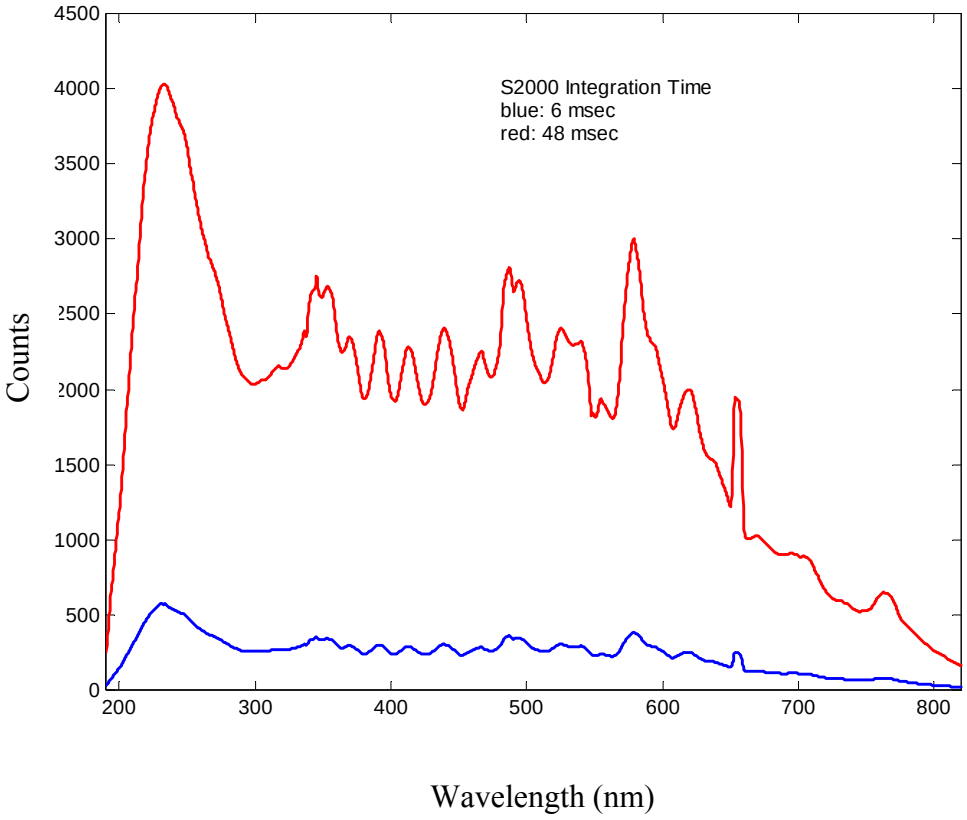

Figure 4.7. UV-VIS beam spectra measured with the Integrated UV-VIS MAMW spectrometer with different integration times. The UV-VIS beam intensity is proportional to the integration time. No neutral density filter was used for this measurement.

The detection of the low-angle scattered light requires the use of well-collimated narrow width incident beam. This becomes possible with the use of a collimation lens and a couple of narrow width slits installed before and after the sample cell. The narrow width slits adjust the width of the incident beam and the scattered light that enters the receiving optics. Unlike fiber, the collimation lens ensures large collimation length of the incident beam near the sample cell and thus, enables the optimum separation of the sample cell and the receiving optics. Together with the adjustable integration time, the use of narrow width slits and collimation lens enables the detection of the low-angle scattered light.

The development of the Integrated UV-VIS MAMW spectrometer becomes feasible by the adoption of UV lenses, integration time multiplexing, and narrow width slits. Because it can perform not only scattering but also transmission and fluorescence spectroscopy, it is an integrated spectrometer. The Integrated UV-VIS MAMW spectrometer has the capabilities of performing:

1. low angle scattering measurement starting from 4^{o} with simultaneous detection of multi-wavelength light from 200 nm to 820 nm,
2. UV-VIS transmission measurement with wavelengths for analysis ranging from 200 nm to 800 nm, and
3. UV-VIS fluorescence spectra measurement.

As a result, the Integrated UV-VIS MAMW spectrometer can yield abundant information necessary to characterize micron and sub-micron size particles. Moreover,

the use of lenses allows room to install polarization optics to measure the 16-element Mueller matrix for light scattering, linear or circular dichroism in transmission, and fluorescence anisotropy.

4.2. Instruments

Specifications of the instruments used to build the Integrated UV-VIS MAMW spectrometer are described in this section. Particularly, the characteristics of each instrument are provided in detail because the development of the Integrated UV-VIS MAMW spectrometer was possible by fully enabling them.

4.2.1. Light Source

Ocean optics DT-1000 deuterium tungsten-halogen light source is selected as the light source of the Integrated UV-VIS MAMW spectrometer. It provides the continuous UV to short NIR light in the spectral range of 200 ~ 1100 nm. Its dimension is 310 mm (L) x 172 mm (W) x 175 mm (H). The output power of deuterium lamp is 30 W and that of tungsten-halogen lamp is 6.5 W. The peak-to-peak stability is 0.05 % (maximum) and drift is ± 0.5% per hour.[43] Fig. 4.8.a is the photograph of DT-1000 light source and Fig. 4.8.b shows its inside structure. Fig. 4.9 is the schematic of bulbs and a UV-VIS beam focusing lens. Visible light emitted from the tungsten-halogen (T-H) bulb diffuses everywhere. As a result, the shadow of filament is removed and the diffused beam

a

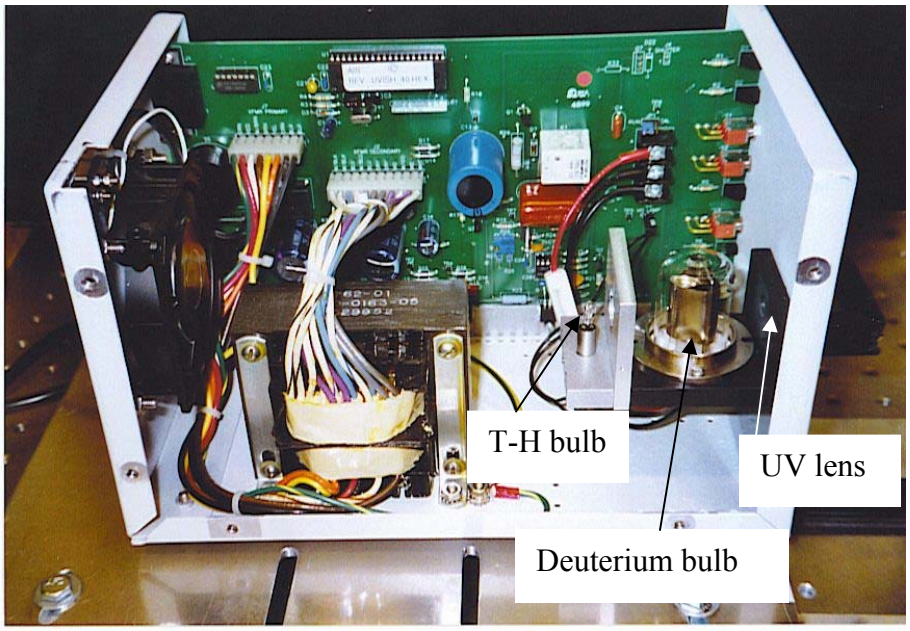

b

Figure 4.8. Photographs of Ocean Optics DT-1000 light source. a) Exterior view. b) Inside structure.

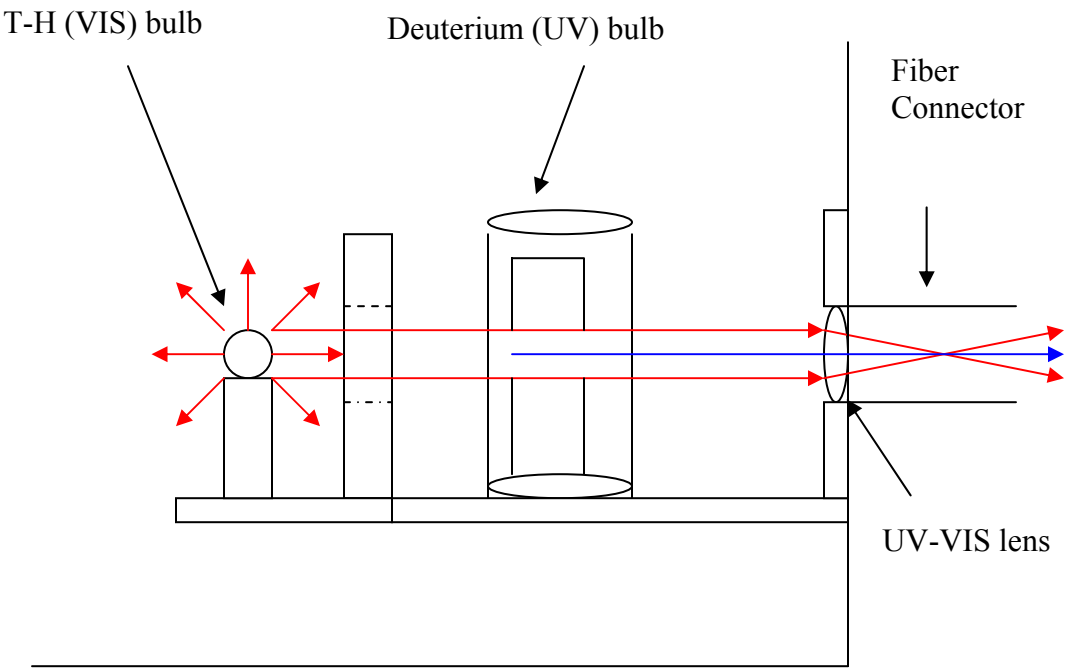

Figure 4.9. Illustration of UV-VIS beam combination inside the DT-1000 light source.

becomes spatially uniform. Part of the diffused beam passes through the hole made in aluminum plate that separates tungsten-halogen and deuterium bulbs and enters the deuterium bulb, the source of UV light. The metal reflectance plate inside the deuterium bulb also has a hole and allows the penetration of the visible light. Therefore, without the use of any beam-combiner, the visible light is combined with the UV light and the combined beam can be placed in a single optical path. The combined UV-VIS beam enters the fused silica lens with 5 mm diameter and 10 mm focal length. The lens originally has the role of focusing the UV-VIS beam to the tip of optical fiber that is connected to the DT-1000 light source. The output UV-VIS beam from the DT-1000 light source is collected and collimated by fused silica lens with 50 mm diameter and 76 mm focal length and sent to the sample cell. In case of the Oriel 6333 visible light source, which was used for the prototype MAMW spectrometer, the lamp stability was not good because it uses air convection system to cool down the bulb. The intensity fluctuation of visible output became noticeable after 3 hours operation.[2] On the other hand, for the DT-1000 light source, a cooling fan is adopted to cool down the bulbs and thus, very good stability of the output beam intensity is achieved. Once the lamp output is stabilized, less than 1 percent of the maximum intensity fluctuation was observed even after the 10 hours of continuous usage. Spatially uniform beam quality and long-term output power stability make the DT-1000 light source suitable as the light source for the Integrated UV-VIS MAMW spectrometer.

4.2.2. Optics

Multiangle-multiwavelength spectroscopy covers spectral range from UV to short NIR region. Therefore uncoated UV grade fused silica lenses, which are transparent from 190nm to 2100 nm, are selected to deliver incident and scattered light. Total of five lenses are used in the construction of the Integrated UV-VIS MAMW spectrometer. For convenience, each lens will be designated by L1, L2, L3, L4 and L5, respectively. L1 represents the lens for the incident UV-VIS beam collimation. L2 is the lens for focusing the incident light to the sample cell in case of fluorescence measurement. L3 designates the objective lens that collects light from the sample cell. L4 represents the lens for steering the collected light to the focusing lens, and L5 is the focusing lens that focuses the received beam to the spectrometer. Table 4.1 shows the specification of these lenses. All the lenses except L5 are plano-convex lenses because this type of lens is proper to obtain good collimated beam. Ideally the use of achromatic lenses is desirable because they minimize chromatic aberration, the variation of lens focal length with different wavelength light. The effect of chromatic aberration is significant in case of UV light. However, there are no commercially available achromatic lenses that cover spectral range from UV to visible and thus, the idea of using the achromatic lenses is abandoned. In case of L5, bi-convex lens is chosen in order to secure more power and thus, improve the signal sensitivity at the detector end.

Table 4.1. Specification of lenses used for the Integrated UV-VIS MAMW spectrometer

Lens	Manufacturer	Model	Focal length	Diameter	f-number* (f/#)
L1	Thorlabs	LA4078	75mm	51mm	1.5.
L2	Newport	SPX019	76mm	25mm	3.0
L3	Newport	SPX016	50mm	25mm	2.0
L4	Newport	SPX016	50mm	25mm	2.0
L5	Newport	SBX019	25mm	25mm	1.0

* f/# = focal length of lens / lens diameter

4.2.3. Slits

Slits are necessary to obtain a narrow-width uniformly collimated beam to irradiate the sample cell and to allow only the scattered or transmitted light within the angle of acceptance enters the detector. Initially a couple of slits with adjustable width were made using aluminum plates and razor blades. Fig. 4.10 shows the schematic of these slits. Both slits have the same dimension of 51 mm x 51 mm x 3 mm. The size of razor blade is 17 mm (W) x 42 mm (H). A rectangular aperture of 9 mm (W) x 25 mm (H) was made in the middle of each plate. The maximum achievable slit width is determined by this aperture width. Desired slit width can be obtained by sliding two razor blades that are placed in the grooves on the top and bottom of the plate. It is pointed out that slits, especially the one between the cuvette and the objective lens, should be made using sharp edges such as razor blades to prevent any stray light entering the receiving optics through the reflection at the edges.[58] However, it was observed that the edge of the razor blade also deflects light due to its dimension. Thus, the idea of using the sharp edges was discarded. To minimize the reflection from the slit or the slit mount, the razor blades are either wrapped with black tapes or stained using a black marker pen and the aluminum plates are covered with black felt.

During the last phase of research, the structure of the slits was slightly modified to minimize the amount of background UV light, which originates from stray reflection, entering the receiving optics. This is described in detail in Section 5.3.5.

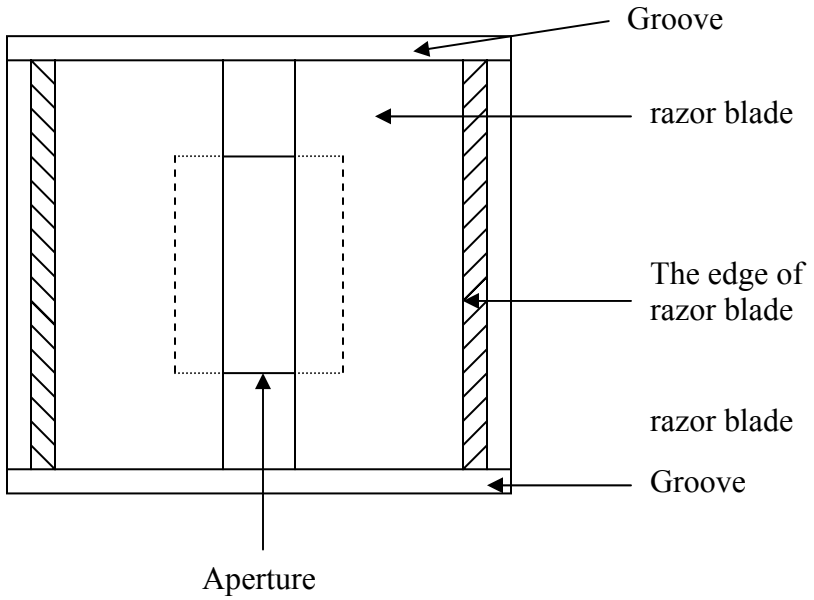

Figure. 4.10. Schematic of the slit with adjustable width. The size of the rectangular aperture is 9mm (W) x 25 mm (H).

4.2.4. Sample Cell

The sample cell plays an important role in the UV-VIS MAMW spectroscopy because the shape of the sample cell also imposes limitation on measurable scattering angles. Moreover, the required corrections of the measured results vary depending on the shape of the sample cell. Different shapes of sample cells are available for the light scattering measurements. These include rectangular, cylindrical, semi-octagonal, octagonal, and other cells of various shape.[2] Dr. Bacon summarized the relation between the shape of the sample cell and the limitation it imposes on the scattering measurements.[2] In case of cylindrical cells, the measurement of light scattering for a wide range of angles is possible. In addition, refraction correction is not necessary. However, they were not used for the MAMW spectrometer due to the fact that low angles are not accessible because of multiple reflections from the walls.[53] Instead, two different quartz sample cells, a rectangular fluorescent cuvette and an octagonal cell were used for the measurement of the UV-VIS MAMW spectra.

The octagonal cell that permits measurements on all sides of the cuvette was adapted from the semi-octagonal cell developed by Brice et al.[2,8] It was used as the sample cell for the prototype MAMW spectrometer. It is a custom product made by Precision Glass, Inc. The cuvette is made of Spectrosil® quartz plates and transparent from170 nm to 2700 nm. In order to minimize refraction effects, only 1 mm thick plates were used to make it. Its width is 25 mm and height is 50 mm. The octagonal cell yields eight perpendicular faces at observation angles of 45, 90, 135, 180, 225, 270, 315, and 360 degrees. Consequently, it allows the simultaneous measurement of scattering,

fluorescence and transmission spectra. On the other hand, the corners of the octagonal cell obstruct scattering measurements at 22.5, 67.5, 112.5, 157.5, 202.5, 247.5, 292.5, and 337.5 degrees. The measurement results acquired using the octagonal cell may require corrections for reflection and refraction. The octagonal cuvette is not much used for the Integrated UV-VIS MAMW spectrometer because it is very fragile while its replacement is not easy due to expensive cost and substantial waiting time for production. Therefore, its usage was limited for the scattering measurements that require measurements at observation angles greater than 35^{o}.

For main experiments, a commercially available quartz rectangular fluorescent cell was adopted (Starna Cells, Inc. Model # 23-Q-10). All four windows of the cell are polished and transparent. Its dimension is 12.5 mm (W) x 12.5 mm (L) x 48 mm (H) and path length is 10 mm. Because it is made of Spectrosil® Far UV quartz, it has no background fluorescence. This cuvette was used for the scattering measurements of up to 35^{o} in observation angle due to the refraction from the second face. The scattering measurement results acquired using the rectangular cuvette particularly needs the correction of:

1) refraction because the scattered light does not incident perpendicularly on the face of the cuvette except at the angles of 0, 90, 180, and 270 degrees and
2) the variation of the scattered-light path length because the scattered-light path length is not identical at all the angles.

The methods of implementing the required corrections that are originated from the shape of the sample cell are described in detail in section 5.3.

4.2.5. Goniometer

A goniometer from the Brice-Phoenix type spectrophotometer system was used to build the UV-VIS MAMW spectrometer. The Brice-Phoenix type spectrophotometer is so reliable that it has been actively used for light scattering experiments requiring absolute calibration.[8] The diameter of the goniometer turntable is ~ 40 cm. The minimum angular resolution that is achievable by this turntable is 0.2^{o}. All the angular adjustments were carried out by manually rotating the goniometer turntable.

4.2.6. Spectrometer

The nature of MAMW spectroscopy requires the use of portable spectrometer that can be installed on the goniometer arm. Ocean Optics S2000 production CCD diode array spectrometer was chosen as the spectrometer for both the prototype and the current Integrated UV-VIS MAMW spectrometer because of its good spectral resolution, high light throughput, and low levels of stray light detection.[2]

S2000 production spectrometer is a kind of S2000 spectrometer but different from typical S2000 spectrometer in appearance. Unlike typical S2000 spectrometer, optical bench of S2000 production spectrometer, S-optical bench that is used for the all S2000 series spectrometer, is mounted on an electronics board with 100 mm x 130 mm size. S2000 production spectrometer is different from PC 2000 spectrometer that also has

s-optical bench mounted on the pc board for installation into the motherboard of a desktop PC.[43] *S2000 production or PC 2000 spectrometer has the same features of typical S2000 spectrometer because all of them use S-optical bench. Therefore, all these are virtually identical spectrometers.*

The dimension of S-optical bench is 89 mm x 63 mm x 18 mm. The S-optical bench is designed to accept light from a single optical fiber. Fig. 4.11 shows the schematic of S-optical bench.[43] The focal length of the S2000 spectrometer is 42 mm and the f-number (f/#), which can be obtained by dividing the focal length of the collimating mirror by its diameter, is 3.3.[62] A Czerny-Turner type grating that has groove density of 600 lines/mm and spectral range of 200 ~ 850 nm with blaze wavelength at 400 nm is fixed in place at the time of manufacture. The efficiency curve for this grating is shown in Fig.4.12.[43] Light diffracted by grating is caught on the Sony ILX511 shallow-well linear CCD array silicon detector. It is composed of 2048 pixels and each pixel has size of 14 μm x 200 μm. The well depth of each pixel is 62,500 electrons. It has the sensitivity of 90 photons per count or 2.9×10^{-17} joules per count at 400 nm. The corrected linearity is greater than 99.8%. The maximum signal to noise ratio of detector is 250:1 at full signal and its spectral range is 200 ~ 1100 nm. For our S2000 production spectrometer, the standard window of the CCD detector is replaced by a quartz window coated with a phosphor material in order to enhance the performance of the spectrometer for UV applications. The entrance slit is 25 μm wide and 1 mm high. The corresponding pixel resolution for 25 μm width is ~ 4.2 pixels.

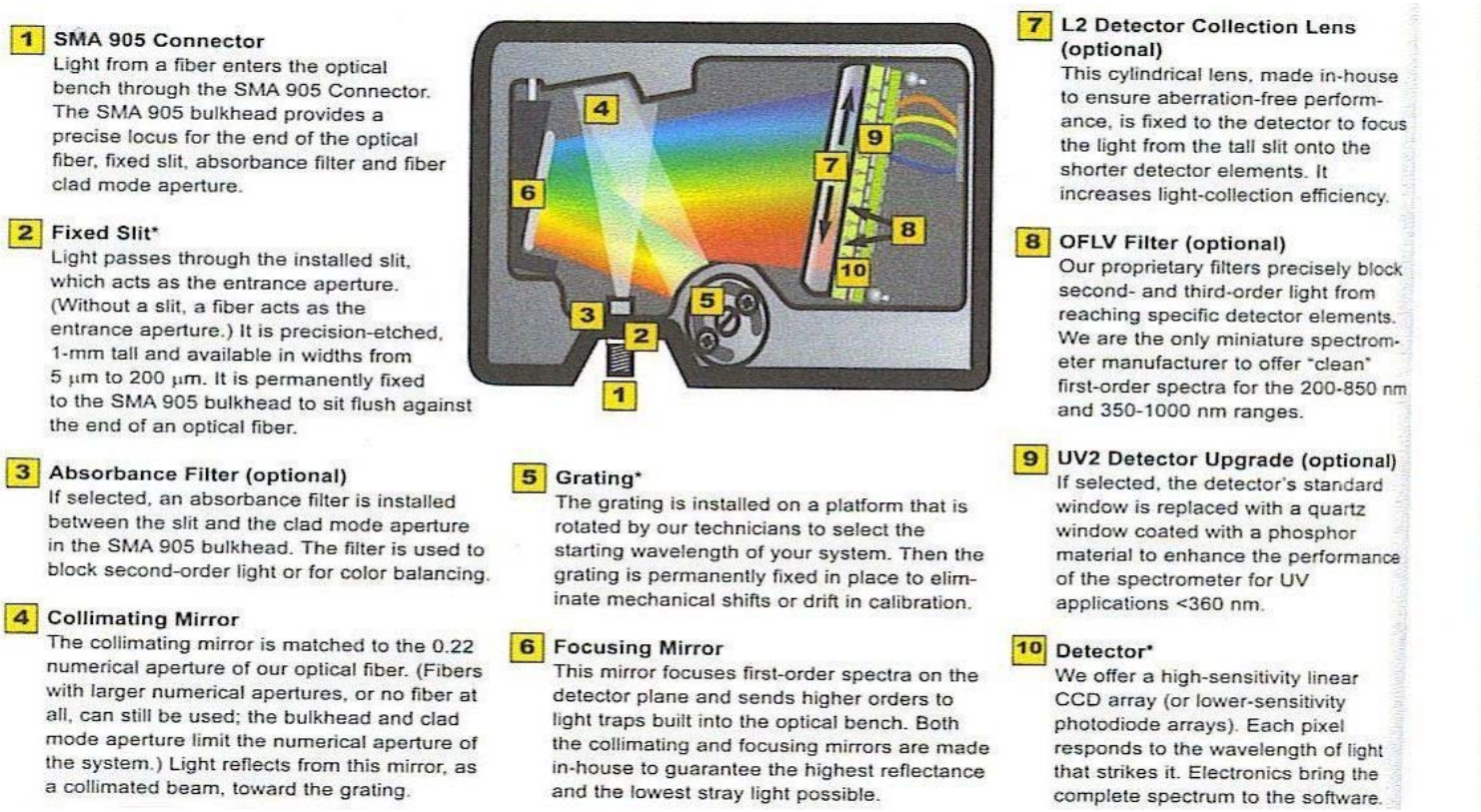

Figure. 4.11. Schematic of the optical layout of S-optical bench that is used for all the S2000 series spectrometer.[43] (Courtesy of Ocean Optics, Inc.)

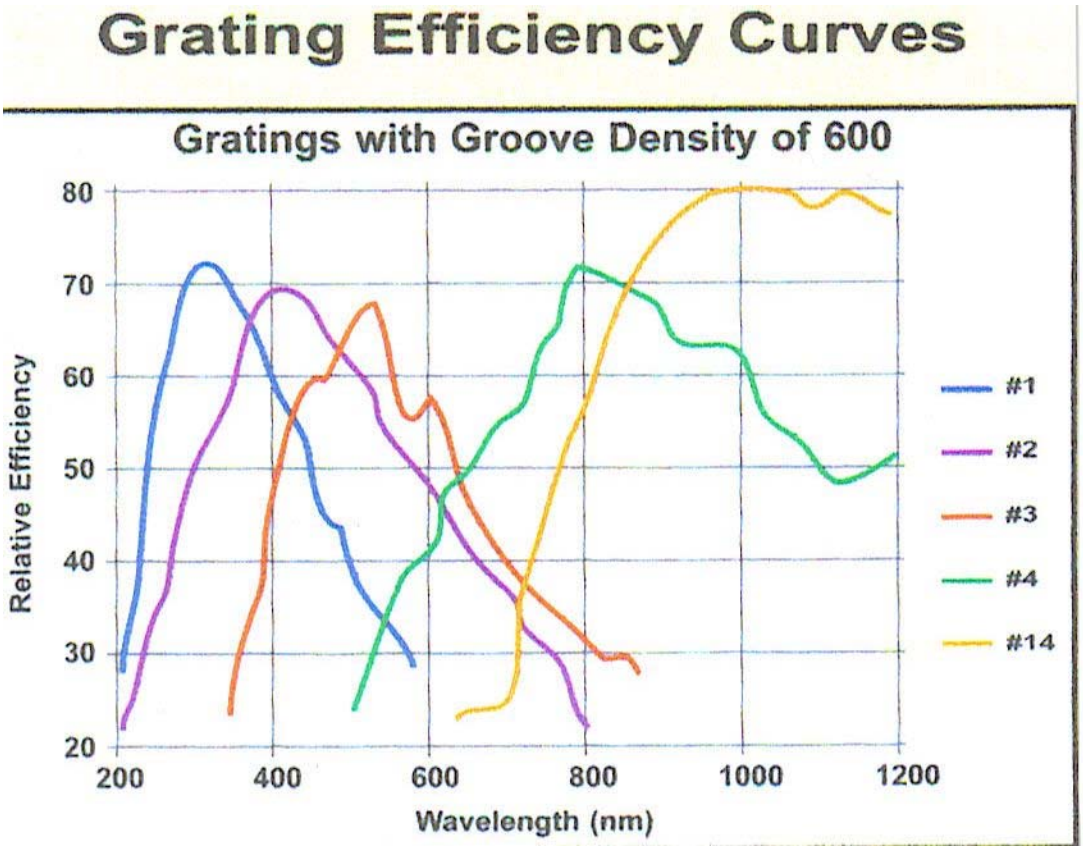

Figure 4.12. Grating efficiency curves for the S-optical bench.[43] # 2 grating that covers 200 nm to 800 nm is currently used for the S2000 production spectrometer. (Courtesy of Ocean Optics, Inc.)

The optical resolution, measured as Full Width Half Maximum (FWHM), of the spectrometer is given by[43]

$$\text{Optical resolution (nm)} = \frac{\text{Gratings spectral range (nm) x pixel resolution(pixels)}}{\text{Total detector elements (pixels)}} \quad (4.1)$$

Thus, the optical resolution of the current S2000 production spectrometer is 1.33 nm.

The rate of data acquisition is determined by the data acquisition card. An Ocean Optics ADC – 500 analog-to-digital conversion (ADC) board has been used for the data acquisition. It has12 bit, 4 channel conversion and maximum 500 kHz A/D frequency.

The spectrometer is controlled by OOIBase32 Spectrometer Operating Software, a 32-bit, user-customizable, advanced acquisition and display program. It can collect data from up to 8 spectrometer channels simultaneously and display the results in a single spectral window. With OOIBase32, different spectroscopic measurements are possible using scope mode, absorbance mode, transmission mode, and relative irradiation mode. The scope mode can be used to measure sample signal, reference, and background noise directly. Time domain experiment is also possible via external hardware trigger function, though not used in this research.[43] In addition, OOIBase32 software has a function to control spectrometer integration time. The nominal dynamic range of S2000 spectrometer is 2×10^8. However, the practical dynamic range is limited by signal to noise ratio and it can be enhanced by using signal averaging functions that increases the signal to noise ratio. In OOIBase32 software, time base and spatial base signal averaging are available.

The time based analysis is done by a recursive filter of $\mathbf{n_s}$ average samples where the newest sample replaces the oldest. If observed spectral structures are broad, spatial averaging or boxcar averaging can be used to improve signal to noise ratio. This can be done by averaging $\mathbf{n_p}$ pixel values side by side and replaces the center value with an averaged value. Because spatial and time based algorithms are uncorrelated, the improvement in signal to noise ratio is the product of the two processes.[62] Ocean Optics S2000 series spectrometers are optimized for minimum stray light. It is manufactured to remove possible sources of stray light except scattered light from the grating. Because the exposure to stray light from the grating is rather uniform across the CCD array, this can be measured and mathematically removed. OOI base32 software has algorithms to do this. In addition, this software automatically corrects electrical-dark signal and prevents the drift of dark current.[62]

4.3. Set Up

This section describes the design criteria and the overall lay out of the Integrated UV-VIS MAMW spectrometer. Especially, optics lay out and alignment procedures are described in detail.

4.3.1 Design Criteria for the Integrated UV-VIS MAMW Spectrometer

Different spectrometer requires different design criteria depending on its applications. In case of the Integrated UV-VIS MAMW spectrometer following design criteria should be satisfied:[2,56]

1. Maximum sensitivity – it should have sensitivity over orders of magnitude to detect scattered light originates from a wide range of scattering angles,
2. Quick measurement – multiangle-multiwavelength spectra should be measured within the temporal equilibrium of samples,
3. Information rich – Measured spectra should produce ample information necessary to characterize complicated particles using the JPPD,
4. Reproducibility – stability of the instruments should be guaranteed and
5. Statistically meaningful data – measured data should be statistically reliable.

Among them requirements 1 to 3 are directly related to the available instruments, especially, the output power of light source and detector sensitivity. Therefore, much attention was paid to secure the stability of the instruments and the acquisition of statistically meaningful data during the design stage.

4.3.2 Description of the Integrated UV-VIS MAMW Spectrometer Set Up

The prototype MAMW spectrometer had been built inside the Brice-Phoenix type spectrometer. For this type of spectrometer, sample cell and detector are set in a metal box to prevent ambient light entering the detector. However, this box was removed during the construction of the Integrated UV-VIS MAMW spectrometer for large room and ease of alignment. Background light can be prevented from entering the detection optics by turning off room light during the measurement.

Fig. 4.13 is the photograph of the Integrated UV-VIS MAMW spectrometer and Fig.4.14 is its schematic. The light source, Ocean optics DT-1000 UV-VIS light source, is secured on the optical bench. A fused silica neutral density filter is placed in front of the lamp and used to adjust the beam intensity during the alignment procedure if necessary. The UV- VIS light proceeds to the collimation lens L1. Because of the large diameter of lens L1, 50 mm, there is no loss of incident light and good collimated beam with comparable UV and visible light cross sections is obtained. The diameter of UV beam is 22 mm and that of visible beam is 18 mm at the location of sample cell. In addition, large diameter reduces aberration effects. A focusing lens L2 may be installed after the lens L1 in case of fluorescence measurement. This lens focuses the incident light for fluorescence excitation. L2 is removed during the scattering or transmission measurement. The theory of light scattering requires parallel incident light, not converging or focused beam. If the incident light is converging or focused, its intensity varies across the beam path and thus, defining the scattering volume becomes very difficult. Therefore, the use of narrow width slits that permits parallel incident beam is desirable. A narrow width slit with adjustable slit width is installed in front of the sample cell. Initially, the location of this slit was 1 cm away from the sample cell. However, during the last phase of research, it was relocated a few cm away from the sample cell to minimize the amount of background UV light entering the receiving optics. The sample holder is located in the middle of the goniometer turntable. Another slit is installed in front of the object lens L3 that is focused at the center of the sample cell.

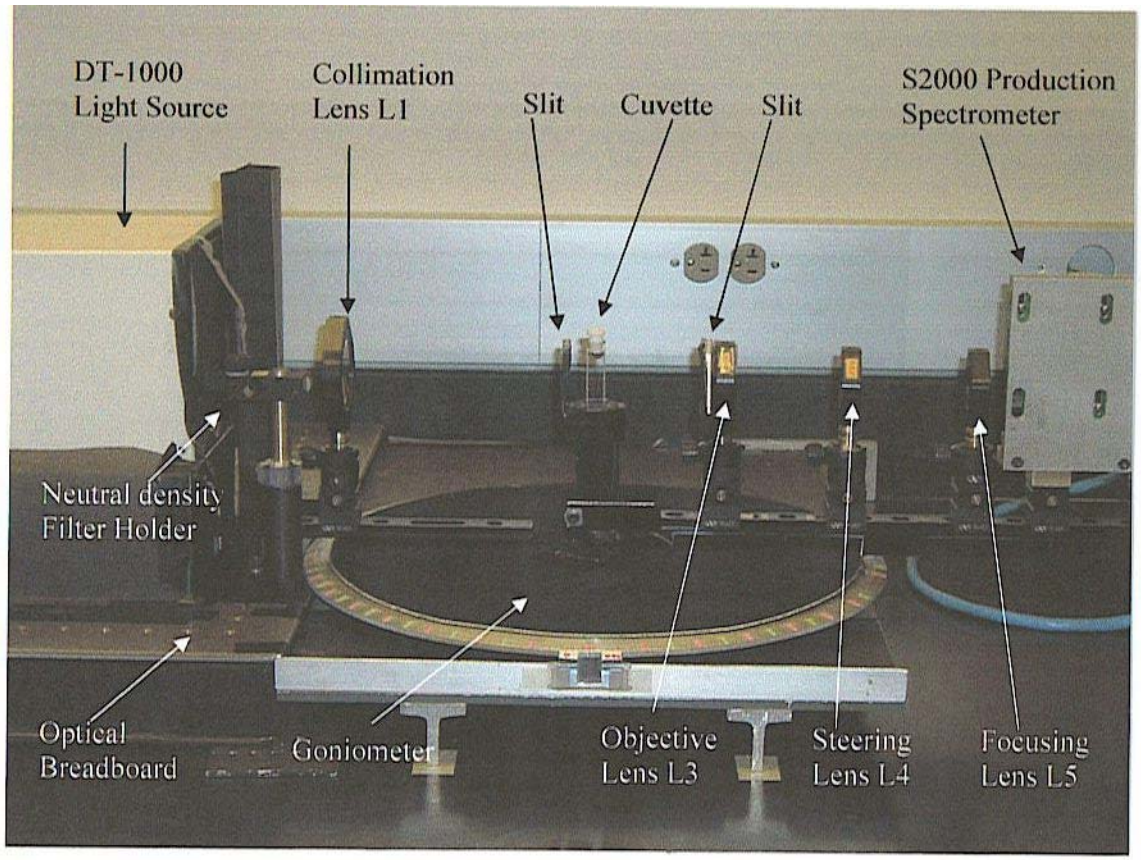

Figure 4.13. Photograph of the Integrated UV-VIS MAMW spectrometer.

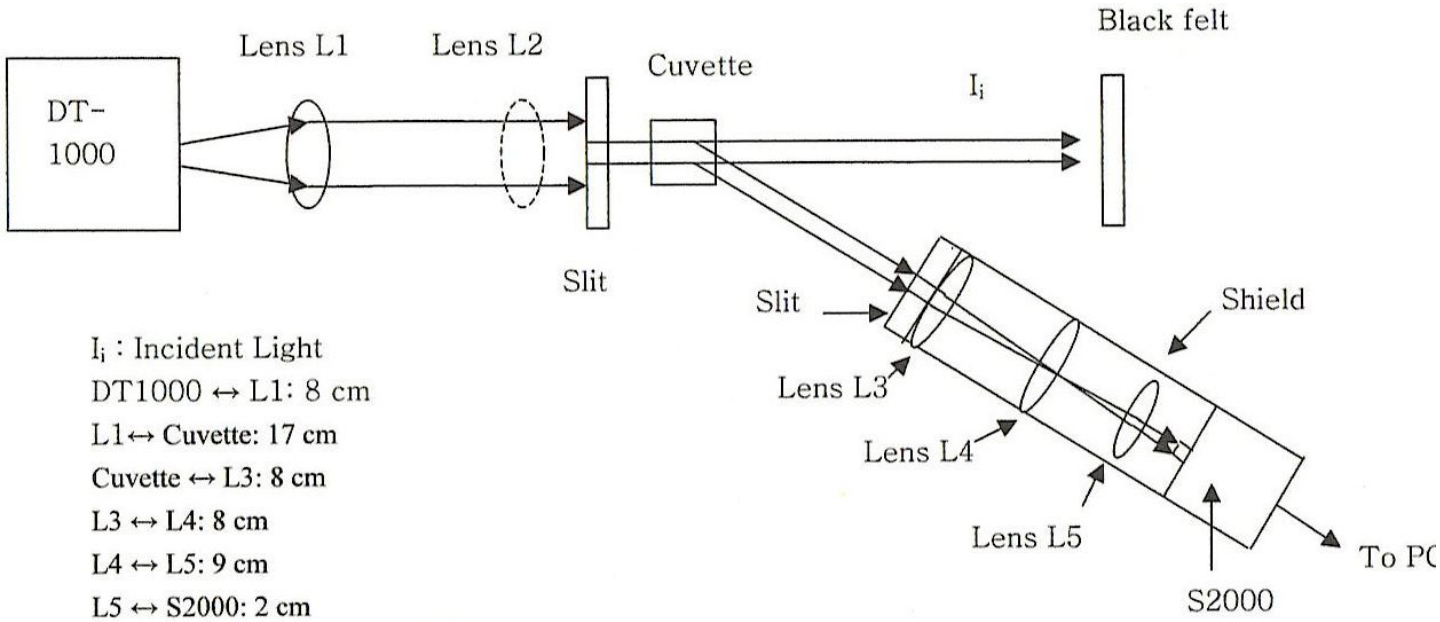

Figure 4.14. Schematic of the Integrated UV-VIS MAMW spectrometer.

L3 collects scattered, transmitted or fluorescence light from the sample cell. The focal length of L3 is 76 mm. With this focal length, optimum angular resolution can be achieved without much loss of the scattered light from the sample cell. The collected beam is focused to the lens L4 that prevents the loss of collected beam and thus, increases the intensity of light that is sent to the focusing lens L5. The location of L4 was determined empirically by observing the shape and intensity of the incident UV-VIS beam spectrum on the monitor screen. The focusing lens L5 focuses the received light to the detector. The narrow slit width of the S2000 spectrometer, 25 μm, prevents the majority of stray light entering the spectrometer. The f/# of S2000 spectrometer is 3.3. Therefore, a lens with the same f/#, 25mm diameter and 76 mm focal length, should be used to focus the detected beam to the spectrometer because it optimizes the amount of detected light incident on the spectrometer grating. However, due to the physical dimension of the goniometer arm, it was unable to install 76 mm focal length lens. Instead, two shorter focal length lenses (L4, and L5) were used to increase the amount of light entering the spectrometer as much as possible. The receiving optics and the spectrometer are installed on the goniometer arm that can be rotated for scattering or fluorescence measurement. The alignment of the goniometer turntable was accomplished by obtaining the maximum signal intensity at 0^{o}. The receiving optics and the spectrometer are shielded to prevent unwanted background light entering the detector as shown in Fig.4.15. In addition, all the shiny parts are covered with black felt to minimize background light. The construction of the Integrated UV-VIS MAMW spectrometer

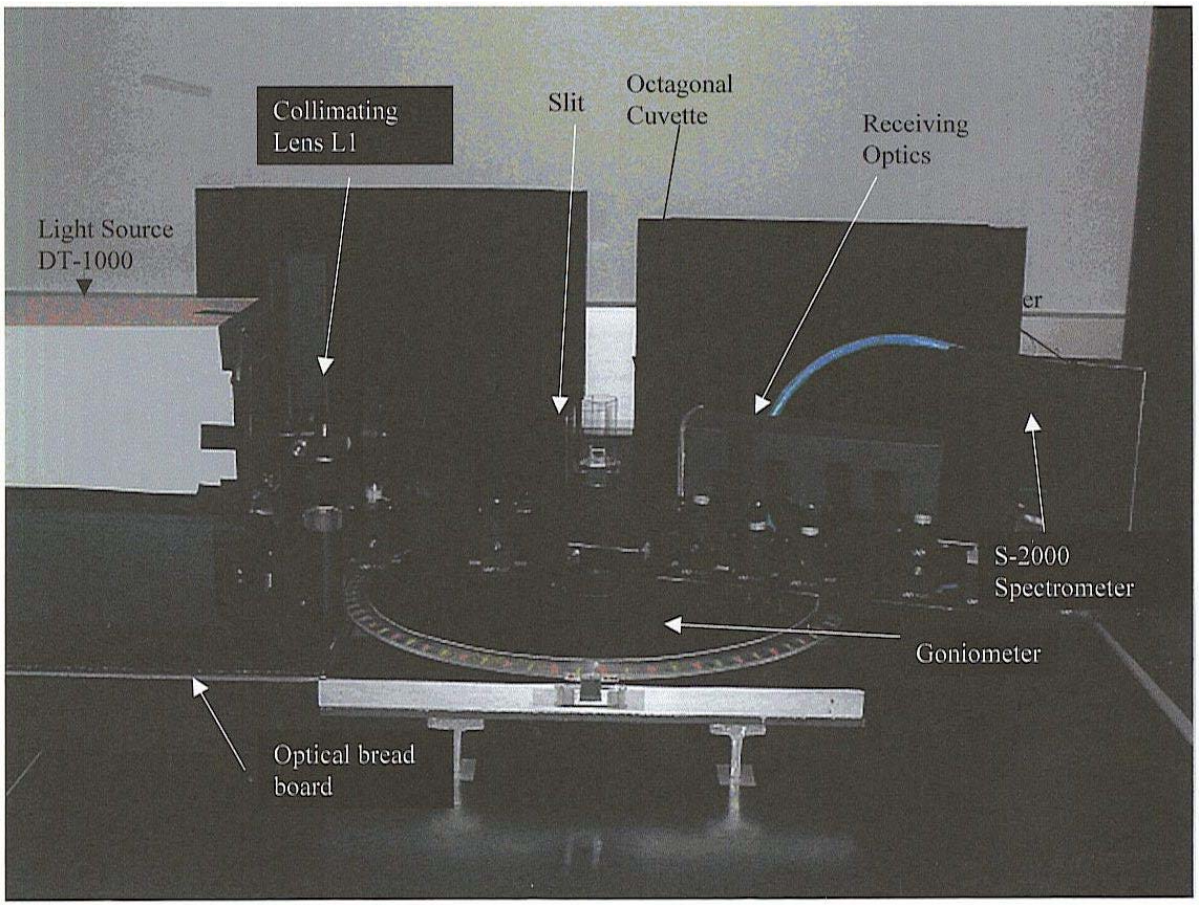

Figure 4.15. Photograph of the shielded Integrated UV-VIS MAMW spectrometer. The receiving optics and the spectrometer were covered to prevent unwanted background light entering the detector

requires the accurate optics alignment due to the use of lenses. Detected signal is very sensitive to the alignment. For precise alignment, the position of optics or detector should be adjustable in all directions. This can be done by installing all the lenses and the detector on the stages (Newport, Model MT-X linear stage) that allow 9.5 mm movement in the perpendicular direction to the incident light. By placing these stages on the rails, one in front of the sample cell and another after the sample cell, the adjustment in the direction parallel to the incident light also becomes possible. The rail after the cuvette has the role of the goniometer arm. All the optics and spectrometer are locked after the alignment.

The goniometer arm can rotate from 0^o to 150^o in the clockwise direction and 0^o to 140^o in the counterclockwise direction. However, the actual scattering measurement was done up to 60^o in the clockwise direction due to the weak scattered light intensity at large angles or the difficulty of alignment. Fig.4.16 is the UV-VIS MAMW response surface of polystyrene 1 μm standard in water measured up to 60^o in observation angle using octagonal cuvette. If more intense light source is available, measurable angular range can be extended further. Because the majority of the scattered light is limited in the low-angle direction, measurement of up to 35^o in observation angle yielded information necessary to characterize particle standards used in this dissertation research.

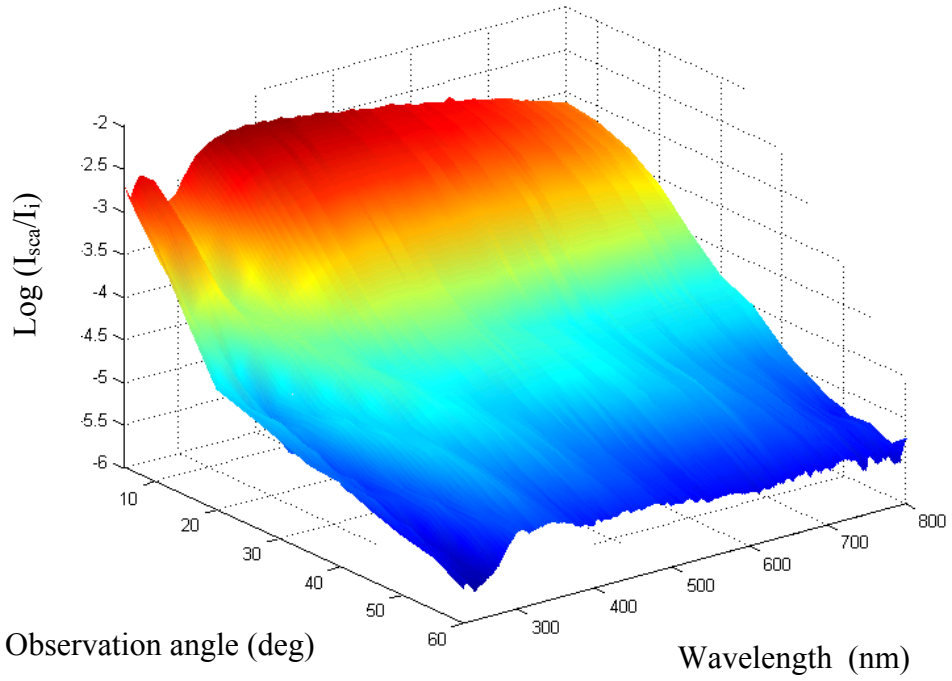

Figure 4.16. UV-VIS MAMW response surface of polystyrene 1 μm standard in water. Measurement was performed up to 60^{o} in observation angle using the octagonal cuvette.

4.4. Reproducibility

The reliability of the particle characterization results obtained by the Integrated UV-VIS MAMW spectrometer depends on the accuracy and reproducibility of the measured data. Errors that affect the accuracy and reproducibility of the experimental results can be classified into instrumental errors and experimental or human errors. Instrumental errors, which are inherent in the instruments and thus inevitable, include the fluctuation of the incident light intensity and the detector stability. However, as stated in Section 4.2, Ocean Optics DT-1000 light source is very stable light source and S2000 production spectrometer is optimized for the minimum stray light. Besides, its electrical dark signal is automatically corrected to prevent the drift of dark current by the operating software OOIBase32. On the other hand, experimental errors - mechanical stability of the system, manual rotation of the goniometer arm, optics alignment, and sample preparation- can be reduced during the development or measurement stage by exercise of care, implementation of improvement ideas, and practicing relevant protocols. Much effort was made to reduce the experimental errors. This resulted in the achievement of substantial UV-VIS beam spectrum reproducibility, less than 1 % fluctuation after 10 hours continuous usage.

4.4.1. The Angular Adjustment of Goniometer.

The goniometer of the UV-VIS spectrometer is mechanically stable and reliable. However, the manual rotation of the goniometer arm was the greatest source of error in case of the prototype MAMW spectrometer.[2] This may be attributed to the single angle

marker used to decide the rotated angle of the goniometer arm (Fig.4.17.a) due to parallax by eyes. To solve this situation, the principle of micrometer was applied. Several lines with 1^{o} resolution were drawn on the couple of white paper tape pieces. Then these pieces are attached to both sides of the angle marker as shown in Fig.4.17.b. By using these line-drawn paper tapes, it has been possible to reduce the angular resolution of the goniometer to approximately 0.05^{o} from previous 0.2^{o} in the prototype MAMW spectrometer. As a result, errors caused by the manual rotation of the goniometer arm are reduced considerably.

4.4.2. Optics Alignment

Although the use of the lenses as light delivery tool leads to the development of the Integrated UV-VIS MAMW spectrometer, it also resulted in the difficulty and delicacy of the optics alignment. Slight misalignment of optics easily resulted in the change of whole UV-VIS beam spectrum. Therefore, securing the beam reproducibility was a significant challenge for the development of the UV-VIS MAMW spectrometer. This issue was resolved by the use of the overlay function of the OOIBase32 software that allows simultaneous display of up to 8 spectra. The UV-VIS beam is aligned to acquire the best possible spectrum. The scope mode of the OOIBase32 software is used for this alignment. The shape of the UV-VIS beam spectrum is empirically determined because the calibration of UV-VIS beam spectrum for the whole wavelength region of 200 nm to 800 nm is virtually impossible.[63] Once the optimum UV-VIS beam spectrum is acquired, it is recorded as the standard UV-VIS beam spectrum and stored in the

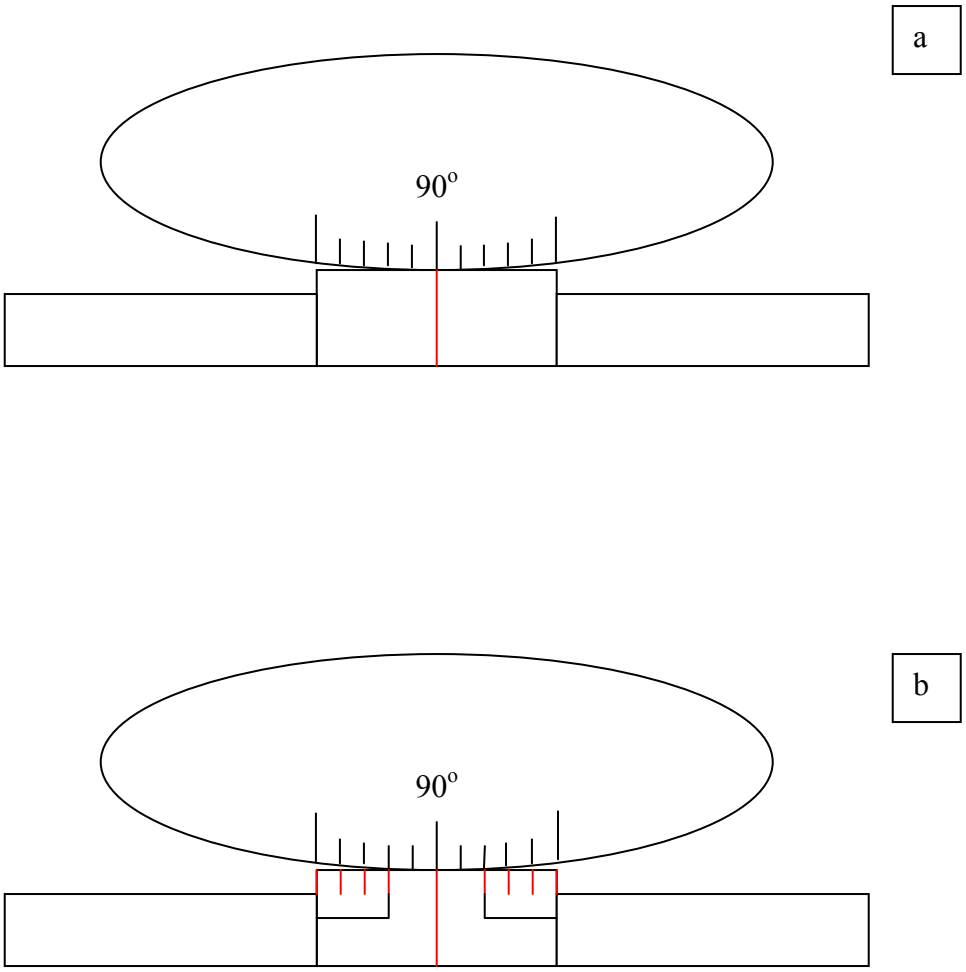

Figure 4.17. Schematics of goniometer turntable angular position markers. a) Single line marker used in the prototype MAMW spectrometer. b) Micrometer-principle-applied multiple markers used for the Integrated UV-VIS MAMW spectrometer.

computer. Thereafter, if there is any change of optics or the necessity of re-alignment, the standard UV-VIS beam spectrum is displayed using the overlay function of the OOIBase32 software. By overlapping the incident UV-VIS beam spectrum to this standard UV-VIS beam spectrum and adjusting the location of optics, precision alignment becomes possible. Optics holders like posts, bases or x-positioners are locked at their locations once the best UV-VIS beam spectrum is acquired. In addition, the micrometer principle is applied to the adjustment of the optics holders too and the line-drawn paper tapes were attached to the optics posts to help the recovery of alignment.

4.4.3. UV-VIS Beam Spectrum Reproducibility Measurement

The implementation of the measures necessary to minimize the experimental errors results in the substantial improvement in the reproducibility of the incident beam spectrum compared to that of the prototype MAMW spectrometer. For the prototype MAMW spectrometer, 6 % error in the reproducibility of the incident visible beam spectrum due to the readjustment of the goniometer arm was reported.[2] On the other hand, the UV-VIS beam spectra measured during the 10 hours continuous usage of the Integrated UV-VIS MAMW spectrometer yielded less than 1 % error in the reproducibility as shown in the beam profile Fig.4.18. This ensures the reliability of the data measured with the Integrated UV-VIS MAMW spectrometer.

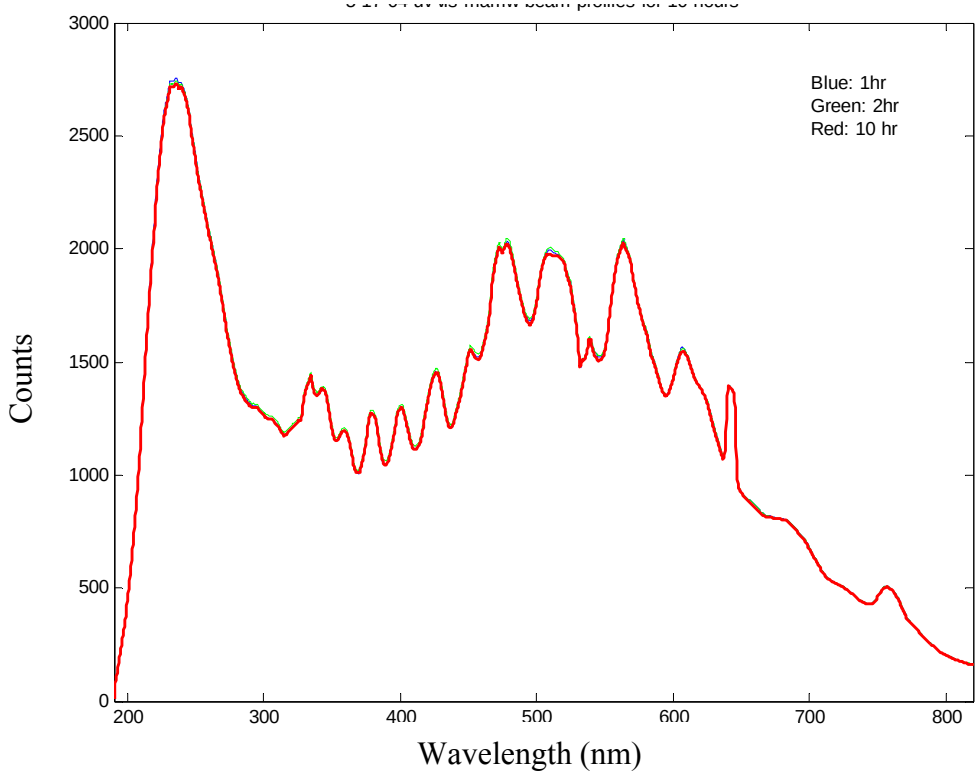

Figure 4.18. UV-VIS beam spectra variations during 10 hours continuous usage after the intensity stabilization. The maximum difference is less than 1 %. Note that the spectra measured after an hour (Blue) and two hours usage (Green) are not easy to differentiate because of the excellent reproducibility of the incident UV-VIS beam spectra.

4.5. Angle of Acceptance

Angle of acceptance plays an important role for transmission or light scattering experiment. The use of improper angle of acceptance can easily lead to spurious experimental results and thus, the reproducibility of the experimental results may not be guaranteed. These are primarily due to the angular averaging effects that depends on the angle of acceptance variation. A method to define angle of acceptance for the Integrated UV-VIS MAMW spectrometer and the effect of the angle of acceptance on the measured results are investigated in this section.

4.5.1. Definition of the Angle of Acceptance

The angle of acceptance is described as the sum of half the angle of divergence or convergence of the incident beam and half the angle subtended by detector.[61] However, if the incident beam is well collimated, the angle of acceptance can be defined as the half the angle received by detector. If lens is used for receiving optics, the exact angle of acceptance is defined by the lens-pinhole optical system. Fig. 4.19 shows a typical lens-pinhole optical system.[22] For this set up, the angle of acceptance is

$$\theta_{aa} = \tan^{-1}(r_p / f_o) \qquad (4.2)$$

where θ_{aa} is the angle of acceptance, r_p is the radius of the pinhole and f_o is the focal length of the objective lens.[7] In case of the Integrated UV-VIS MAMW spectrometer, the incident UV-VIS beam is well collimated and the receiving optics is comprised of lenses.

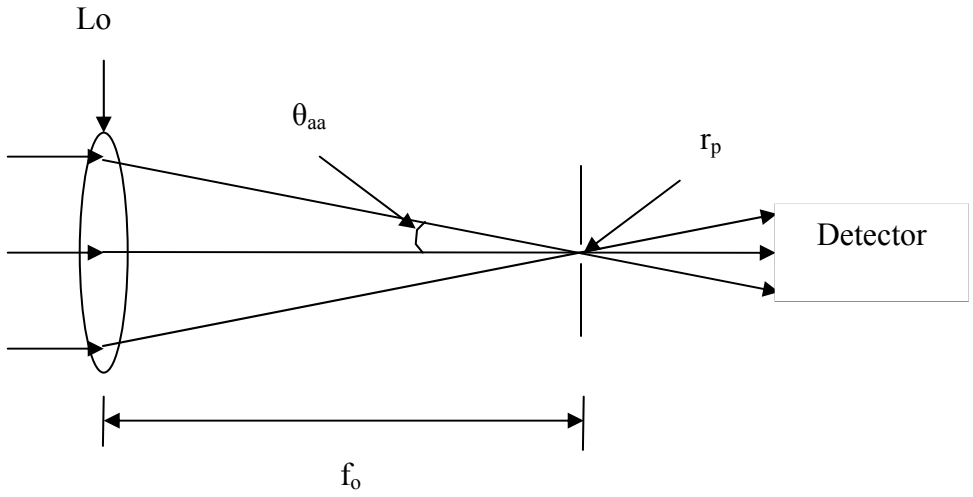

Lo: Objective lens
θ_{aa}: Angle of acceptance
f_o: Focal length of pinhole
r_p: Radius of pinhole

Figure 4.19. Schematic defining the angle of acceptance in case of the lens-pinhole system. Adapted from Reference 22.

Therefore, the definition of the angle of acceptance for the lens-pinhole optical system should be adopted as the angle of acceptance for the Integrated UV-VIS MAMW spectrometer. However, without the use of achromatic lenses, estimation of the exact angle of acceptance is not possible due to chromatic aberration of UV-VIS beam. With current set up, which employs plano-convex lenses, focusing both UV and visible beam into a single spot is not possible. In addition, UV light is invisible and the estimation of focused beam spot size for UV beam is not an easy task. As a substitution, the definition of the angle of acceptance used for the prototype MAMW spectrometer, half the angle received by the detector, is adopted as the approximate angle of acceptance for the Integrated UV-VIS MAMW spectrometer.

4.5.2. Effect of the Angle of Acceptance

The use of proper angle of acceptance is important in the extinction measurements, especially for large particles due to the enhanced forward scattering in the narrow forward direction. The use of inadequate angle of acceptance may lead to spurious results and lack of reproducibility. For example, Fig.4.20 shows two transmission spectra of purified red blood cell.[41] The top represents transmission spectrum measured by HP 8453 spectrometer and the bottom is diffusive transmission spectrum measured by Perkin Elmer Lamda 900 spectrometer. Although the same sample is used for measurements, the resulting spectra have totally different profiles due to the different angle of acceptances of the two spectrometers. This is an example that the extinction or forward scattering measurement results can be affected by the angle of acceptance of the spectrometer.

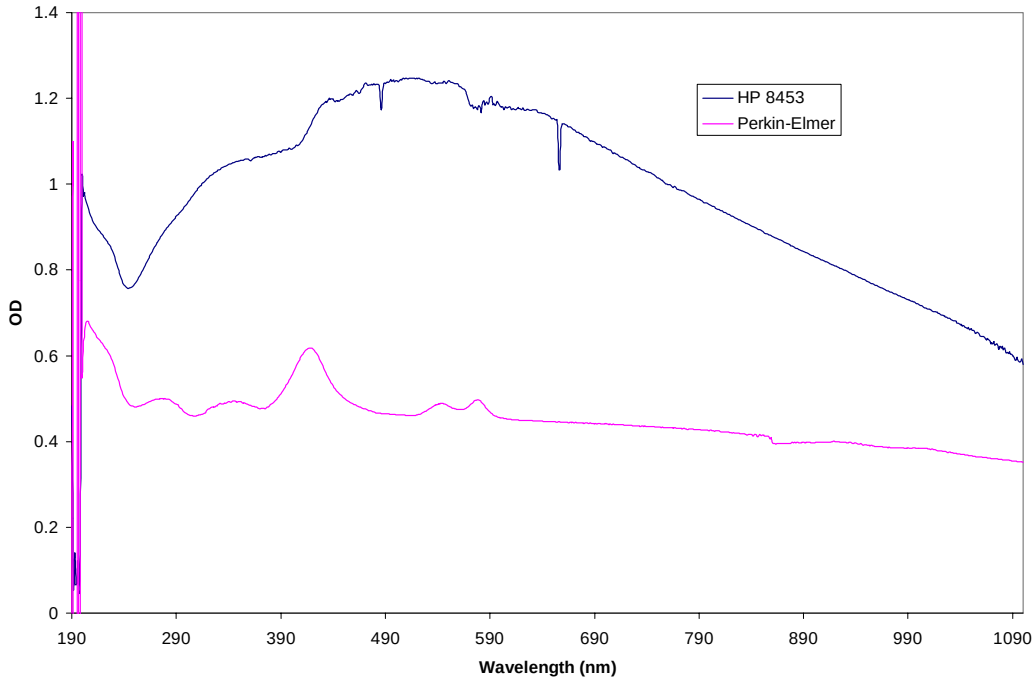

Figure 4.20. Optical density spectra of purified red blood cell measured by HP 8453 spectrometer and Perkin Elmer Lamda 900 spectrometer. Inconsistency between two spectra is due to different angle of acceptance of the two spectrometers. Cited from Reference 41.

The effect of the angle of acceptance is not absolute but relative and it depends on particle sizes. For small particles, forward scattering is negligible and thus, measured extinction will not be much affected by the change of the angle of acceptance. On the other hand, large particles enhance forward scattering as particle size increases. Consequently, large particles will be more affected by the change of the angle of acceptance. Experiment was performed to confirm this proposition using polystyrene spheres of three different sizes-300 nm, 3 μm, and 10 μm. For this measurement, the Integrated UV-VIS MAMW spectrometer was temporarily disintegrated. The schematic for this experimental setup is shown in the Fig. 4.21. All the lenses except the collimation lens L1 are removed because lenses virtually increase beam path length and hence, reduce the angle of acceptance. Extinction of each sample was measured at three different locations within the incident UV-VIS beam collimation length. This is virtually identical to measuring the extinction of each sample with different angle of acceptance. The measured results are plotted as optical density because the forward-scattered light cannot be excluded. Fig. 4.22 is the optical density spectra of polystyrene 300 nm spheres in water measured at approximately 2 cm, 7 cm and 17 cm away from the sample cell, respectively. Fig. 4.23 and Fig. 4.24 correspond to polystyrene 3 μm spheres and polystyrene 10 μm spheres, respectively. In cases of polystyrene 300 nm spheres and polystyrene 10 μm spheres, the results are not much affected by the location of the spectrometer. On the other hand, the optical density spectra of polystyrene 3 μm spheres vary depending on the distance from the sample cell. For polystyrene300 nm spheres, particle size is small and thus, forward scattering is negligible. Hence, the change of the

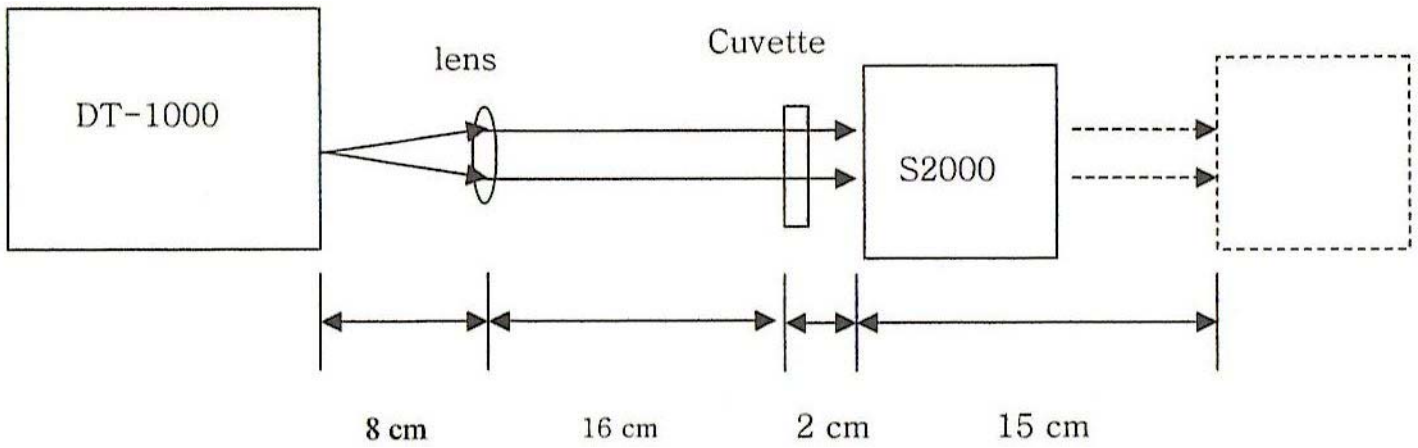

Figure 4.21. Schematic of the experimental set up measuring the effect of angle of acceptance changes on the measured optical density spectra of particles with different sizes.

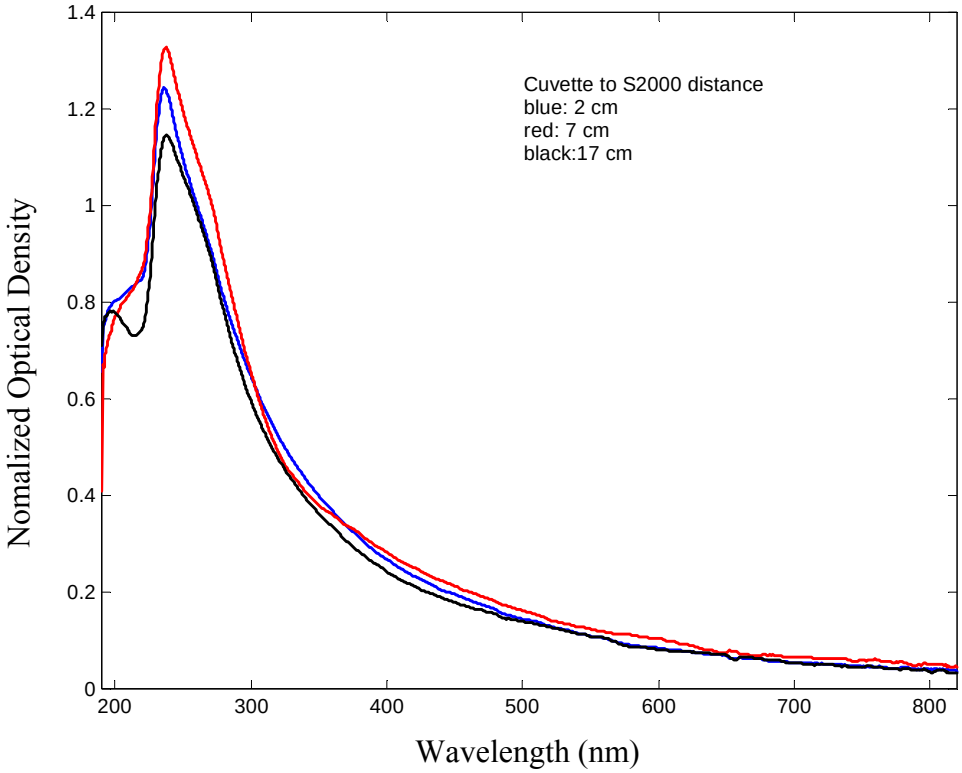

Figure. 4.22. The optical density spectra of polystyrene 300 nm spheres in water measured at approximately 2 cm, 7 cm, and 17 cm away from the sample cell using the experimental set up shown in the Fig.4.21.

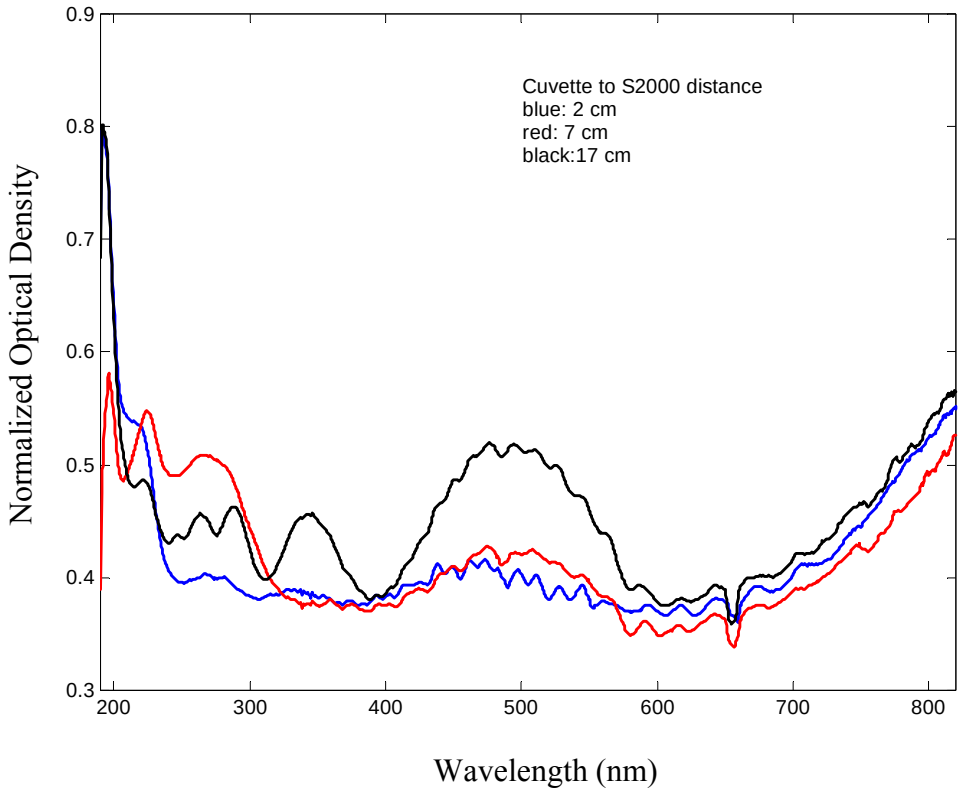

Figure. 4.23. The optical density spectra of polystyrene 3 μm spheres in water measured at approximately 2 cm, 7 cm, and 17 cm away from the sample cell using the experimental set up shown in the Fig.4.21. Optical density measured at 17 cm shows correct profile.

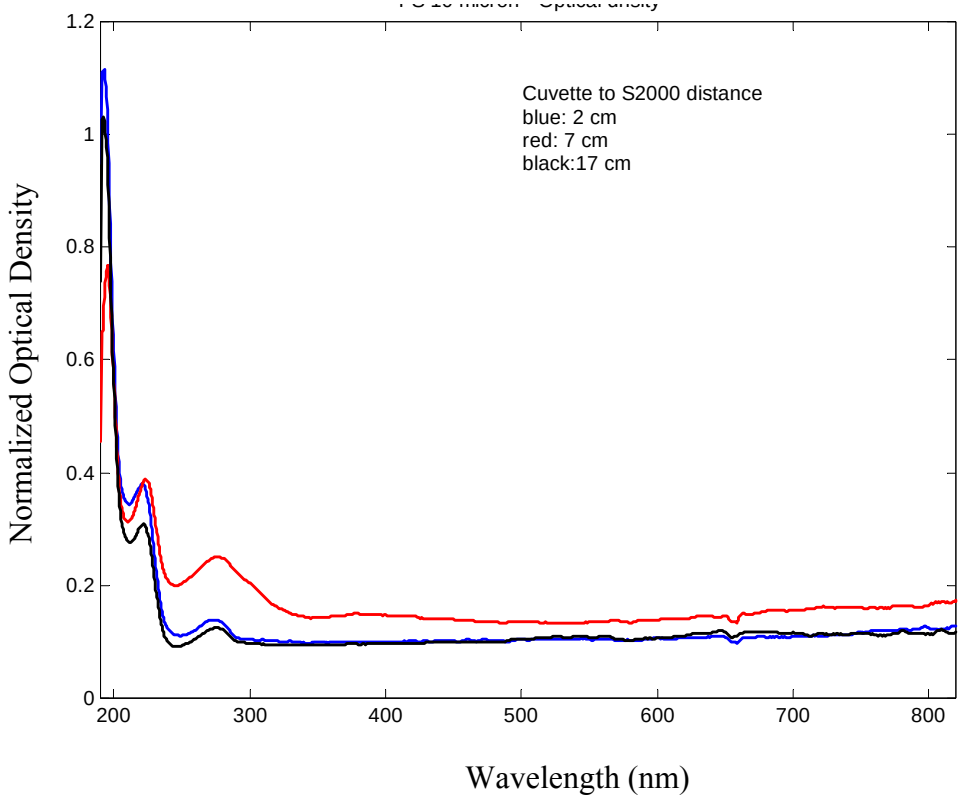

Figure. 4.24. The optical density spectra of polystyrene 10 μm spheres in water measured at approximately 2 cm, 7 cm, and 17 cm away from the sample cell using the experimental set up shown in the Fig.4.21.

angle of acceptance did not affect the results. In case of polystyrene 10 μm spheres, forward-scattered light is limited in the narrow angle and hence, the observation of the effect of the angle of acceptance change requires longer incident beam collimation length that is not obtainable with current setup. For polystyrene 3 μm spheres, the measured optical density spectra subject to the angle of acceptance changes. This proves the proposition that the effect of the angle of acceptance change is not absolute but depends on particle sizes. Therefore, the effect of the angle of acceptance should be considered during the set up of the spectrometer.

For extinction measurement, the use of small angle of acceptance is desirable. In case of the Integrated UV-VIS MAMW spectrometer, the measured optical density spectra of polystyrene spheres with different sizes are consistent with those obtained using HP8453 diode array spectrometer. The use of objective lens virtually increases collimation length and thus, results in narrowing the angle of acceptance. However, for scattering experiment, less strict standard can be applied to determine the angle of acceptance because forward-scattered light is limited to the narrow angles close to the forward direction. In addition, the reduction of the angle of acceptance sacrifices the signal sensitivity and thus, limits the measurable angular range for scattering experiment. On the other hand, the angle of acceptance cannot be increased without limit because the increment of the angle of acceptance results in averaging out the maxima and the minima of the measured spectra. Therefore, acquiring the exact scattering feature is not possible with large angle of acceptance. Dr. Bacon investigated the relation between the angle of

acceptance and the averaging effect by theoretical simulations and concluded that the angle of acceptance of 4^o is allowable for the measurement of the MAMW spectra of polystyrene 10 μm spheres without the loss of the maxima and the minima.[2] Therefore, 4^o was chosen as the upper limit of the approximate angle of acceptance for the Integrated UV-VIS MAMW spectrometer. For actual measurement, slit width of up to 6 mm that corresponds to approximately 2^o of angle of acceptance was used. However, the determination of slit width requires the consideration of additional correction factors like refraction, reflection, or particle sizes. These are discussed in Section 5.3.

CHAPTER 5. MEASUREMENT

This chapter describes topics related to measurement and data analysis including sample preparation, correction factors, and calibration. The reliability of spectroscopic measurement results depends not only on the instrument used but also on the status of sample. Therefore, careful sample preparation and handling are indispensable. The measured results require correction before calibration. The necessary correction factors for the Integrated UV-VIS MAMW spectrometer include: refraction, scattering volume and data normalization. Procedures to implement these correction factors are provided. In addition, the effect of the background UV light and data representation strategies are discussed. Quantitative validation of measurement results requires calibration. Considering the experimental set up and measurement purpose, a relative calibration is considered desirable for the Integrated UV-VIS MAMW spectrometer. Procedures necessary to accomplish the relative calibration are described in the calibration section.

5.1 Sample

The reliability and reproducibility of any spectroscopic measurement results depend not only on the instrumentation but also on the reproducibility of the sample preparation protocol. In this research, the feasibility of the Integrated UV-VIS MAMW spectrometer

to characterize micron and sub-micron size particles was tested using commercially available polystyrene standards. Therefore, this section provides information related to the polystyrene standards and the sample preparation protocol. In addition to polystyrene, whole blood sample was chosen as an example of application of UV-VIS MAMW spectroscopy to biological systems.

5.1.1 Polystyrene Standards

Polystyrene standards with different sizes or compositions were selected for this research because their optical properties are well known, and are actively used as calibration standards for instruments measuring light scattering.[28] Table 5.1. lists the data reported by the manufactures for the polystyrene standards used in this dissertation. The optical property of polystyrene is shown in Fig. 5.1.[26] Both real and imaginary parts of refractive index have a resonant band below 230 nm. Therefore, polystyrene strongly absorbs, reflects and refracts deep UV light. Thereafter, the real part of refractive index, Fig.5.1(a), decays exponentially until 500 nm and becomes stable at wavelengths longer than 500 nm. The imaginary part has slight values only in the wavelengths between 230 nm and 280 nm as exhibited in Fig.5.1(b). Due to the resonant absorption of polystyrene, the measured UV-VIS MAMW spectra have weak intensities at wavelengths below 230 nm. As a result, the measured UV-VIS MAMW spectra were plotted for the wavelengths longer than 230 nm.

Table 5.1. List of polystyrene standards used for this dissertation research

No	Standard	Manufacturer	Catalog No.	Mean Diameter
1	Polystyrene 20 nm sphere	Duke Scientific Corporation	3020A	20nm ± 2.0 nm
2	Polystyrene 150 nm sphere	Duke Scientific Corporation	3150A	150nm ± .0 nm
3	Polystyrene 300 nm sphere	Duke Scientific Corporation	3300A	300nm ± 5.0 nm
4	Polystyrene 500 nm sphere	Duke Scientific Corporation	3500A	499nm ± 5.0 nm
5	Polystyrene 1.0 μm sphere	Duke Scientific Corporation	4010A	1.020μm ± 0.022 μm
6	Polystyrene 3.0 μm sphere	Duke Scientific Corporation	4203A	3.063μm ± 0.027 μm
7	Polystyrene 4.0 μm sphere	Duke Scientific Corporation	4204A	4.000μm ± 0.033 μm
8	Polystyrene 8.0 μm sphere	Duke Scientific Corporation	4208A	7.979μm ± 0.055 μm
9	Polystyrene 10.0 μm sphere	Duke Scientific Corporation	4210A	10.15μm ± 0.06 μm
10	Green Fluorescent-Dyed Polystyrene 3.0 μm sphere	Duke Scientific Corporation	G0300	N/A
11	Red-Dyed Polystyrene 3.0 μm bead	Polysciences, Inc	17137	2.923μm ± 0.105 μm
12	Polystyrene 1.87 μm sphere	Magsphere, Inc.	PS1587A*	1.87μm ± 0.12 μm
13	Peanut-shaped Polystyrene Latex 1.85 μm standard	Magsphere, Inc.	PS1305B*	1.85μm ± 0.53 μm

* Lot number

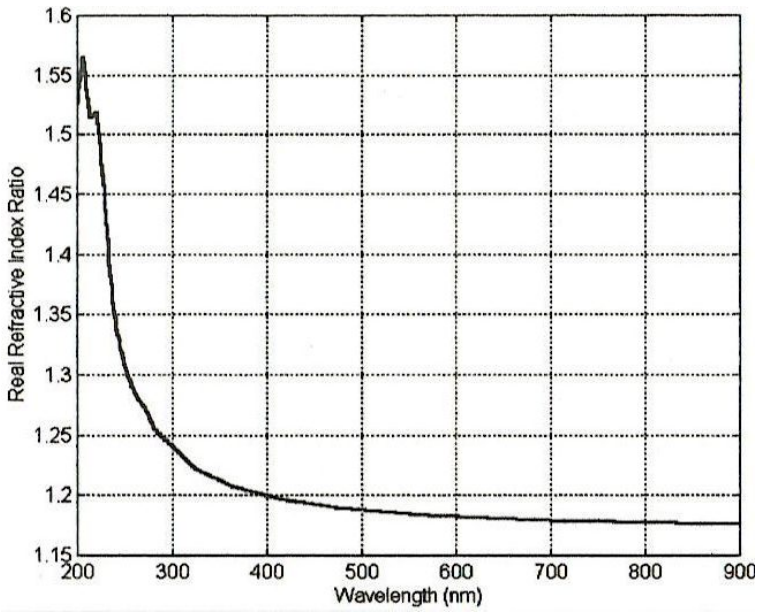

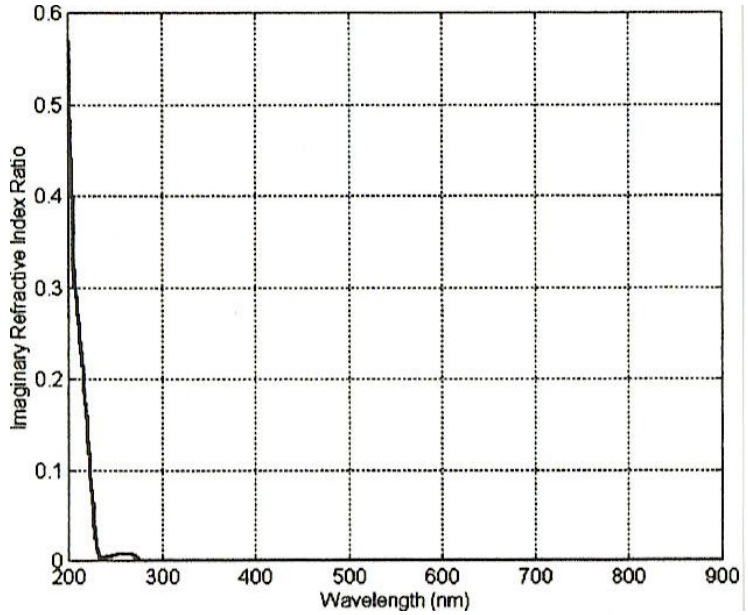

Figure 5.1. The optical properties of polystyrene. a) Real part of refractive index. b) Imaginary part of refractive index. Adapted from Reference 26.

5.1.2 Sample Preparation

Static light scattering theory is based on dilute sample concentration, i.e., enough distance between particle and particle to avoid interactions among particles. Therefore, sample preparation is crucially important for the UV-VIS MAMW spectroscopy. Improper sample preparation can easily lead to spurious results due to multiple scattering, aggregation, settling, or particle deposition. For instance, sample aggregation changes the particle size or shape and settling affects the concentration. Therefore, much attention has to be paid for sample preparation. The details of the sample preparation procedures are provided in the protocol for sample preparation. Note that sample sonication is implemented before the dilution of polystyrene standards with solvent, after the dilution, and just before the measurement because ultrasonic vibrations can break aggregated particles apart.[23]

Protocol for Sample Preparation

1. Prepare 0.005% Sodium Dodecyl Sulfate (SDS) solution as solvent for polymer standards by diluting SDS with deionized (DI) water.
2. Sonicate polymer standards for 30 sec before dilution.
3. Dilute polymer standards with solvent. The proper concentrations of polymer suspensions vary depending on the sizes of polystyrene standards. They should be determined using the measured UV-VIS transmission spectra.
4. Sonicate the diluted polymer suspensions for 3 min. If prepared samples are not used immediately, sonicate them for 3 ~ 5 min just before the measurements.

For the UV-VIS MAMW spectroscopy, an optical density (OD) = 1 was used as guideline in order to stay within the linear response of the detector. Fig. (5.2.a) is an example of variations of the measured optical density spectra of polystyrene 0.3 μm suspensions depending on sample concentration. The measurements were performed using an identical cuvette. As sample concentration was increased, less light entered the detector. Consequently, the measured optical density of the sample was linearly increased within the range of the linearity of the detector (red, green). Further increment of sample concentration led to the block of short wavelength UV light. This resulted in the observation of noisy signal caused by detector noise that can be easily appreciated on the measured optical density spectrum (blue).

Not only sample concentration but also the sample cell path length affects the measured optical density. For the measurement of optical density spectra shown in Fig.5.2.b, sample cells with different path lengths were used while sample concentrations were kept constant. In case of the octagonal cuvette, its path length is about 2.5 times longer than the fluorescent cuvette. This results in the enhanced optical density proportional to the beam path length ratio (red) compared to that measured using the fluorescent cuvette (blue).

The use of uncontaminated reference solution and very clean cuvette is also important for the UV-VIS MAMW spectroscopy.[66] This is especially critical for the measurement of scattering by extremely small or very large polystyrene particles because of their weak scattering intensities in the UV region at low angles.

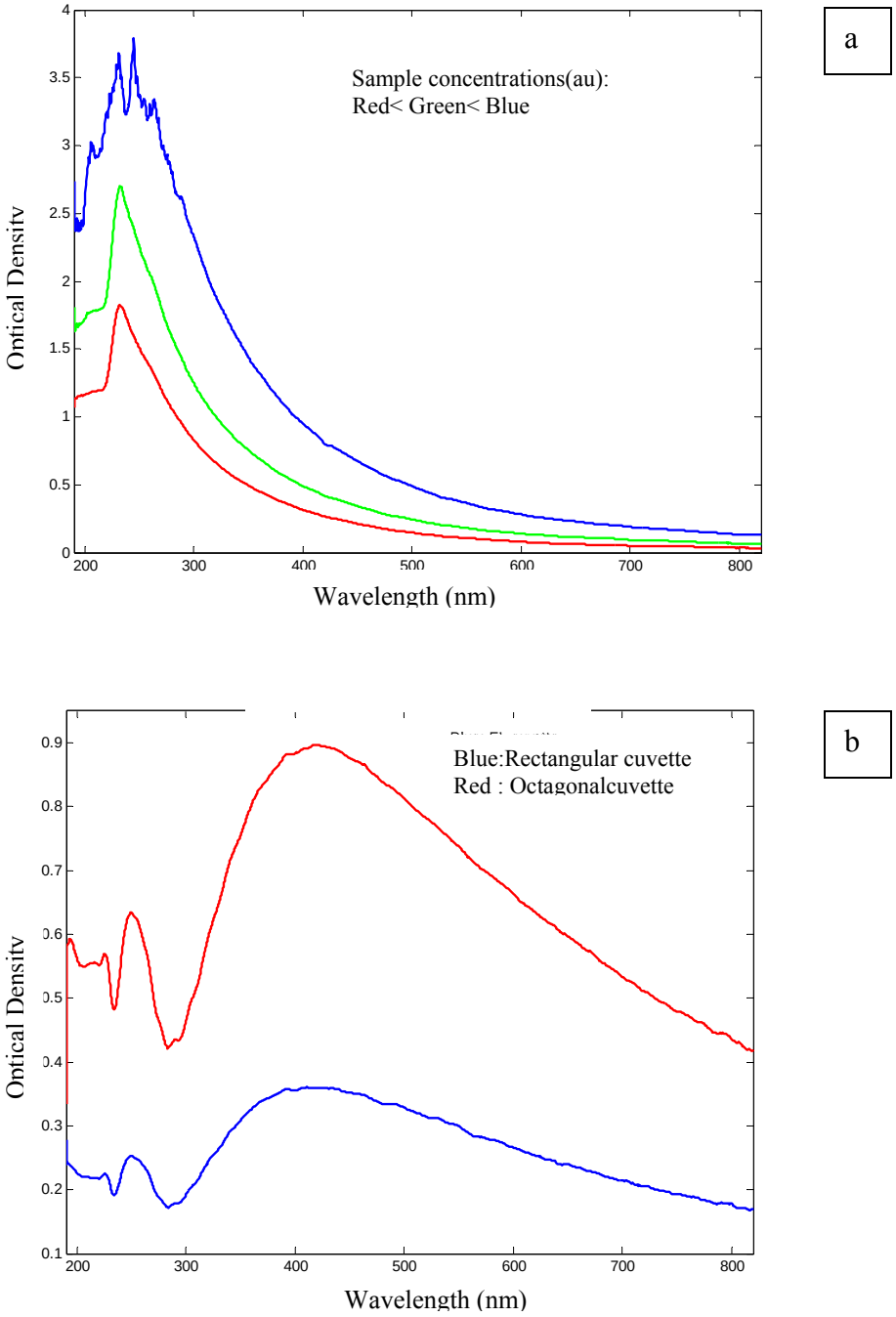

Figure. 5.2. Measured optical density variation of polystyrene standards in water. a) Optical density variation of polystyrene 0.3 μm spheres depending on sample concentration. b) Optical density variation of polystyrene 1.0 μm spheres depending on the beam path length.

5.2. Measurement

One of the merits of the Integrated UV-VIS MAMW spectrometer is that one single instrument can measure scattering, optical density or transmission, and fluorescence for particle characterization. Although these are totally different branches of spectroscopy, their measurement requires common procedures – measurement of sample and reference signal intensity for scattering and fluorescence and additional dark current measurement for optical density. However, data processing requires different procedures. In this section, signal analysis and measurement procedures are described.

5.2.1. Signal Analysis

When incident light irradiates a sample in the sample cell, light absorbed or scattered by the sample or fluorescence light from the sample can be detected by the spectrometer and yields signals to be displayed on a monitoring system. If $I_{os}(\theta)$ designates observed sample signal intensity due to light from the sample detected by the spectrometer located at angle θ, then $I_{os}(\theta)$ can be written as[65]

$$I_{os}(\theta) = I_{ts}(\theta) + D_s(\theta) + B_s(\theta) \qquad (5.1)$$

where $B_s(\theta)$ and $D_s(\theta)$ represent background light intensity and dark current recorded during the sample signal measurement and $I_{ts}(\theta)$ is the true sample signal intensity. Likewise, the reference signal intensity due to reference solution at observation angle θ,

becomes[65]

$$I_{or}(\theta) = I_{tr}(\theta) + D_r(\theta) + B_r(\theta) \tag{5.2}$$

where $I_{or}(\theta)$, $B_r(\theta)$, $D_r(\theta)$, and $I_{tr}(\theta)$ correspond to terms in Eq. (5.1). The sample scattering signal intensity $I_{sca}(\theta)$ can be found by subtracting the observed reference signal intensity from the observed sample signal intensity:[65]

$$\begin{aligned} I_{sca}(\theta) &= I_{os}(\theta) - I_{or}(\theta) \\ &= \{I_{ts}(\theta) - I_{tr}(\theta)\} + \{D_s(\theta) - D_r(\theta)\} + \{B_s(\theta) - B_r(\theta)\} \end{aligned} \tag{5.3}$$

The terms in the second and the third parentheses can be neglected; the dark current terms depend only on the integration time and the electronic noise of S2000 production spectrometer that is very stable and the background light terms are very small and nearly constant because the measurements are performed in a dark room. In addition, any background light sources like the lamp indicator light are blocked and the detection optics are covered to minimize background light entering the detector. Fig. 5.3. shows reference solution signal intensities measured from 20^o to 40^o in observation angle with 5^o resolution. These intensities are scaled by multiplying the measured intensities by the appropriate integration time ratio. At angles larger than 20^o, the scattering intensities resulting from the reference solution are negligible and the detected signal intensities are

primarily due to the dark current. Although the measurements were performed at different observation angles with different integration time, the resulting reference signal intensities which are primarily due to the dark current and the background light are highly reproducible and very stable. Consequently, the difference between the observed sample signal intensity and the observed reference signal intensity yields an excellent approximation to the true sample signal intensity

$$I_s(\theta) = I_{ts}(\theta) - I_{tr}(\theta) \tag{5.4}$$

The terms $I_{ts}(\theta)$ and $I_{tr}(\theta)$ include correction factors due to the spectrometer set up such as reflection, refraction, etc. These terms can be corrected after the measurement. In the case of transmission, a separate measurement of the dark current intensity at 0^o is required because the dark current is the primary source of noise.

5.2.2. Measurement Procedures

For the measurement of the joint particle property distribution, sample quality and a clean cuvette are as important as the instrument and the experimental set up. Therefore, the cuvette needs to be washed thoroughly to minimize reflection from the cuvette wall due to contamination and the quality of the standard needs to be confirmed by measuring the optical density with the reference spectrometers HP8452 or HP 8453 spectrometer before any UV-VIS MAMW spectra measurements. Once the sample has been prepared,

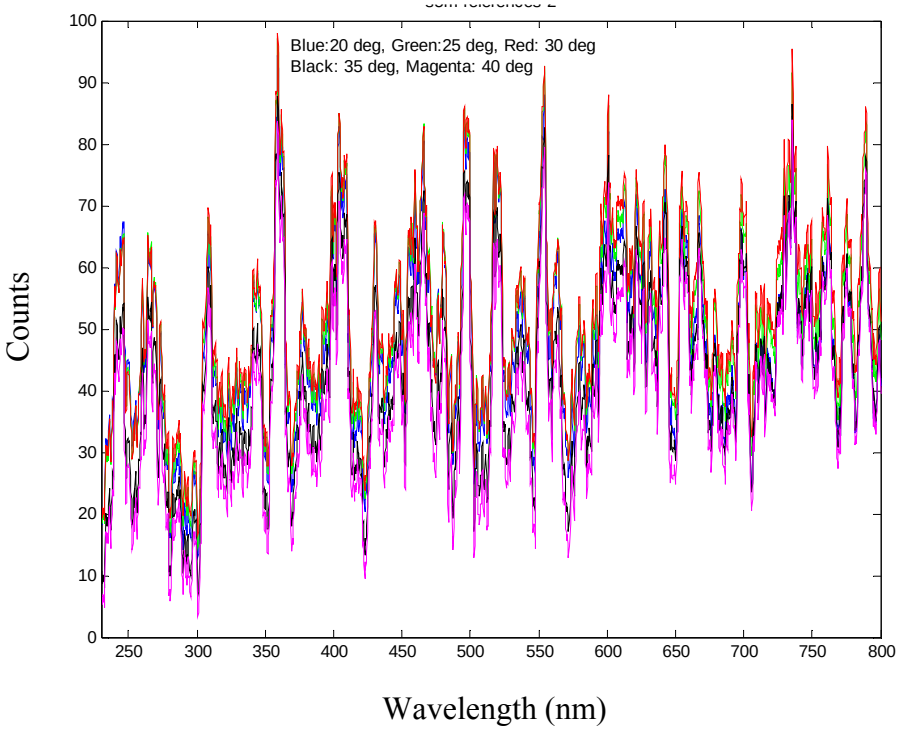

Figure 5.3. Reference solution signal intensities measured from 20^{o} to 40^{o} with 5^{o} resolutions in observation angle. Signal intensities were adjusted for the integration time used for the measurement.

turn on the DT-1000 UV-VIS light source and wait for about 40 minutes to warm up the lamps. Then the incident UV-VIS beam spectrum needs to be measured using the scope mode of OOIBase32, S2000 spectrometer operating software, and compared to the UV-VIS beam spectrum that was recorded during the optics alignment for the Integrated UV-VIS MAMW spectrometer. The optics alignment procedure is described in Section 4.4.2. If both UV-VIS beam spectra are not consistent, then optics alignment should be checked. After lamp warm up and the confirmation of the incident UV-VIS beam spectrum, the optical density needs to be measured and recorded first.

As stated in the chapter 4, two quartz cuvettes, rectangular fluorescent cuvette and octagonal cuvette, were used for the UV-VIS MAMW spectra measurements. Their shapes and relevant correction factors are described in Section 4.2.4 and the procedures of implementing the required corrections are discussed in Section 5.3. If the rectangular fluorescent cuvette is used, scattering measurements are performed up to 35^{o} in observation angle due to the refraction caused by the shape of the cuvette**.** On the other hand, if the octagonal cuvette is used for the measurement, the upper limit of the measurable scattering angle is not restricted by sample cell shape.

For scattering measurement, integration times of up to 5000 msec have been used as needed depending on the sample and scattering angle. Changing integration time requires time for the signal to re-stabilize prior to take sample spectra. For each measurement, the spectrometer settings for signal averaging include an average sample number of 5 and an average boxcar number of 10. These numbers yield clean signals

while minimizing measurement time. The details of the average sample number and the average boxcar number are explained in Section 4.2.6**.** The total measurement time depends on the integration time. For 5000 msec integration time, the signal is recorded every 25 seconds. Due to signal stabilization and data recording the overall scattering measurements take 30-40 minutes, 15-20 minutes for sample scattering measurement and additional 15-20 minutes for reference scattering measurement. Typically, reference scattering measurement was performed after sample scattering measurement because it requires the information of integration time used for sample scattering measurement. Reference scattering measurement requires thorough washing of cuvette to minimize scattering due to particles remaining in the cuvette wall. In the case of fluorescence, measurements at 90^{o} are repeated after changing the optics set up. The details of the measurement procedures are summarized in the protocol for measurement.

Protocol for Measurement

1. Measure the optical density of sample using HP 8452 or HP 8453 reference spectrometer to check the sample quality.
2. Turn on the DT-1000 UV-VIS light source and wait for lamp warm up. It takes 20 min for tungsten-halogen lamp and 40 min for deuterium lamp.
3. Measure the incident UV-VIS beam spectrum at 0 deg using the scope mode of OOIBase32 software. Use the overlay function of OOIBase32 software and ensure that the measured UV-VIS beam spectrum is consistent with the UV-VIS

beam spectrum recorded during the optics alignment of the UV-VIS MAMW spectrometer. If both spectra are not consistent, check the optics alignment.

4. Block the incident UV-VIS beam and measure the dark current at 0^o using the scope mode. Remove the block after the measurement.
5. Fill the cuvette with solvent and measure the reference spectrum at 0^o using the scope mode.
6. Fill the cuvette with sample and measure the sample spectrum at 0^o using the scope mode. Record the optical density as experiment file.
7. Measure the sample scattering from 5^o to 35^o in 5^o increment while varying integration time as needed. Use the scope mode of OOIBase32 software for this and all the remaining measurements.
8. Fill the cuvette with solvent and measure the reference scattering from 5^o to 35^o in 5^o increment while varying integration time as needed. For both sample scattering and reference scattering measurements, the same integration time must be used at the corresponding angles.
9. Measure the fluorescence intensity and the reference intensity at 90^o in case of fluorescence measurement.
10. Turn off the DT-1000 UV-VIS light source and record the operation hours.

5.3. Correction Factors

This section describes the procedures for implementing the necessary corrections for the measured UV-VIS MAMW spectra. The correction factors include reflection,

refraction, scattering path length and scattering volume corrections. Among them reflection, refraction and scattering path length corrections are closely related to the shape of the sample cell used for the scattering measurement as discussed in the section 4.2.4. In case of scattering volume correction, it is inevitable regardless the type of sample cell used for scattering measurement because the scattering volume continuously changes as the goniometer arm rotates through the angles of interest. In addition to the above correction factors, the effect of slit structure and slit-to-cuvette distance on the measured UV-VIS MAMW spectra is discussed. Also the correlation between the shapes of the incident UV-VIS beam spectra used for the data normalization and the shapes of the resulting UV-VIS MAMW spectra is examined.

5.3.1 Reflection Correction

Differences in refractive indices across the interfaces between cuvette wall and liquid and cuvette wall and air result in the reflection of scattered light. Therefore, a reflection correction is required to compensate for scattering due to the reflected light. Reflection at the interface of cuvette wall and air is much larger than that of liquid and cuvette wall because the refractive index of air is 1. According to Tommimatsu & Palmer, [57] the required reflection correction depends on the type of sample cell and it differs depending on the shape, material, thickness, etc. of the sample cell. Fig.5.4 illustrates the scattering geometry for the explanation of the reflected light contributions in a conventional cylindrical cell.[51] In this case, $I_{sca}^{\det}(\theta)$ is the intensity of scattered light arriving at the detector, $I_{sca}(\theta)$ is the intensity of the directly scattered light and

$I_{sca}(180^{o} - \theta)$ is the intensity of the scattered light due to the reflection of the incident beam[51]

$$I_{sca}^{\det}(\theta) = I_{sca}(\theta) + f_r R_p \exp(-2\alpha r_{sc}) I_{sca}(180^{o} - \theta) \tag{5.5}$$

where the coefficient f_r compensates all deviations from the ideal reflection model like the contribution of the light that is reflected more than once, R_p is Fresnel's reflectivity coefficient for normal incidence, and $\exp(-2\alpha r_{sc})$ is the attenuation of the scattered light due to reflection. Here, α represents the absorption coefficient of sample solution and r_{sc} is the radius of the sample cell.[51] The Fresnel's reflectivity coefficient for normal incidence R_p is expressed as[51]

$$R_p = \left(\frac{n_{i1} - n_{i2}}{n_{i1} + n_{i2}} \right)^2 \tag{5.6}$$

where n_{i1} and n_{i2} are the refractive indices of the material on both sides of the interface for the wavelength of the incident light. For rectangular cuvette, R_p needs to be replaced by the Fresnel formulas for reflection of light obliquely incident on a plane boundary.[7]

For the Integrated UV-VIS MAMW spectrometer, reflection corrections require measurement of scattered light at observation angles greater than 140^{o} that is not feasible with the current setup. Nevertheless, reflection correction can be neglected for forward

scattering because reflection does not cause appreciable differences in the intensity ratio until after 90^{o}.[53] Reflection correction is indispensable for large angle scattering (backward direction) where the reflected light intensity is comparable to the scattered light intensity coming from the scattering volume.[51] Given these considerations reflection corrections were not implemented in this research.

5.3.2 Refraction Correction

The geometry of the rectangular cuvette requires refraction correction because the angle between the cuvette wall and the scattered light is not perpendicular. Fig.5.5 illustrates the refraction of the scattered light due to the refractive index differences at interfaces between sample suspension and the cuvette wall and between the cuvette wall and air.[2] The scattering angle can be obtained by applying the Snell's law consecutively to the above interfaces

$$n_s \sin\theta = n_q \sin\theta_q \tag{5.7}$$

$$n_q \sin\theta_q = n_a \sin\theta_a \tag{5.8}$$

where n_s, n_q, and n_a are the refractive indices of sample suspension, cuvette material, and air, respectively, at the wavelength of interest and θ, θ_q and θ_a represent

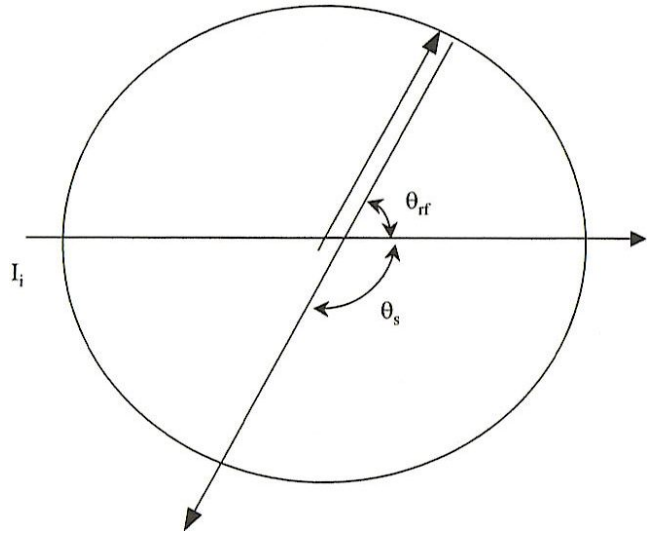

I_i: incident light

$I_{sca}^{det}(\theta)$: scattered light arriving at the detector

θ: scattering angle

$\theta_{rf:}$ $(180^o - \theta)$

Figure 5.4. Scattering geometry explaining the reflected light contributions in case of conventional cylindrical cell. Adapted from Reference 51.

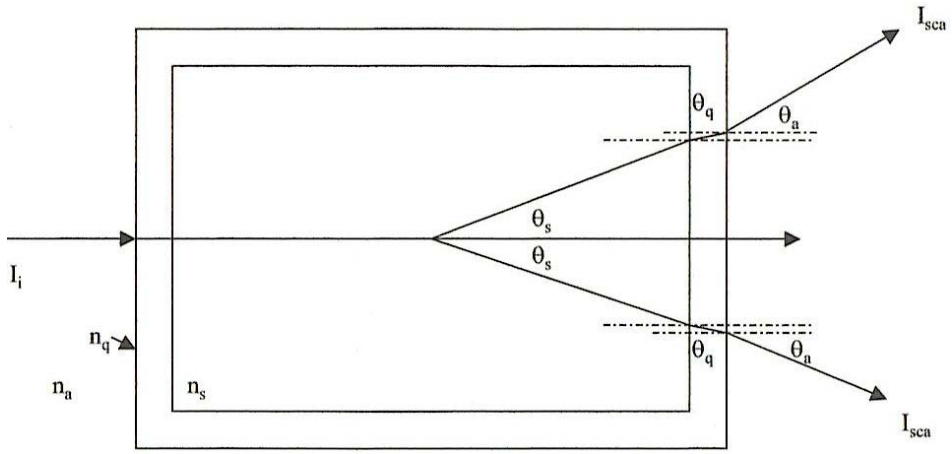

n_s: refractive index of sample suspension at the wavelength of interest
n_q: refractive index of cuvette material at the wavelength of interest
n_a: refractive index of air
θ: scattering angle
θ_q: refracted angle at the interface of sample suspension and cuvette wall
θ_a: refracted angle at the interface of cuvette wall and air.

Figure 5.5. Diagram explaining the geometry of scattered-light refraction. For illustration purpose, the horizontal side of the cuvette is magnified. Adapted from Reference 2.

angle, refracted angle at the interface of sample suspension and cuvette wall, and refracted angle at the interface of cuvette wall and air, respectively. Actually, θ_a is the observation angle and $n_a = 1$.

The incident UV-VIS beam is multiwavelength. Therefore, the exact refraction and scattering volume corrections require the use of the continuous refractive indices of cuvette material, Spectrosil® Quartz, at all the wavelengths from 230 nm to 800 nm. However, the examination of the refraction as well as the scattering volume correction results acquired using the refractive indices of Spectrosil® Quartz at 200nm, 254nm, and 800 nm show that the complicated corrections using the continuous refractive indices of Spectrosil® Quartz can be avoided if a proper refractive index is selected for the corrections. The analysis of the above correction results as well as the procedure obtaining the unknown refractive indices of Spectrosil® Quartz are provided in Appendix B. For the refraction correction, $n_q = 1.506$ at 254 nm that is the median value of the manufacturer-provided six different refractive indices of the Spectrosil® quartz was chosen.[54] As for the refractive index of polystyrene standards, the refractive index of water at 254 nm, 1.3716, was selected because polystyrene standards diluted in water were used for measurements and the concentrations of the standards were thin. Table 5.2 shows the results of refraction corrections obtained for the angles from 5^o to 40^o with 5^o resolution. The corrected scattering angles are approximated as 4^o, 7^o, 11^o, 14^o, 18^o, 21^o, 25^o and 28^o, respectively.

Table 5.2. Differences in observation angle and refractive-index-corrected actual scattering angle.

Observation angle θ_a	Angle refracted by the cuvette wall θ_q	Corrected scattering angle θ
5^o	3.3^o	3.6^o
10^o	6.6^o	7.2^o
15^o	9.9^o	10.9^o
20^o	13.1^o	14.4^o
25^o	16.3^o	17.9^o
30^o	19.4^o	21.4^o
35^o	22.4^o	24.7^o
40^o	25.3^o	28.0^o

Fig.5.6 is the UV-VIS MAMW response surface of polystyrene 1.0 μm standard in water. Fig.5.6.a is plotted for the observation angle and Fig.5.6.b is plotted for the refraction corrected scattering angle. Both response surfaces are identical in shape, intensity and wavelengths but refraction corrected Fig.5.6.b is angularly contracted as expected. Fig.5.7 is the contour plot of the UV-VIS MAMW response surface of polystyrene 1.0 μm standard in water. Fig.5.7.a is the contour plot before the refraction correction and Fig.5.7.b is the contour plot after the refraction correction. These contour plots again confirm the angular contraction by refraction correction. Fig.5.8.a is the simulated plot of the UV-VIS MAMW response surface of polystyrene 1.0 μm standard in water and Fig.5.8.b is the corresponding contour plot. The comparison of the UV-VIS MAMW response surface before the refraction correction with that after the refraction correction shows that the refraction-corrected UV-VIS MAMW response surface fits better to the theoretically-simulated UV-VIS MAMW response surface. Therefore, experimental results acquired using a rectangular cuvette have been corrected for refraction.

5.3.3 Scattering Path Length Correction

For rectangular cuvette, the scattering path length increases as the scattering angle increases until the scattered light passes the corners of the cuvette where the faces of the cuvette parallel to the incident light meet the 1st face of the cuvette where the forward scattered light passes. Consequently, more scattered light can be absorbed by the sample

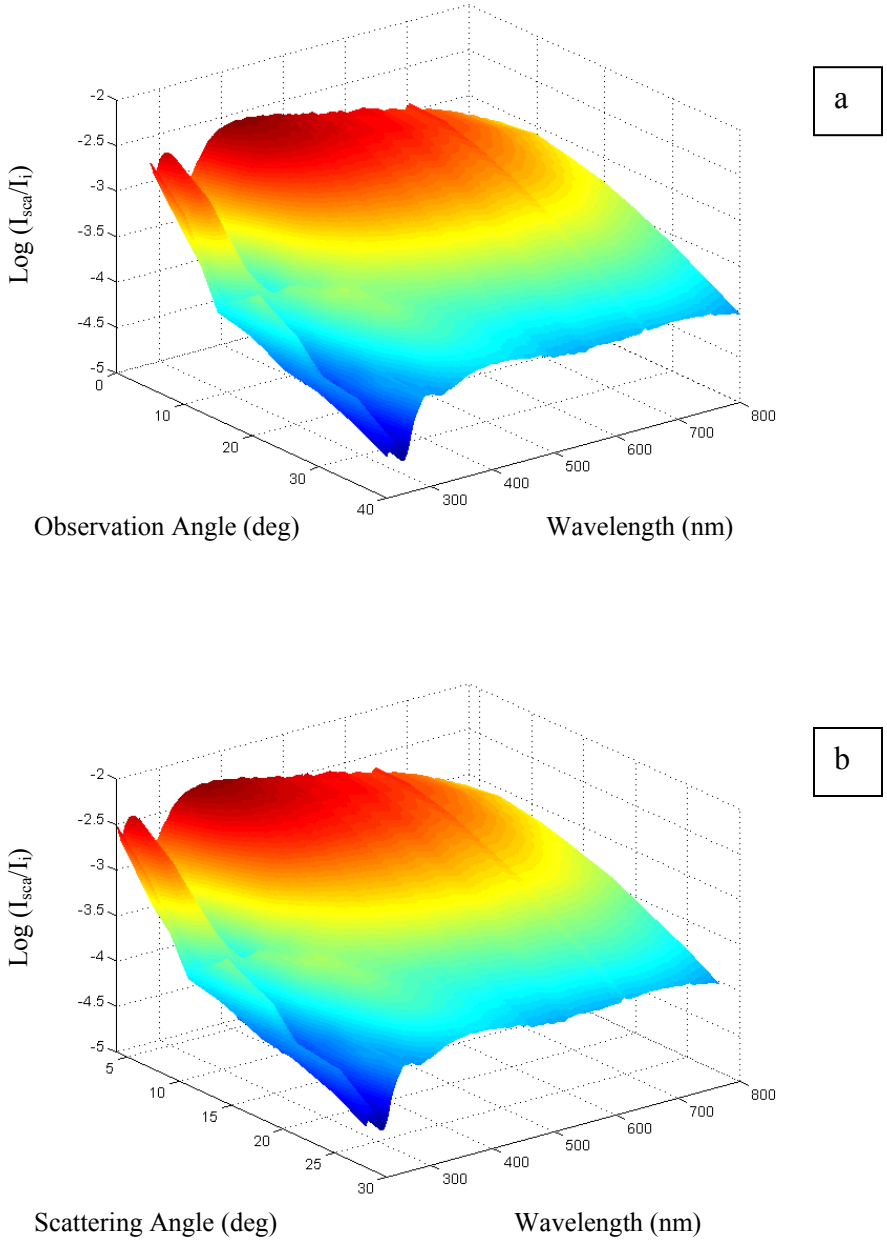

Figure 5.6. UV-VIS MAMW response surfaces of polystyrene 1.0 μm standard in water. a) Plotted for the observation angle of 5^o – 40^o. b) Plotted for the refraction-corrected scattering angle of 4^o – 28^o.

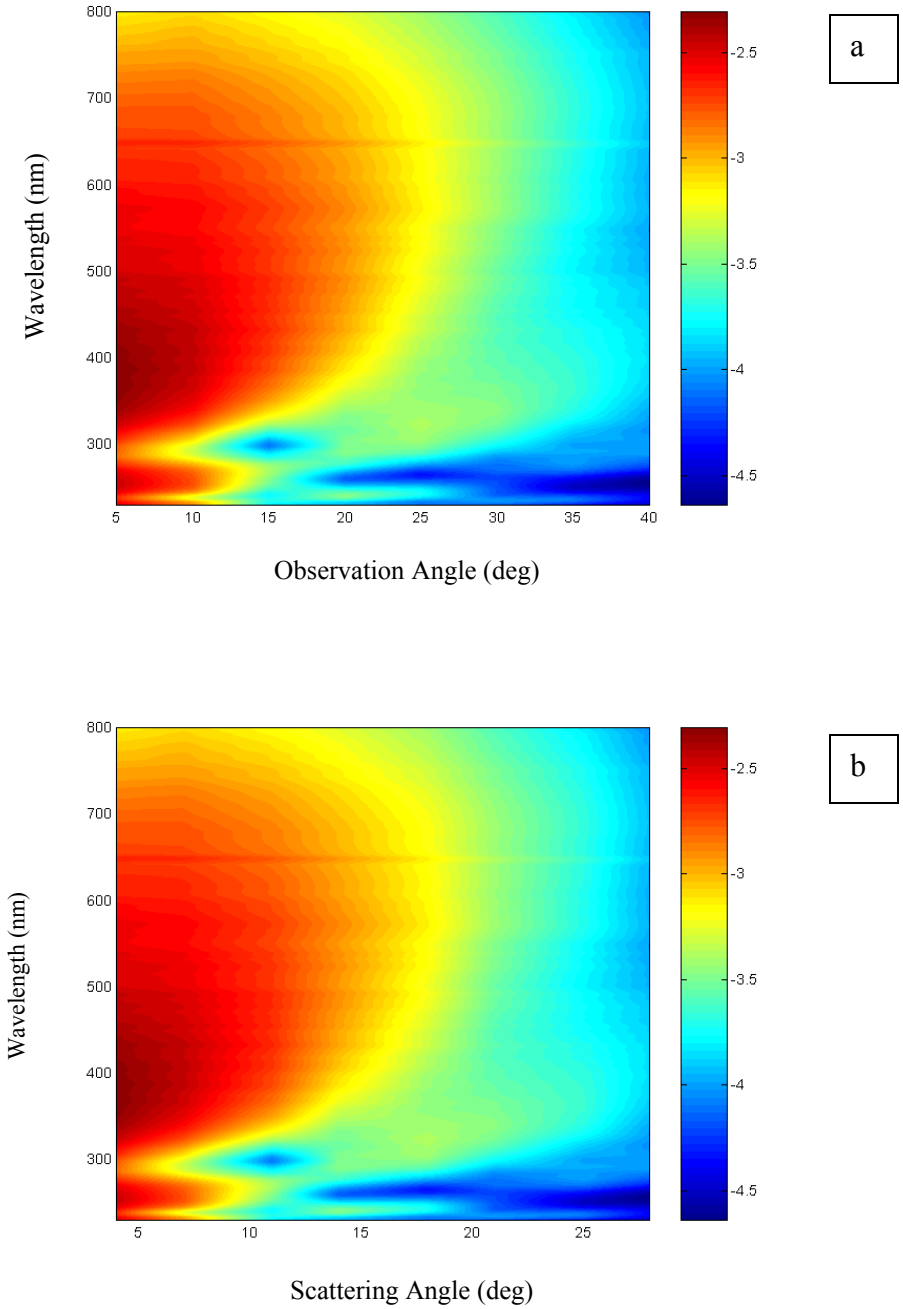

Figure 5.7. Contour plots of the UV-VIS MAMW response surfaces of polystyrene 1.0 μm standard in water, Fig.5.6. a) Plotted for the observation angle of 5^o – 40^o. b) Plotted for the refraction corrected scattering angle of 4^o – 28^o.

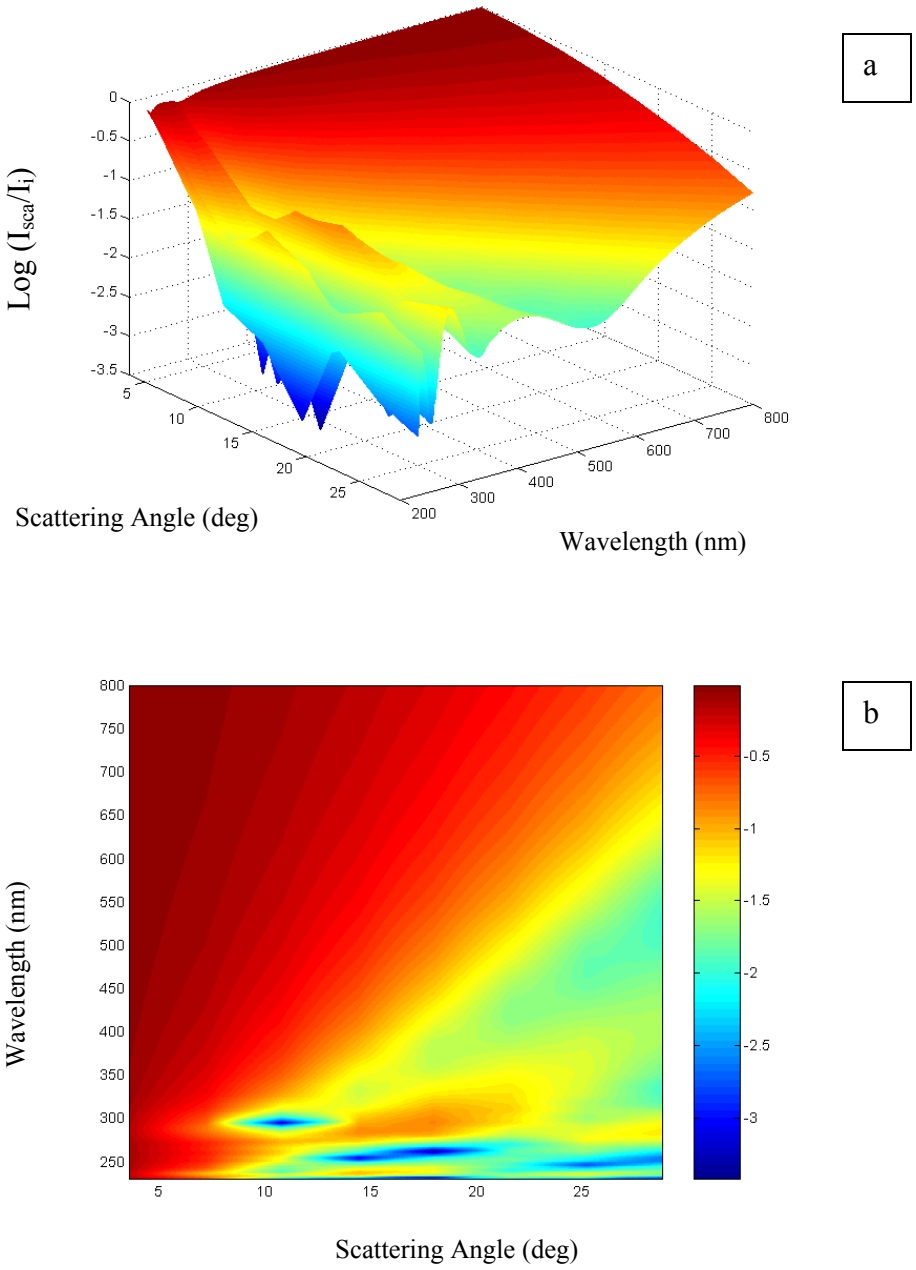

Figure 5.8. Simulated plots of UV-VIS MAMW spectra of polystyrene 1.0 µm standard in water. a) Simulated plot of the UV-VIS MAMW response surface for the angular range of 4^o – 29^o. b) Corresponding contour plot.

suspension at large scattering angle than at low scattering angle until the scattered light reaches the edge of the 1st face. Therefore, scattering path length correction is inevitable.

Fig.5.9 shows the geometry of the scattering path length variation as a function of scattering angle θ in case of the rectangular cuvette. The reduced scattered light intensity I_{rsca} at scattering angle θ is

$$I_{rsca}(\theta\ ) = I_{sca}(\theta_0)\, e^{-\alpha \Delta l_s} \tag{5.9}$$

where $I_{sca}(\theta_0)$ is the scattered light intensity at $\theta = 0^{\circ}$, α is the absorption coefficient and Δl_s is the scattering path length increment. Δl_s can be rewritten as a function of scattering angle θ

$$\Delta l_s = (\frac{1}{\cos\theta} - 1)\, d_h \tag{5.10}$$

where d_h is half the inside path length of the rectangular cuvette. If Eq. (5.10) and Eq. (2.56) are substituted into Eq. (5.9), then

$$I_{rsca}(\theta) = I_{sca}(\theta)\, e^{-\frac{4\pi k}{\lambda}(\frac{1}{\cos\theta} - 1)d_h} \tag{5.11}$$

For polystyrene, the imaginary part of the refractive index k is 0.04 at 230 nm, 0.006 at 250 nm, and 0 at wavelengths longer than 283 nm. Therefore, scattering path length correction may be ignored in case of polystyrene standards. For other standards, scattering path length correction requires the information of optical properties of the sample. If this information is not available, the octagonal cuvette, which has virtually identical scattering path length at every angle, can be used to avoid the scattering path length correction.

5.3.4 Scattering Volume Correction

The scattering volume is defined as the intersection of the incident beam with the detector field of view that continuously changes as the goniometer arm rotates as shown in Fig. 5.10.[7] Therefore, it is inevitable to correct the measured scattered light intensity using a proper correction factor. Typically, the scattering volume correction is done by multiplying $\sin\theta$ by the measured scattered light intensity at the corresponding scattering angle.[7] However, as Wyatt pointed out, the simple multiplication of $\sin\theta$ may become a new source of error, especially, at low scattering angles.[66] This seems to originate from the fact that the value of $\sin\theta$ at every scattering angle is always constant for that angle regardless the spectrometer setup while the actual scattering volume at every scattering angle varies depending on the sample cell path length, the incident beam height, and the width of the slits. For instance, in case of the current UV-VIS MAMW spectrometer setup that uses the slits with 6 mm width and the rectangular fluorescent

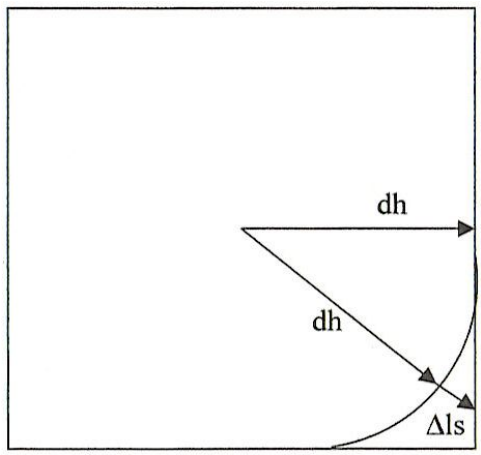

d_h : half the inside path length of rectangular cuvette

Δl_s : scattering path length increment

Figure 5.9. Diagram illustrating the necessity of the scattering path length correction in case of a rectangular cuvette.

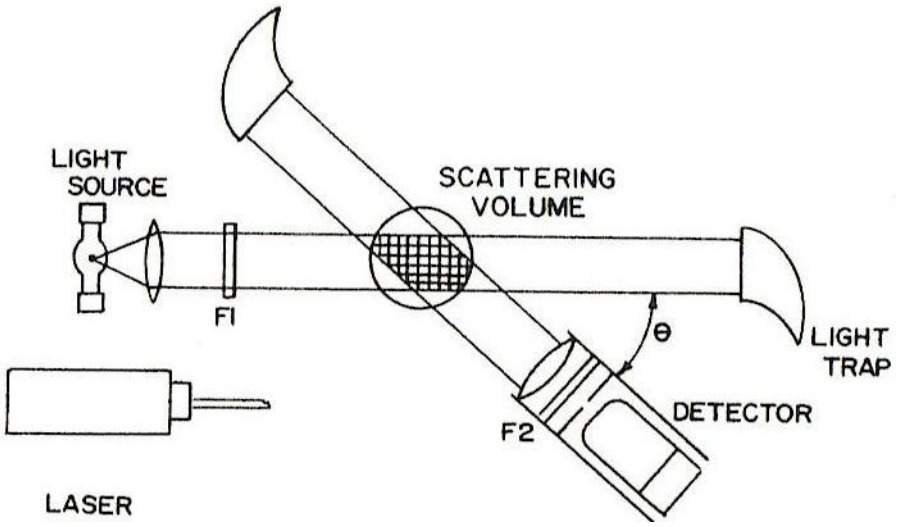

F1, F2: Possible polarization filters
θ: scattering angle

Figure 5.10. Schematic explaining scattering volume changes. Cited from Reference 7.

cuvette with 10 mm path length, the scattering volume has the maximum 6 x 10 x 20 mm^3 (1200 mm^3) at 0^o and the minimum 6 x 6 x 20 mm^3 (720 mm^3) at 90^o. Here 20 mm represents the approximate height of the incident UV-VIS beam. The resulting maximum to minimum scattering volume ratio is 1.67. On the other hand, if the slit widths are changed into 3mm, the maximum and the minimum scattering volume become 600 mm^3 and 180 mm^3, respectively. The corresponding maximum to minimum scattering volume ratio increases to 3.33. Furthermore, in addition to the constant $\sin\theta$ regardless the spectrometer setup, the value of $\sin\theta$ approaches 0 as scattering angle is nearing 0^o and thus, results in the reduced scattered light intensity at low angles. Therefore, it can be concluded that the scattering volume changes may not be represented as $\sin\theta$, especially at low angles if the incident beam and the detector field of view have some widths and the sample cell path length is not large. Consequently, the scattering volume correction should be done not by the universal application of the simple $\sin\theta$ multiplication but by multiplying the ratio of the scattering volume change at each scattering angle that is calculated from the actual experimental setup. Hereafter, two different terms, sine correction and calculated-volume correction, will be used to differentiate the scattering volume correction done by multiplying $\sin\theta$ and that performed using the calculated scattering volume.

Fig. 5.11 shows a diagram used to calculate the approximate scattering volume changes for the Integrated UV-VIS MAMW spectrometer. For the calculation of the scattering volume, the refraction-corrected scattering angles in Table 5.2 are used.

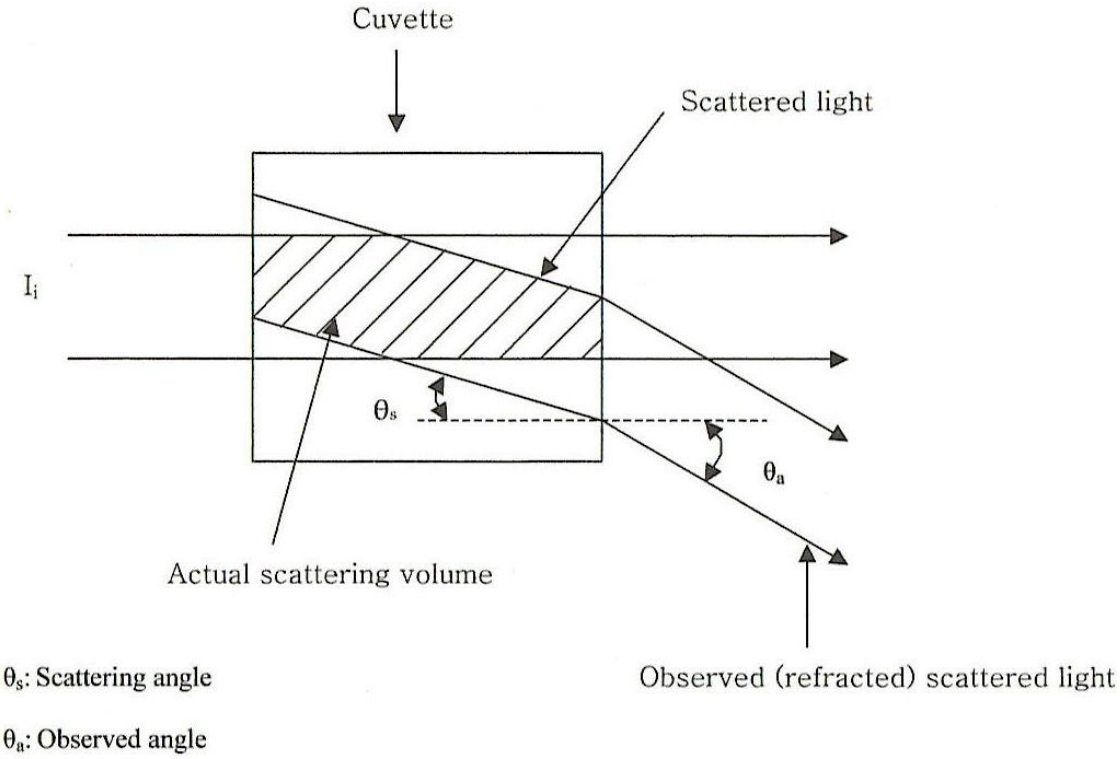

Figure 5.11. Schematic of geometry used for scattering volume correction.

The results are summarized in Table 5.3 in case of the 3 mm width slit usage for the UV-VIS MAMW spectrometer setup and Table 5.4 for the 6 mm width slit installation case. The multiplication factors are obtained by dividing the scattering volume at each scattering angle into the scattering volume at 4^o. These results are used to correct the scattering volume when plotting the UV-VIS MAMW response surfaces. Fig. 5.12 shows the UV-VIS MAMW response surfaces of polystyrene 1.0 μm standard in water. Fig. 5.12.a is the plot without scattering volume correction and Fig. 5.12.b is the case when $\sin\theta$ is used for correction. Fig. 5.12.c shows the results of using the multiplicative factors in Table 5.4 and Fig. 5.12.d is the simulated response surface. In case of the sine-corrected Fig. 5.12.b, the scattering intensity at low angles is decreased while the scattering intensity at large angles is enhanced compared to Fig. 5.12.a, the case without correction. On the other hand, the calculated-volume-corrected Fig. 5.12.c shows similar profile to Fig. 5.12.a. Compared with the simulated plot Fig. 5.12.d, the calculated-volume correction matches well at low angles while the sine correction fits better at large angles in case of the polystyrene 1.0 μm standard in water. Fig. 5.13 shows the UV-VIS MAMW response surfaces of polystyrene 8.0 μm standard in water. Fig. 5.13.a is the plot without scattering volume correction and Fig. 5.13.b is the plot obtained by multiplying $\sin\theta$. Fig. 5.13.c is the calculated-volume-corrected plot obtained using the multiplicative factors in Table 5.4 and Fig. 5.13.d shows the simulated response surface. Note that the sine-corrected Fig. 5.13.b matches better to the simulated plot Fig. 5.13.d than the calculated-volume-corrected Fig.13.c in case of the polystyrene 8.0 μm standard.

Table 5.3. Calculated scattering volume in case of the 3 mm width slit installation for the Integrated UV-VIS MAMW spectrometer setup.

Observation Angle θ_a (deg)	Scattering Angle θ (deg)	Scattering Volume (mm^3)	Multiplicative Factor
5	4	560	1.0
10	7	520	1.08
15	11	500	1.12
20	14	480	1.17
25	18	450	1.24
30	21	400	1.40
35	25	370	1.51

Table 5.4. Calculated scattering volume in case of the 6 mm width slit installation for the Integrated UV-VIS MAMW spectrometer setup.

Observation Angle θ_a (deg)	Scattering Angle θ (deg)	Scattering Volume (mm^3)	Multiplicative Factor
5	4	1150	1.0
10	7	1120	1.03
15	11	1070	1.07
20	14	1030	1.12
25	18	1020	1.13
30	21	1010	1.14
35	25	970	1.19

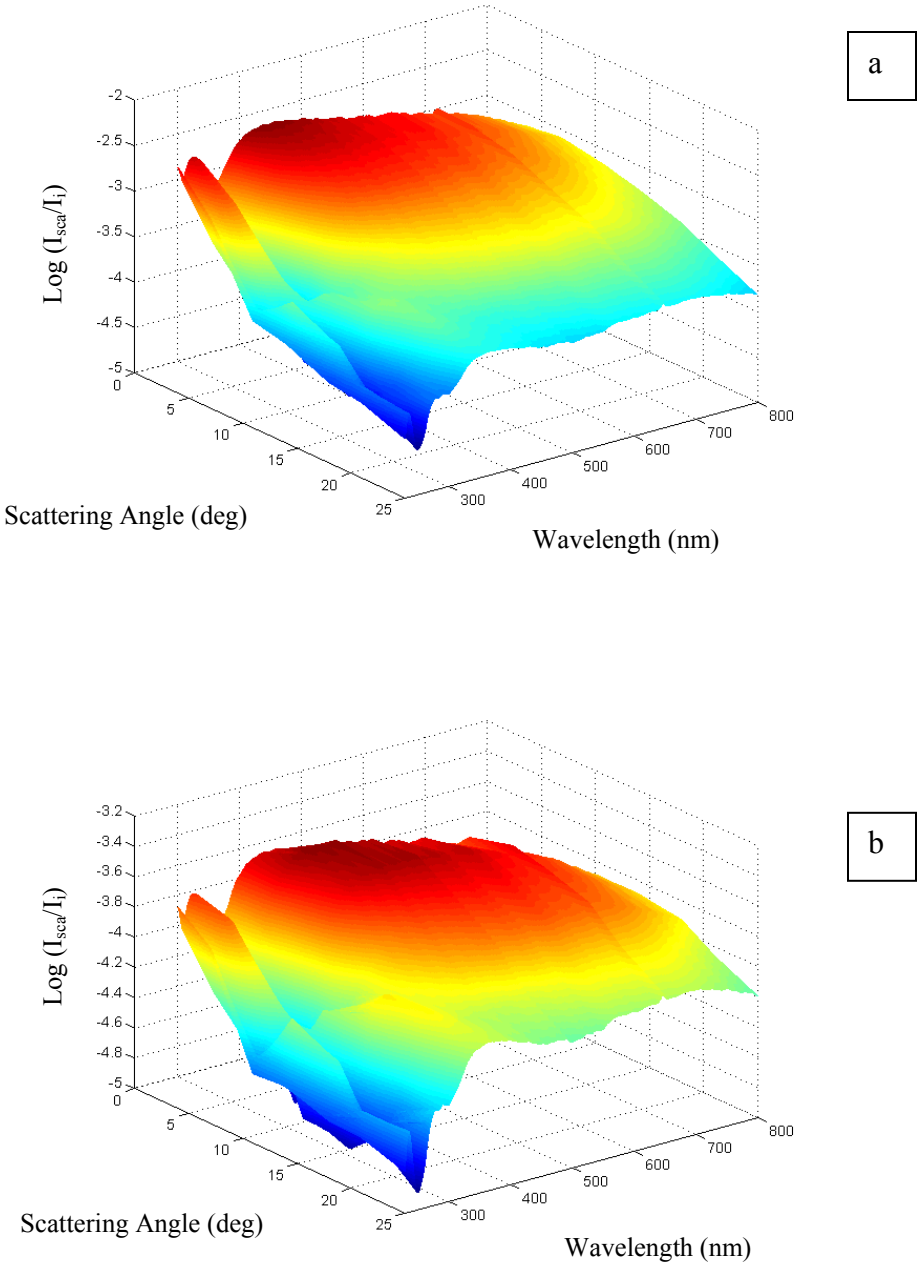

Figure 5.12. UV-VIS MAMW response surfaces of polystyrene 1.0 μm standard in water plotted for the demonstration of the scattering volume correction. a) UV-VIS MAMW response surface without scattering volume correction. b) UV-VIS MAMW response surface with the sine correction.

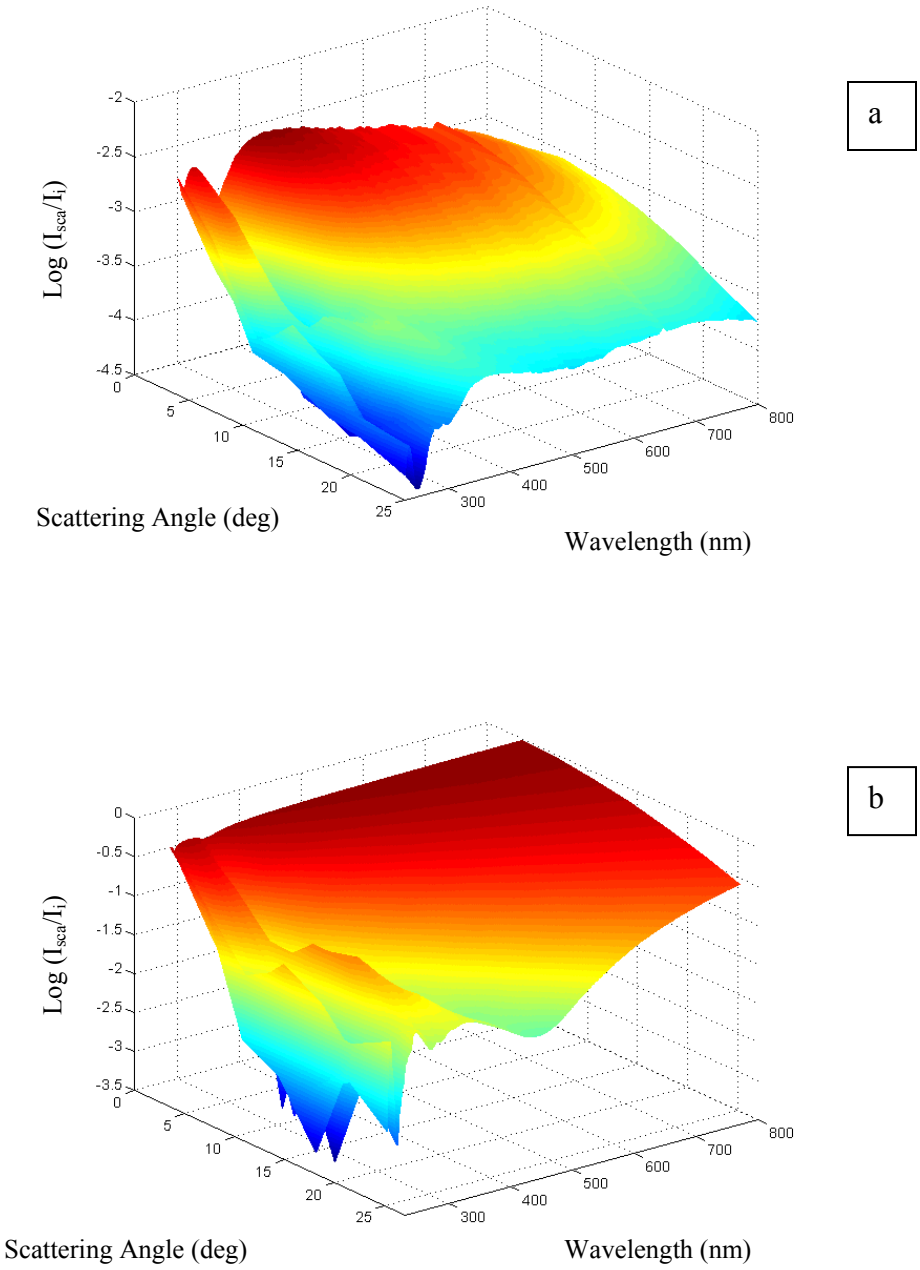

Figure 5.12. (Continued). c) UV-VIS MAMW response surface with the scattering volume correction. d) Simulated UV-VIS MAMW response surface.

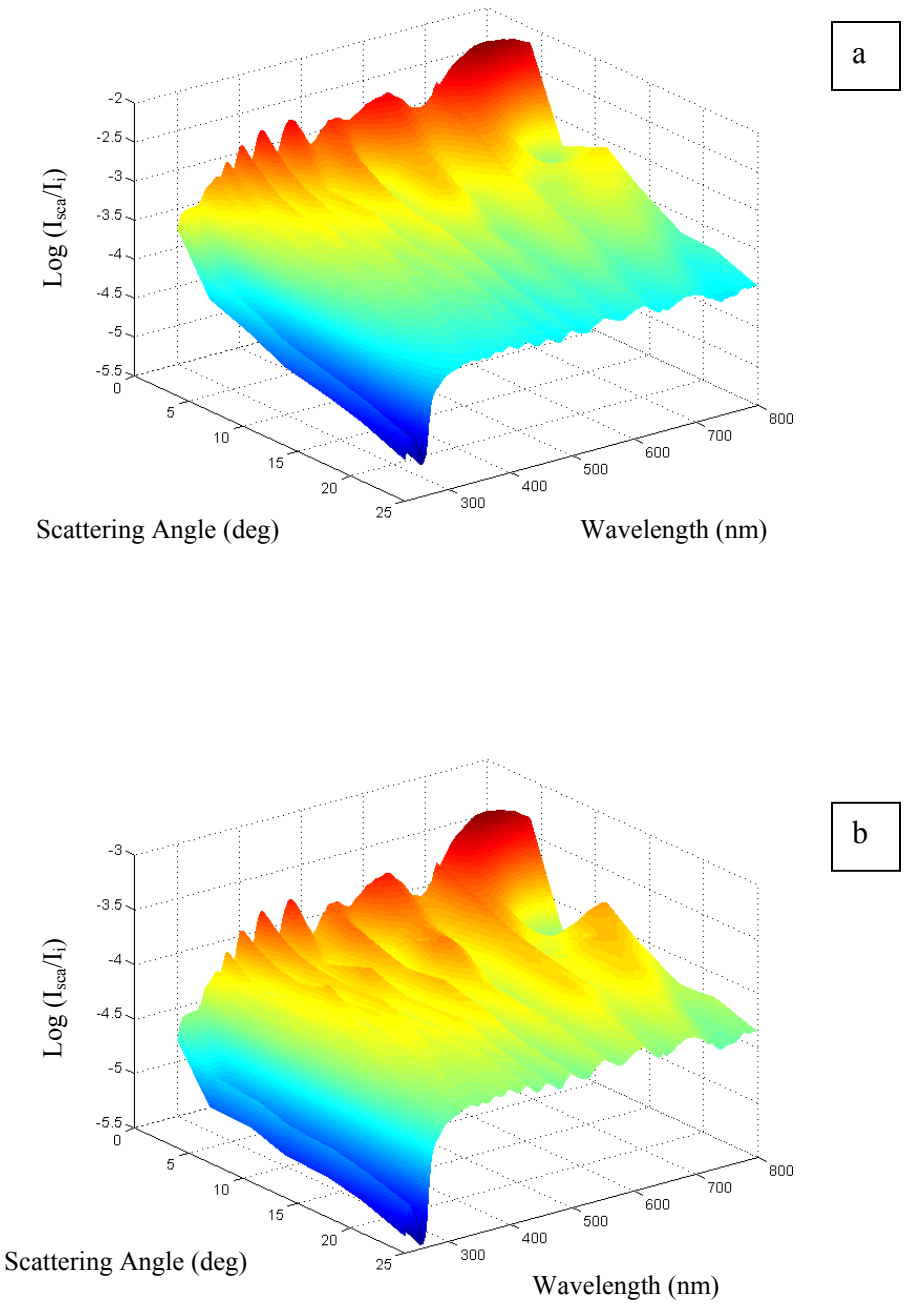

Figure 5.13. Scattering volume corrected UV-VIS MAMW response surface of polystyrene 8 µm standard in water plotted for the demonstration of the scattering volume correction. a) UV-VIS MAMW response surface without scattering volume correction. b) UV-VIS MAMW response surface with the sine correction.

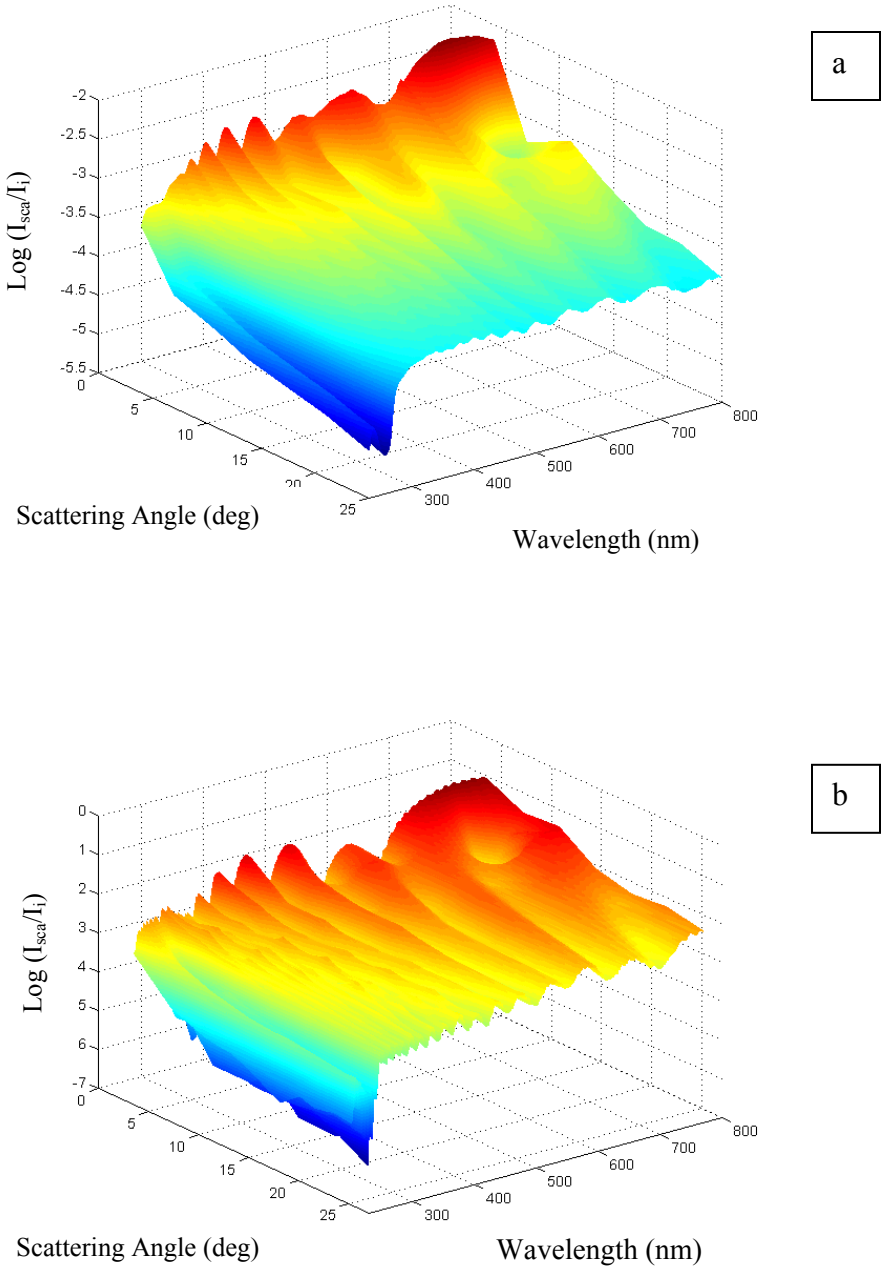

Figure 5.13. (Continued). c) UV-VIS MAMW response surface when scattering volume correction is done. d) Simulated UV-VIS MAMW response surface.

Fig. 5.14 shows the effect of the scattering volume correction. Fig. 5.14.a shows the effect of the scattering volume correction for the polystyrene 1.0 μm standard in water as a function of the observation angle at a wavelength of 633 nm, and Fig. 5.14.b shows the effect of scattering volume correction for the polystyrene 8.0 μm standard in water as a function of the observation angle at a wavelength of 633 nm. For the polystyrene 1.0 μm standard, the sine correction does not fit at low angles. For the polystyrene 8.0 μm standard, both the calculated-volume correction and the sine correction show a decreased scattering intensity at low angles. The reasons why the calculated-volume correction does not fit well at large angles or for large particles compared with the sine correction are not clear. Nevertheless, for UV-VIS MAMW scattering, the calculated-volume correction is adopted as the best available approximation because the scattering volume change depends on individual spectrometer set up and scattering cell geometry and a correction will have to be applied every time. The unconditional use of the sine correction, especially at low angle scattering, should be avoided. Further study is recommended to elucidate the best scattering volume correction, especially, at low angles.

5.3.5 Effect of Slit Width and Location

Refraction, reflection from the cuvette wall, and scattering volume are the main correction factors for the light scattering experiment. However, for the Integrated UV-VIS MAMW spectrometer, the stray reflection of UV light from the slit edge and the slit mount in front of the cuvette should also be considered.

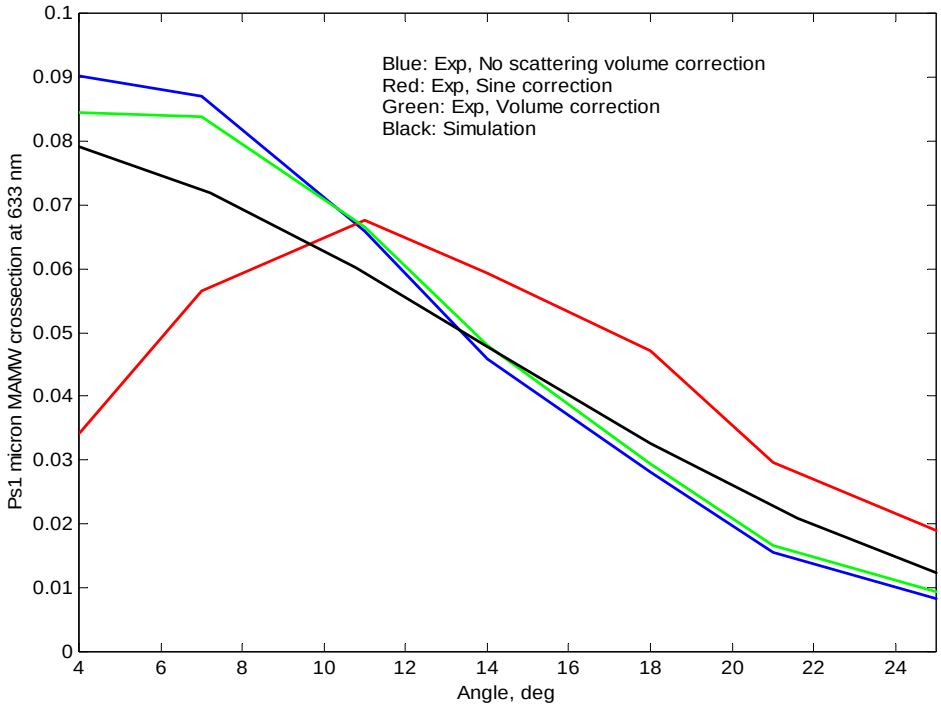

Figure 5.14. Effect of scattering volume correction on the UV-VIS MAMW response surfaces as a function of scattering angle and a constant wavelength of 633 nm.
a) polystyrene 1.0 μm standard in water. The sine correction yields decreased scattered light intensity at low angles.

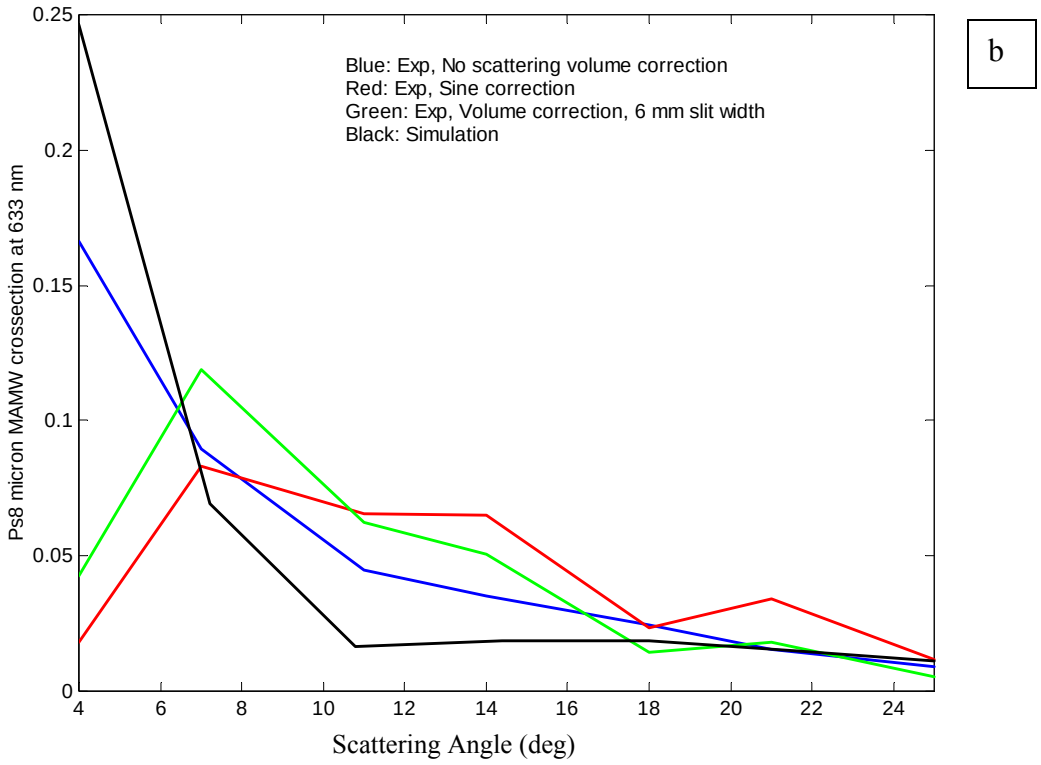

Figure 5.14. Continued. b) polystyrene 8.0 μm standard in water: Both the calculated-volume correction and the sine correction yield decreased scattered light intensity at low angles.

At first, the location of the slit in front of the cuvette was made as close as possible to the cuvette in order to minimize any diffraction of UV light from the slit. The possibility of the UV-VIS light reflection from slit edge and slit mount due to the close distance between the slit and the cuvette was ignored because the use of narrow width slits that can minimize the errors caused by stray reflection.[53] However, the change in the slit-to-cuvette distance became inevitable during the last stage of research due to the following observations:

1) reference scattering measurement at 5^{o} with a few thousand milliseconds integration time that was far higher than the typical integration time used at this angle showed strong scattered light intensity in the UV region and
2) no strong UV light intensity was recorded if this measurement was repeated without the cuvette.

The source of this background UV light was investigated. Among the possibilities, part of the incident UV-VIS beam became the source of the background UV light was excluded because:

1) during the spectrometer set up the incident UV-VIS beam path was traced using a white index card to ensure that no part of the incident beam or background light enters the slit in front of the objective lens if the observation angles are equal to or greater than 5^{o} and

2) if part of the incident UV-VIS beam is refracted and enters the detector, there should be signal saturation due to its strong intensity and the large integration time. However, no such signal saturation was observed.

The fact that no background UV light was recorded without the cuvette attributed the source of this background UV light to the stray reflection from the slit edge and the slit mount. The reason can be easily explained using Fig.5.15, the diagrams illustrating the source of the background UV light. If there is no cuvette, there is no refraction of any UV light as shown in Fig.5.15.a and thus, results in no strong background UV light detection. On the other hand, if there is a cuvette, part of the incident UV beam is reflected by the cuvette wall and then reflected again by the slit edge or the slit mount. The stray UV light reflected from the slit edge or the slit mount incidents on the cuvette obliquely. Then it is refracted by the cuvette wall as shown in Fig.5.15b. The short wavelength UV light is refracted more than the long wavelength UV light because of the large refractive index differences between spectrosil quartz and air at deep UV light wavelength. This reflected-then-refracted UV light becomes the source of the background UV light.

Methods to prevent the reflected UV light from entering the receiving optics were considered. These include:

1) reduction of the width of both slits from 6 mm to 3 mm,
2) changing the location of the slit in front of the cuvette. It was relocated at the position 5 cm away from the sample cell. However, it should be noted that the slit

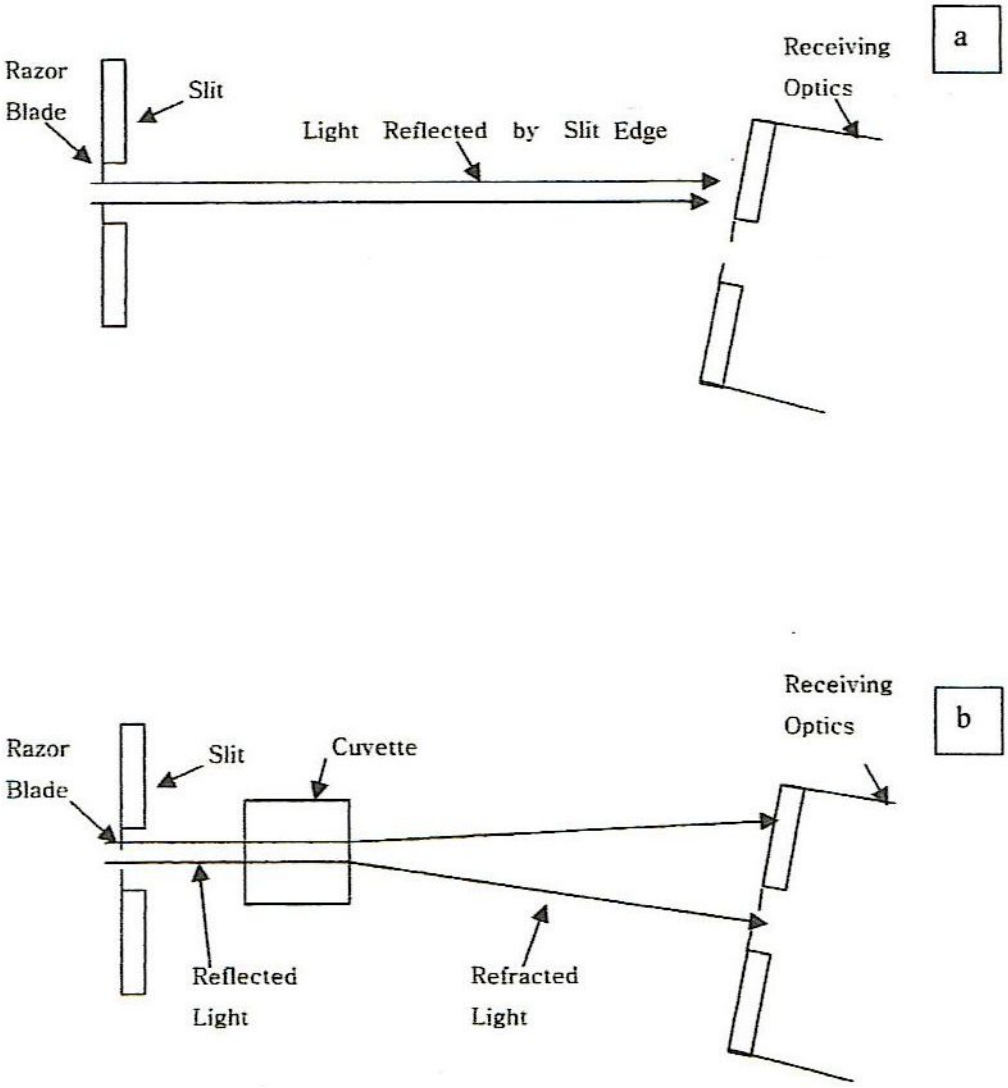

Figure 5.15. Diagram explaining the source of background UV light. a) Without cuvette, no background UV light enters the receiving optics. b) With cuvette, reflected-then-refracted background UV light enters the receiving optics.

in front of the cuvette cannot be located too far away from the cuvette because of the UV beam divergence after passing the slit and

3) As shown in Fig.5.16, changing the slit structure from single block (Fig.5.16.a) to double block and erecting a side wall adjacent to the slit entrance on the incident beam path side (Fig.5.16.b)

In addition, thorough cleaning of the cuvette after every sample change reduced further the amount of background UV light. The cleanness of the cuvette can be assessed using the transmission spectrum of deionized water. Implementation of these methods ensured the systematic reduction of the background UV light and the reproducibility of the measurement results. As a result, the measurement of the UV-VIS MAMW spectra of polystyrene 20 nm spheres that is the minimum size standard available from Duke Scientific became possible. Previously, the measurement of the UV-VIS MAMW spectra of polystyrene spheres less than 150 nm was impossible due to the strong background UV light at low angles as shown in Fig.5.17. Besides, Fig.5.18, the measured UV-VIS MAMW spectra of polystyrene 300 nm spheres, showed peculiar features in the short wavelength UV region at low observation angles. It should be noted that slit structures and slit-to-cuvette distances used for the measurement of the UV-VIS MAMW spectra presented in this dissertation were varied depending on the samples. Slit widths and slit-to-cuvette distances used for the measurement of each polystyrene standard are summarized in the Table 5.5. The changes in the slit structure and the slit-to-cuvette distance depending on the samples resulted in the lack of the consistency of the setup

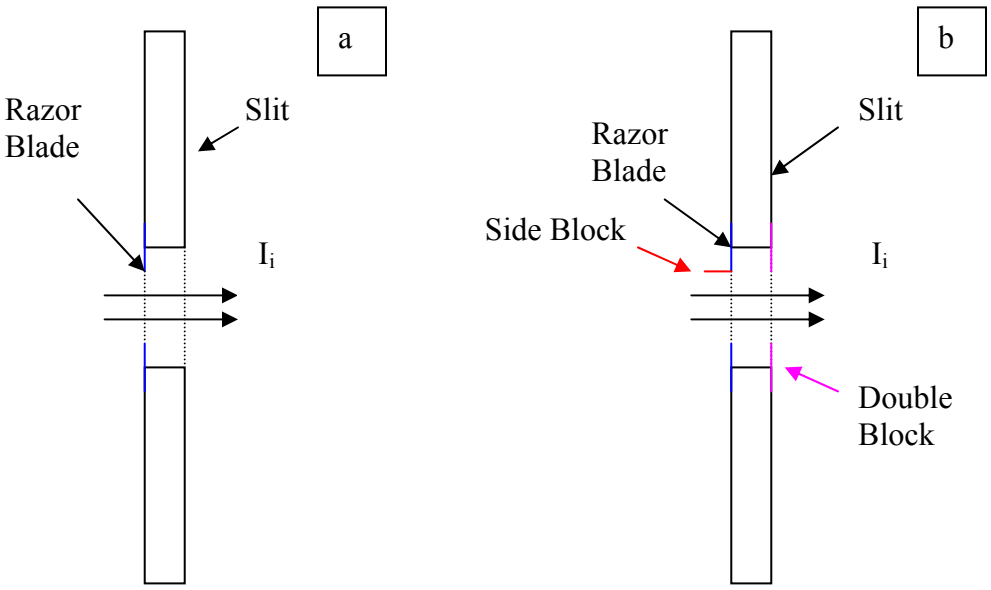

Figure 5.16. Modified slit structure for the prevention of the background UV light.
a) Before the modification. b) After the modification – Double block and side block are added.

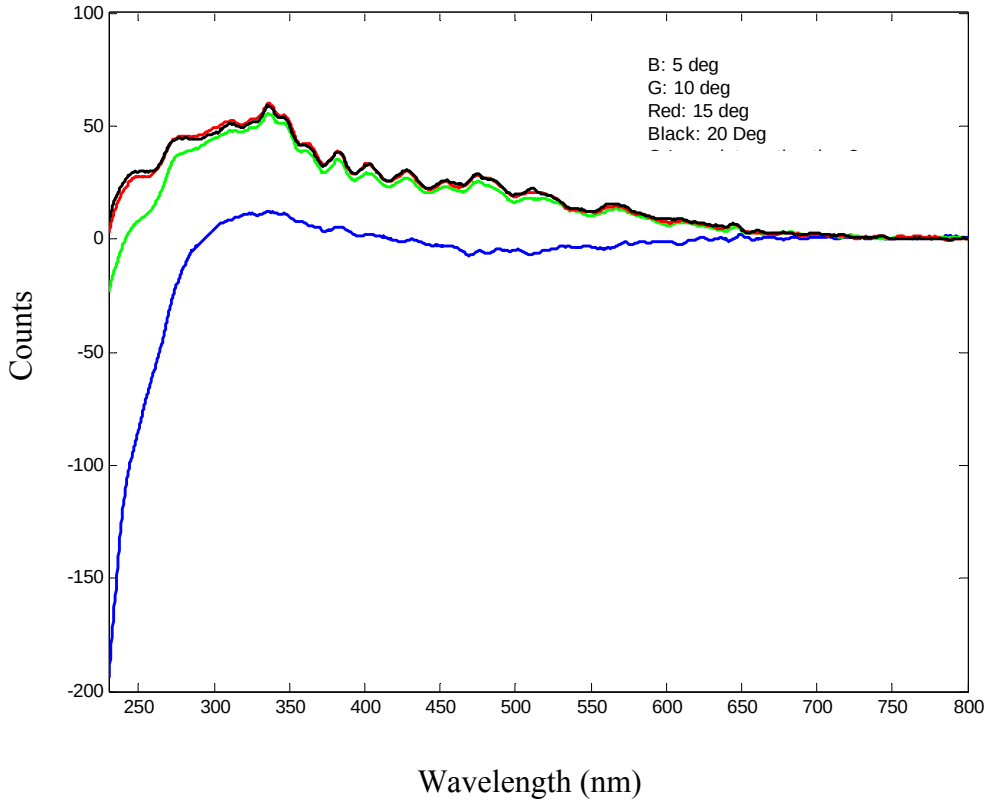

Figure 5.17. UV-VIS MAMW scattering profiles of polystyrene 150 nm spheres at observation angles from 5^{o} to 20^{o}. Note the negative scattered light intensity in case of 5^{o}.

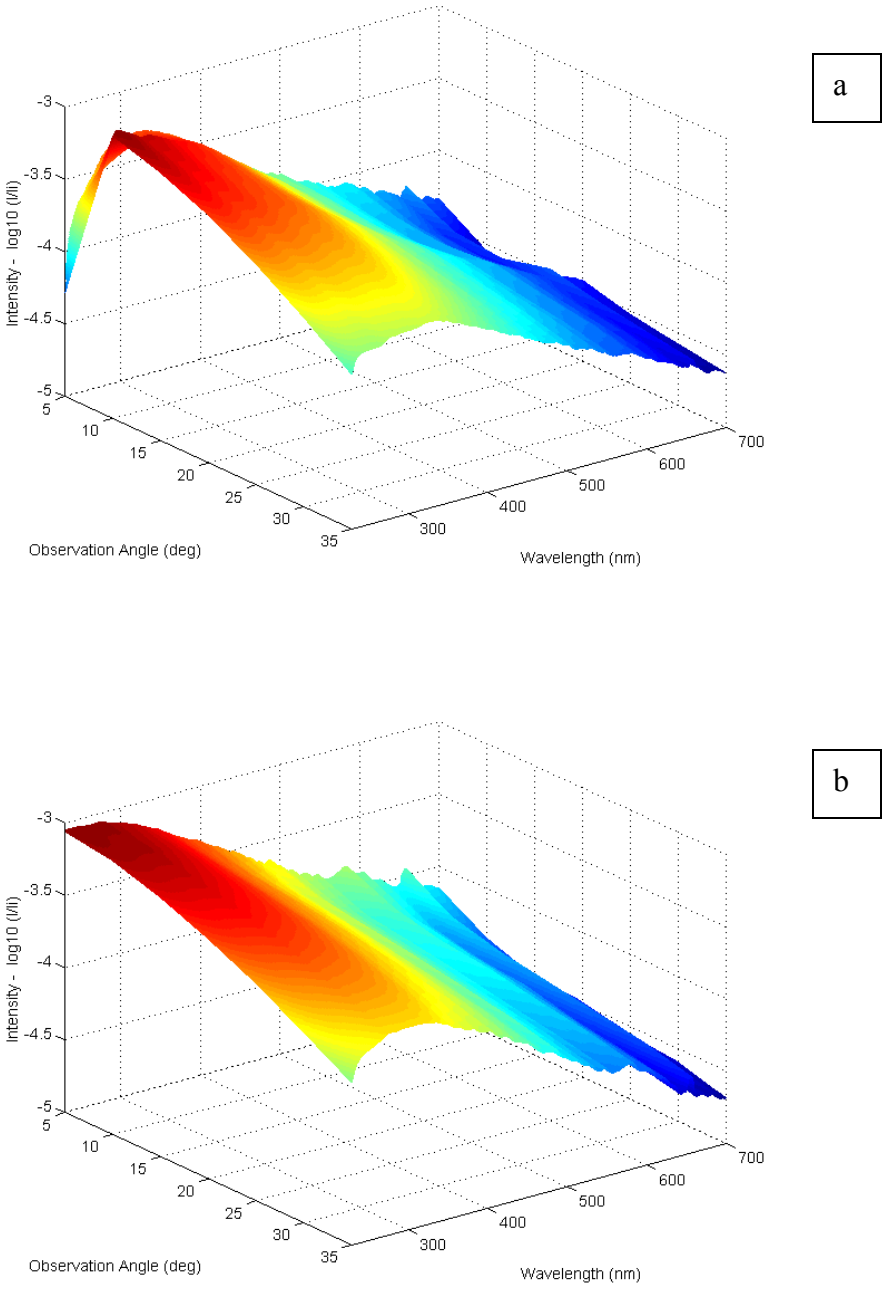

Figure 5.18. Measured UV-VIS MAMW spectra of polystyrene 300 nm spheres in water. a) Measured with the background UV light. b) Measured after the elimination of the background UV light.

used for the measurement. Therefore, it is inevitable to investigate to what extent the loss of the consistency of the setup is acceptable for the UV-VIS MAMW spectra measurement.

First of all, it should be noted that regardless the slit structure and the slit-to-cuvette distance only the scattered light that are paraxial or parallel to the scattering angle of measurement enters the spectrometer due to the use of lenses. In other words, even if the slit structure and the slit-to-cuvette distance is changed the detection of the scattered light that is originated from angles other than the scattering angle of measurement is not probable. On the other hand the amount of the background UV light that enters the detector may vary depending on slit structure and slit-to-cuvette distance. Consequently, if scattered light intensity of the standard is far stronger than the background UV light intensity, the measurement result is not much affected by the setup changes and vice versa.

For micron size polystyrene standards (1 μm – 8 μm), their scattered light intensity in the UV region is strong and thus, the background UV light does not much affect the measured results. Fig 5.19 shows the UV-VIS MAMW response surfaces of polystyrene 4μm standards in water. 3 mm slit width was used for the measurement reported in Fig. 5.19.a and 6 mm slit width was used for the measurement reported in Fig. 5.19.b. The results are consistent although slits with different widths were used for the measurements. The variation in the slit-to-cuvette distance also has a negligible effect on the measurement results. Fig.5.20 shows the UV-VIS MAMW response surfaces of polystyrene 1.87 μm spheres in water. For this measurement, slits with the same width

Table. 5.5. Slit width and distance used for the UV-VIS MAMW spectra measurement

Standard	Slit width (mm)	Distance between slit and cuvette (cm)
Polystyrene 20 nm sphere	3	5
Polystyrene 500 nm sphere	3	5
Polystyrene 1.0 μm sphere	6	1
Polystyrene 4.0 μm sphere	6	1
Polystyrene 8.0 μm sphere	6	1
Polystyrene 10.0 μm sphere	3	5
Polystyrene 1.87 μm sphere	3	5
Peanut-shaped Polystyrene 1.85 μm standard	3	5
Polystyrene 3.0 μm sphere	6	1
Green fluorescent-dyed Polystyrene 3.0 μm sphere	6	1
Whole blood samples (Normal, Sickled)	6	1

reported in Fig. 5.19.a and 6 mm slit width was used for the measurement reported in Fig. 5.19.b. The results are consistent although slits with different widths were used for the measurements. The variation in the slit-to-cuvette distance also has a negligible effect on the measurement results. Fig.5.20 shows the UV-VIS MAMW response surfaces of polystyrene 1.87 μm spheres in water. For this measurement, slits with the same width were used while the slit-to-cuvette distance was changed from 1 cm (Fig.5.20 a.) to 5 cm (Fig.5.20 b.). Both results are consistent even if the slit-to-cuvette distance was varied. Therefore, it can be concluded that the changes in the slit structure or the slit-to-cuvette distance do not much affect the measured UV-VIS MAMW spectra of micron-size polystyrene standards that are smaller than 10 μm.

On the other hand, sub-micron size polystyrene standards have weak scattered light intensity in the short UV wavelength region. Thus, the background UV light can significantly distort the measured results. For polystyrene 10 μm standard, it has weak scattered light intensity in the UV region due to the absorption of UV light by free surfactants detached from the polystyrene standards and the diffraction caused by the increased particle size. Therefore, the measurement of the UV-VIS MAMW spectra of polystyrene 10 μm standard in the deep UV region is not capable if there is strong background UV light.

In conclusion the elimination of the background UV light by changing slit structure and slit-to-cuvette distance is indispensable for the UV-VIS MAMW spectra measurement of sub-micron size polystyrene standards or polystyrene 10 μm standard.

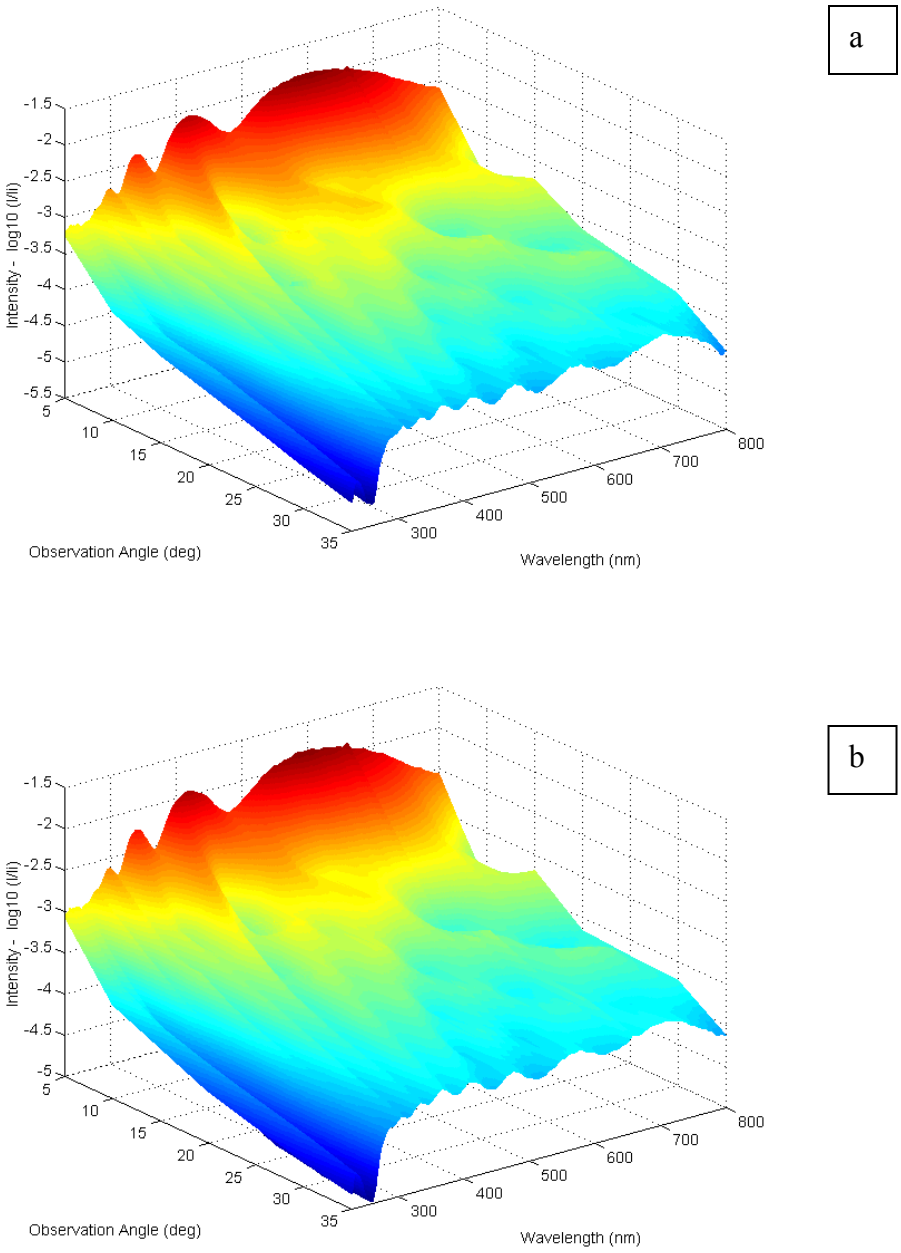

Figure 5.19. Effect of the slit width variation on the measured UV-VIS MAMW response surfaces of polystyrene 4.0 μm standard in water. For both measurements the slit-to cuvette distance was kept constant. a) 3 mm slit width was used for the measurement. b) 6 mm slit width was used for the measurement.

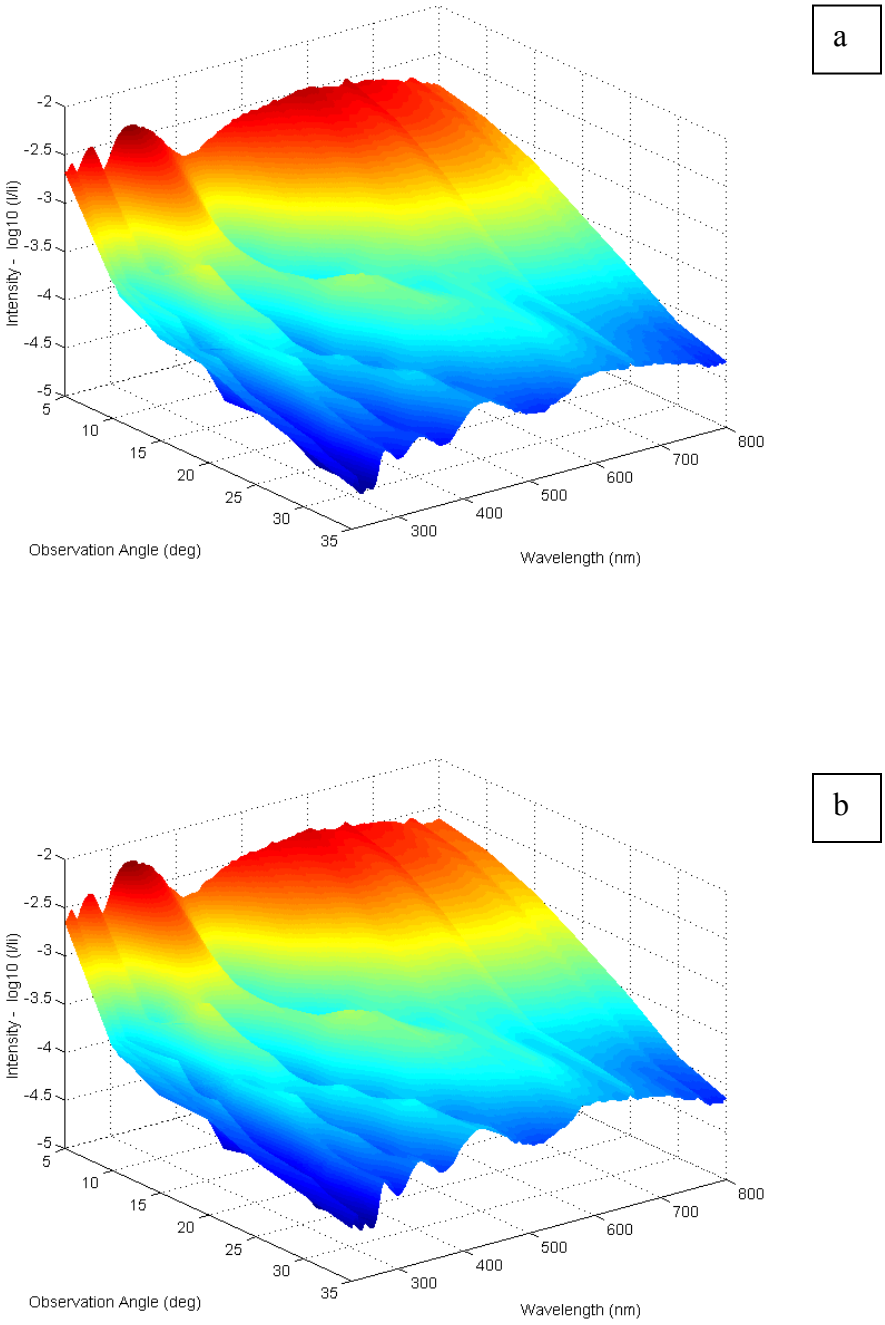

Figure 5.20. Effect of the slit-to cuvette distance variation on the measured UV-VIS MAMW response surfaces of polystyrene 1.87 μm spheres in water. For both measurement, the slit width was kept constant. a) Slit is1 cm away from cuvette. b) Slit is about 5 cm away from cuvette.

Further systematic investigation is recommended to elucidate the best slit width and the slit-to-cuvette distance for the Integrated UV-VIS MAMW spectrometer. Micro positioning equipment and modular optics will be required for this study to ensure the reproducibility of the optics alignment.

5.3.6 Data Normalization

Comparison of the results obtained by the theoretical simulation with the experimental measurement necessitates data normalization to remove the effects of the sample concentration and/or particle number variation.[2] In the case of optical density, normalization can be accomplished by dividing the measured spectra by the area under the corresponding optical density curve.[1] For UV-VIS MAMW scattering, the criteria or standard for data normalization can be found from Eq. (2.34) that requires the use of the incident light intensity to normalize the scattered light intensity. Ideally, the incident light intensity I_i should be measured at 0^o without the sample cell. However, the use of the sample cell and reference solution decreases the incident light intensity due to reflection, refraction, etc. Therefore, the reference UV-VIS beam intensity measured at 0^o with the cuvette filled with the reference solution may be chosen as the incident light intensity for the normalization of the scattered light intensity.

For the normalization of the UV-VIS MAMW scattering measurement results**,** not only the incident UV-VIS beam intensity, but the shape of the incident UV-VIS beam spectrum is also important because the measured scattered light intensity is normalized not by a single data point but by a multiwavelength light spectrum (i.e., the 570

wavelengths used to plot the UV-VIS MAMW spectra). This requires rigorous optics alignment and ensuring the reproducibility of the incident UV-VIS beam spectrum. If the shape of the reference beam spectrum is significantly different from that of the incident beam spectrum, the resulting UV-VIS MAMW response surfaces can also be different. Consequently, the reference beam that has the different spectral shape compared with that of the incident beam is not acceptable for the normalization standard. For instance, Fig.5.21.a, the incident UV-VIS beam spectrum measured at 0^o, Fig.5.22.a, the reference UV-VIS beam spectrum measured at 0^o, and Fig.5.24.a, the reference UV-VIS beam spectrum measured at 5^o show similar spectral shapes. Hence, the resulting UV-VIS MAMW response surfaces obtained by normalizing the measured scattered light intensity using any one of the above UV-VIS beam spectra are also consistent. This becomes evident from Fig.5.21.b, Fig.5.22.b, and Fig.5.24.b, the UV-VIS MAMW response surfaces of the polystyrene 3 μm standard in water acquired using Fig.5.21.a, Fig.5.22.a, and Fig.5.24.a as the normalization standard, respectively. Therefore, any one of these three UV-VIS beam spectra Fig.5.21.a, Fig.5.22.a and Fig.5.24.a seems to be acceptable as the normalization standard. On the other hand, Fig.5.23.a, the incident UV-VIS beam spectrum measured at 3^o and Fig.5.25.a, the reference UV-VIS beam spectrum measured at 15^o show different spectral shape compared with Fig.5.21.a. As a result, the UV-VIS MAMW response surfaces of the polystyrene 3 μm standard in water Fig.5.23.b and Fig.5.25.b, obtained using Fig.5.23.a and Fig.5.25.a as the normalization standard respectively, show different and noisy response surfaces. Therefore, it can be concluded

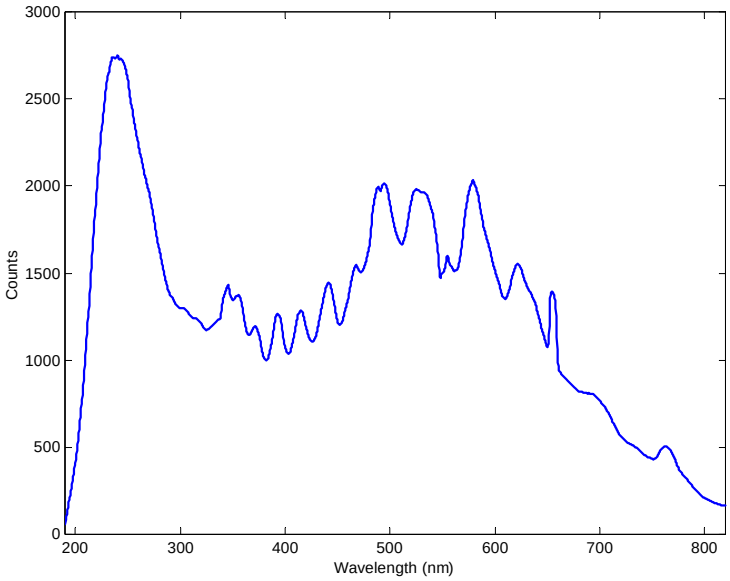

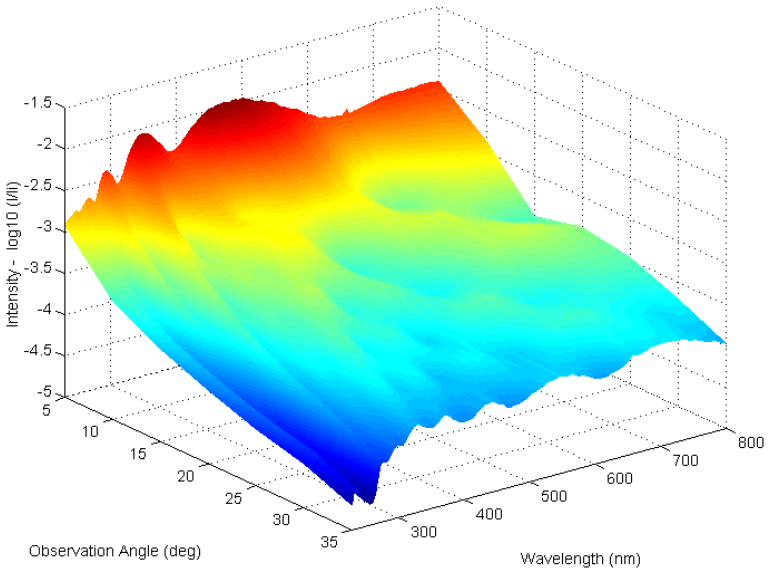

Figure 5.21. Incident UV-VIS beam spectrum used for normalization and the resulting UV-VIS MAMW response surface. a) Incident UV-VIS beam spectrum measured at 0^{o}. b) UV-VIS MAMW response surface of the polystyrene 3 μm standard in water obtained by normalizing the measured results using the incident UV-VIS beam spectrum.

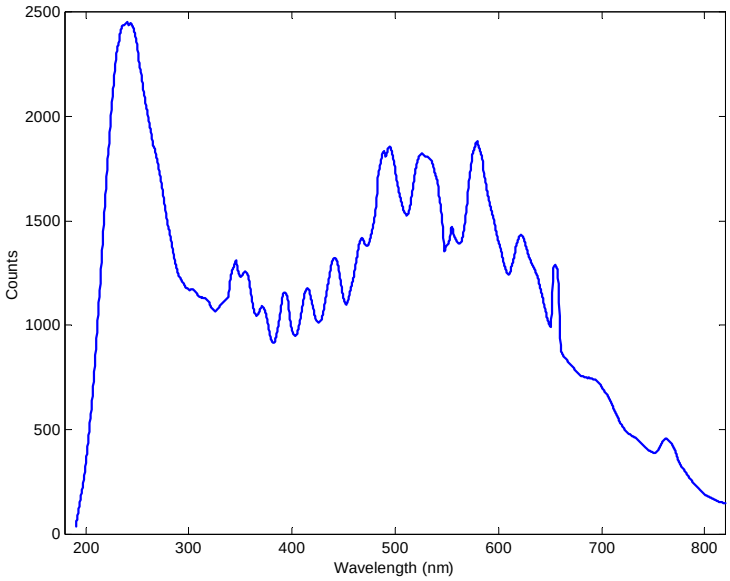

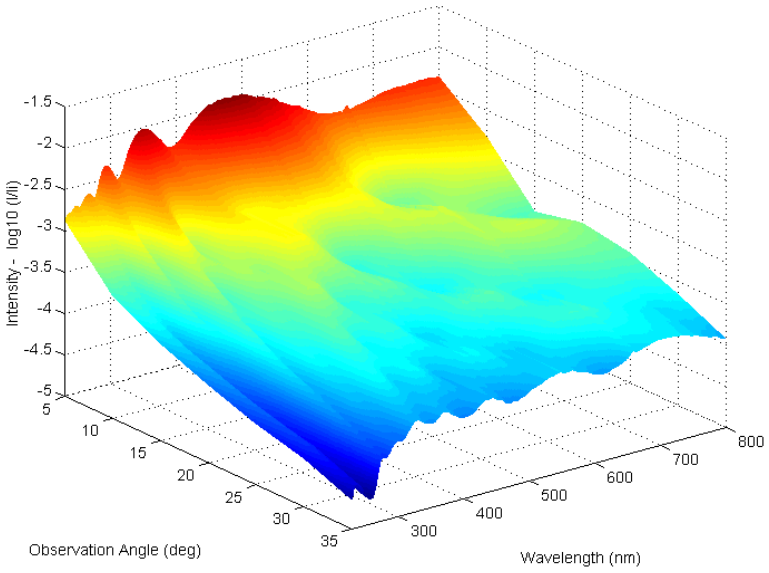

Figure 5.22. Reference UV-VIS beam spectrum used for normalization and the resulting UV-VIS MAMW response surface. a) Reference UV-VIS beam spectrum measured at 0^{o}. b) UV-VIS MAMW response surface of the polystyrene 3 µm standard in water obtained by normalizing the measured results using the reference UV-VIS beam spectrum.

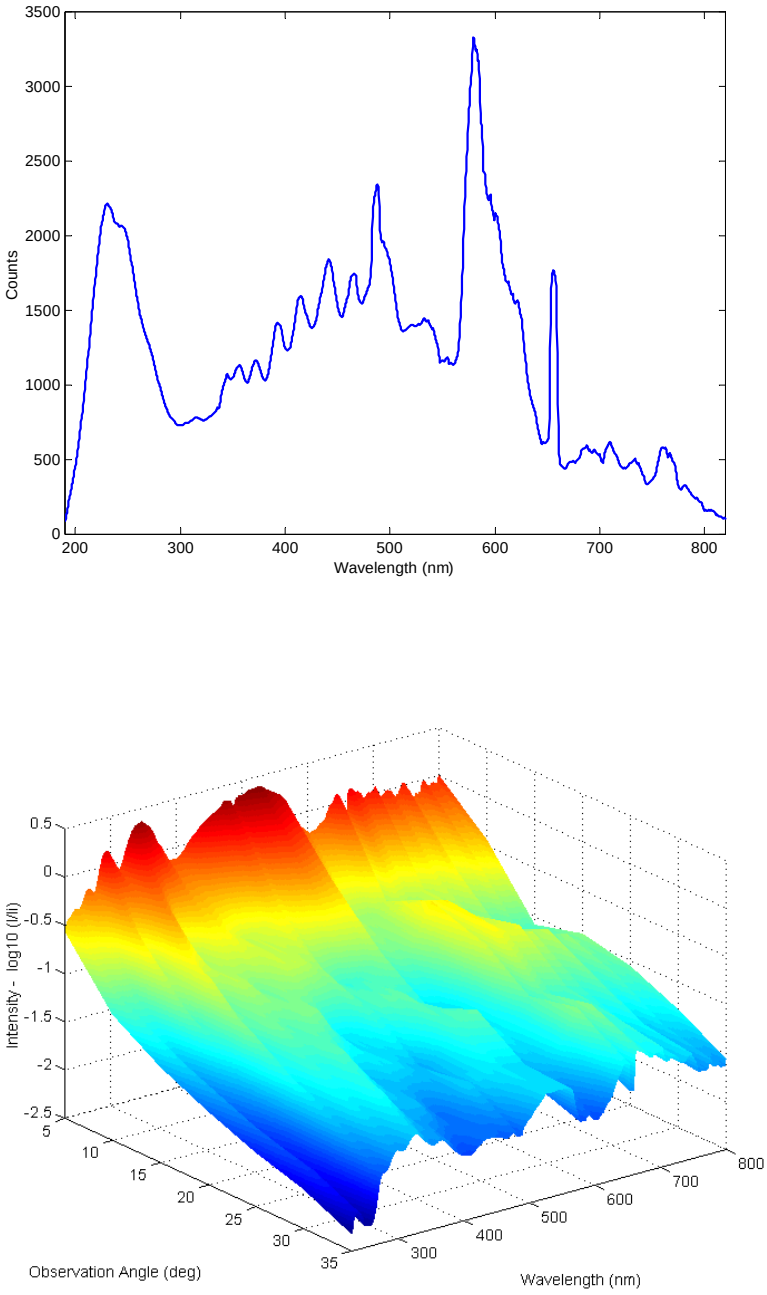

Figure 5.23. Incident UV-VIS beam spectrum measured at 3^{o} used for normalization and the resulting UV-VIS MAMW response surface. a) Incident UV-VIS beam spectrum measured at 3^{o}. b) UV-VIS MAMW response surface of the polystyrene 3 μm standard in water obtained by normalizing the measured results using the incident UV-VIS beam spectrum measured at 3^{o}.

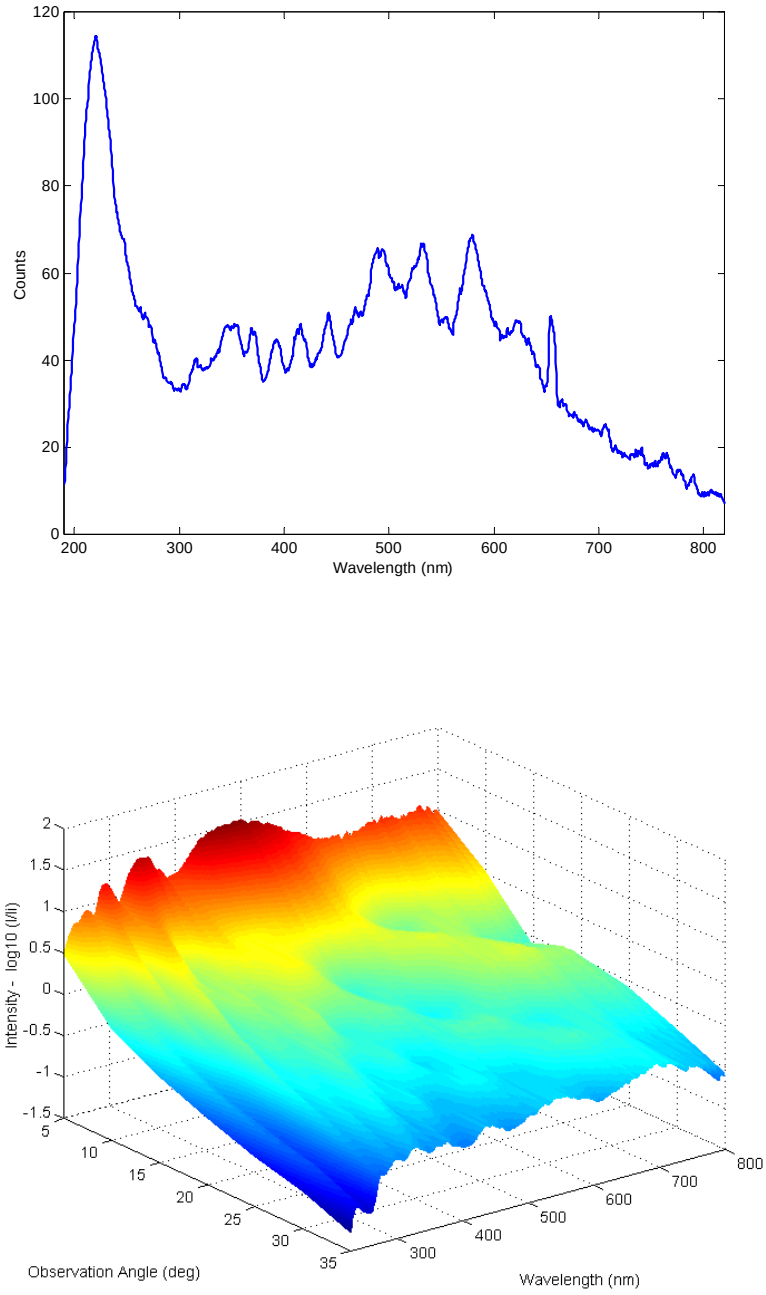

Figure 5.24. Reference UV-VIS beam spectrum measured at 5^{o} used for normalization and the resulting UV-VIS MAMW response surface. a) Reference UV-VIS beam spectrum measured at 5^{o}. b) UV-VIS MAMW response surface of the polystyrene 3 μm standard in water obtained by normalizing the measured results using the reference UV-VIS beam spectrum measured at 5^{o}.

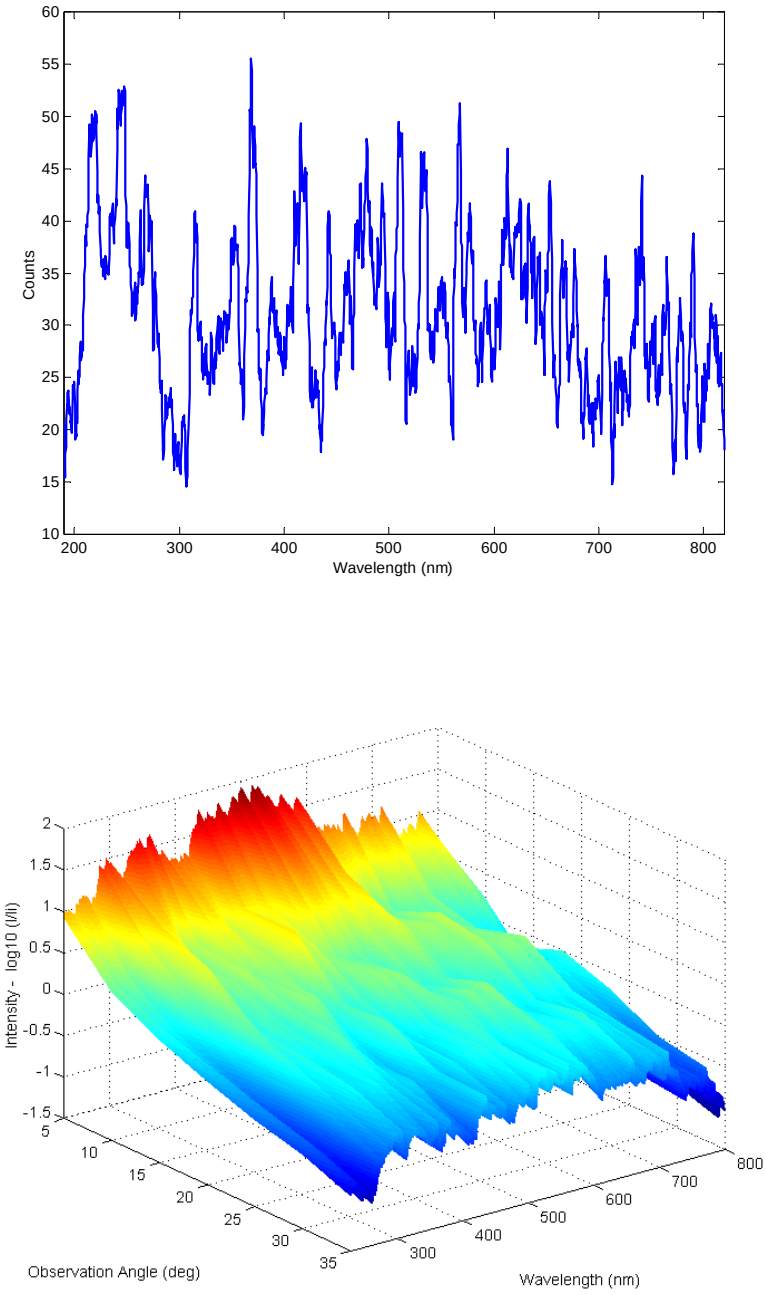

Figure 5.25. Reference UV-VIS beam spectrum measured at 15^{o} used for normalization and the resulting UV-VIS MAMW response surface. a) Reference UV-VIS beam spectrum measured at 15^{o}. b) UV-VIS MAMW response surface of the polystyrene 3 μm standard in water obtained by normalizing the measured results using the reference UV-VIS beam spectrum measured at 15^{o}.

that the UV-VIS beam spectra shown in Fig.5.23.a and 5.25.a are not adequate for the normalization standard.

Clearly, the features of the measured UV-VIS MAMW response surfaces depend on the shape of the normalization beam spectrum. Therefore, it is necessary to investigate which UV-VIS beam may be used as the normalization standard. Fig. 5.26 shows an incident UV-VIS beam spectrum recorded with different optics setup; the lens L4 was removed and 3 mm width slits were used. Fig. 5.27 and Fig.5.28 are the measured UV-VIS MAMW response surfaces of polystyrene 1 μm spheres and polystyrene 4 μm spheres in water, respectively, obtained using this set up. Although the shape of this incident UV-VIS beam spectrum is different from that shown in Fig.5.21.a., the corresponding UV-VIS MAMW response surfaces are distinctive for each particle standard and consistent with the results shown in Fig.5.6.a or Fig.5.19.a except the wavelength range at longer than 750nm where the incident UV-VIS beam spectrum Fig. 5.26 shows weak intensity. Therefore, it can be concluded that if the incident UV-VIS beam spectrum has enough intensity for the whole wavelength range, slight changes in the shape of the UV-VIS beam spectrum do not significantly affect the measured UV-VIS MAMW response surfaces. Together with the flexibility to choose the normalization standard, this proves that the particle characterization by the simultaneous detection of the JPPD using MAMW spectrometer is a robust technique.

At present, calibration of the UV-VIS beam spectrum at wavelengths shorter than 250 nm is impossible.[63] For that reason, systematic study to establish the acceptable UV-VIS beam spectrum for the Integrated UV-VIS MAMW spectrometer and the

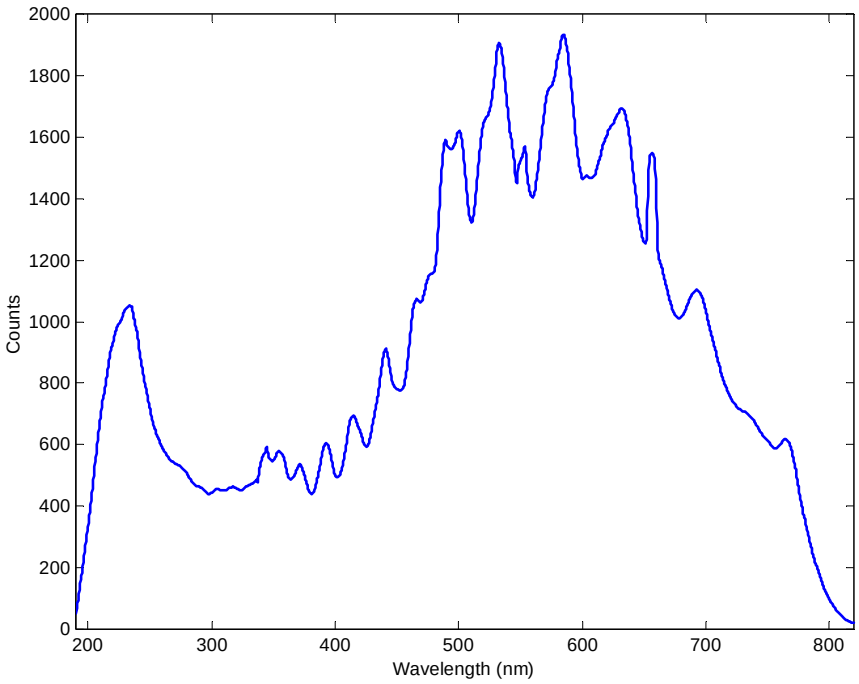

Figure 5.26. Incident UV-VIS beam spectrum recorded with different optics setup. Lens L4 was removed and slits with 3 mm width were used.

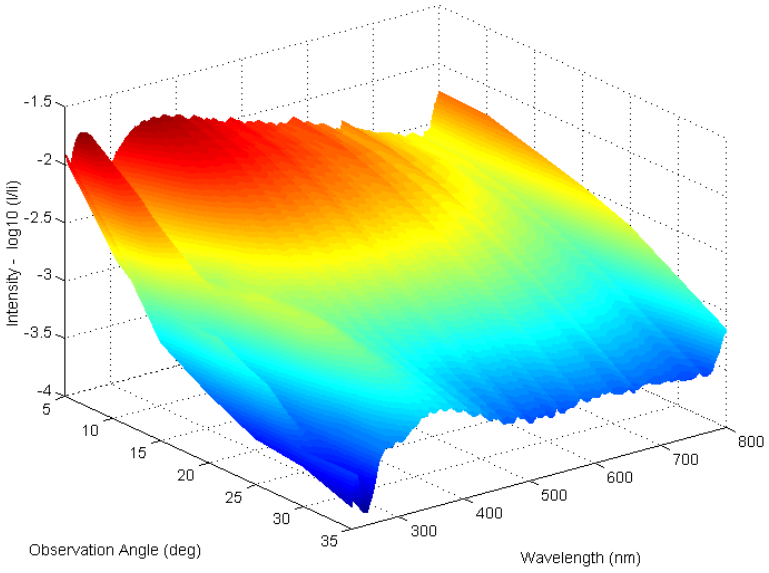

Figure 5.27. Measured UV-VIS MAMW response surfaces of polystyrene 1 μm spheres in water obtained using the UV-VIS beam spectrum in Fig. 5.26 for normalization.

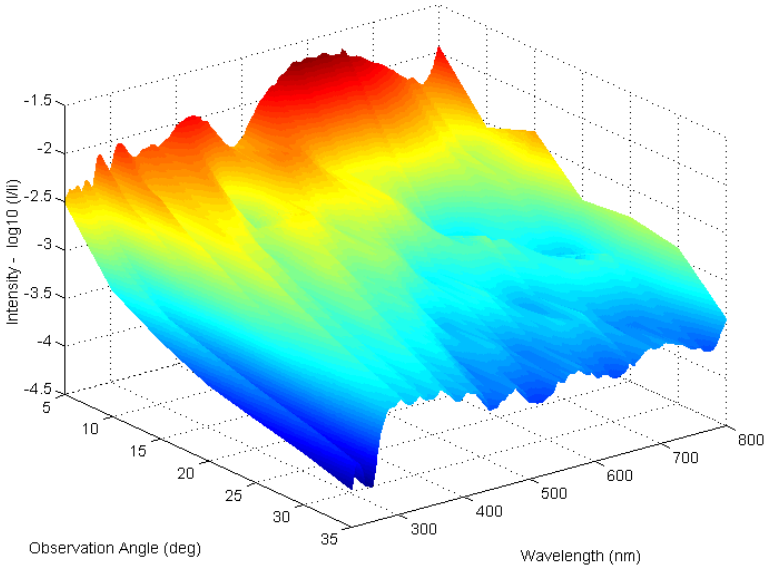

Figure 5.28. Measured UV-VIS MAMW response surfaces of polystyrene 4 μm spheres in water obtained using the UV-VIS beam spectrum in Fig. 5.26 for normalization.

investigation of the effect of the spectral shape changes of the incident UV-VIS beam to the measured UV-VIS MAMW spectra are recommended.

5.4. Data Processing

This section describes the data processing procedures for each of scattering, optical density and fluorescence measurements. Once measured data is processed, it requires the adjustment using correction factors before plotting and further interpretation. All the data processing and plotting were performed using MATLAB; the code used for data processing and plotting is listed in Appendix A. To plot the measured results, it is recommended that the spectrometer generated wavelength interval be used directly to avoid possible wavelength shifts and artificial smoothing arising from MATLAB algorithms.

5.4.1. Optical Density Data Processing

Optical density (OD) is measured using the absorbance mode of the Ocean Optics OOIBase32 software that controls the S2000 production spectrometer. The absorbance mode automatically calculates optical density by utilizing the following equation

$$OD = \log\frac{1}{T} = \log\left\{(I_r(0) - D(0))/(I_s(0) - D(0))\right\} \tag{5.12}$$

where T represents transmission and $I_r(0)$, $I_s(0)$, and $D(0)$ designate the reference signal intensity, the sample signal intensity and the dark current at 0^o, respectively. The optical density measured in the absorbance mode is ready for plotting or further processing. However, for comparison with optical density spectra measured using HP 8453 spectrometer the optical densities are normalized by the area under the curve.

5.4.2 Scattering Data Processing

Once the scattered light intensity at observation angle θ is found by subtracting the reference intensity from the scattered light intensity at that angle, the correction factors are multiplied. For the current prototype UV-VIS MAMW spectrometer only refraction and scattering volume corrections are taken into consideration while reflection and scattering path length corrections are ignored as discussed in Section 5.3. Then the integration time ratio, calculated at every scattering angle for each sample, is multiplied. The integration time used for the measurement of UV-VIS MAMW scattering varies depending on sample and scattering angle as described in Section 5.2.2. After data correction and multiplication for the integration time ratio, the resulting scattered light intensity is normalized by the reference intensity at 0^o. For the UV-VIS MAMW response surface plot, the log value of the normalized scattered light intensity is used. All these procedures are summarized in Eq. (5.13)

$$I_{sca}^{plot}(\theta) = \log\left\{\frac{C(\theta)\{I_s(\theta) - I_r(\theta)\}}{I_r(0)}\right\} \tag{5.13}$$

where $I_{sca}^{plot}(\theta)$ is the plotted scattered light intensity at scattering angle θ , $C(\theta)$ is the correction term taking into account the relevant correction factors and integration time ratio, $I_{sca}(\theta)$ is the scattered light intensity, and $I_r(\theta)$ is the reference light intensity at scattering angle θ. The resulting UV-VIS MAMW response surfaces are plotted for the refraction corrected scattering angle, the observation angle.

5.4.3 Fluorescence Data Processing

Data processing for fluorescence simply requires the subtraction of the measured reference signal intensity from the measured fluorescence signal intensity:

$$I_{fl} = I_{fl}(90) - I_r(90) \tag{5.14}$$

where I_{fl} is fluorescence intensity, $I_{fl}(90)$ and $I_r(90)$ represents fluorescence signal intensity and reference signal intensity measured at 90^o, respectively. In this dissertation research, additional data corrections are not performed in case of fluorescence because the primary purpose of the fluorescence measurement is to demonstrate that the Integrated UV-VIS MAMW spectrometer can perform fluorescence spectroscopy.

5.4.4. Remarks on Measured Result Plotting Using MATLAB

For validation purposes, the measured optical density spectra recorded with the Integrated UV-VIS MAMW spectrometer were compared to the measured optical density spectra obtained using an HP 8453 spectrometer. Although the spectra recorded from

both spectrometers showed the same features, there were unexplainable wavelength shifts as shown in Fig. 5.29 where the optical density spectra of 1 μm polystyrene standards in water are shown. If the optical density spectra measured with another S2000 spectrometer were used for comparison, no appreciable wavelength shifts were observed. At first, these wavelength shifts were attributed to the different angle of acceptance of the Integrated UV-VIS MAMW spectrometer. As described in Section 4.1.3, the Integrated UV-VIS MAMW spectrometer employs lenses as light delivery tool while the Ocean Optics S2000 spectrometer and accompanying light source are designed to use optical fibers to deliver light. Consequently, the incident beam divergence of the integrated UV-VIS MAMW spectrometer can be different from that of the S2000 spectrometer. This leads to the different angle of acceptance of the Integrated UV-VIS MAMW spectrometer because the angle of acceptance can be affected by the incident beam divergence as described in Section 4.5. The relation between the angle of acceptance of the Integrated UV-VIS MAMW spectrometer and the wavelength shifts of the measured spectra was systematically investigated. However, all the efforts including the use of a homemade spatial filter that minimizes the incident UV-VIS beam divergence were not successful. Thereafter, MATLAB program that processes the measured data was re-examined because of the possibility that the wavelength interval generated by mathematical software like MATLAB may not match that generated by S2000 spectrometer.[68]
For instance, there are 1674 data points (an array of 1674 CCDs) from 230.04 nm to 800.13 nm in case of S2000 spectrometer and to match these data points,

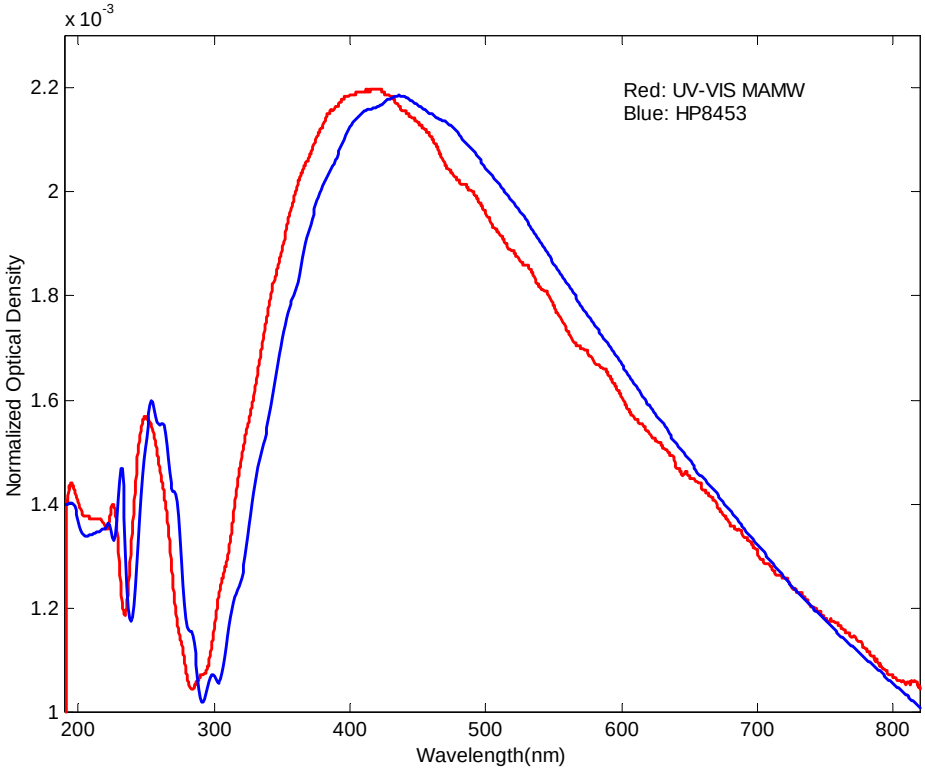

Figure 5.29. Optical density spectra of polystyrene 1 μm standard in water measured with the Integrated UV-VIS MAMW spectrometer (red) and the HP8453 spectrometer (blue). Note the wavelength shifts between two spectra.

the MATLAB code for the wavelength axis of the UV-VIS MAMW response surface was written as x = [230.04: (800.13 - 230.04)/1674: 800.13]. However, it was turned out that the resulting wavelength resolution does not match that generated by the S2000 spectrometer operating software (OOIBase32). After noticing this, the MATLAB code was rewritten to use the wavelength interval defined by the OOIBase32 software directly; the plots made by new code showed no wavelength shifts between the results obtained by the Integrated UV-VIS MAMW spectrometer and HP8453 spectrometer. Fig. 5.30 and Fig. 5.31 show contour plots of the whole blood UV- VIS MAMW response surfaces before and after the wavelength shift correction, respectively. The same observation angles were used for both plots. Before the wavelength shift correction (Fig. 5.30), the peak of hemoglobin absorption band was formed at around 400 nm. This does not match with the result obtained using the prototype MAMW spectrometer (Fig.6.53.a.).[2] After the wavelength shift correction, both plots (Fig. 5.31 and Fig.6.53.a.) show consistent hemoglobin absorption peak position at around 415 nm. *Care should be taken not to use the wavelength intervals generated by mathematical software but to use the spectrometer generated wavelength interval when plotting the measured data.*

5.5 Calibration

Calibration is necessary for the quantitative validation of the joint particle property distribution estimated from UV-VIS MAMW spectra measurement.[2] Calibration methods can be divided into absolute calibration and relative calibration. Due to its

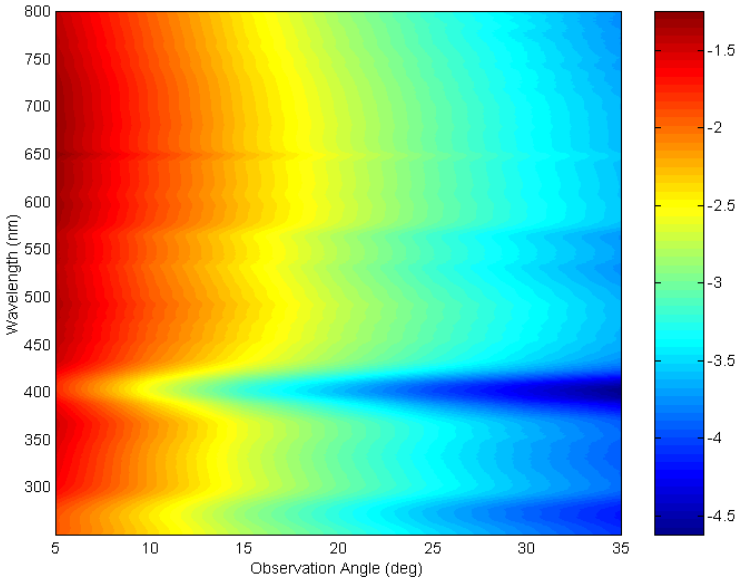

Figure 5.30 Contour plot of the whole blood UV-VIS MAMW response surface before wavelength shift correction. The MATLAB generated wavelength interval was used for plotting.

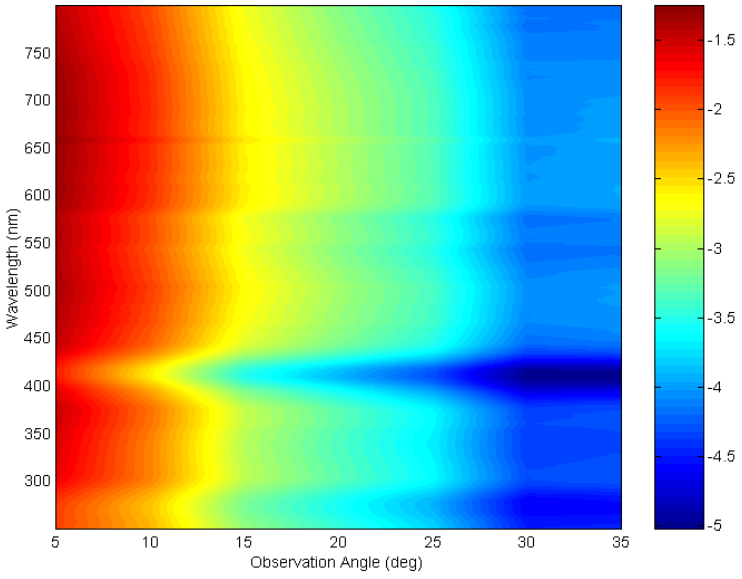

Fig. 5.31 Contour plot of the whole blood UV-VIS MAMW response surface after the wavelength shift correction. The OOIBase32 software generated wavelength interval was used for plotting.

simplicity, the relative calibration was selected for the Integrated UV-VIS MAMW spectrometer. This type of calibration requires the comparison of the measurement results with the theoretically predicted values for the sample system. The implementation of whole calibration procedures requires precise simulation program. Our current UV-VIS MAMW simulation program is being upgraded. Therefore, only the outline of the calibration procedures for the UV-VIS MAMW scattering is provided in this section. For this dissertation research, the measured optical density or fluorescence can be validated by direct comparison with the results obtained using our reference spectrometer HP8453 spectrometer or the data provided by the manufacturer.

5.5.1. Absolute Calibration

Absolute calibration is a method of acquiring calibration constants from the geometry of the apparatus.[66] As such, it requires the calculation of all the geometrical factors involved as well as the measurement of the intensity of the incident light on the sample cell. Consideration of the geometrical factors includes accurate determinations of the detector field of view, corrections for refractive indices of the sample cell and the suspending medium, reflection, and estimation of the scattering volume, etc.[66] Absolute calibration is very difficult to perform and time consuming due to the number and the complexity of the factors considered. Moreover, still some errors can exist and the method is not flexible since it has to be revised every time the system is modified. Unless absolute scattering values are essential, for example, the case of fundamental constant evaluation from light scattering measurements, absolute calibration seems to be

unnecessary. As a consequence, this is not adopted as a calibration method for the integrated UV-VIS MAMW spectrometer.

5.5.2. Relative Calibration

Relative calibration compares the results from independently characterized standards with theoretical calculation to establish the calibration constants.[28, 66] It is relatively easy to perform and flexible. Therefore, it is commonly used as a calibration method for light scattering as well as fluorescence spectroscopy.[32] A number of relative calibration methods for light scattering instrument have been developed. These include:[28, 66]

1. comparison of the scattering from pure liquids such as benzene and toluene with literature values,
2. comparison of the angular scattering intensity with the turbidity (integration of the light scattered overall angles) for a solution of the non-absorbing Rayleigh point scatterers and
3. comparison of the measured scattering intensities of Mie scatterers or suspension of latex particles with the corresponding intensities predicted from Mie theory. Latex particles can be ideal Mie scatterers because of their spherical shapes.

Methods1 or 2 are not the proper choices because the current prototype integrated UV-VIS MAMW spectrometer does not yet have sufficient sensitivity to measure scattering from pure solvents and the measurable angular range is limited. Taking into consideration

the sensitivity and configuration of the current prototype Integrated UV-VIS MAMW spectrometer, it is considered that Method 3 is the most appropriate to use.

5.5.3. Calibration Constants

Obtaining the proper calibration constants at relevant scattering angles and multiplying them by the measured scattering intensities for the sample at every angle completes the whole calibration procedure. In case of the Integrated UV-VIS MAMW spectrometer, the calibration constant at every angle is not a single number but an array of numbers corresponding to each of the wavelengths used. Detailed procedures to estimate calibration constant are given as follows

1. Selection of calibration standards:

Choice of proper size standards is important to obtain the correct calibration constants. Monodisperse polystyrene standards are suitable, not only because they are readily available in a large number of sizes, but also because the optical properties of polystyrene are well established as functions of wavelength and the necessary theoretical calculations can be readily performed. For the calibration of the integrated UV-VIS MAMW spectrometer, it is recommended to use the multiple standards in the size range of 20 nm ~ 10 μm rather than a single standard.

2. Minimization of undesired effects:

Before evaluating the calibration constant, it is necessary to minimize any undesired effects by correcting measured results. Details of correction factors and data correction procedures for the Integrated UV-VIS MAMW spectrometer are described in the section 5.3.

3. Scattering intensity adjustment:

The calculation of calibration constants requires the use of the least squares fit for all angles at all wavelengths. However, for simplicity, the approximation methods of estimating calibration constants rather than the rigorous approaches using the least squares fit are provided in this dissertation.

The adjusted scattering intensity of standard at the scattering angle θ and the wavelength λ can be estimated by subtracting the reference scattering intensity from the standard scattering intensity at the corresponding angle and wavelength:

$$I_{Adj\ meas}^{S\tan dard}(\theta,\lambda)=I_{meas}^{S\tan dard}(\theta,\lambda)-I_{meas}^{S\tan dard\ ref}(\theta,\lambda) \tag{5.15}$$

where $I_{Adj\ meas}^{S\tan dard}(\theta,\lambda)$, $I_{meas}^{S\tan dard}(\theta,\lambda)$, and $I_{meas}^{S\tan dard\ ref}(\theta,\lambda)$ represents the adjusted-measured scattering intensity of the standard, the measured scattering intensity of the standard, and the scattering intensity of the reference recorded during the standard scattering measurement at the scattering angle θ and the wavelength λ, respectively.

4. Approximate Calibration Constant $K(\theta,\lambda)$

The approximate calibration constant $K(\theta,\lambda)$ at scattering angle θ and wavelength λ can be obtained by calculating the ratio of the theoretically-calculated scattering intensity of the standard to the adjusted-measured scattering intensity of the standard as shown in Eq. (5.16)[24]

$$K(\theta,\lambda) = \frac{I^{S\tan dard}_{Theor\ simul}(\theta,\lambda)}{I^{S\tan dard}_{Adj\ meas}(\theta,\lambda)} \tag{5.16}$$

where $I^{S\tan dard}_{Theor\ simul}(\theta,\lambda)$ represents the theoretically-calculated scattering intensity of the standard at the scattering angle θ and the wavelength λ.

5. Data calibration

Multiplying the adjusted-measured scattering intensity of the sample by the approximate calibration constant completes the calibration of measured results:[24]

$$I^{Cal}_{sample}(\theta,\lambda) = < K(\theta,\lambda) >< I^{Sample}_{Adj\ meas}(\theta,\lambda) > \tag{5.17}$$

$$I^{Sample}_{Adj\ meas}(\theta,\lambda) = I^{Sample}_{meas}(\theta,\lambda) - I^{Sample\ ref}_{meas}(\theta,\lambda) \tag{5.18}$$

where $I_{sample}^{Cal}(\theta,\lambda)$ is the calibrated scattering intensity of the sample and $I_{Adj\ meas}^{Sample}(\theta,\lambda)$, $I_{meas}^{Sample}(\theta,\lambda)$, and $I_{meas}^{Sample\ ref}(\theta,\lambda)$ represents the adjusted-measured scattering intensity of the sample, the measured scattering intensity of the sample, the scattering intensity of the reference recorded during the sample scattering measurement at the scattering angle θ and the wavelength λ, respectively.

The implementation of the complete calibration procedures requires a simulation program that can predict the JPPD of particles precisely. At present, theoretically calculated results obtained using our current UV-VIS MAMW simulation program and experimental results do not match well for small particles but show UV-VIS MAMW scattering features for large particles. Further work is necessary to elucidate the reason for the discrepancy, especially for small particles.

CHAPTER 6: RESULTS AND DISCUSSION

.

The capability of the Integrated UV-VIS MAMW spectrometer to characterize micron and sub-micron size particles by the simultaneous measurement of the JPPD was tested. Optical density, UV-VIS MAMW spectra, and fluorescence spectra of polystyrene standards including polystyrene spheres with sizes from 20 nm to 10 μm, peanut-shaped non-spherical particles, and green fluorescent polystyrene spheres were measured. The results demonstrate that the Integrated UV-VIS MAMW spectrometer can detect not only particle size, but also shape and composition information.

As a demonstration of potential applications to biological systems, the UV-VIS MAMW spectra of normal whole blood sample and sickled whole blood sample were measured. The results clearly demonstrate that particle shape and compositional changes can be detected simultaneously by the measurement of UV-VIS MAMW spectra, and that applications, such as medical diagnosis, where such knowledge is important can be developed with this instrumentation.

The analysis of the particle size standards measured with the current prototype UV-VIS MAMW spectrometer, together with the analysis of its optical configuration indicate that the particle characterization capabilities of the Integrated UV-VIS MAMW spectrometer can be further enhanced. Ways to upgrade the Integrated UV-VIS MAMW

spectrometer are discussed. In addition, methods to add new dimensions to the Integrated UV-VIS MAMW spectrometer are described in this section. The Multidimensional (MD) MAMW spectrometer will perform multidimensional spectroscopy measurements simultaneously and thus, maximize the information necessary to completely characterize particle suspensions.

6.1. Measured Optical Density of Polystyrene Spheres

The optical density of polystyrene spheres with sizes of 20 nm, 500 nm, 1 μm, 4 μm, and 10 μm were measured with the Integrated UV-VIS MAMW spectrometer. The measured spectra show features of interference, reddening, ripple structures, and diffraction as well as absorption due to electronic transitions. To validate the MAMW observations, measurements were repeated using the HP 8453 diode array spectrometer and the results obtained from both spectrometers were compared after normalization with the area under curve.

Fig. 6.1 shows the normalized optical density spectra of polystyrene 20 nm spheres in water. Note that the measured optical density spectra were plotted for the wavelength range of 220 nm to 500 nm. The size of particles is small enough to be described by Rayleigh-Debye-Gans theory. The extinction features below 280 nm are dominated by the absorption of polystyrene. The observed spectral features are consistent with the absorption profile of polystyrene provided in Fig.5.1.b. The extinction features below 240 nm are due to absorption by electronic transition. Besides absorption, scattering also contributes to the extinction of incident light. As the wavelength of the

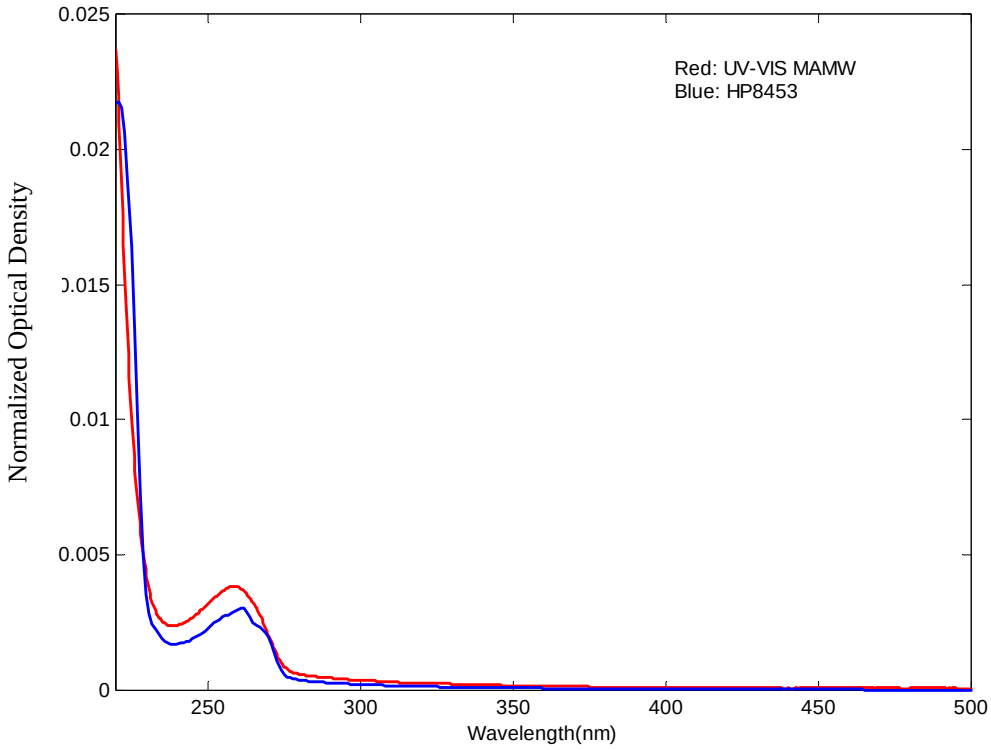

Figure 6.1 Normalized optical density spectra of polystyrene 20 nm spheres in water. Note that wavelength extends from 220 nm to 500 nm.

incident light increases, approximate absorption efficiency a/λ and scattering efficiency a/λ^4 decrease. As a result, no more extinction of incident light is observed at wavelengths longer than 450nm.

Fig. 6.2 shows the normalized optical density spectra of polystyrene 500 nm spheres in water. The measured optical density spectra were plotted for the wavelength range of 200 nm to 820 nm. The broadband peak is an interference peak. Interference caused by phase difference between the forward-scattered light and the incident light that traverses the same physical path outside a sphere gives rise to interference structure: a series of broad, regularly spaced extinction maxima and minima.[7] The requirement for interference between the forward-scattered and the incident light can be obtained by analyzing the numerators of scattering coefficients a_n and b_n.[7] The sudden suppression of the first interference peak near λ = 230 nm is caused by a resonant absorption band of polystyrene. Another characteristics of Fig. 6.2 is reddening: a monotonic decrease of extinction with the increasing wavelength of the incident light. Reddening is caused by enhanced absorption and scattering at the shorter-wavelength blue light than the longer-wavelength red light.[7]

Fig. 6.3 shows the normalized optical density spectra of polystyrene 1.0 μm spheres. Compared to Fig. 6.2, it features more interference structures due to the increased particle size. Extinction is frequently dominated by scattering if the particle is about the same size as or larger than the wavelength of the incident light. Although it is not shown in the spectra measured by the Integrated UV-VIS MAMW spectrometer due to insufficient resolution, ripple structures can be seen in the optical density spectrum

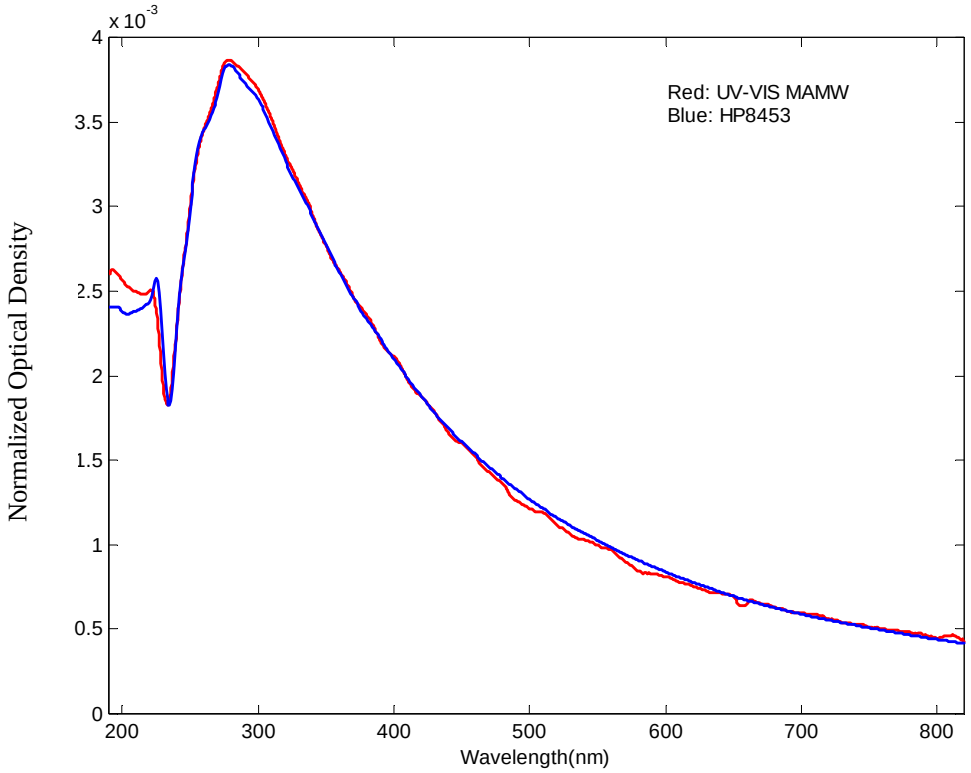

Figure 6.2 Normalized optical density spectra of polystyrene 500 nm spheres in water.

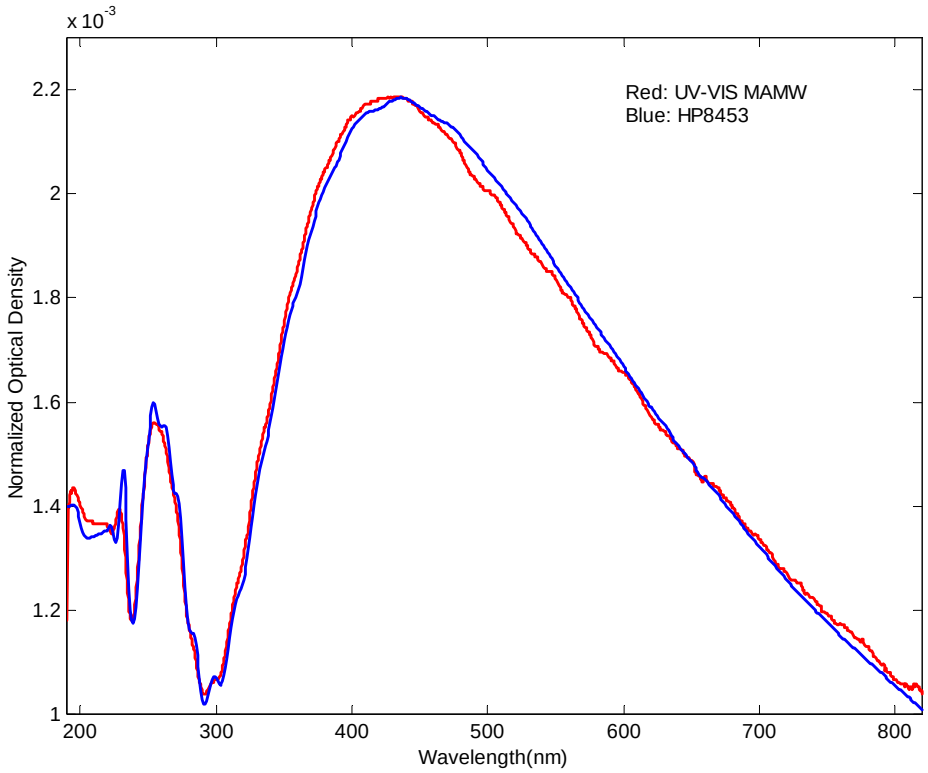

Figure 6.3 Normalized optical density spectra of polystyrene 1 μm spheres in water.

measured by the HP8453 spectrometer at wavelengths between 270 nm and 300 nm. Like interference structures, ripple structures are also strongly damped if absorption becomes large.

Fig. 6.4 shows the normalized optical density spectra of polystyrene 4.0 μm spheres in water. It features interference peaks, ripple structure, and diffraction. Compared to Fig.6.3, the number of interference peaks are increased and shifted toward the longer wavelengths because of the larger particle size. Fig.6.4 clearly shows small ripple structure: sharp and highly irregular fine structure appears at wavelengths longer than 400 nm. Ripple structure arises if the denominators of the scattering coefficients vanish.[7] The strong extinction peak in the deep UV region is due to diffraction that becomes apparent if the particle size is more than 10 times larger than the wavelength of the incident light.[18]

Fig.6.5 shows the normalized optical density spectra of polystyrene 10 μm spheres in water. Due to the particle size, diffraction becomes the dominant cause of extinction. However, the surfactant used to stabilize the particle surface also contributes to the observed extinction in the deep UV region. Therefore, the strong extinction peaks observed at wavelengths shorter than 250 nm are not only caused by diffraction but they are partially due to the surfactant. Clearly, the interpretation of the extinction peaks of large polystyrene particles at wavelengths below 250 nm requires extra caution.[18]
In summary, the optical density spectra of polystyrene spheres with sizes ranging from 20 nm to 10 μm were measured using the Integrated UV-VIS MAMW

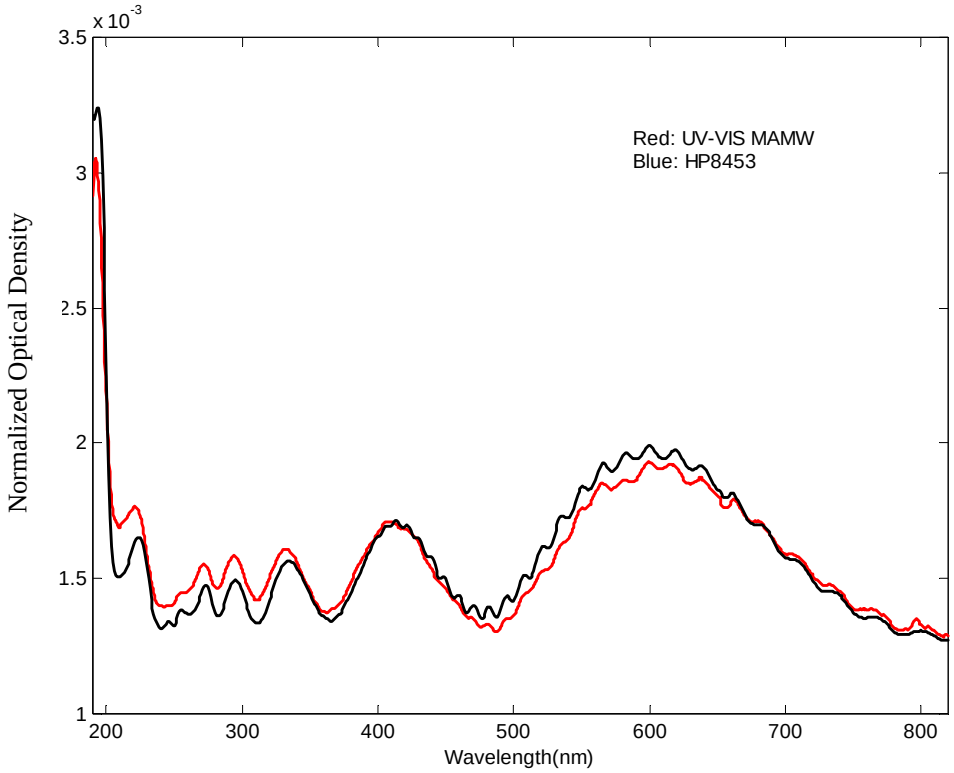

Figure 6.4 Normalized optical density spectra of polystyrene 4 μm spheres in water.

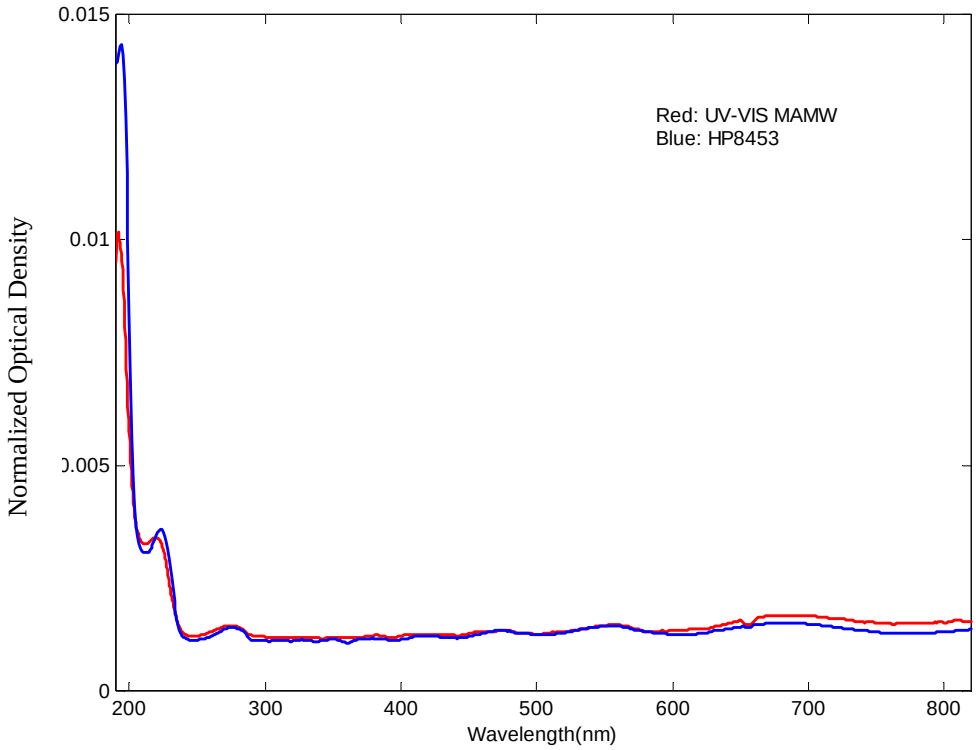

Figure 6.5 Normalized optical density spectra of polystyrene 10 μm spheres in water.

spectrometer. The measured spectra show the characteristics of reddening, interference, ripple structures, diffraction, and absorption due to electronic transitions. The results are in good agreement with the optical density spectra of corresponding polystyrene spheres in water recorded with the HP 8453 spectrometer. This demonstrated the capability of the Integrated UV-VIS MAMW spectrometer to perform transmission spectroscopy. For the optical density spectra of polystyrene 1.0 μm spheres, ripple structures are not explicit compared to the spectra measured by the HP 8453 spectrometer. This is caused by low resolution of the Integrated UV-VIS MAMW spectrometer. *The resolution can be enhanced by using narrower width slits for S2000 production spectrometer.*

6.2. Results of UV-VIS MAMW Spectra Measurement

The capabilities of the Integrated UV-VIS MAMW spectrometer to characterize particles by the simultaneous measurement of the JPPD, mainly size, shape, and chemical composition, were tested by measuring the UV-VIS MAMW spectra of polystyrene standards with different sizes, shape, and composition. The measured UV-VIS MAMW spectra were displayed as UV-VIS MAMW response surface: 3-dimensional (scattering angle, wavelength and the log intensity ratio) plot of the measured UV-VIS MAMW spectra, 2-dimensional (scattering angle and wavelength) contour plot of the response surface, and 2-dimensional (wavelength and the log intensity ratio) wavelength-view plot of the response surface. The measurements demonstrate that the UV-VIS MAMW response surfaces determined by the JPPD of particles can serve as the spectroscopic fingerprint of particles. Compared to the prototype MAMW spectrometer, the

incorporation of broadband UV light source and low angle scattering capacity widens the range of particles that can be characterized with the MAMW spectrometer.

6.2.1. Characterization of Polystyrene Spheres by Size

UV-VIS MAMW spectra of polystyrene spheres with sizes of 20 nm, 500 nm, 1 μm, 4 μm, 8 μm, and 10 μm were measured to test the capabilities of the Integrated UV-VIS MAMW spectrometer for characterizing particles by sizes. The resulting UV-VIS MAMW response surfaces of standards are clearly distinguishable. The measurement results demonstrate that particles as small as 20 nm and as large as 10 μm can be readily characterized using the UV-VIS MAMW scattering measurements.

Fig 6.6 through Fig. 6.8 are the UV-VIS MAMW spectra of polystyrene 20 nm spheres in water. Fig 6.6.a shows the measured UV-VIS MAMW response surface and Fig. 6.6.b represents the simulated UV-VIS MAMW response surface plot. The height of response surface is the log intensity ratio of scattered light to incident light. The surface is a function of the scattering angle and the wavelength of the incident light. The scattering angle is limited from 4^o to 25^o due to refraction by the rectangular cuvette wall. Note that the plotted wavelength range extends from 230 nm to 450 nm. The 3-dimensional view of the UV-VIS MAMW response surface makes it possible to see the absorption and scattering components simultaneously. Fig 6.7.a shows the contour plot of the measured response surface and Fig 6.7.b represents the contour plot of the simulated response surface. The colors designate the height of the surface and the color bar to the

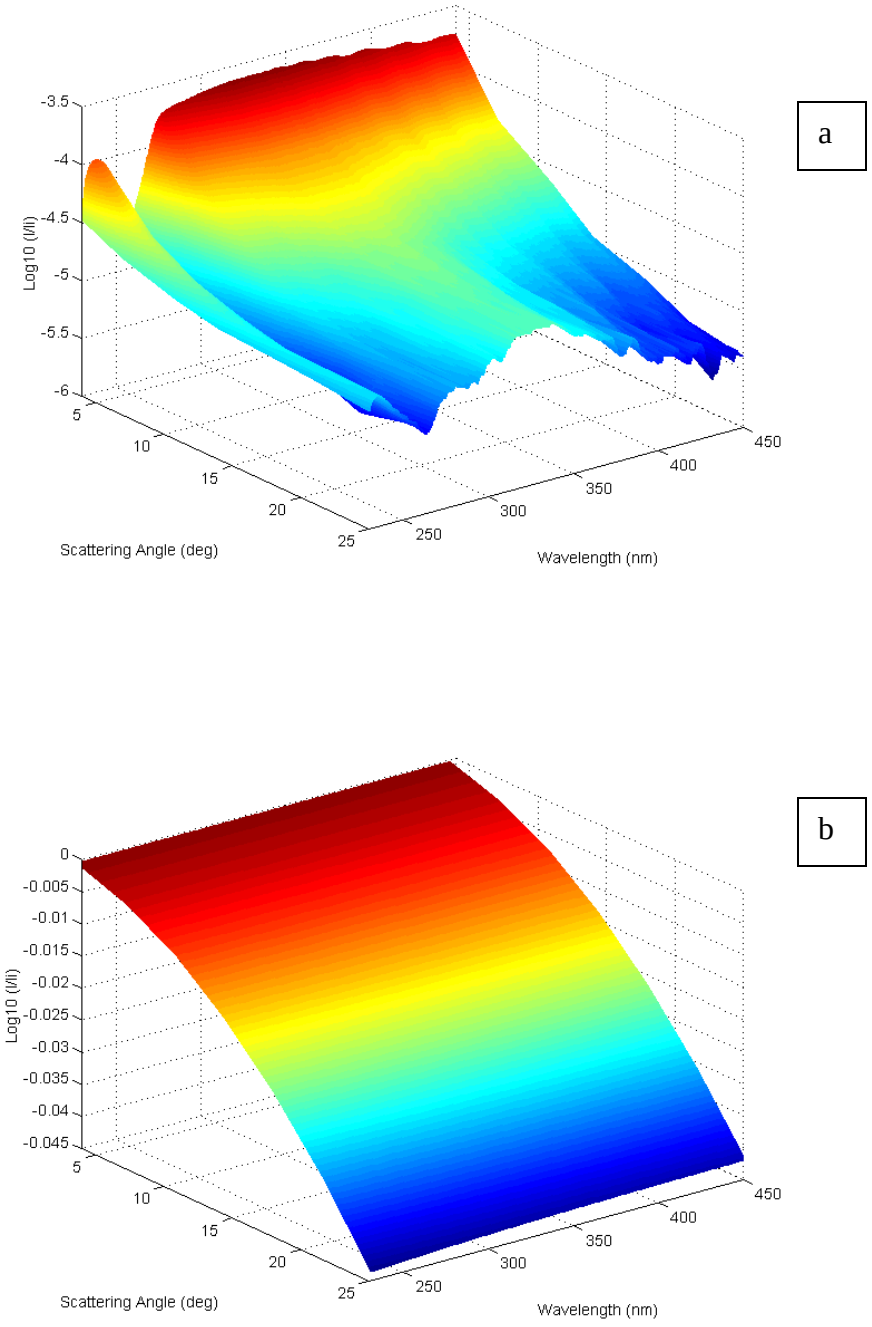

Figure 6.6. UV-VIS MAMW response surfaces of polystyrene 20 nm spheres in water. a) Measured response surface. b) Simulated response surface. Note that wavelength extends from 230 nm to 450 nm.

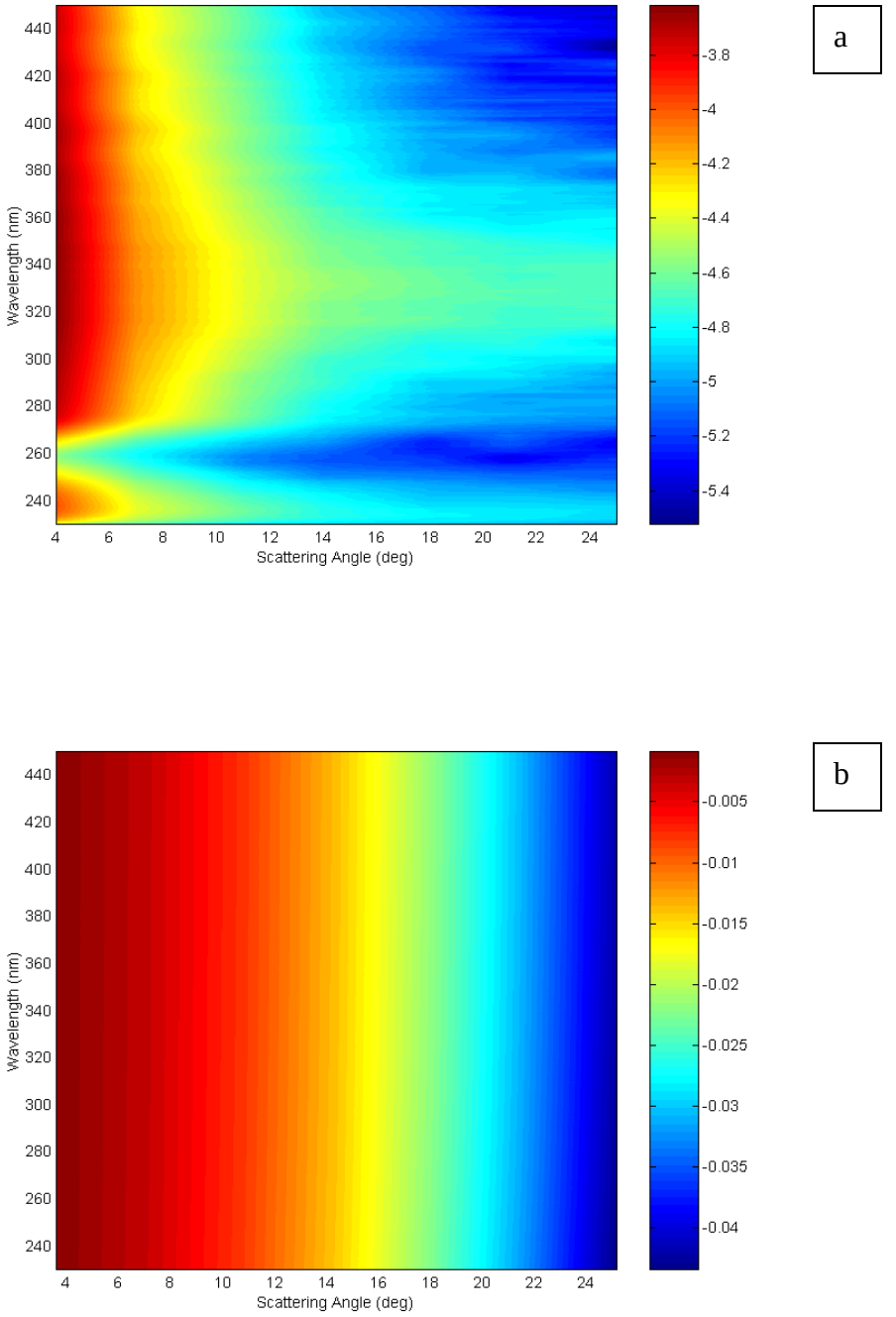

Figure 6.7. Contour plot of the UV-VIS MAMW response surfaces of polystyrene 20 nm spheres in water. a) Contour plot of the measured response surface. b) Contour plot of the simulated response surface.

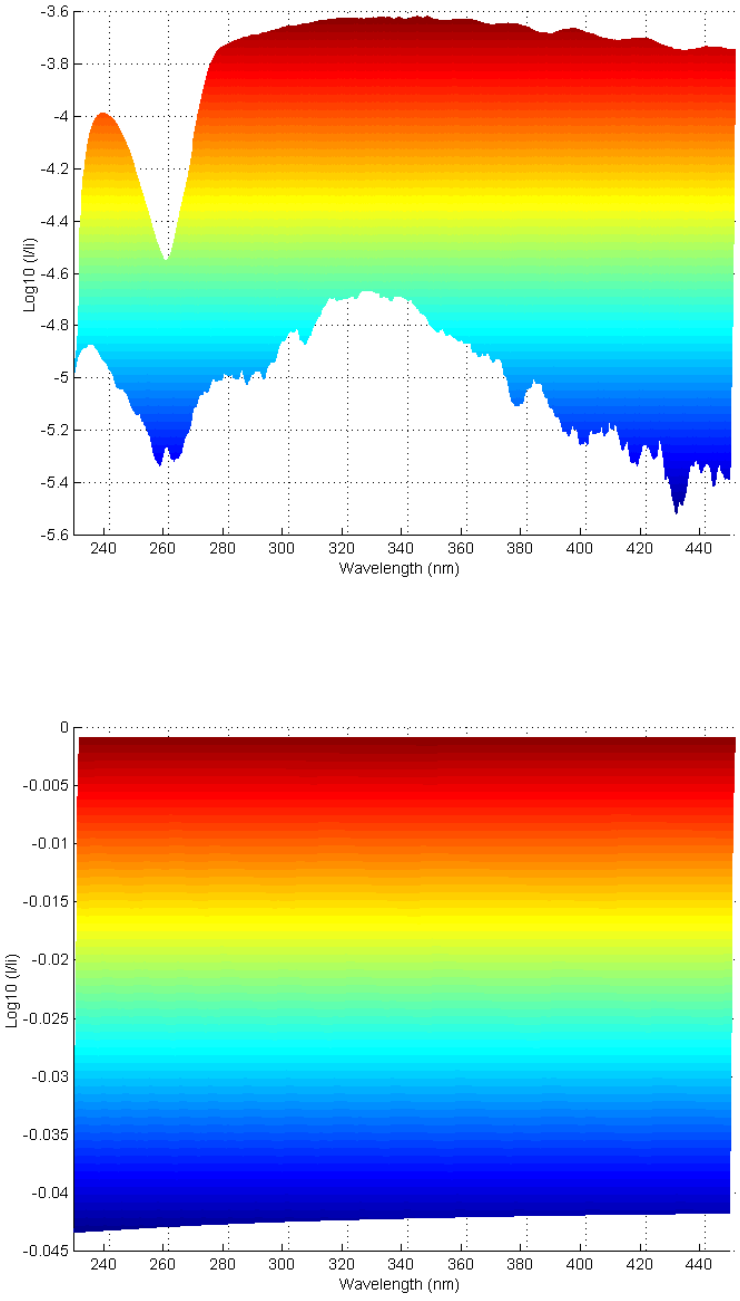

Figure 6.8. Wavelength-view plots of the UV-VIS MAMW response surfaces of polystyrene 20 nm spheres in water. a) Wavelength-view plot of the measured response surface. b) Wavelength-view plot of the simulated response surface.

right of the plot clarifies the height. Fig 6.8.a shows the wavelength-view plot of the measured response surface and Fig 6.8.b represents the wavelength-view plot of the simulated response surface. The wavelength-view plots are functions of log intensity ratio and the wavelength of the incident light.

The distinct aspect of the measured UV-VIS MAMW spectra of polystyrene 20 nm spheres is the bulk absorption band of polystyrene shown at wavelengths below 280 nm. The resonant absorption at wavelengths below 240 nm is caused by electronic transition. Together with absorption, scattering provides additional size information because scattering intensity is enhanced with increasing particle sizes. Scattering extends toward longer wavelengths if particle size increases.

The measurement of polystyrene 20 nm spheres MAMW spectra becomes possible due to the inclusion of multiwavelength UV light source. The minimum particle size that might be characterized with the Integrated UV-VIS MAMW spectrometer is probably 5 nm in case of polystyrene.[19] This indicates that the realm of the application area of the Integrated UV-VIS MAMW spectrometer can be extended to virus detection and nano-particle characterization. The fact that small particle scattering is not only determined by the size but its shape and composition makes this prospect even brighter because of the simultaneous JPPD detection capability of the Integrated UV-VIS MAMW spectrometer.

Fig 6.9.a, Fig 6.10.a, and Fig 6.11a represent the measured UV-VIS MAMW response surface of polystyrene 500 nm spheres in water, the contour plot of Fig 6.9.a, and the wavelength-view plot of Fig 6.9.a, respectively. Fig 6.9.b, Fig 6.10.b, and Fig

6.11.b show the simulated UV-VIS MAMW response surface of polystyrene 500 nm spheres in water, the contour plot of Fig 6.9.b, and the wavelength-view plot of Fig 6.9.b, respectively. Note that the plotted wavelength range extends from 230 nm to 700 nm.

The UV-VIS MAMW spectra of polystyrene 500 nm spheres mainly feature interference and reddening. Comparison of Fig.6.9.a with Fig.6.6.a shows the enhanced scattering structures at angles larger than 15^{o} in Fig.6.9.a because of the increased particle size. Both the measured and the simulated UV-VIS MAMW spectra show that absorption and scattering are limited to the shorter wavelength region. This implies that UV light scattering is a valuable tool to characterize small size particles. The noise in the visible region, which can be clearly appreciated in the wavelength-view plot, appear to be caused by the tungsten-halogen beam spectrum that has considerable structure unlike the UV beam spectrum.

Fig 6.12.a, Fig 6.13.a, and Fig 6.14.a represent the measured UV-VIS MAMW response surface of polystyrene 1 μm spheres in water, the contour plot of Fig 6.12.a, and the wavelength-view plot of Fig 6.12.a, respectively. Fig 6.12.b, Fig 6.13.b, and Fig 6.14.b show the simulated UV-VIS MAMW response surface of polystyrene 1 μm spheres in water, the contour plot of Fig 6.12.b, and the wavelength-view plot of Fig 6.12.b, respectively. Note that the plotted wavelength range extends from 230 nm to 800 nm.

The measured UV-VIS MAMW spectra of polystyrene 1.0 μm spheres in water show further enhancement of low angle scattering due to the larger particle size.

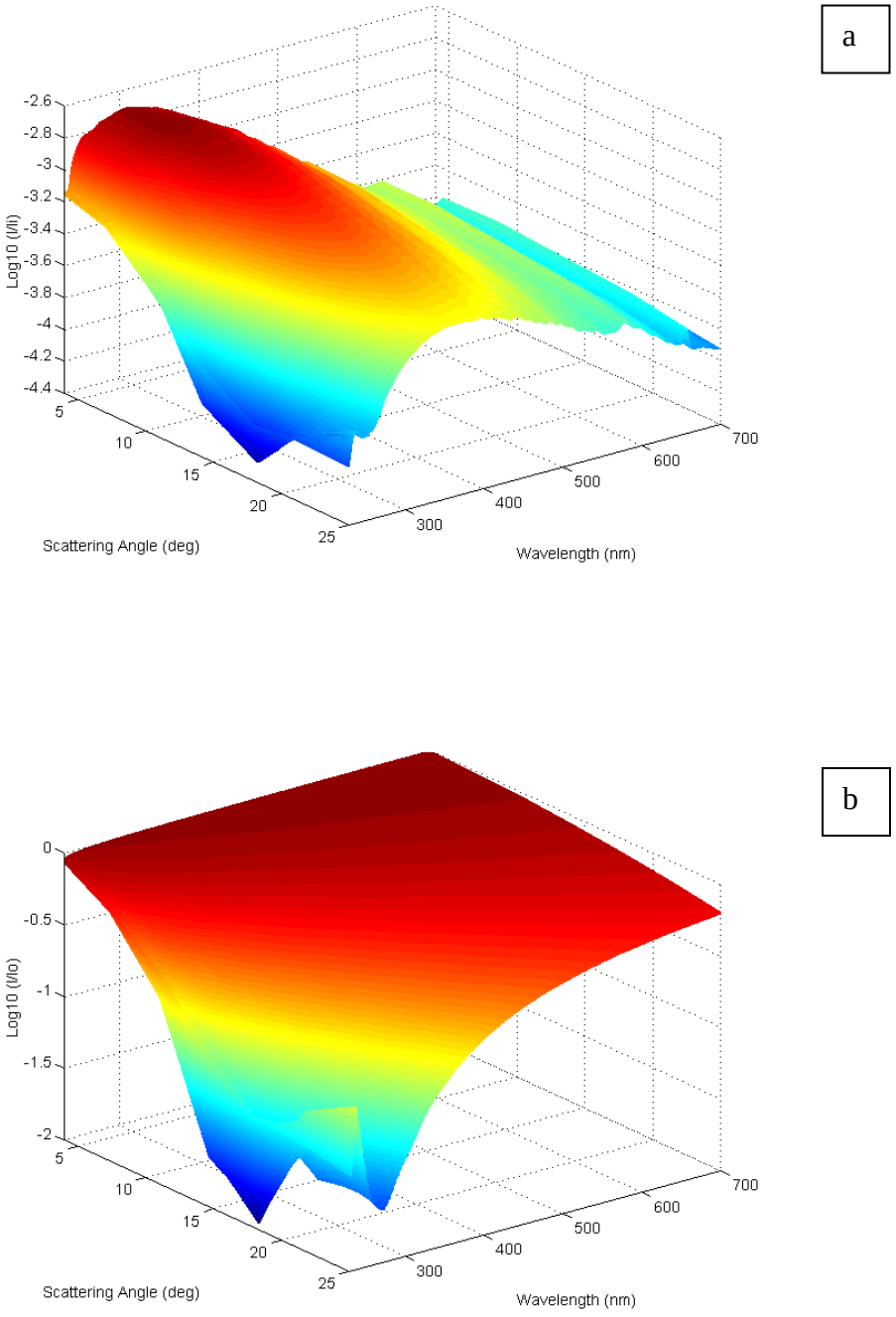

Figure 6.9 UV-VIS MAMW response surfaces of polystyrene 500 nm spheres in water. a) Measured response surface. b) Simulated response surface. Note that wavelength extends range from 230 nm to 700 nm.

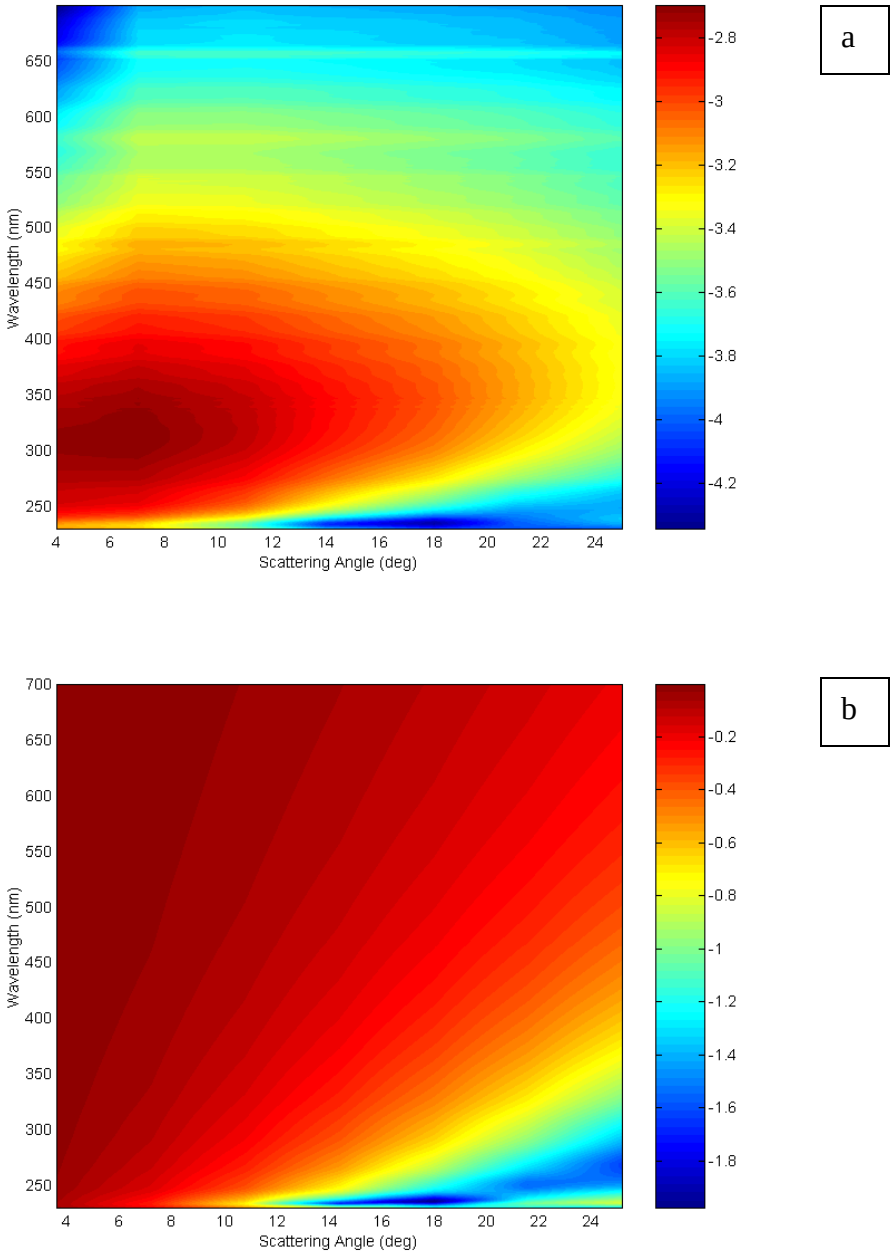

Figure 6.10. Contour plot of the UV-VIS MAMW response surfaces of polystyrene 500 nm spheres in water. a) Contour plot of the measured response surface. b) Contour plot of the simulated response surface.

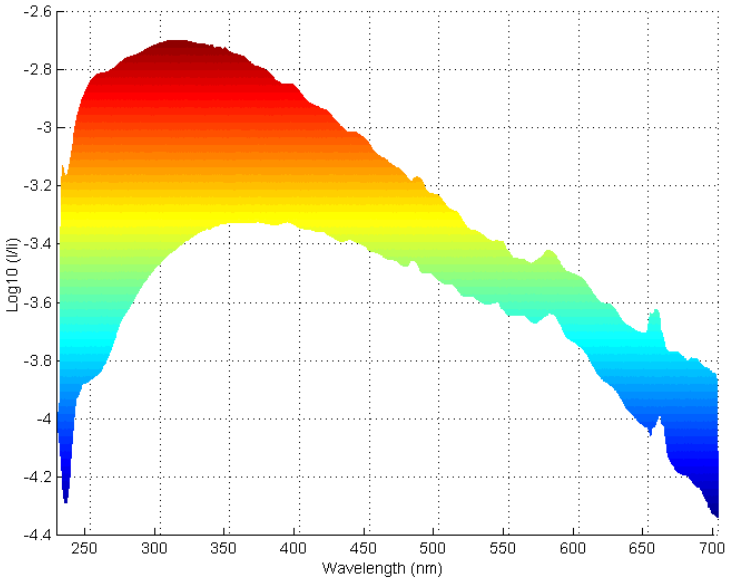

a

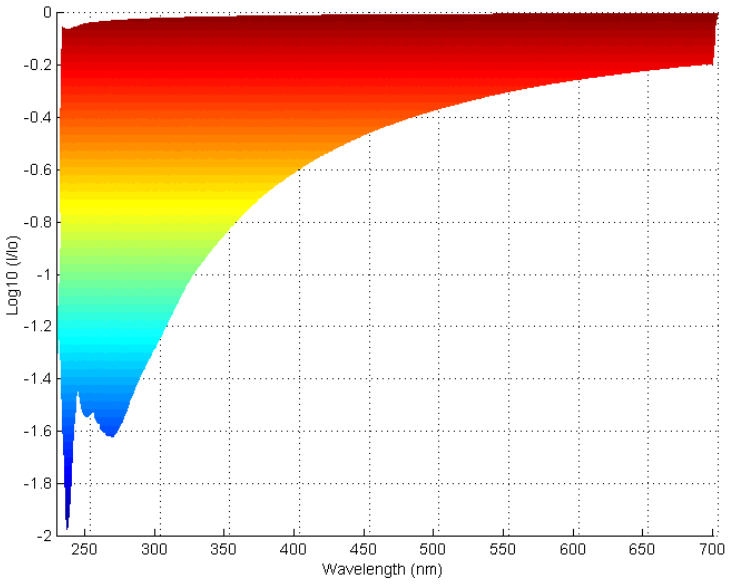

b

Figure 6.11. Wavelength-view plots of the UV-VIS MAMW response surfaces of polystyrene 500 nm spheres in water. a) Wavelength-view plot of the measured response surface. b) Wavelength-view plot of the simulated response surface.

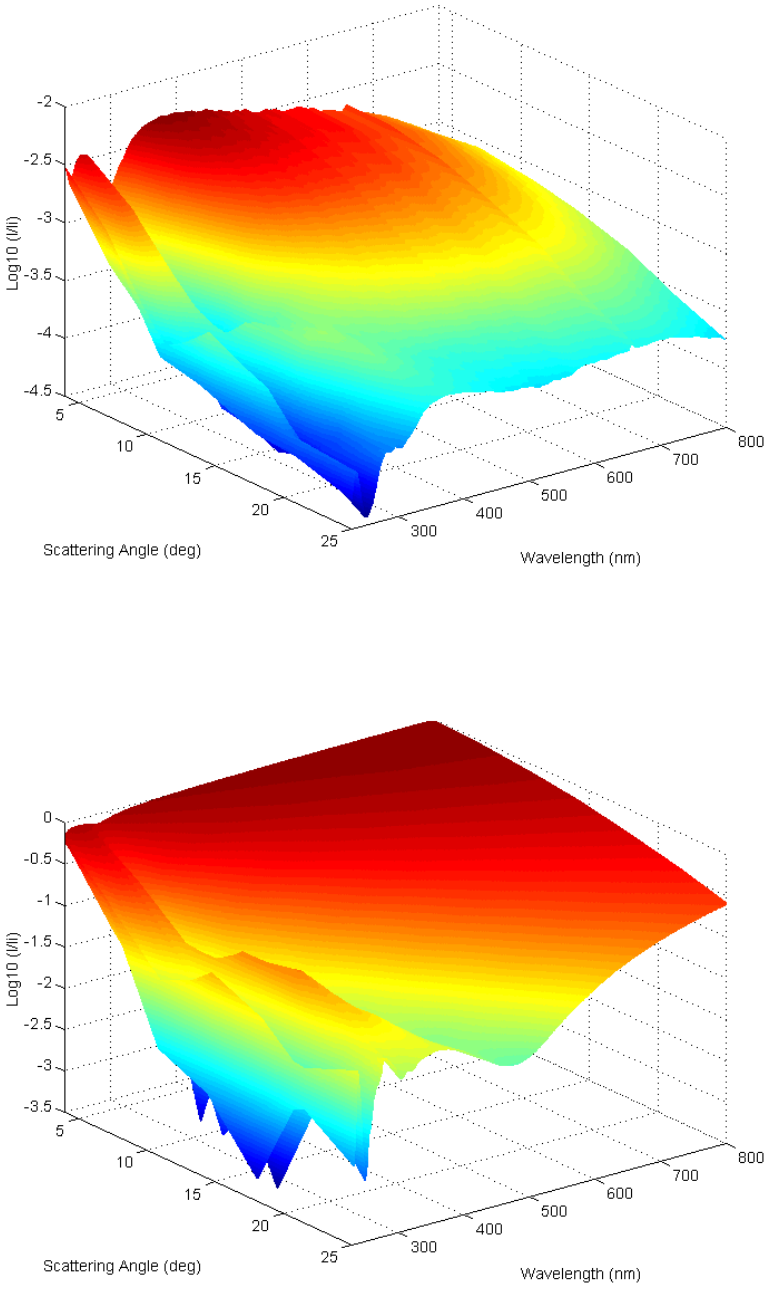

Figure 6.12 UV-VIS MAMW response surfaces of polystyrene 1 µm spheres in water. a) Measured response surface. b) Simulated response surface.

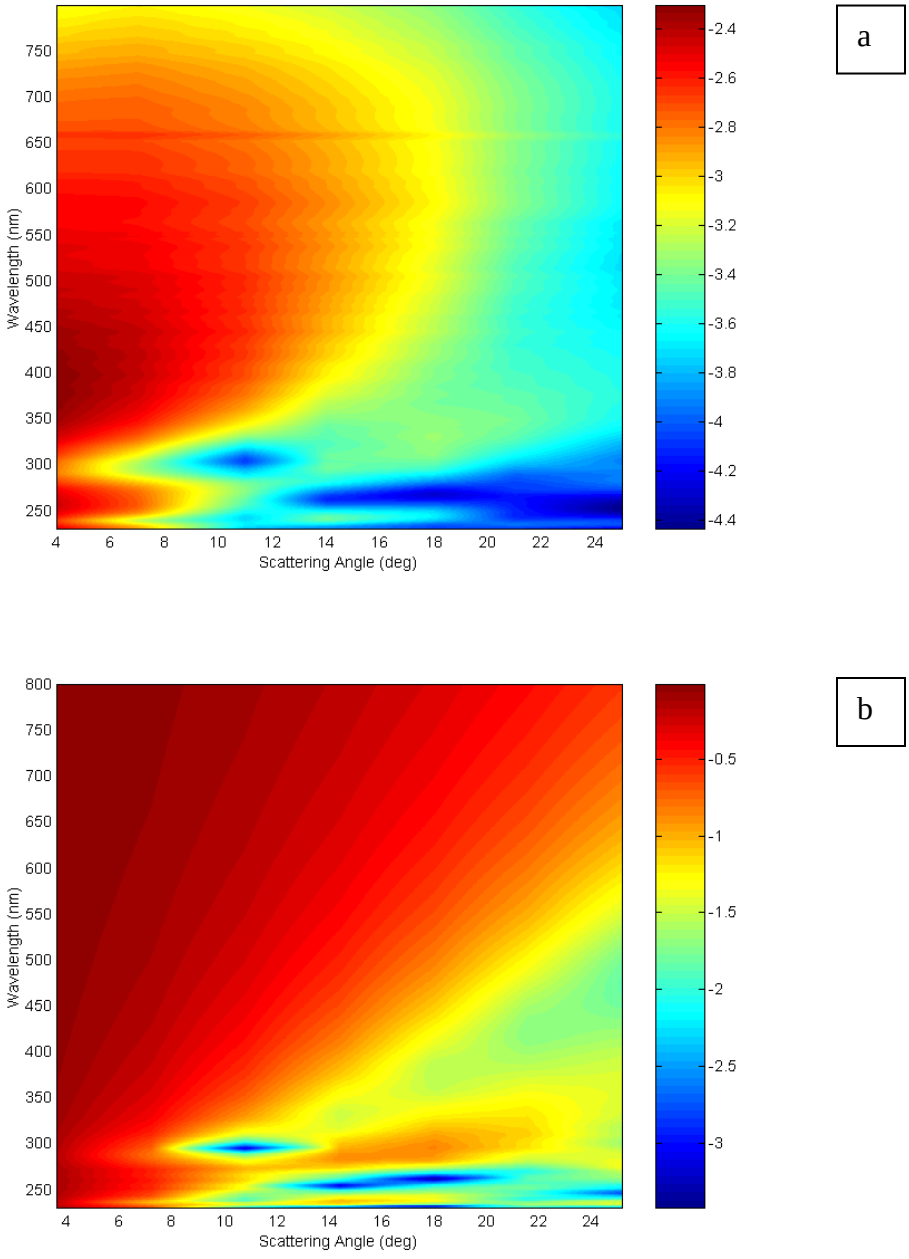

Figure 6.13. Contour plot of the UV-VIS MAMW response surfaces of polystyrene 1 µm spheres in water. a) Contour plot of the measured response surface. b) Contour plot of the simulated response surface.

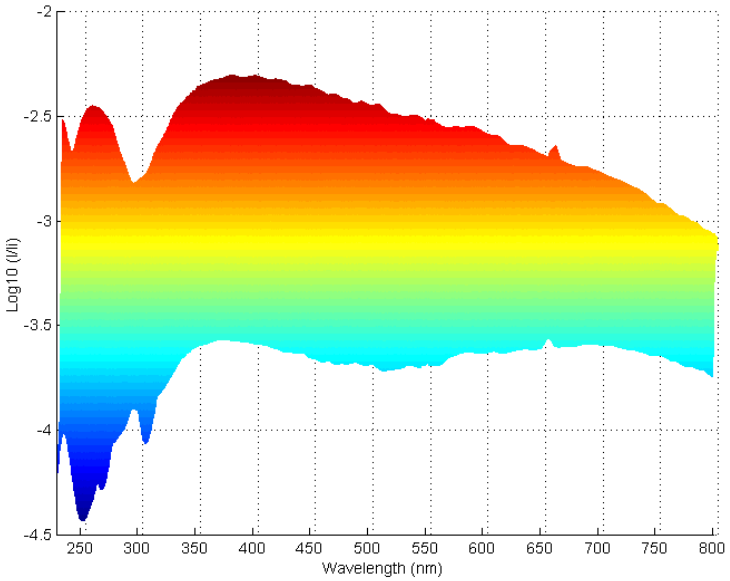

a

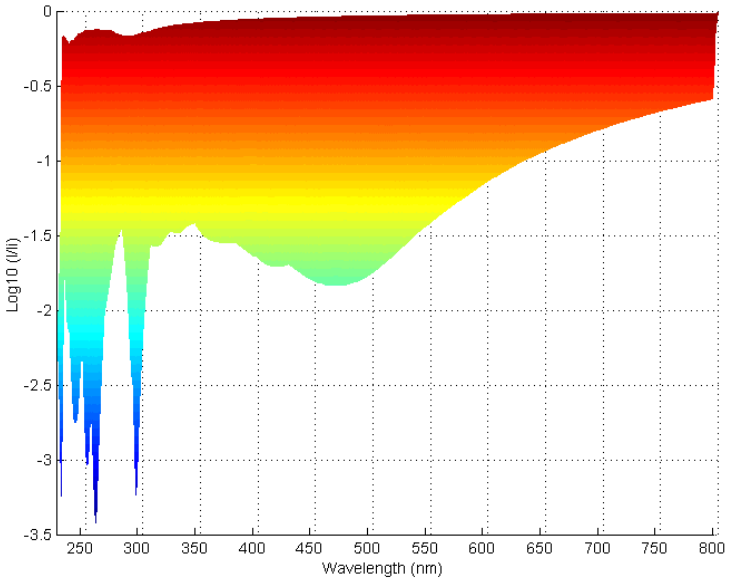

b

Figure 6.14. Wavelength-view plots of the UV-VIS MAMW response surfaces of polystyrene 1 µm spheres in water. a) Wavelength-view plot of the measured response surface. b) Wavelength-view plot of the simulated response surface.

Particle size increases result in the enhanced scattering at low angle and at longer wavelengths as well as the increased fine structures on both measured and simulated UV-VIS MAMW spectra. Fig 6.14. a, the wavelength-view plot of the measured response surface, suggests that interference is the main characteristic of polystyrene 1.0 μm spheres. Noise probably due to the structured tungsten-halogen beam spectrum also appears in the visible region. Experimental and simulation results are in better agreement compared to those of smaller size particles.

Fig 6.15.a, Fig 6.16.a, and Fig 6.17.a represent the measured UV-VIS MAMW response surface of polystyrene 4 μm spheres in water, the contour plot of Fig 6.15.a, and the wavelength-view plot of Fig 6.15.a, respectively. Fig 6.15.b, Fig 6.16.b, and Fig 6.17.b show the simulated UV-VIS MAMW response surface of polystyrene 4 μm spheres in water, the contour plot of Fig 6.15.b, and the wavelength-view plot of Fig 6.15.b, respectively. Note that the plotted wavelength range extends from 230 nm to 800 nm.

The measured UV-VIS MAMW spectra of polystyrene 4.0 μm spheres in water show more fine structure spread on the whole response surface or contour and the wavelength-view plots. Increased interference peaks also can be seen at low angles. Although it is unclear from the measured spectra, the ripple structure can be observed in the simulated plots. Deep and straight structures shown at wavelengths below 300 nm in both experimental and simulation plots seem to be caused by diffraction.

Fig 6.18.a, Fig 6.19.a, and Fig 6.20.a represent the measured UV-VIS MAMW response surface of polystyrene 8 μm spheres in water, the contour plot of Fig 6.18.a,

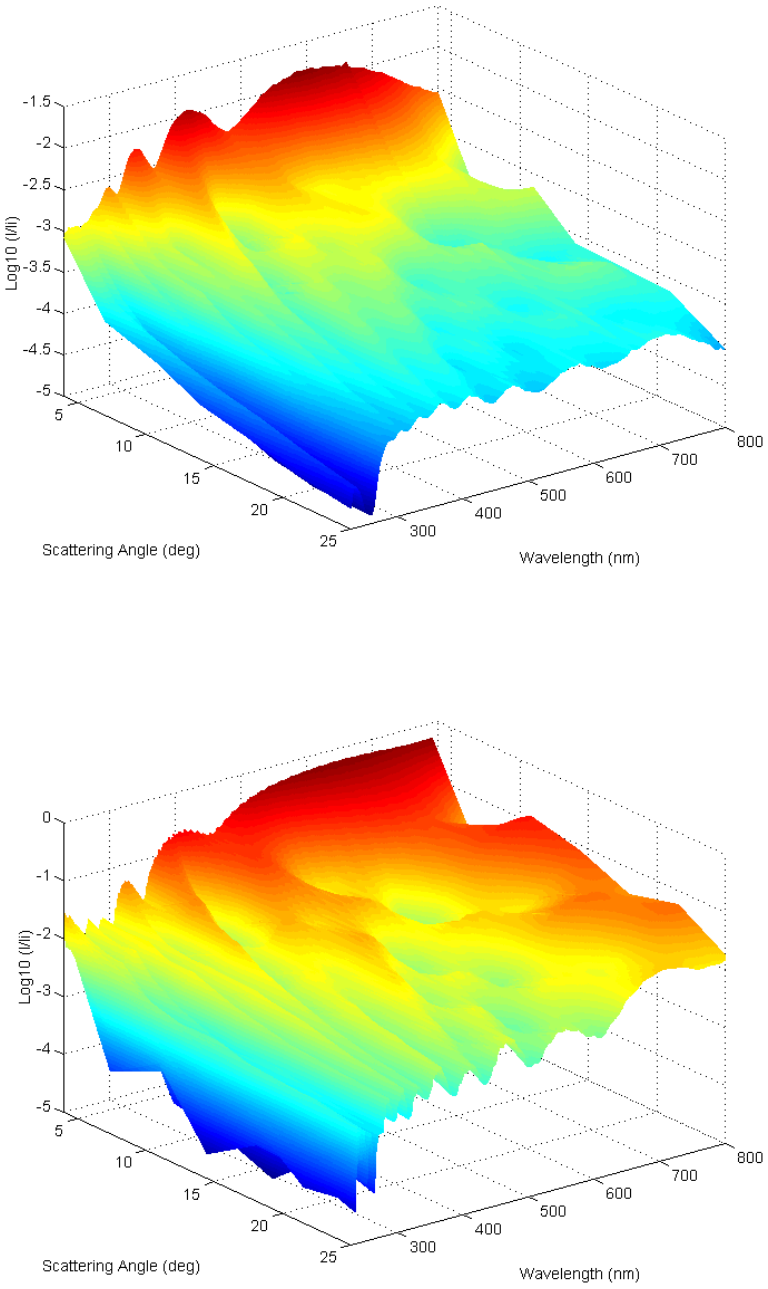

Figure 6.15 UV-VIS MAMW response surfaces of polystyrene 4 µm spheres in water. a) Measured response surface. b) Simulated response surface.

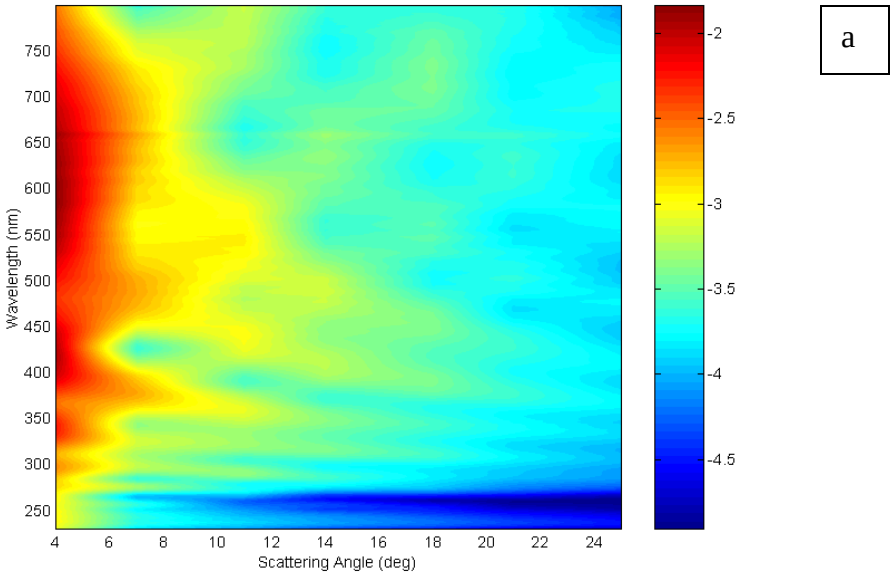

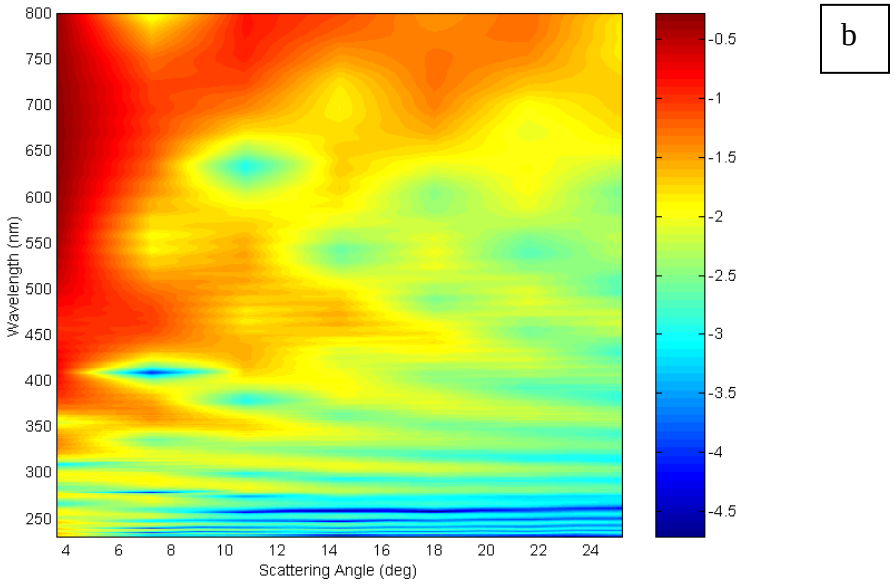

Figure 6.16. Contour plot of the UV-VIS MAMW response surfaces of polystyrene 4 µm spheres in water. a) Contour plot of the measured response surface. b) Contour plot of the simulated response surface.

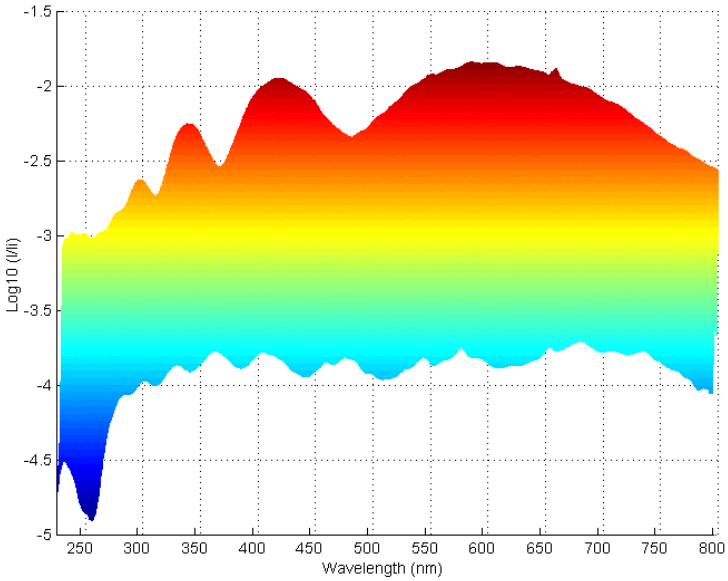

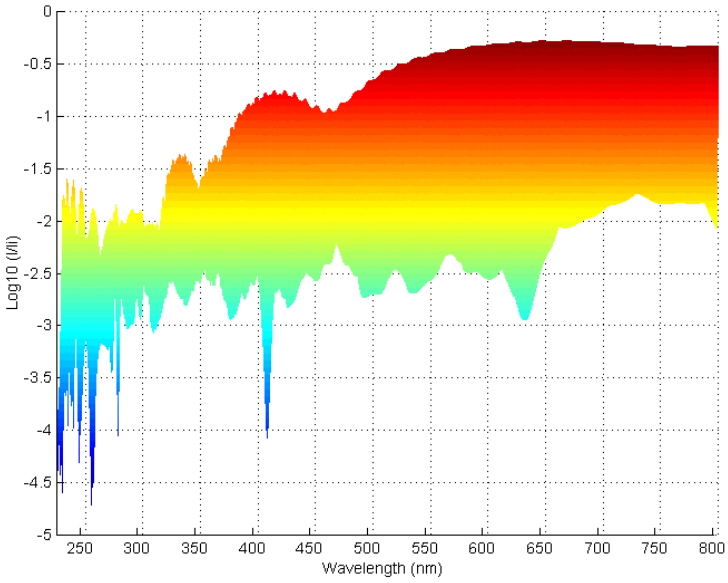

Figure 6.17. Wavelength-view plots of the UV-VIS MAMW response surfaces of polystyrene 4 µm spheres in water. a) Wavelength-view plot of the measured response surface. b) Wavelength-view plot of the simulated response surface.

and the wavelength-view plot of Fig 6.18.a, respectively. Fig 6.18.b, Fig 6.19.b, and Fig 6.20.b show the simulated UV-VIS MAMW response surface of polystyrene 8 μm spheres in water, the contour plot of Fig 6.18.b, and the wavelength-view plot of Fig 6.18.b, respectively. Note that the plotted wavelength range extends from 230 nm to 800 nm.

Due to the increased particle size, the measured and the simulated UV-VIS MAMW spectra of polystyrene 8.0 μm spheres in water show a large peak shift toward the short near infrared (NIR) region. Increased particle size also enhances diffraction and results in the straight structures shown on the majority of response surfaces. Simulated plots are in good agreement with experimental results.

Fig 6.21.a, Fig 6.22.a, and Fig 6.23.a represent the measured UV-VIS MAMW response surface of polystyrene 10.0 μm spheres in water, the contour plot of Fig 6.21.a, and the wavelength-view plot of Fig 6.23.a, respectively. Fig 6.21.b, Fig 6.22.b, and Fig 6.23.b show the simulated UV-VIS MAMW response surface of polystyrene 10.0 μm spheres in water, the contour plot of Fig 6.21.b, and the wavelength-view plot of Fig 6.23.b, respectively. Note that the plotted wavelength range extends from 230 nm to 800 nm.

Straight structures that seem to be caused by diffraction spread on the whole response surfaces of polystyrene 10.0 μm spheres in water. UV-VIS MAMW spectra of polystyrene 8.0 μm spheres and that of polystyrene 10.0 μm spheres are clearly distinguishable at low angles while looking similar at large angles.

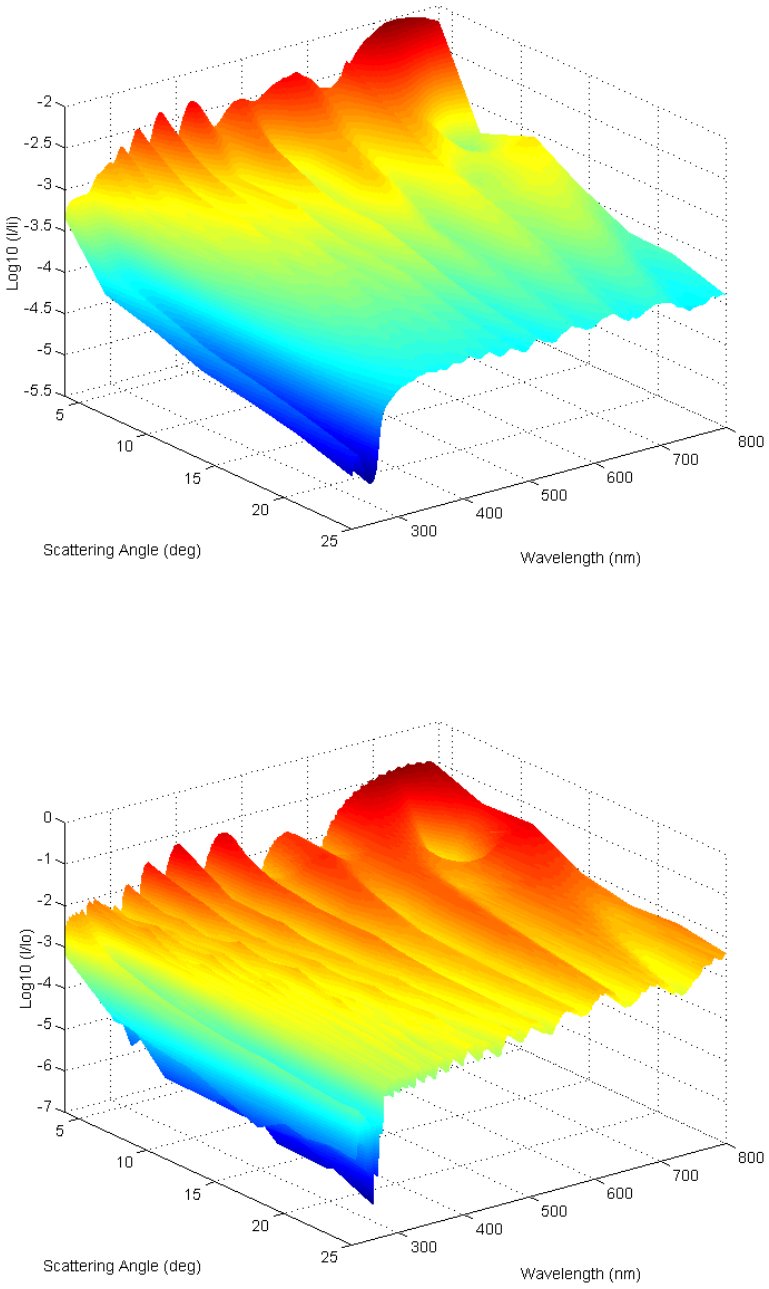

Figure 6.18. UV-VIS MAMW response surfaces of polystyrene 8 µm spheres in water. a) Measured response surface. b) Simulated response surface.

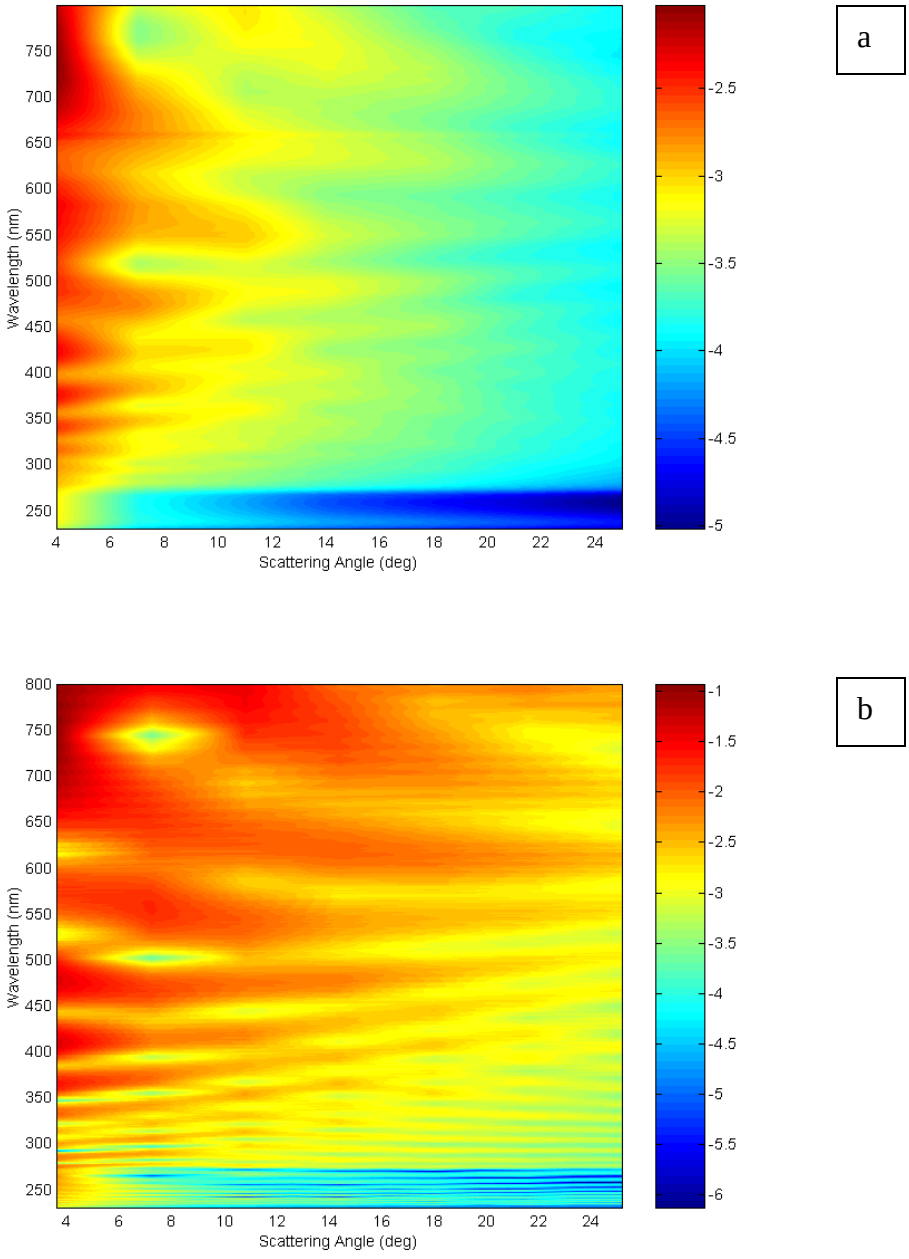

Figure 6.19. Contour plot of the UV-VIS MAMW response surfaces of polystyrene 8 μm spheres in water. a) Contour plot of the measured response surface. b) Contour plot of the simulated response surface.

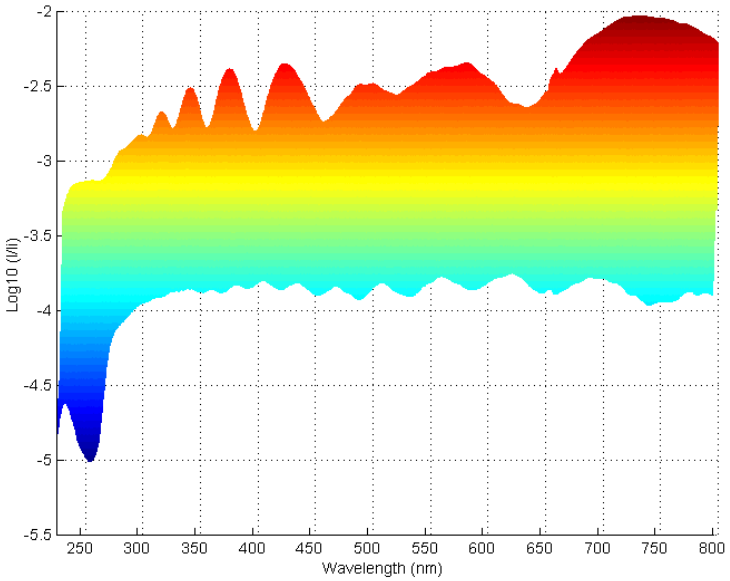

a

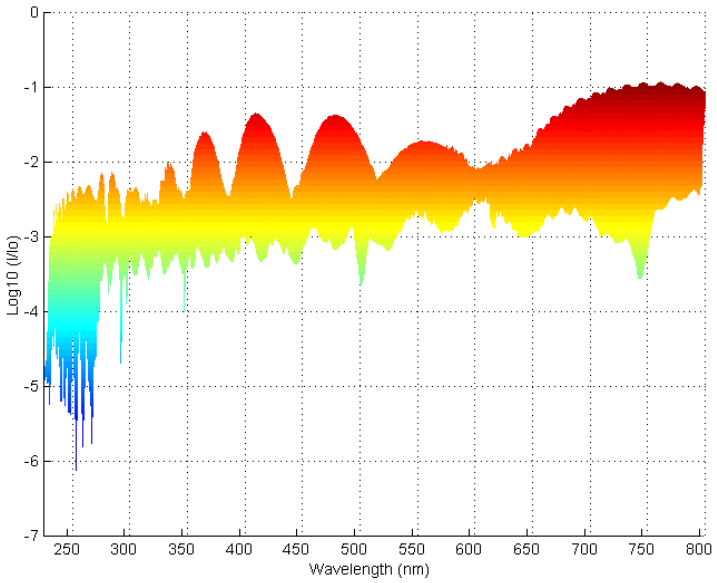

b

Figure 6.20. Wavelength-view plots of the UV-VIS MAMW response surfaces of polystyrene 8 µm spheres in water. a) Wavelength-view plot of the measured response surface. b) Wavelength-view plot of the simulated response surface.

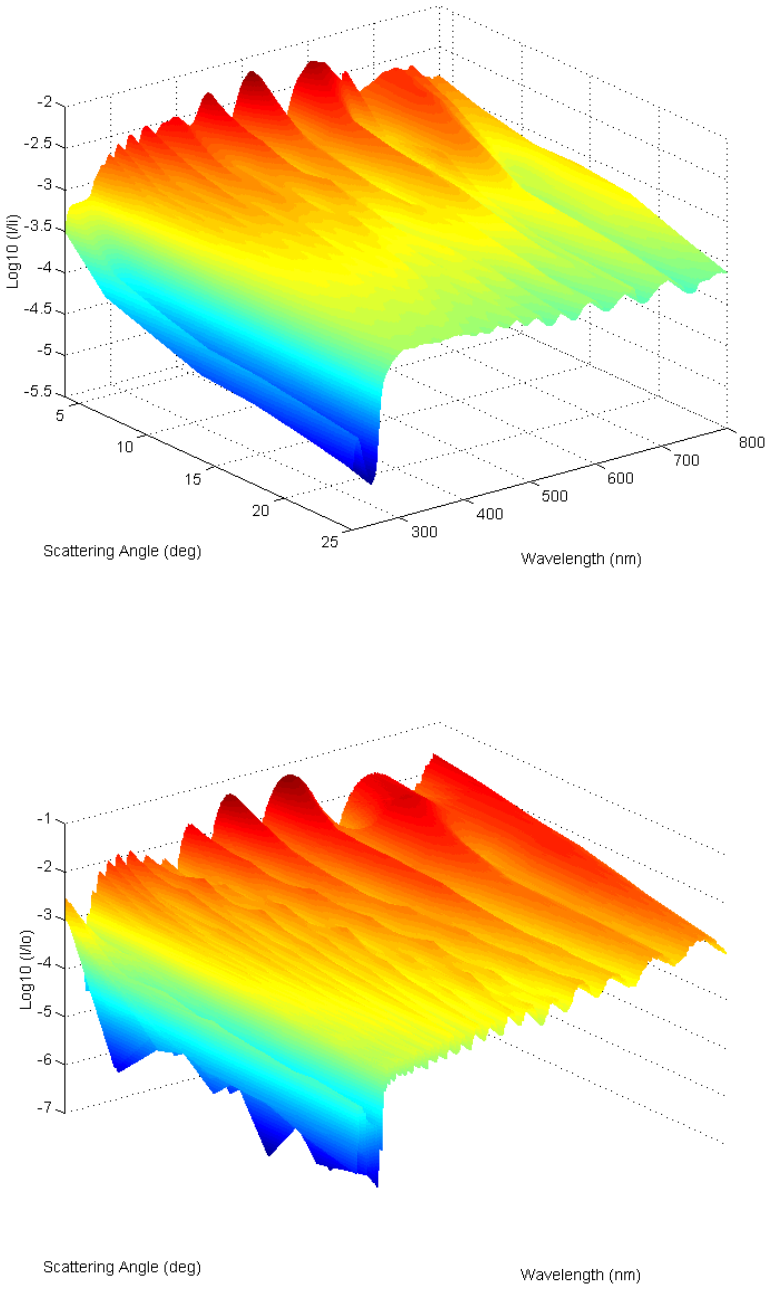

Figure 6.21. UV-VIS MAMW response surfaces of polystyrene 10 µm spheres in water. a) Measured response surface. b) Simulated response surface.

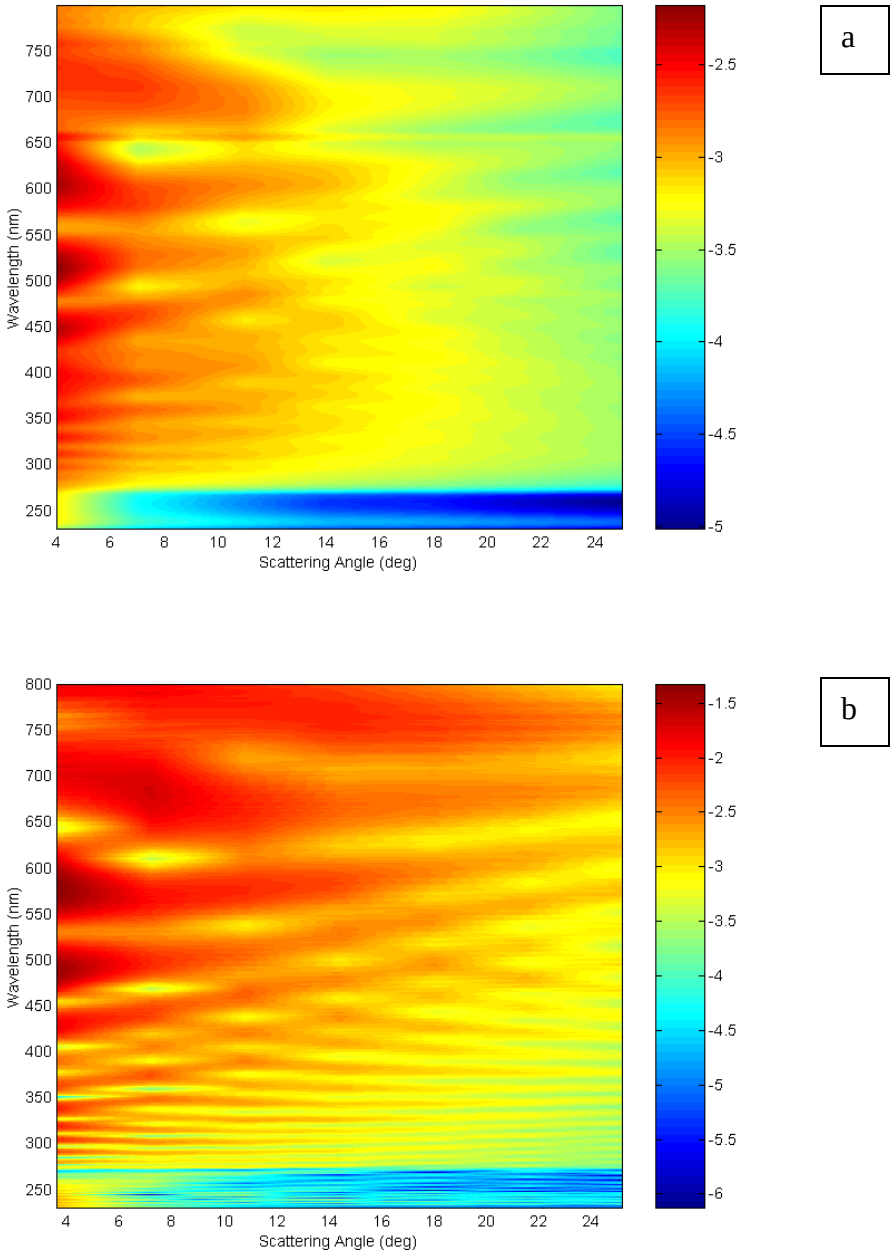

Figure 6.22. Contour plot of the UV-VIS MAMW response surfaces of polystyrene 10 μm spheres in water. a) Contour plot of the measured response surface. b) Contour plot of the simulated response surface.

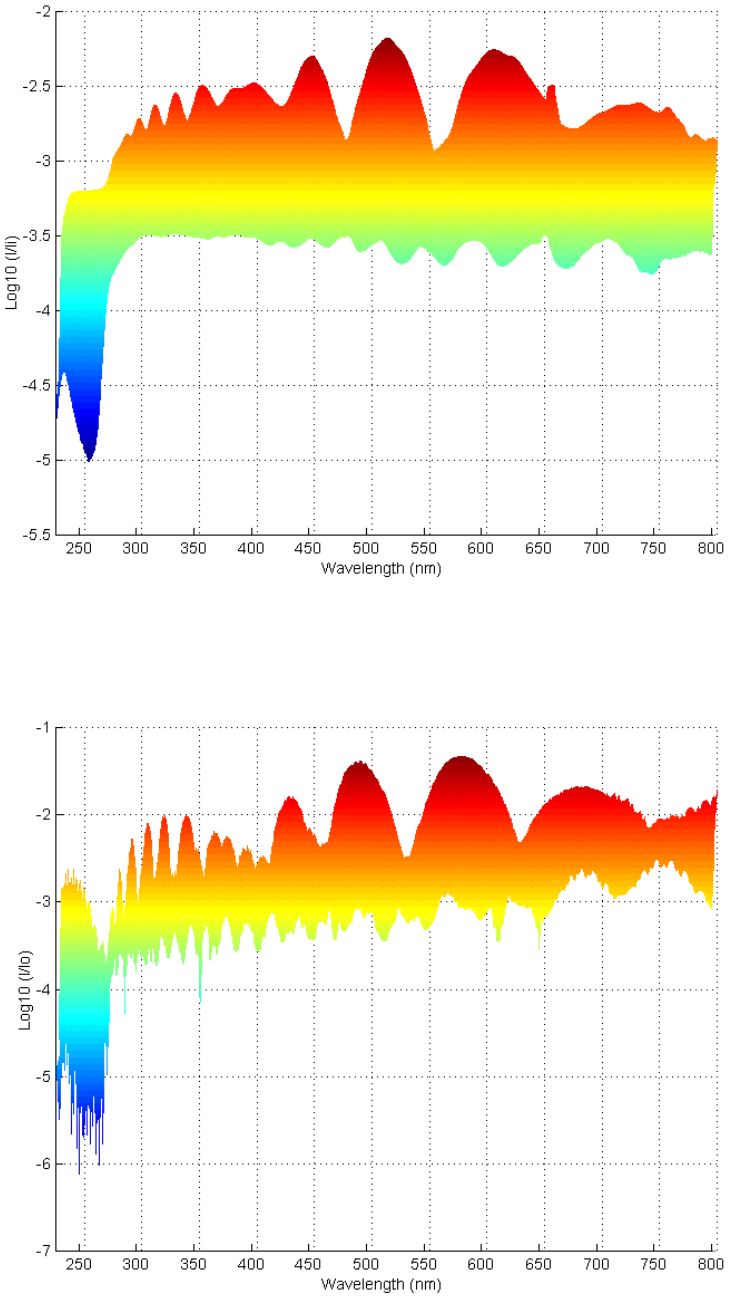

Figure 6.23. Wavelength-view plots of the UV-VIS MAMW response surfaces of polystyrene 10 µm spheres in water. a) Wavelength-view plot of the measured response surface. b) Wavelength-view plot of the simulated response surface.

This confirms that the incorporation of low angle scattering capability into the Integrated UV-VIS MAMW spectrometer results in the large size particle characterization capability. Further shift of the large peak toward the short NIR region can be inferred from the comparison of both measured and simulated UV-VIS MAMW spectra of polystyrene 10.0 μm spheres in water with those of polystyrene 8.0 μm spheres. This suggests that the use of a spectrometer grating which can resolve short NIR light and narrower width slit in the detection optics may enhance the large size particle characterization capability of the Integrated UV-VIS MAMW spectrometer further.

The capabilities of the Integrated UV-VIS MAMW spectrometer for particle size analysis and characterization was tested by measuring the UV-VIS MAMW spectra of polystyrene spheres with sizes of 20 nm, 500 nm, 1 μm, 4 μm, 8 μm, and 10 μm. The measurement results showed that particles as small as 20 nm and as large as 10 μm can be characterized with the Integrated UV-VIS MAMW spectrometer due to the incorporation of broadband UV light source and low angle scattering capacity. In addition, the measured results showed the possibility of widening the particle size range that can be characterized by the MAMW spectrometer. Methods of upgrading the Integrated UV-VIS MAMW spectrometer for further enhancement of large size particle characterization capability have also been discussed.

6.2.2. Measured UV-VIS MAMW Spectra of Non-spherical Polystyrene Standards

Current methodologies for the characterization of non-spherical particles by light scattering include:[7]

1. Forward scattering measurement - the results are compared with those obtained from area-equivalent spheres,
2. Polarization measurement - especially linear polarization and
3. Backscattering measurements.

At present, the first method is actively used to size non-spherical particles. For the second and the third methods, emphasis is on the acquisition of spectra that can be used to differentiate spherical and non-spherical particles consistently. Motivated by the fact that new light scattering techniques which can be used to characterize non-spherical particles are needed, experiments using a 1.85 μm peanut-shaped polystyrene latex and a 1.87 μm spherical polystyrene latex were designed and performed to test the capabilities of the Integrated UV-VIS MAMW spectrometer for the differentiation between spherical particles and non-spherical particles. The results demonstrate the sensitivity of the Integrated UV-VIS MAMW spectrometer to particle shape effects.

6.2.2.1 Non-spherical Particles

Peanut-shaped polystyrene latex particles of average size 1.85 μm (Lot # PS1305B) and spherical polystyrene latex particles of average size 1.87 μm (Lot # PS1587A) were purchased from Magsphere Inc. Peanut-shaped particles are chemically fused and cannot

be separated or broken into pieces by physical methods like ultrasonic shaking. Fig. 6.24 shows scanning electron microscopy (SEM) images of the spherical particles and peanut-shaped particles respectively. For SEM imaging, dried sample solutions at higher concentrations than those utilized for the measurement of the UV-VIS MAMW spectra were used for the ease of imaging.

6.2.2.2 Light Scattering by Ensembles of Non-spherical Particles

Scattering properties of non-spherical particles are different from those of spherical particles due to not only particle shape but also continuously changing particle orientation. Therefore, resulting spectra can be different even if the same shape particles are taken for scattering measurements. Fig. 6.25.a and Fig. 6.25.b, SEM images of two peanut-shaped particles, provide an example of the same shape particles placed in different orientations (perpendicular and parallel). Consequently, the particle orientation relative to the incident light must also be evaluated in order to assess the particle shape.

Fig. 6.26 shows a microscopy picture of the concentrated peanut-shaped particles. For ease of imaging, a concentrated stock solution was used. Although the distribution of particles and their orientation shown under the microscope are continuously changing, the measured UV-VIS MAMW spectra of peanut-shaped particles are reproducible because the Integrated UV-VIS MAMW spectrometer measures the scattered light from the ensemble of particles, not from single or a few particles.

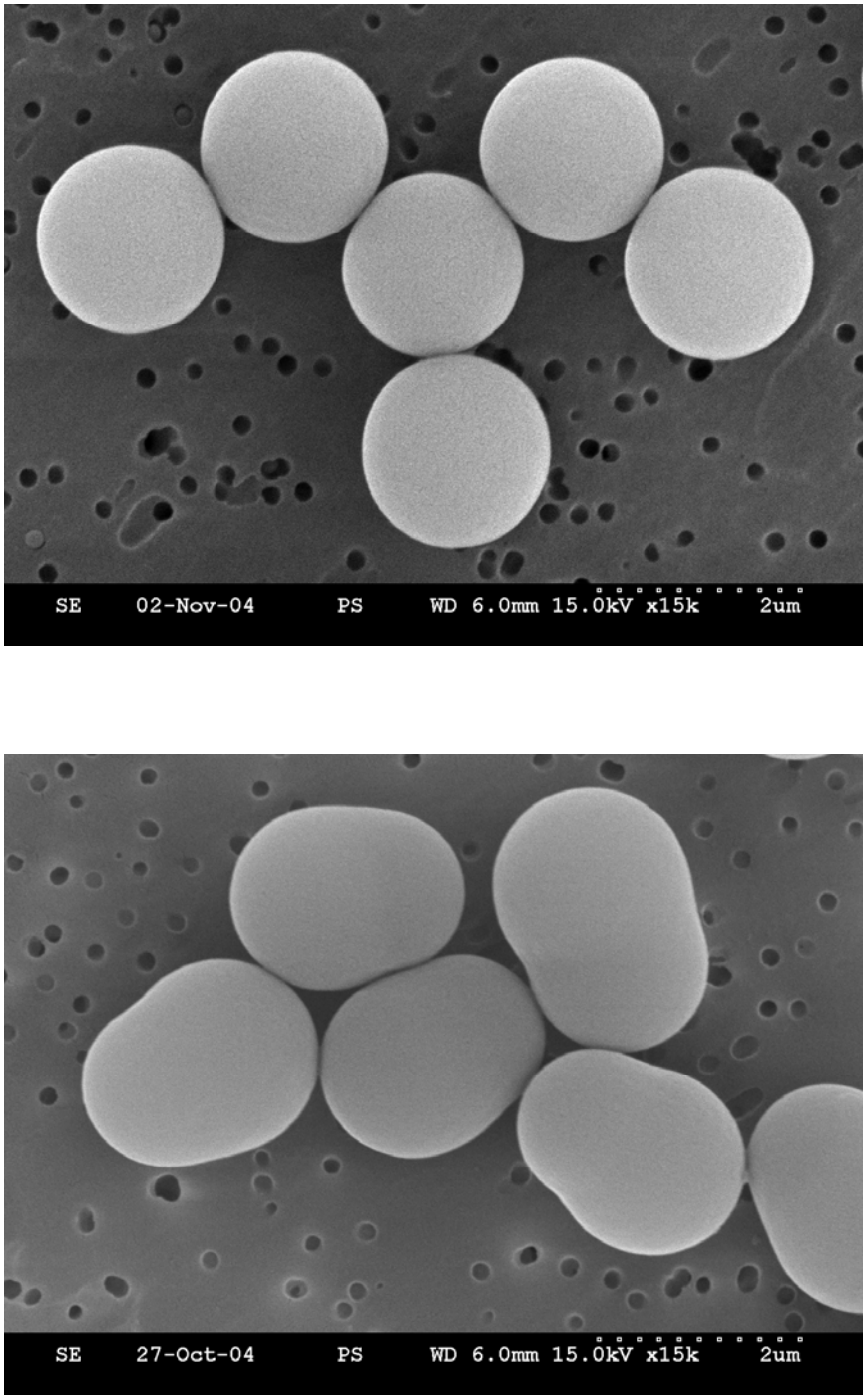

Figure. 6.24. Scanning electron microscopy (SEM) images of polystyrene 1.9 μm size standards. a) Spherical particles. b) Peanut-shaped particles.

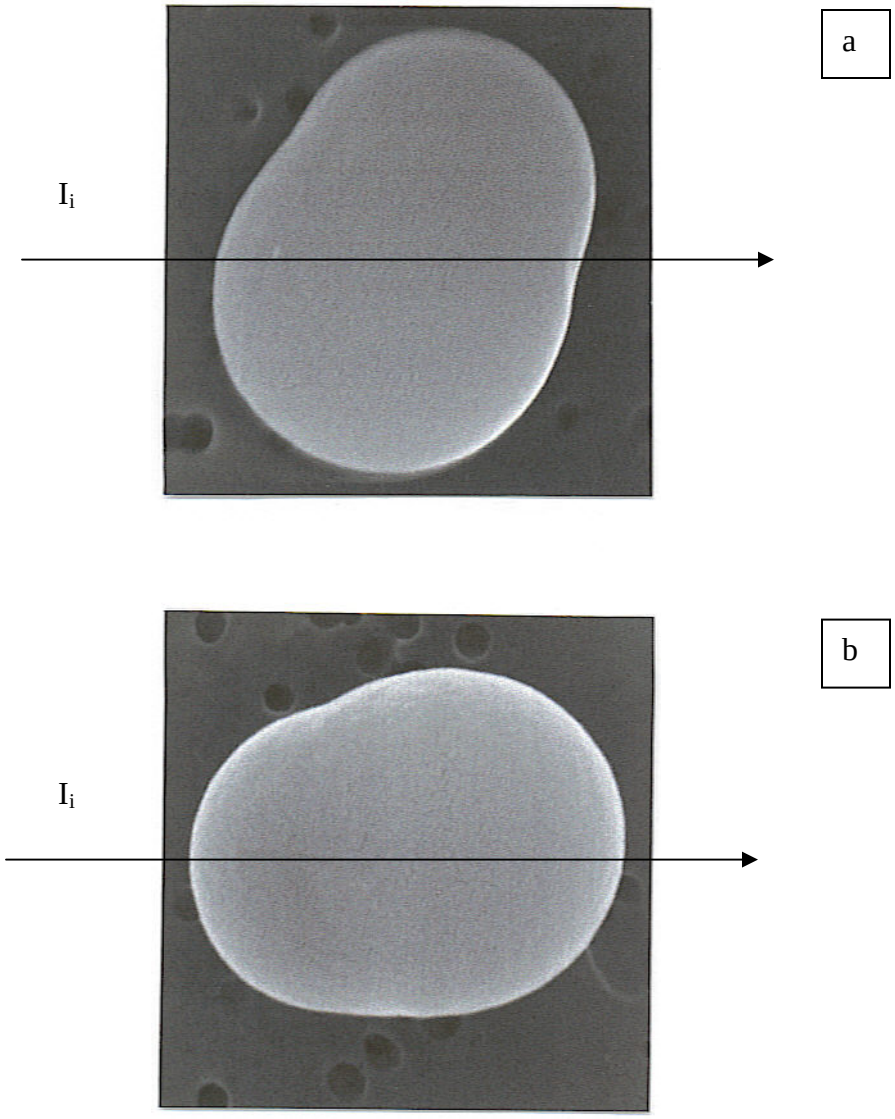

I_i: Incident light

Figure. 6.25. SEM images of two peanut-shaped particles placed in different orientations. a) Particle is oriented perpendicular to the incident light. b) Particle is oriented parallel to the incident light.

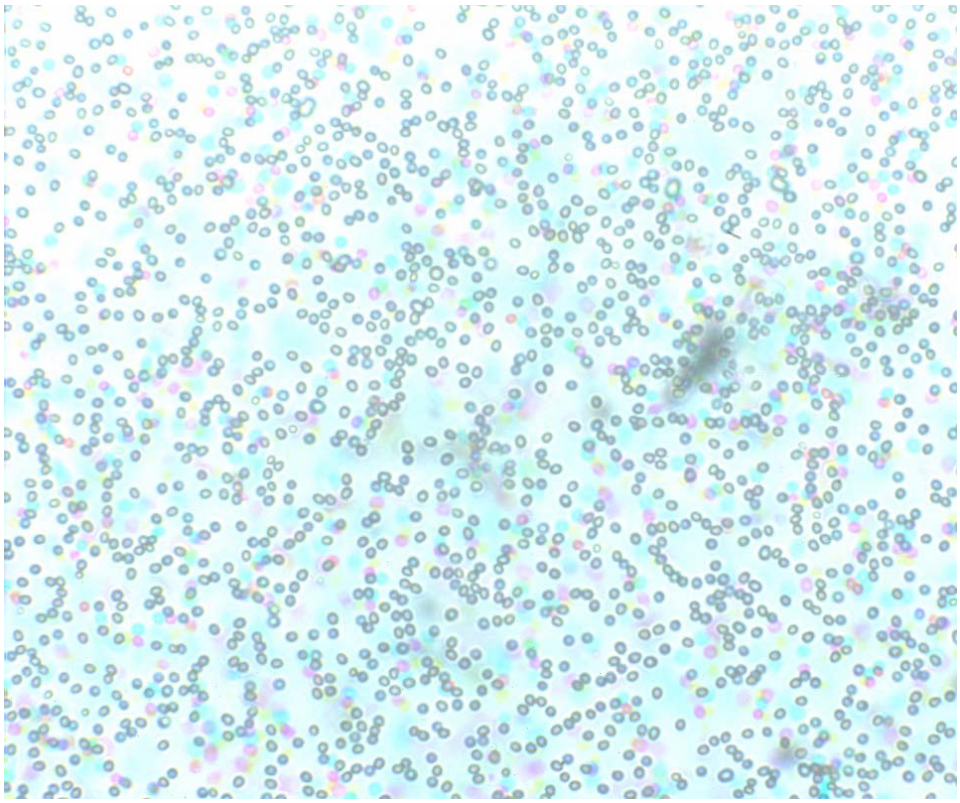

Figure 6.26. Microscope picture of concentrated peanut-shaped particle suspension.

6.2.2.3 Results of the UV-VIS MAMW Spectra Measurements of 1.9 μm Size Spherical Particles and Peanut-Shaped Particles

Fig 6.27.a, Fig 6.28.a, and Fig 6.29.a represent the measured UV-VIS MAMW response surface of polystyrene 1.87 μm spheres in water, the contour plot of Fig 6.27.a, and the wavelength-view plot of Fig 6.27.a, respectively. Fig 6.27.b, Fig 6.28.b, and Fig 6.29.b show the measured UV-VIS MAMW response surface of peanut-shaped polystyrene 1.85 μm standards in water, the contour plot of Fig 6.27.b, and the wavelength-view plot of Fig 6.27.b, respectively.

The results are different across the complete wavelength range from 230 nm to 800 nm. The more dramatic differences being apparent in the UV region. To see the differences clearly, the measured spectra are plotted again for the UV region (Fig. 6.30 ~ Fig. 6.32) and for the visible region (Fig. 6.33 ~ Fig. 6.35).

The observed differences seem to result from:

1) absorbance differences between spherical and peanut-shaped non-spherical particles due to beam path length variations caused by peanut-shaped particle orientation changes and
2) destructive interference in the vicinity of peanut-shaped particles, especially by UV light due to the increased particle size parameter resulting from shorter wavelength light.

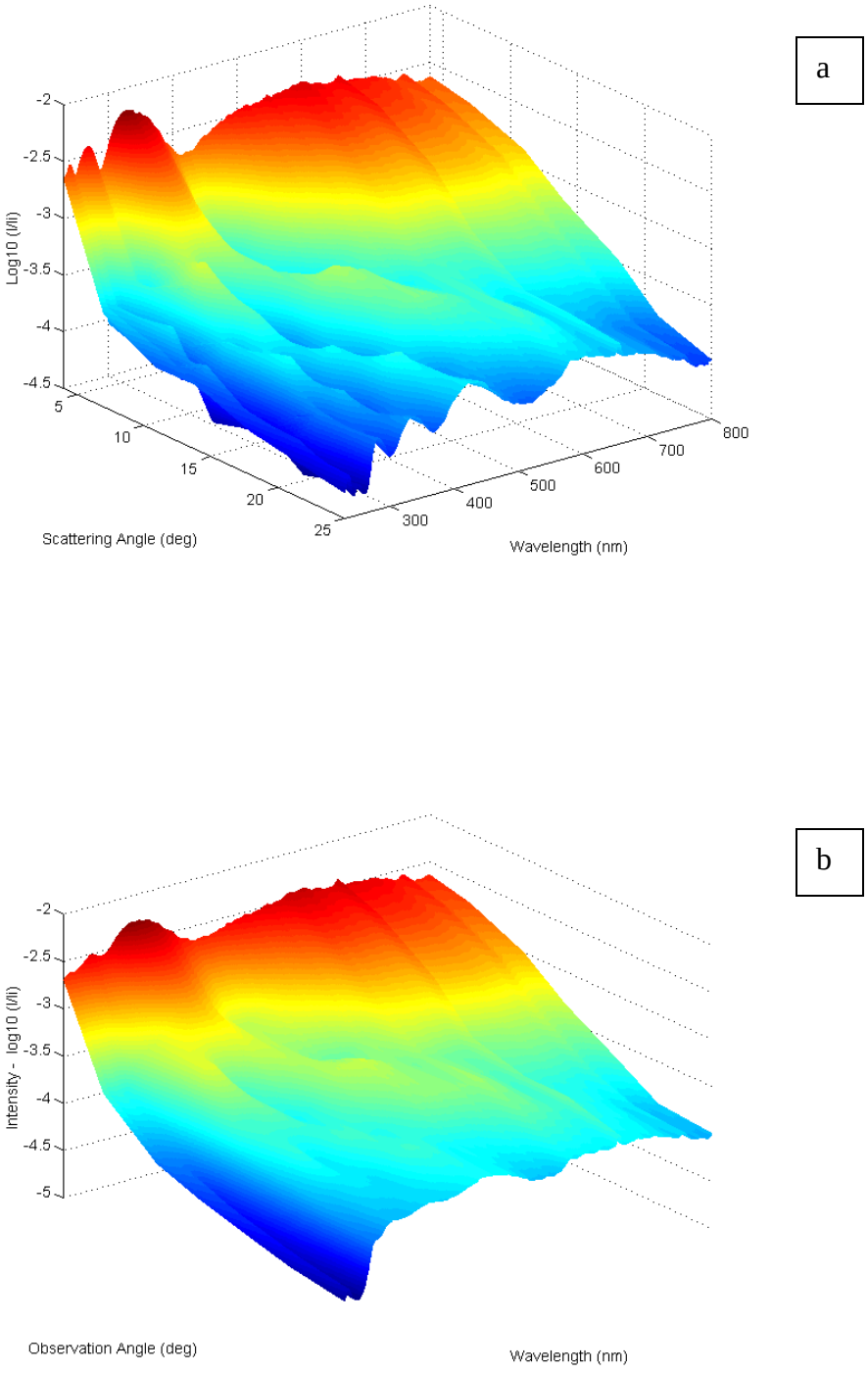

Figure 6.27. Measured UV-VIS MAMW response surfaces of polystyrene 1.9 μm size standard in water. a) Spheres. b) Peanut-shaped particles. Note that the plotted wavelength range extends from 230 nm to 800 nm.

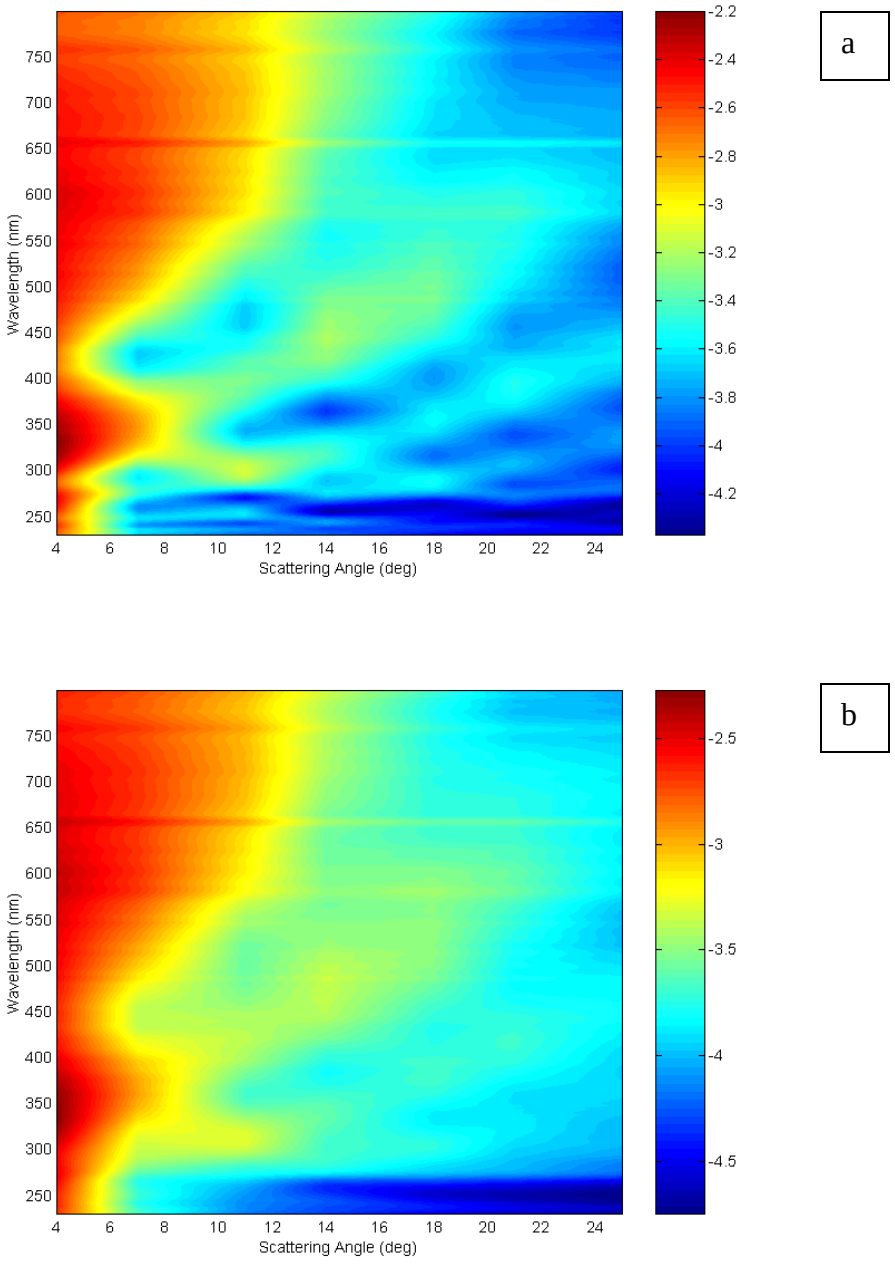

Figure 6.28. Contour plots of the measured UV-VIS MAMW response surfaces of polystyrene 1.9 µm size standards in water. a) Spheres. b) Peanut-shaped particles. Note that the plotted wavelength range extends from 230 nm to 800 nm.

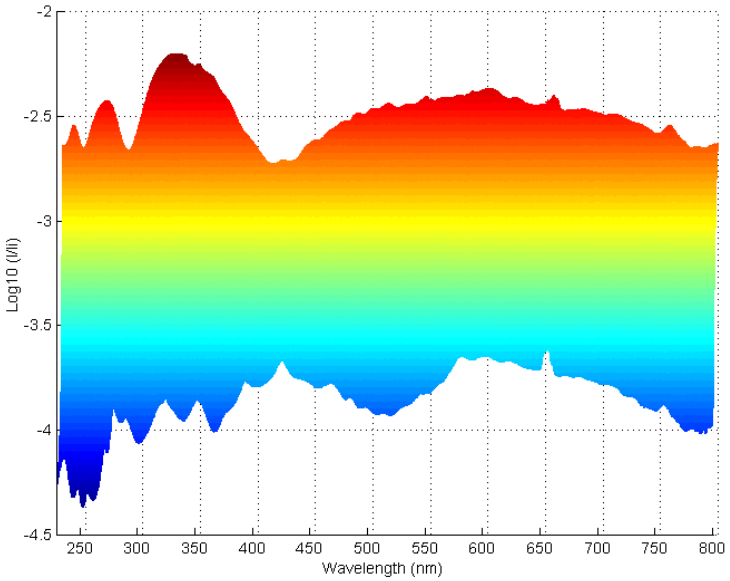

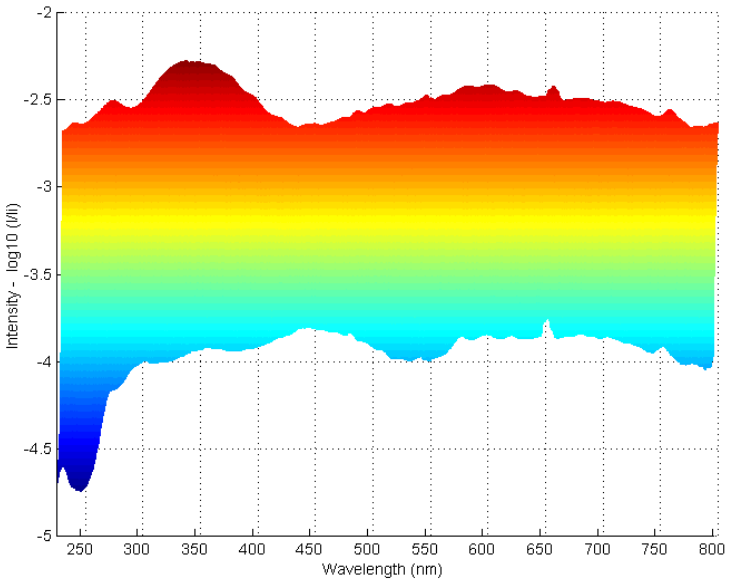

Figure 6.29. Wavelength-view plots of the measured UV-VIS MAMW response surfaces of polystyrene 1.9 µm size standards in water. a) Spheres. b) Peanut-shaped particles. Note that the plotted wavelength range extends from 230 nm to 800 nm.

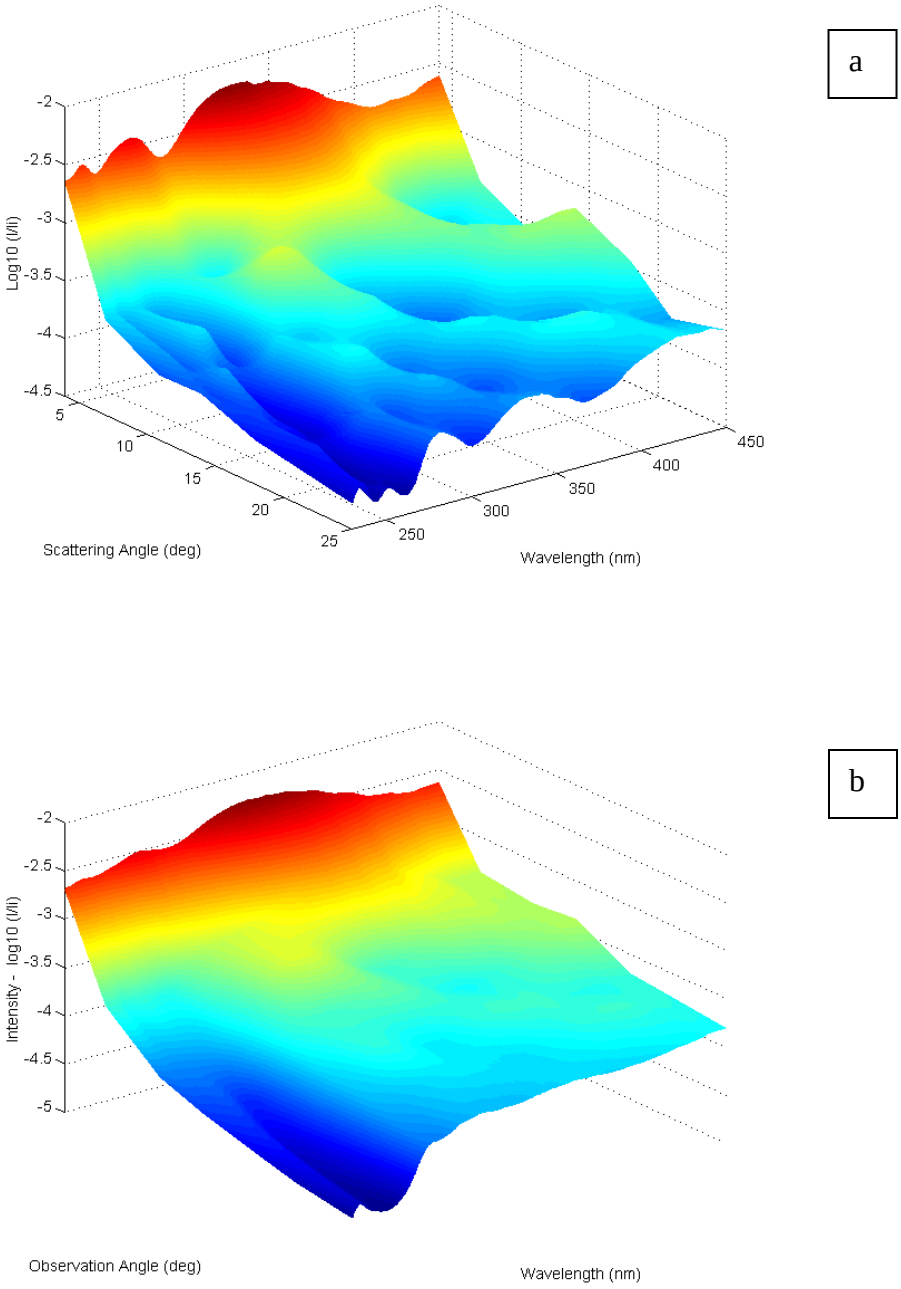

Figure 6.30. Measured UV MAMW response surfaces of polystyrene 1.9 μm size standards in water. a) Spheres. b) Peanut-shaped particles. Note that the plotted wavelength range extends from 230 nm to 450 nm.

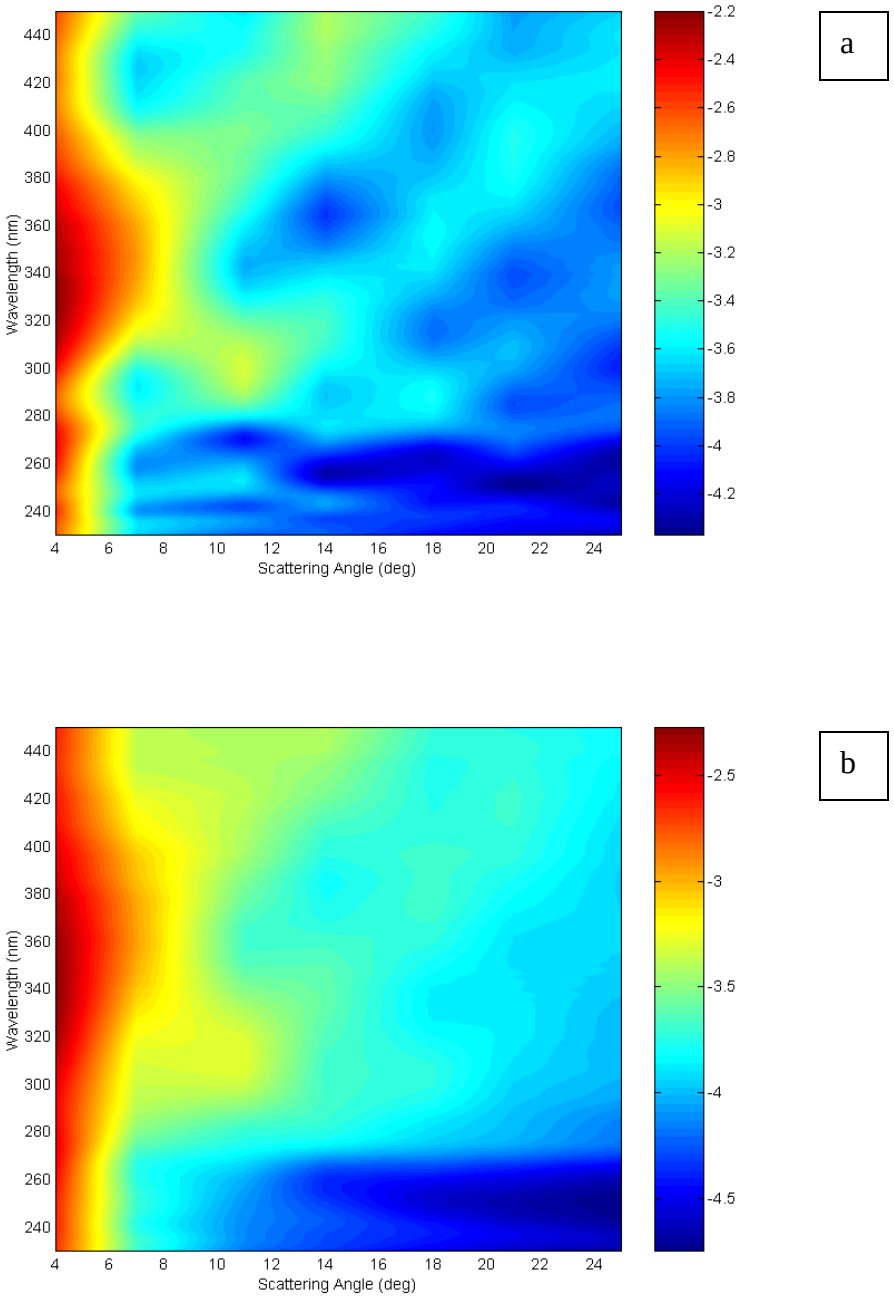

Figure 6.31. Contour plots of the measured UV MAMW response surfaces of polystyrene 1.9 µm size standards in water. a) Spheres. b) Peanut-shaped particles. Note that the plotted wavelength range extends from 230 nm to 450 nm.

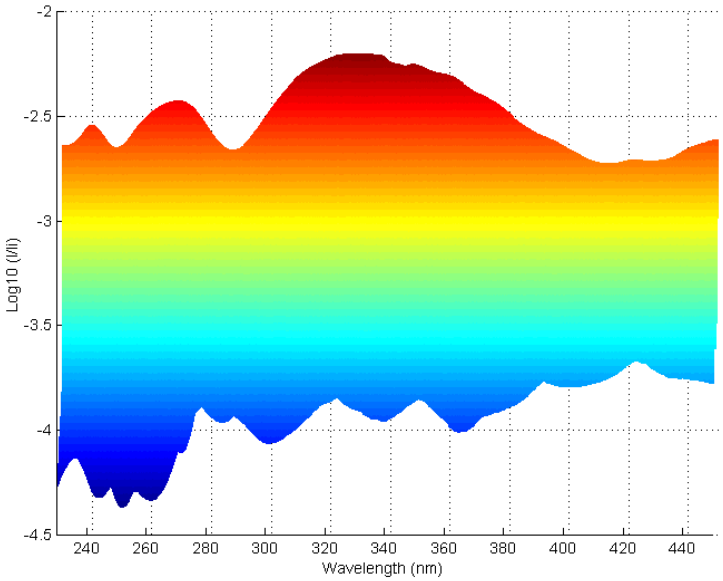

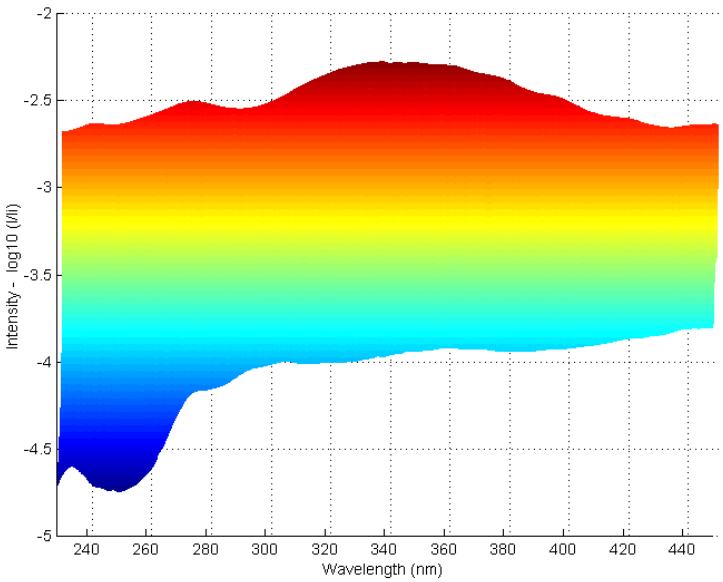

Figure 6.32. Wavelength-view plots of the measured UV MAMW response surfaces of polystyrene 1.9 µm size standards in water. a) Spheres. b) Peanut-shaped particles. Note that the plotted wavelength range extends from 230 nm to 450 nm.

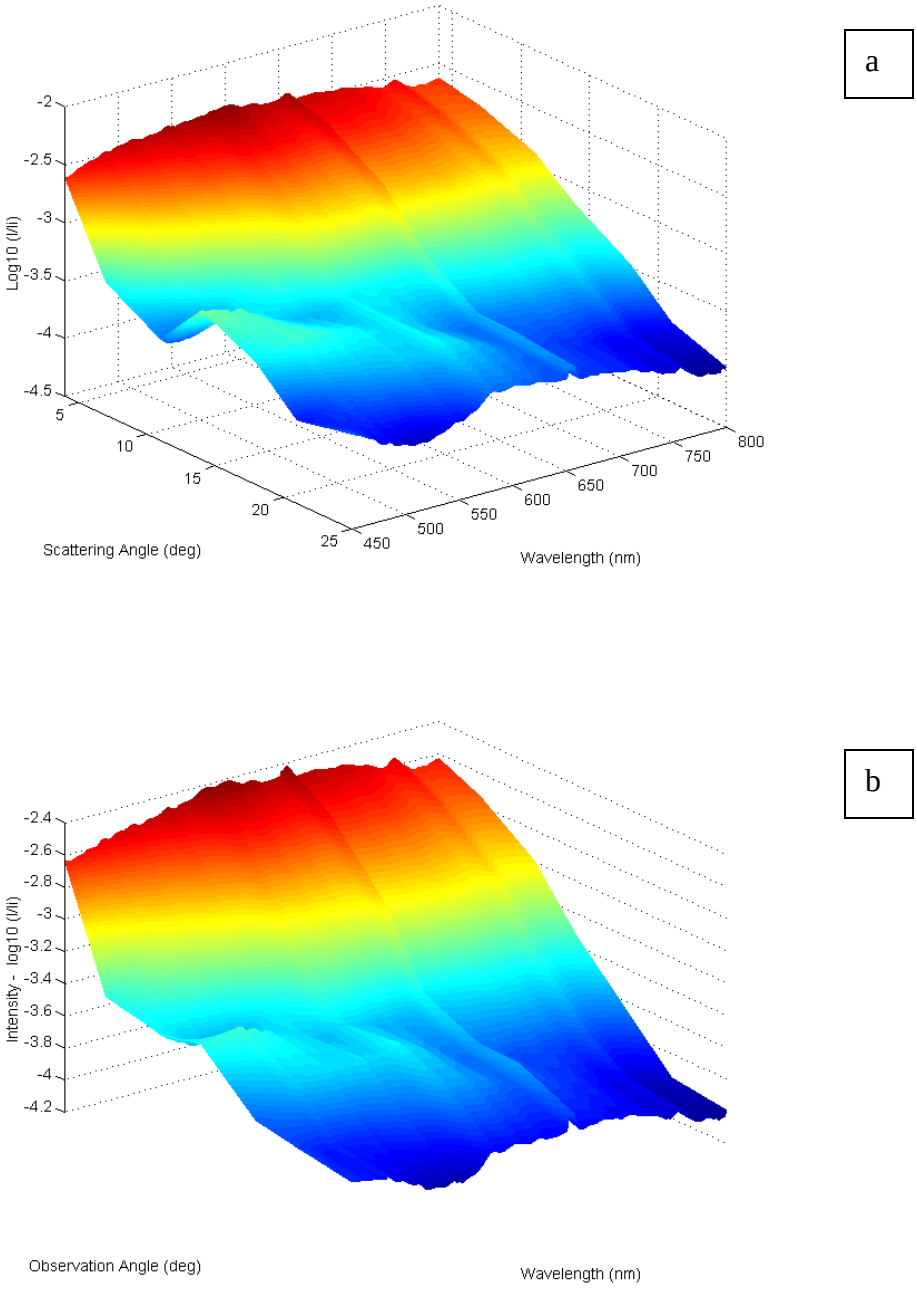

Figure 6.33. Measured VIS MAMW response surfaces of polystyrene 1.9 µm size standards in water. a) Spheres. b) Peanut-shaped particles. Note that the plotted wavelength range extends from 450 nm to 800 nm.

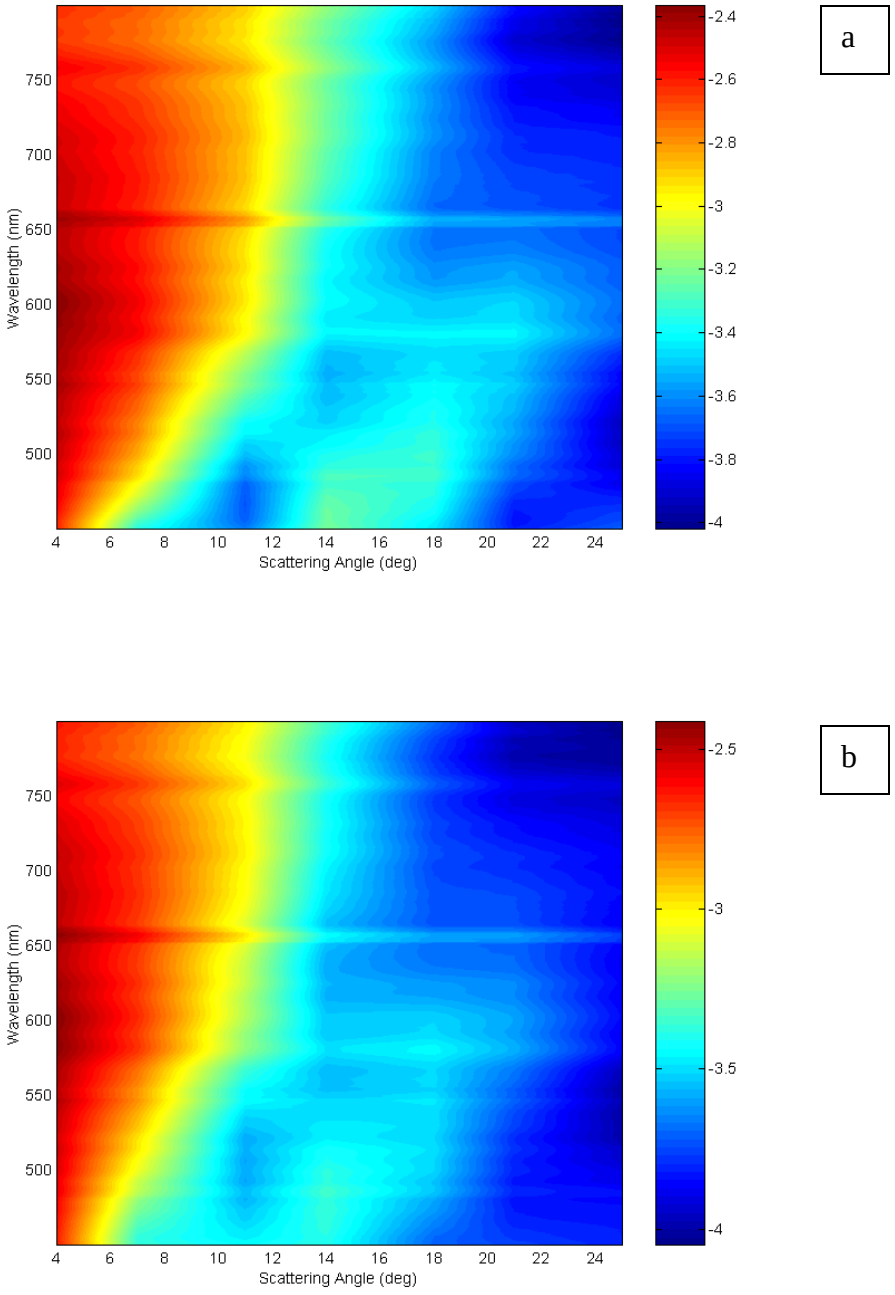

Figure 6.34. Contour plots of the measured VIS MAMW response surfaces of polystyrene 1.9 µm size standards in water. a) Spheres. b) Peanut-shaped particles. Note that the plotted wavelength range extends from 450 nm to 800 nm.

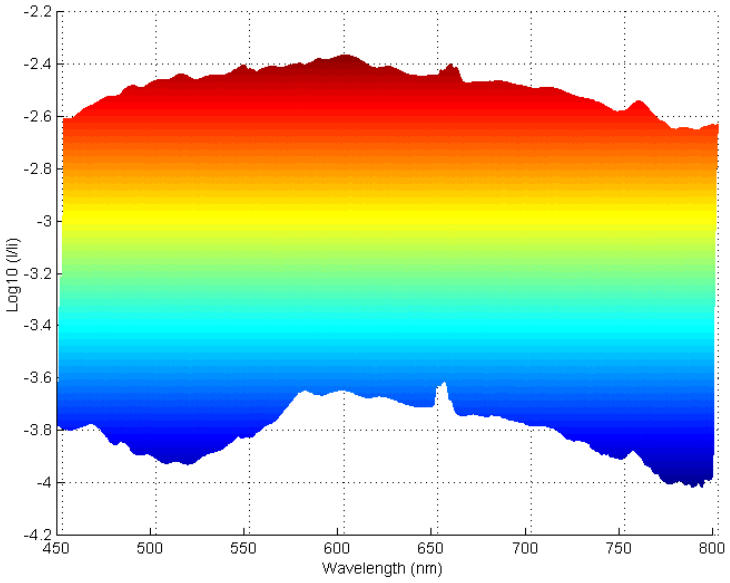

a

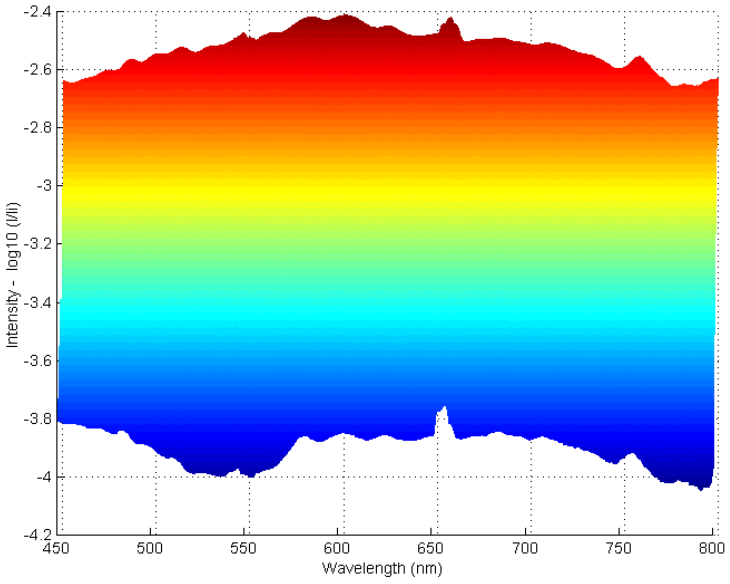

b

Figure 6.35. Wavelength-view plots of measured VIS MAMW response surfaces of polystyrene 1.9 µm size standards in water. a) Spheres. b) Peanut-shaped particles. Note that the plotted wavelength range extends from 450 nm to 800 nm.

Therefore, it maybe concluded that the well-known supposition that scattering properties of non-spherical particles can be approximated to those of spheres with equivalent sizes may hold depending on particle size parameter.

In conclusion, the measurement of the UV-VIS MAMW spectra of both peanut-shaped particles and spherical particles of the same sizes shows clear differences, especially in the UV region. This demonstrates:

1) the capability of UV-VIS MAMW spectroscopy to distinguish particle shape and
2) the potential of the Integrated UV-VIS MAMW spectrometer to be another modality of non-spherical particle characterization by light scattering.

6.2.2.4. Proposed Set Up of an Integrated UV-VIS MAMW Spectrometer with Enhanced Backscattering Measurement Capacity

As described in the beginning of this section, polarized light scattering and back scattering provide both theoretical and experimental methodologies for the study and characterization of non-spherical particles because of their sensitivity to the particle shape and/or orientation.[7] Therefore, the implementation of these methodologies will further enhance the capabilities of the Integrated UV-VIS MAMW spectrometer to infer or characterize non-spherical particles. Currently, the Integrated UV-VIS MAMW spectrometer employs unpolarized light only. In addition, the geometry of our current prototype UV-VIS MAMW spectrometer hinders the measurement of backscattering.

Methods of implementing backscattering and polarized light scattering measurements are discussed in this section.

Fig. 6.36 shows a schematic of an enhanced Integrated UV-VIS MAMW spectrometer design that will have the capability of backscattering and polarized light scattering measurements. It incorporates polarization optics for the Mueller-matrix measurement and a new double slit for the backscattering measurement.

A pair of linear polarizer and half-wave plate will be installed in both the incident beam path and the scattered beam path. Theoretically, this will enable the measurement of the 16-element Mueller matrix (the combination of all the possible polarized light scattering measurements). As stated in section 3.2.2, measurement of the Mueller matrix allows of the acquisition of all the information obtainable from light scattering.

Measurement of backscattered light can be implemented by the use of a double slit in the path of the incident beam. One slit will be used as entrance for the incident beam to the sample cell and the other slit which will be located at a calculated position that will allow the optimum detection of backscattered light. Both slits will be located closely and thus, the incident beam is required to be shaped before arriving at the double slit. This can be accomplished by installing additional single rectangular slit just after the collimation lens L1.

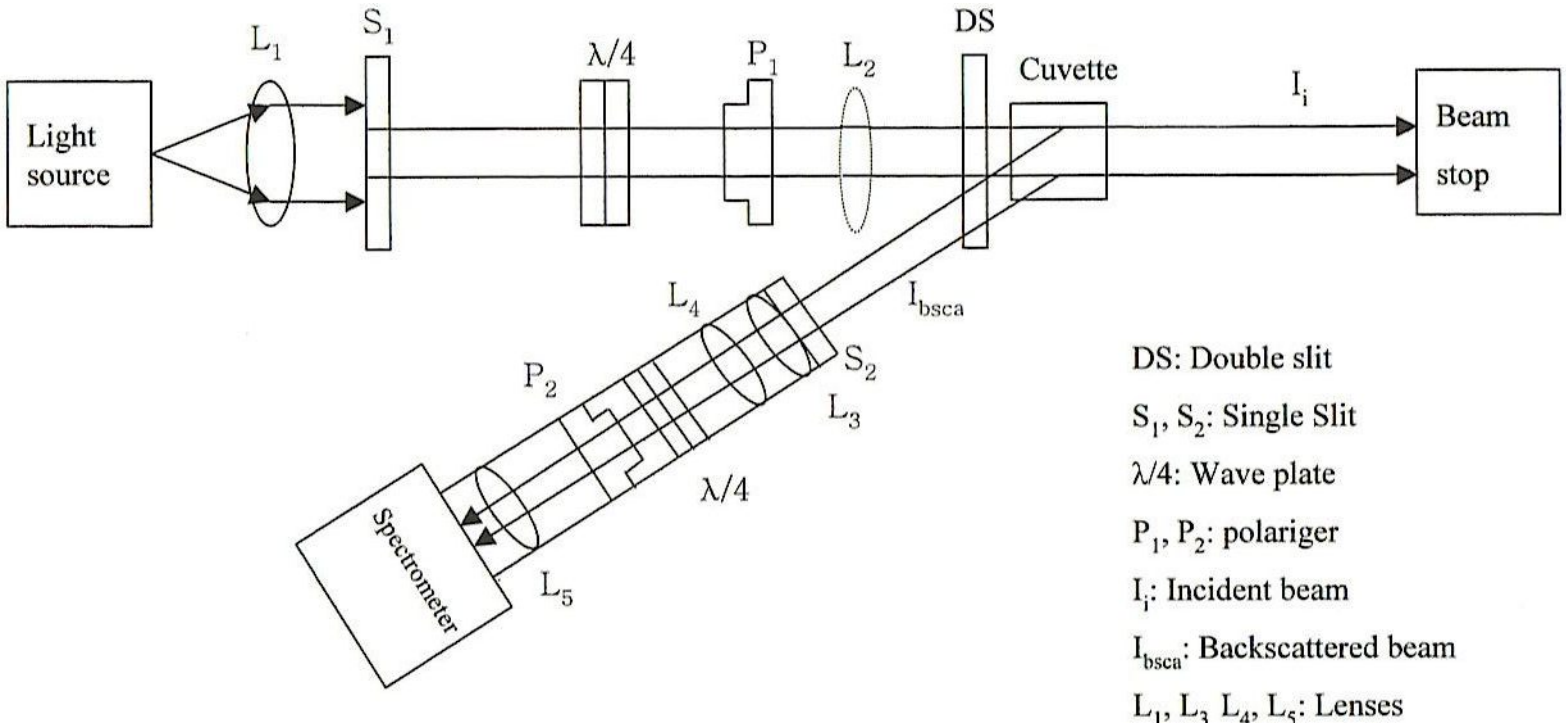

Figure. 6.36. Schematic of the Integrated UV-VIS MAMW spectrometer with enhanced backscattering measurement capacity.

6.2.3. Characterization of Polystyrene Standards by Composition

The capability of the Integrated UV-VIS MAMW spectrometer to characterize particle composition was tested using Duke Scientific polystyrene 3.0 μm spheres (Duke Scientific catalog No. 4203A) and green fluorescent polystyrene 3.0 μm spheres (Duke Scientific catalog No. G0300). Both standards have the same specifications except for the compositional differences. The green fluorescent dye has an excitation maxima at 468 nm and an emission maxima at 508 nm. It also has a weak excitation band at around 330 nm.

Before the measurement of the UV-VIS MAMW spectra, the effect of the dye on the incident UV-VIS beam spectrum was investigated. For this purpose, the optical density spectra of polystyrene 3.0 μm spheres, green fluorescent polystyrene 3.0 μm spheres, and red dye coated polystyrene 3.0 μm spheres in water were measured. The red dye coated polystyrene 3.0 μm spheres are from Polysciences, Inc. (Polyscience catalog No. 17137). For convenience, each standard will be designated as ps3.0 (polystyrene 3.0 μm spheres), pf 3.0 (green fluorescent polystyrene 3.0 μm spheres), and pr 3.0 (red dye coated polystyrene 3.0 μm spheres) respectively. Fig. 6.37 shows the measured optical density spectra of ps3.0, pf3.0, and pr3.0 polystyrene spheres in water**.** For comparison purposes, the measured spectra are normalized with the area under the curve. The optical density spectra of ps3.0 and pf3.0 standards show no appreciable differences in the visible region. On the other hand, that of pr3.0 standard shows reduced optical density in the visible region between 430 nm and 580 nm. This is attributed to different manufacturing procedures of the pf3.0 and pr 3.0 standards. In case of pf3.0, green fluorescent dye is incorporated into the polymer matrix

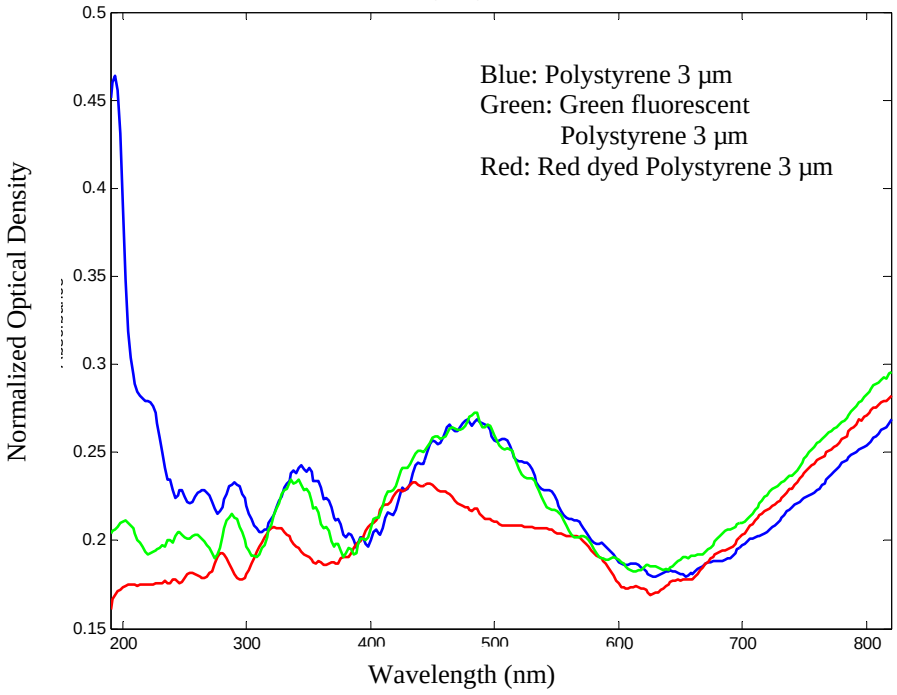

Figure. 6.37. Measured optical density spectra of 3.0 µm size polystyrene: spheres, green fluorescent, and red dyed. The spectrum of the red dyed polystyrene spheres has a different profile because the dye is surface coated. The HP 8452 spectrometer was used for this measurement.

during polymerization. This method prevents dye leaching in aqueous media and minimizes photobleaching.[13] Therefore, green fluorescent dye behaves like intrinsic particle chromophore. For the pr3.0 standard, the dye is coated on the surface of sphere.[48] As a result, majority of the dye stays at the surface of particle and thus, the analysis of the measurement results clearly requires the inhomogeneous particle model for the acquisition of correct particle size information. Consequently, pr 3.0 standard was not chosen for the feasibility test in this dissertation research.

The measurements were performed using the octagonal cuvette to see the effect of the fluorescent dye clearly. Because refraction is negligible, the measured angular range could easily be extended up to 60^{o}. The results are expressed in terms of the observation angle not the scattering angle. Fig 6.38.a, Fig 6.39.a, and Fig 6.40.a represent the measured UV-VIS MAMW response surface of polystyrene 3.0 μm spheres in water, the contour plot of Fig 6.38.a, and the wavelength-view plot of Fig 6.38.a, respectively. Fig 6.38.b, Fig 6.39.b, and Fig 6.40.b show the measured UV-VIS MAMW response surface of green fluorescent polystyrene 3.0 μm spheres in water, the contour plot of Fig 6.38.b, and the wavelength-view plot of Fig 6.38.b, respectively.

Both response surfaces show almost the same features except the locations at around 300 nm and 450 ~ 550 nm and approximate angular range of 30^{o} ~ 60^{o} where the intensity of the response surface of pf 3.0 standard is enhanced due to the fluorescent dye. This can be seen clearly from the contour plots and the wavelength-view plots. Typically, light scattering or optical density measurements do not yield fluorescence information.

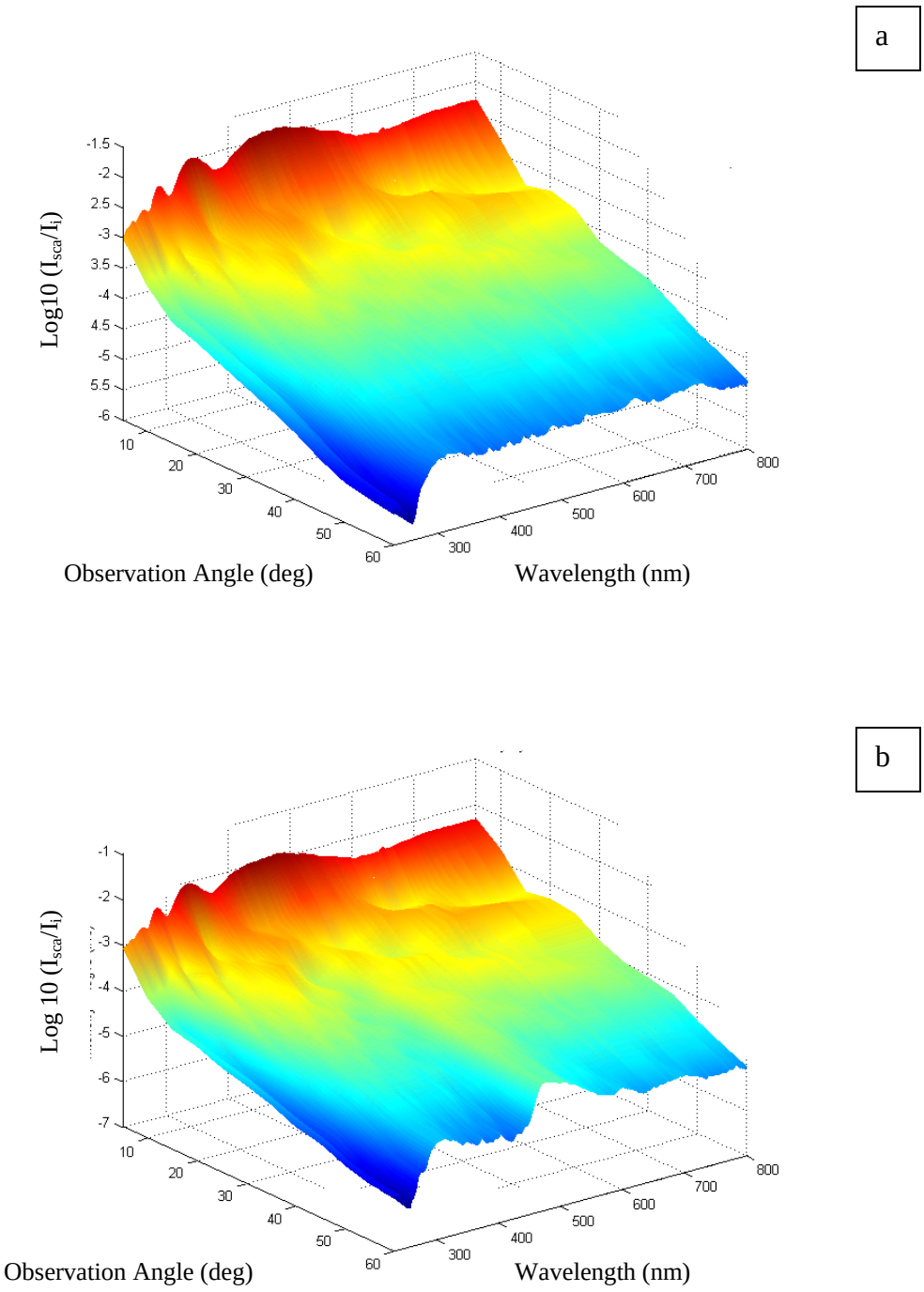

Figure 6.38. Measured UV-VIS MAMW response surfaces of polystyrene 3.0 µm standards in water. a) Polystyrene spheres. b) Green fluorescent polystyrene spheres. In case of b), both particle size and composition (green fluorescence) information is available from the response surface. The measurements were conducted with an octagonal cuvette and the results are plotted as function of the observation angle.

a

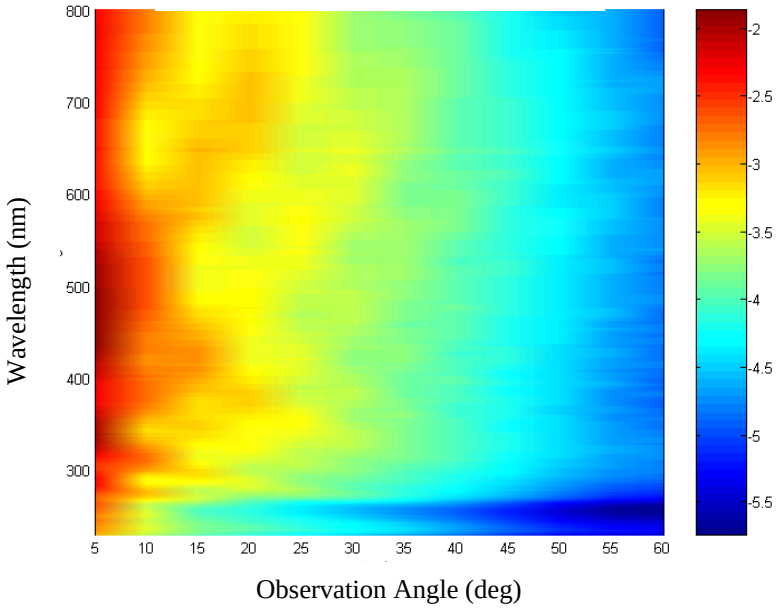

b

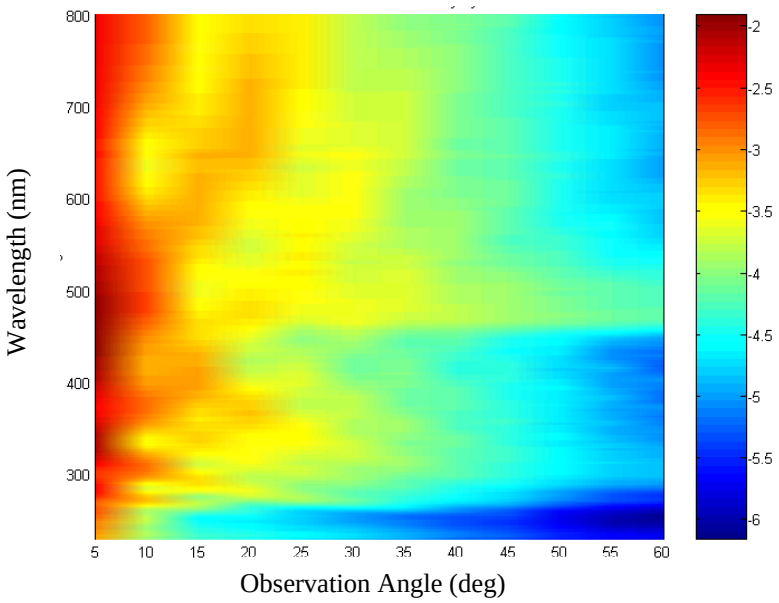

Figure 6.39. Contour plots of the measured UV-VIS MAMW response surfaces of polystyrene 3.0 µm standards in water. a) polystyrene spheres. b) green fluorescent polystyrene In case of b), fluorescence information can be seen at around 500 nm.

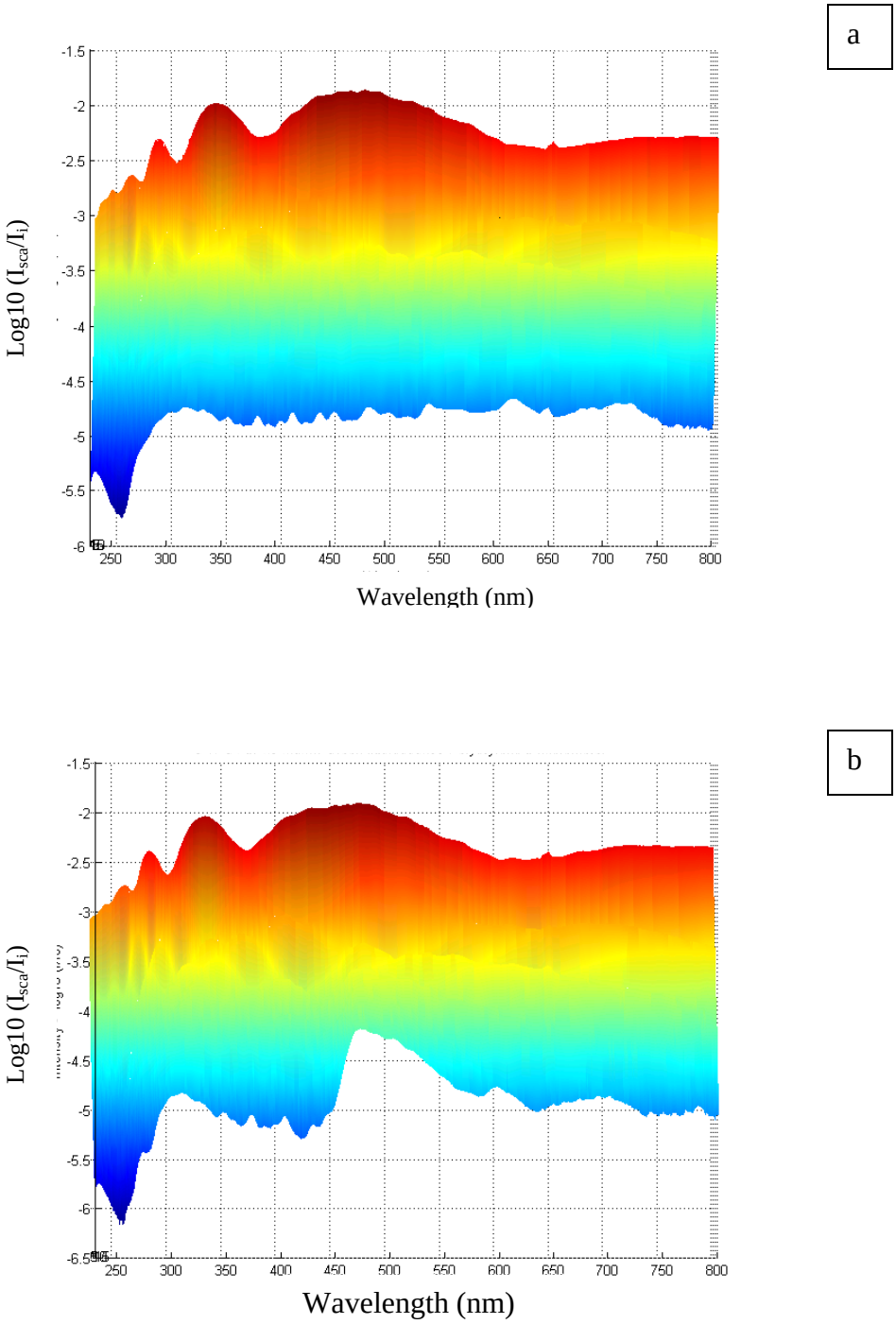

Figure 6.40. Wavelength-view plots of the measured UV-VIS MAMW response surfaces of polystyrene 3.0 µm standards in water. a) polystyrene spheres. b) green fluorescent polystyrene. The size and fluorescence composition information can be readily appreciated.

However, the measurement of the UV-VIS MAMW spectra can yield particle size and fluorescence information simultaneously. This is especially useful for biological particle characterization.

The capability of the Integrated UV-VIS MAMW spectrometer to measure particle composition was tested using polystyrene 3.0 μm size spheres and green fluorescent polystyrene 3.0 μm size spheres. The resulting UV-VIS MAMW spectra show differences due to particle composition - green fluorescent dye. This demonstrates the capability of the Integrated UV-VIS MAMW spectrometer to measure particle composition. This capability is also demonstrated in other parts of this dissertation: observation of polystyrene bulk absorption band from polystyrene 20 nm spheres UV-VIS MAMW spectra and the disappearance of hemoglobin doublet in sickled red blood cells. All these results demonstrate the potential of the Integrated UV-VIS MAMW spectrometer for the characterization of micron and sub-micron size particles in terms of size and chemical composition.

6.3. Results of Frequency Domain Fluorescence Emission Spectrum Measurement

The capability of the Integrated UV-VIS MAMW spectrometer to perform the frequency domain fluorescence spectroscopy was tested by measuring the fluorescence emission spectrum from green fluorescent polystyrene 3.0 μm spheres that was acquired from Duke Scientific Corporation. The green fluorescent dye has the excitation maxima at 468 nm and the emission maxima at 508 nm as shown in Fig. 6.41.[13] Its Stokes shift is 40 nm. In addition, it has weak excitation band at around 330 nm. Fig.6.42.a shows UV

excitation and Fig.6.42.b exhibits visible excitation of green fluorescent dye.[13] Both excitations lead to the emission of fluorescent light with peak intensity at around 515 nm.

Fig.6.43 shows the photograph of fluorescence measurement set up and Fig. 6.44 illustrates the schematic of the experimental set up. A fused silica convex lens with f/# 2.0 (25 mm diameter and 50 mm focal length, L2) was installed in front of the cuvette to focus the incident UV-VIS beam into the sample cell. Lens L4 described in Section 4.2.2 was removed to improve the signal sensitivity at the detector end. If necessary, a bandpass filter with the center wavelength at 470 nm and 10 nm FWHM (THORLABS, Inc., Model No FB470-10) or a bandpass filter with the center wavelength at 510 nm and 10 nm FWHM (THORLABS, Inc., Model No FB510-10) was alternately installed at the location of lens L4 to measure a portion of the excitation (470 nm) or the emission (510 nm) spectrum. For typical fluorescence measurement setup, the bandpass filter that transmits only the excitation light and blocks the other light is installed in front of the sample cell. However, with the current prototype UV-VIS MAMW spectrometer setup, it was inevitable to install the bandpass filter for the excitation light after the sample cell because of the weak visible light intensity from DT-1000 light source. Deviations from the typical fluorescence measurement setup, i.e. the use of single detector and the alternate installation of bandpass filters, became possible due to the use of goniometer, a fluorescence sample with known excitation and emission spectra, and the CCD detector (S2000 production spectrometer) that allows the simultaneous detection of the broadband UV-VIS-NIR beam.

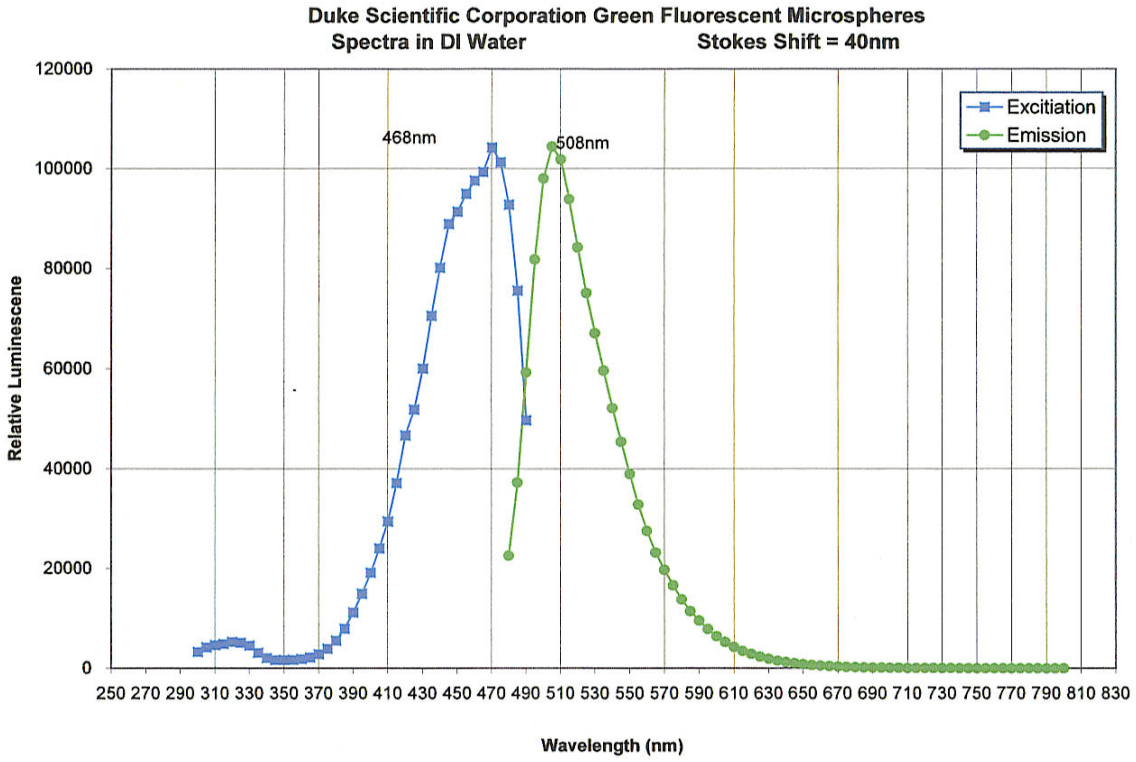

Figure 6.41. Spectral information of Duke Scientific Corporation green fluorescent michrospheres. [13]

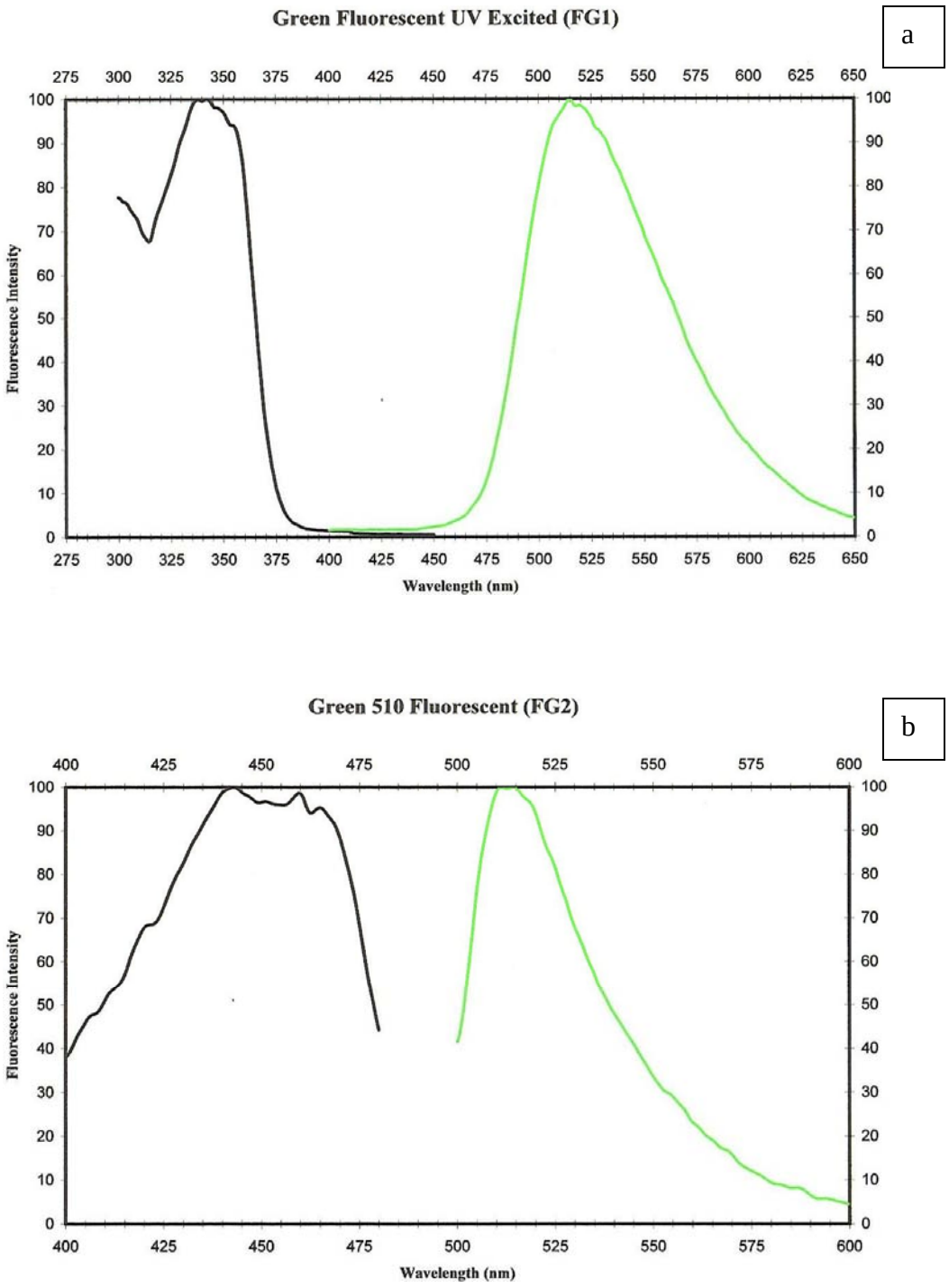

Figure 6.42. Green fluorescent dye excitation. a) UV excitation. b) Visible excitation. Both excitation lead to the emission of fluorescent light with peak intensity at around 515 nm.[13]

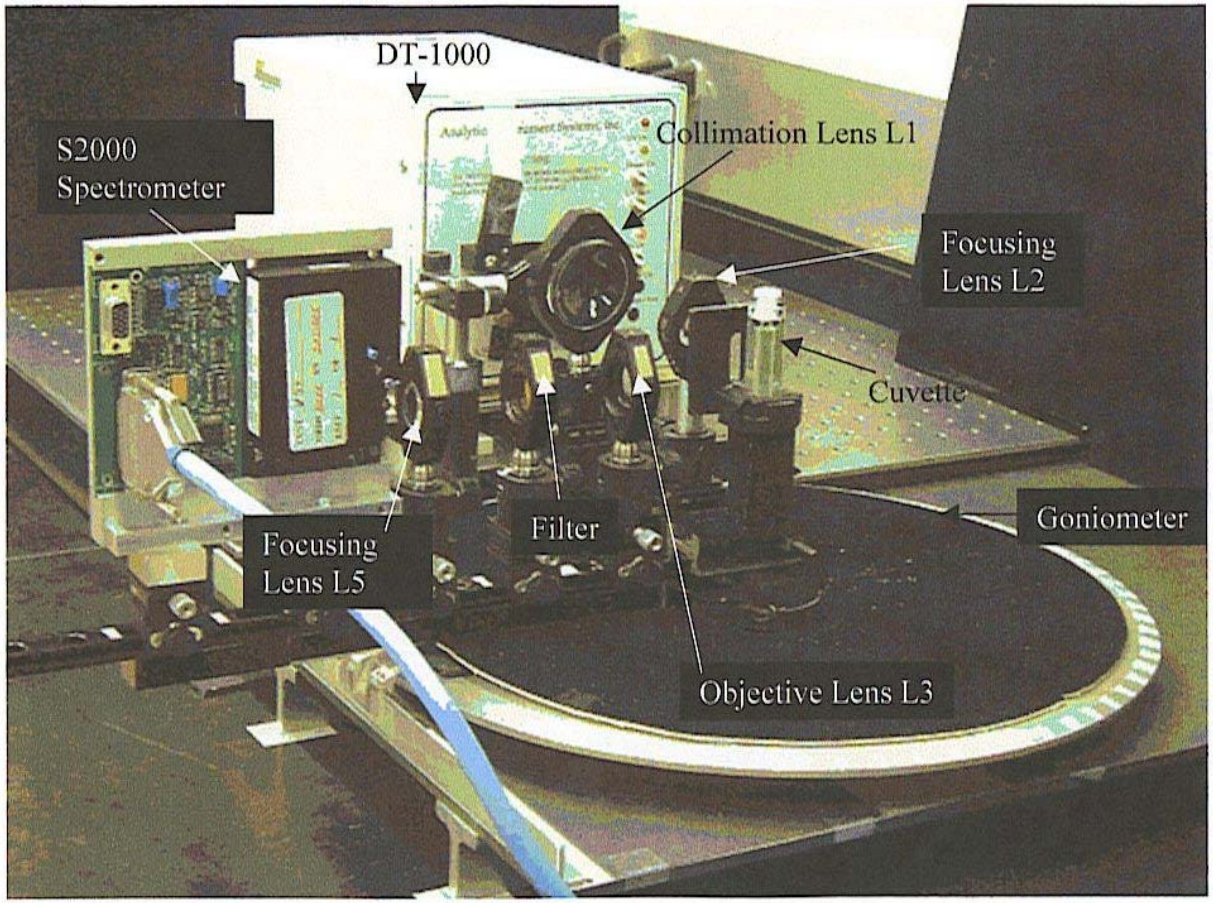

Figure 6.43 Photograph of fluorescence measurement set up. Note that the locations of lens L5 and S2000 production spectrometer were moved closer to the sample cell to maximize the amount of light detected by the spectrometer.

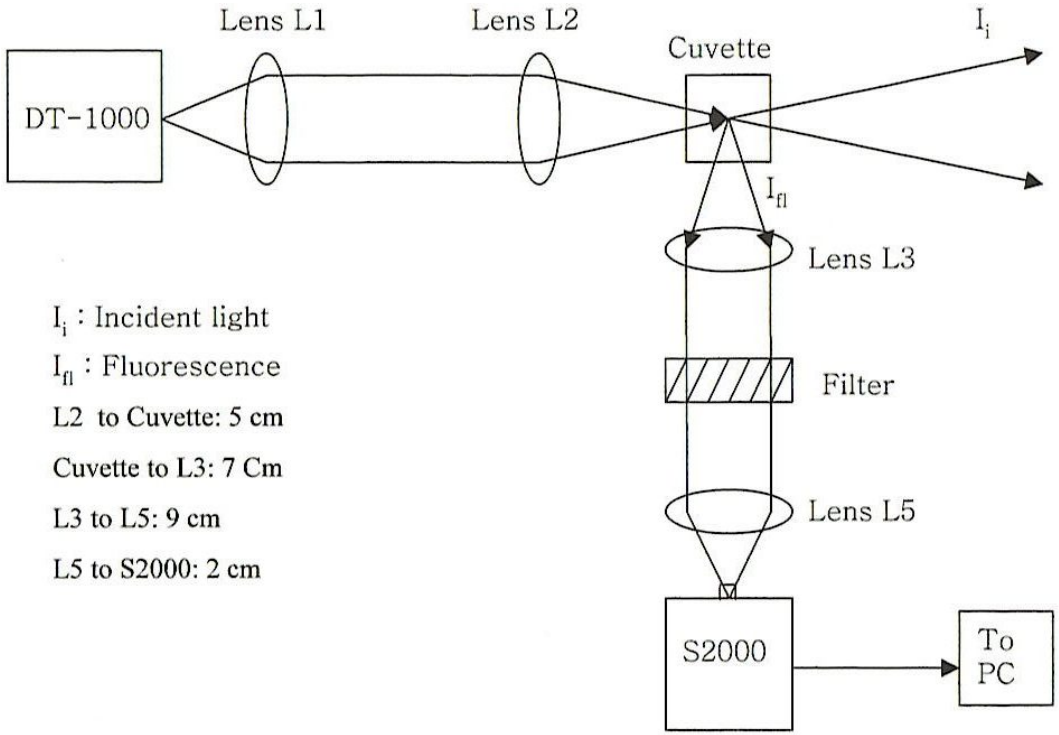

Figure 6.44. Schematic of the fluorescence measurement set up.

Note that lens L5 and S2000 production spectrometer were moved closer to the sample cell to maximize the amount of light detected by the spectrometer. During the measurement, the integration time was held at 5000 msec and the average sample number for the signal averaging was held at 5. Therefore, the detected fluorescence emission spectrum was displayed on the monitor screen and if necessary recorded with the OOIBase32 software at every 25 sec.

Fig.6.45 shows the measured excitation and fluorescence emission spectra. It displays excitation (absorption) spectrum with peak intensity at 490 nm and fluorescence emission spectrum with peak intensity at 515 nm. The absorption and the fluorescence emission spectra are overlap due to broad excitation and emission band. Consequently, the locations of peak intensities are slightly shifted from those shown in the manufacturer's data sheet. The broad but weak peak at around 330 nm is due to a UV absorption band. A series of small peaks after 550 nm are caused by scattered light. This was confirmed by repeating the measurement using polystyrene 3.0 μm spheres. Both results, the measured spectra of polystyrene 3.0 μm spheres and those of green fluorescent polystyrene 3.0 μm spheres, are plotted in Fig. 6.46 for comparison purposes.

Fig. 6.47. a shows the bandpass-filtered absorption (red – 470 nm) and fluorescence emission (green – 510 nm) spectra of the green fluorescent polystyrene spheres and the corresponding bandpass-filtered scattered-light spectra(blue - 470 nm, black – 510 nm) from polystyrene spheres measured at 90^{o}.

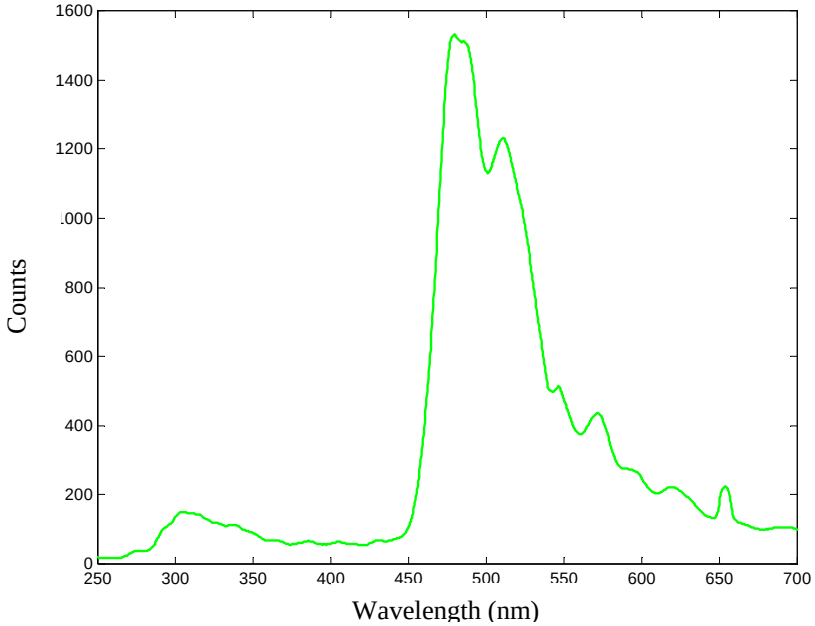

Figure 6.45. The excitation and fluorescence emission spectra measured with the Integrated UV-VIS MAMW spectrometer. It displays the excitation (absorption) spectrum with peak intensity at 490 nm and the emission (fluorescence) spectrum with peak intensity at 515 nm.

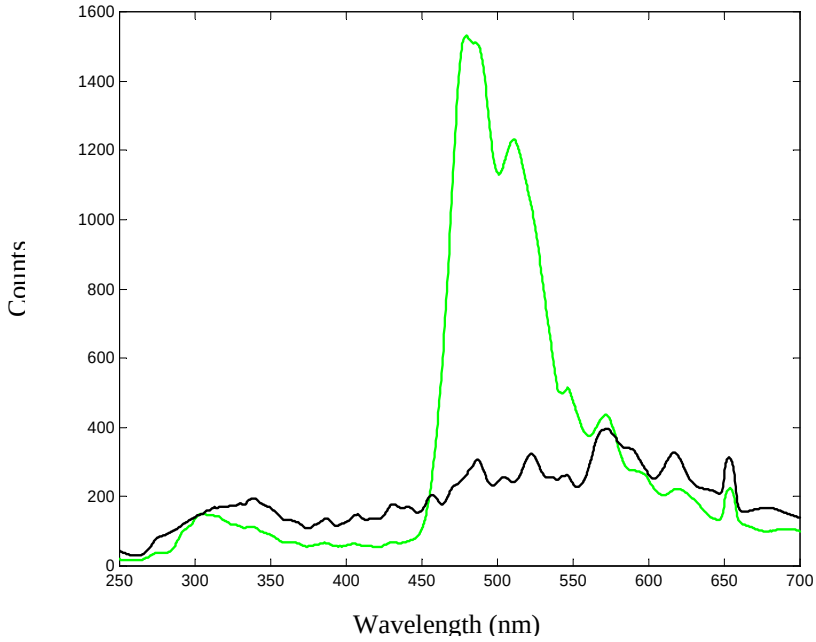

Figure 6.46. The excitation and fluorescence emission spectra (green) and the scattered-light spectrum of the particle of the same size (black) measured with the Integrated UV-VIS MAMW spectrometer.

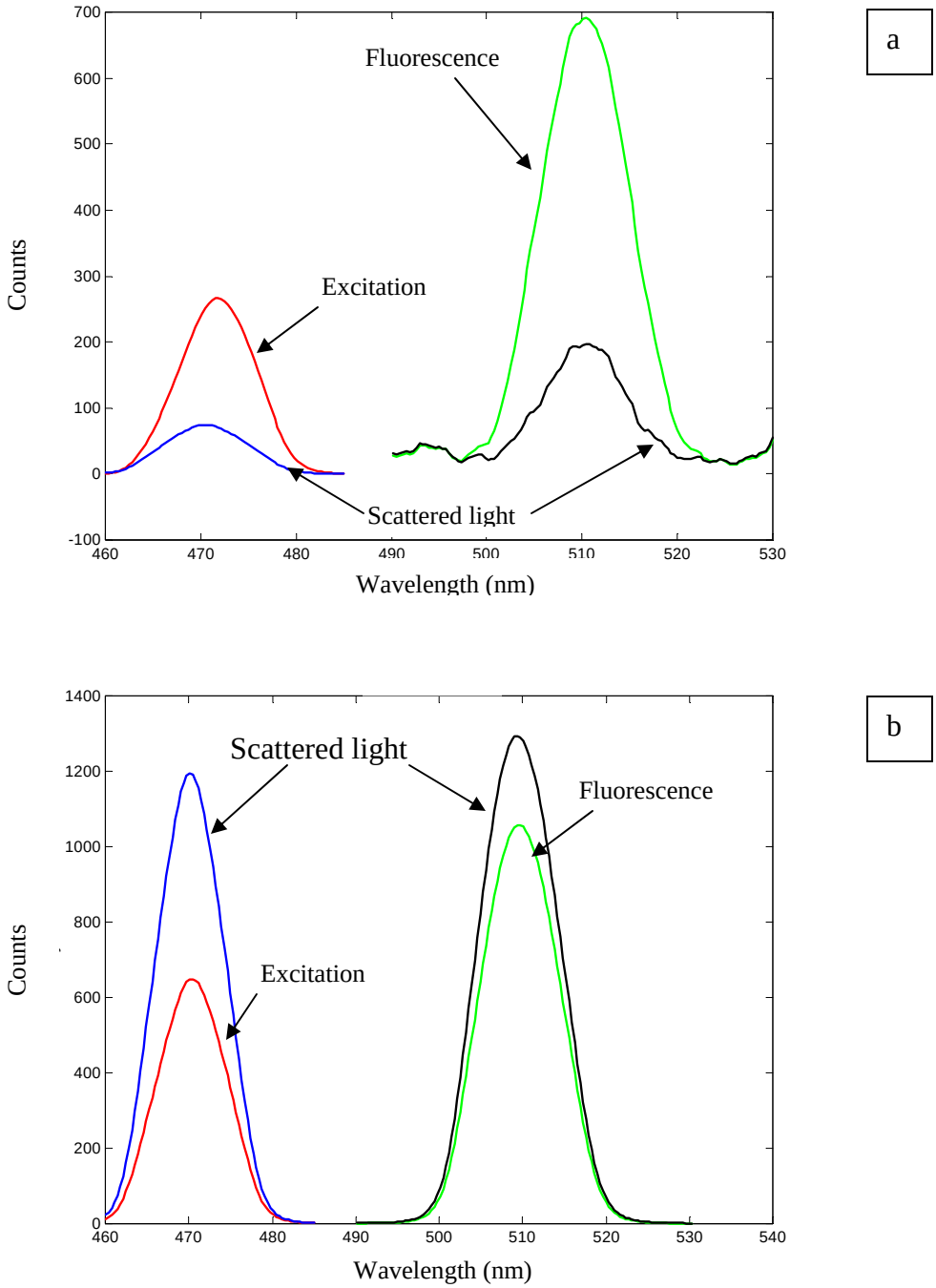

Figure 6.47. Band pass-filtered absorption, fluorescence**,** and scattered light spectra. a) Measured at 90^{o}. b) Measured at 20^{o}.

Fig. 6.47. b represents the results of the same measurements repeated at 20^{o}. In case of Fig. 6.47. a, the intensities of both absorption and fluorescence light are stronger than those of the scattered-light from polystyrene spheres. However, in Fig. 6.47. b, the scattered light has stronger intensities compared with those of the absorption or the fluorescence light. This further confirms the measurement of fluorescence spectra by the Integrated UV-VIS MAMW spectrometer.

The possibility of performing the frequency domain fluorescence spectroscopy with the Integrated UV-VIS MAMW spectrometer was tested and confirmed. The result is consistent with the data provided by the manufacturer of the fluorescence standard. However, practical application of fluorescence spectroscopy with the Integrated UV-VIS MAMW spectrometer requires the use of stronger light source, especially in the visible region. The power of the tungsten-halogen bulb used in this measurement was only 6.5 W. Weak visible light intensity was partially compensated by using large CCD detector (S2000 production spectrometer) integration times (5000 msec). One of the merits of the CCD detector usage in the frequency domain fluorescence spectroscopy is that no scan of absorption or fluorescence light is required. Unlike photomultiplier tubes (PMT), the CCD detector can immediately record whole absorption and fluorescence spectra. This allows room to increase the detector integration time substantially and thus, permits the use of tungsten-halogen (visible) or Deuterium (UV) lamp that has weak power compared to several hundred W Xenon lamp as the excitation light source. Therefore, single Deuterium tungsten-halogen light source can be used for UV-VIS MAMW scattering, transmission, and fluorescence measurement.

Additional fluorescence measurements using various samples are recommended to elucidate further requirements inevitable to the practical application of the frequency domain fluorescence spectroscopy with the Integrated UV-VIS MAMW spectrometer.

6.4. Results of the UV-VIS MAMW Spectra Measurement of Whole Blood Samples

UV-VIS MAMW spectra of normal whole blood samples and sickled whole blood samples were measured. The resulting spectra showed differences due to changes in red blood cell (RBC) morphology**,** and compositional changes in sickled blood samples. These experiments confirmed the capability of the Integrated UV-VIS MAMW spectrometer to detect particle shape and compositional change simultaneously. The implication of the measured results and the potential of the Integrated UV-VIS MAMW spectrometer for biological particle characterization and for the application to the medical area are discussed.

6.4.1.Sample Preparation and Measurement

Whole blood samples from a sickle cell anemia patient were obtained from Florida Blood Services (FBS). Part of the blood sample was kept in its normal status and part of it was used to induce the sickling of cells by deoxygenating the sample. Sickle cell anemia induces red blood cell (RBC) morphology changes from ellipsoid into holly-leaf or crest shape when oxygen is deprived.[11] Fig 6.48.a shows a picture of normal red blood cells which have the shape of biconcave discs and Fig 6.48.b shows a picture of sickle cells.[37]

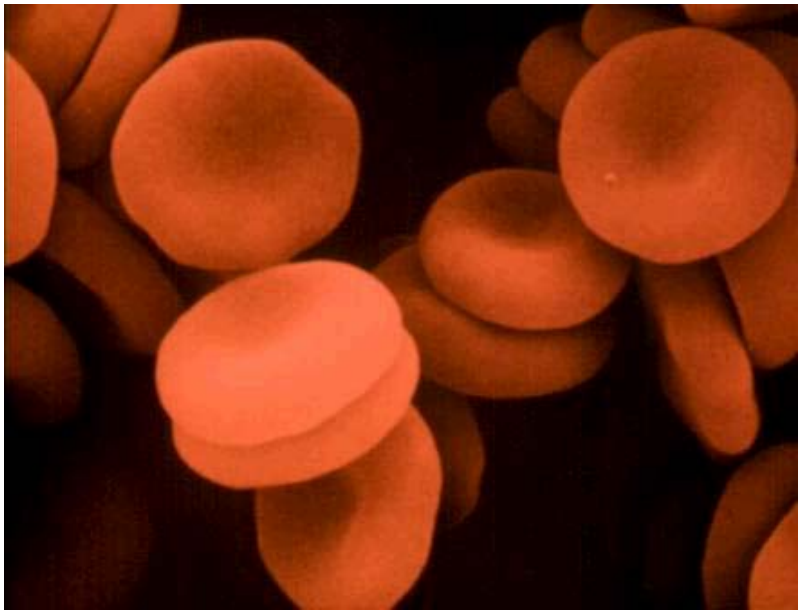

a

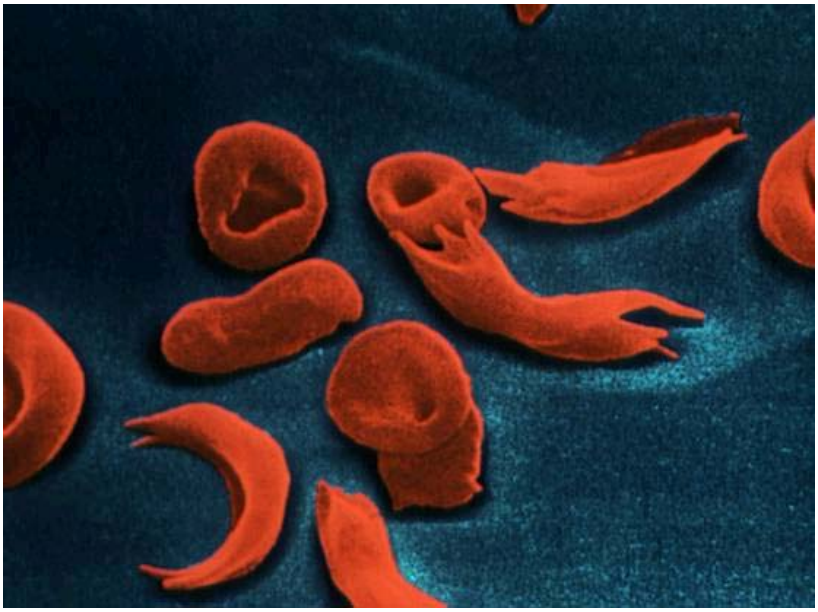

b

Figure 6.48. Picture of red blood cells and sickled blood cells. a) Red blood cells have a biconcave disc shape of ~ 8 μm. b) The crescent-non-spherical blood cell (bottom, left) shows sickled red blood cells. Cited from Reference 37.

Because Red blood cells and sickle cells have different morphology and composition, the observation of the UV-VIS MAMW spectra of both samples and the comparison of the results provide an opportunity to confirm the simultaneous detection of particle shape and compositional changes.

In the laboratory, sickling can be induced by adding proper amount of Sodium meta Bisulfate (SMBS) to the blood sample. SMBS deoxygenates red blood cells. The addition of 1 to 2 drops of 2 % SMBS solution to one drop of blood enables the observation of sickle cells under the microscope.[11] On the first day of drawing sample, 100 μl of 2% SMBS solution was added to 100 μl blood to induce sickling. However, the microscope observation showed no sickle cells. Probably, a leak of air, which was remained on the top empty portion of sample tube, into the blood sample seemed to prevent deoxygenation. On the second day, more concentrated SMBS solution was added to blood samples and each sample tube was filled and sealed tightly to prevent air leakage. Dr. Debra Huffman at the College of Marine Sciences, University of South Florida confirmed that more than 80 ~ 90 % of sickling was induced in one sample.

UV-VIS MAMW spectra of the normal blood sample were measured on the first day and those of the normal and the sickled blood samples were taken on the second day. For UV-VIS MAMW measurements, both the normal and the sickled blood samples are diluted in the saline at the concentration of approximately 10^{-4}. Fig. 6.49.a shows the normalized intensity profile of saline and SMBS saline solution, respectively. The scope mode of OOIBase32 software was used for these measurements. SMBS is a strong absorber of UV light and results in the reduction of the incident light intensity at

wavelengths below 250 nm. However, above 250 nm, both reference solutions show the same features. Therefore, measured results are not affected by the optical property differences of reference solutions. This can also be confirmed in the expanded plot of Fig. 6.49.a, shown in Fig. 6.49.b that is plotted for the wavelength range from 500 nm to 600 nm where hemoglobin doublets are located. The measured results are plotted from 250 nm to avoid any artifacts due to differences in the optical properties of the suspending media.

6.4.2. Measured UV-VIS MAMW Spectra of Normal Whole Blood Sample

Fig. 6.50.a is MAMW response surface of pure red blood cells in saline measured with the prototype MAMW spectrometer[2] and Fig 6.51.a is its contour plot. Fig. 6.50.b is UV-VIS MAMW response surface of normal whole blood in saline taken by the Integrated UV-VIS MAMW spectrometer on the day of blood sample extraction and Fig 6.51.b is its contour plot.

Because red blood cells are the most numerous element in blood, their spectral features are similar to those of whole blood.[35] For Fig. 6.50.a and Fig. 6.51.a, only partial aspects of RBC spectra are shown. Especially, the major hemoglobin absorption band at 415 nm was truncated. On the other hand, Fig. 6.50.b and Fig. 6.51.b provide complete blood spectra from 250 nm to 800 nm. The absorption band at 260 nm ~280nm originates from DNA, RNA, and protein. Absorption bands at around 330 nm, 415 nm and doublet at around 570 nm are due to hemoglobin.[47]

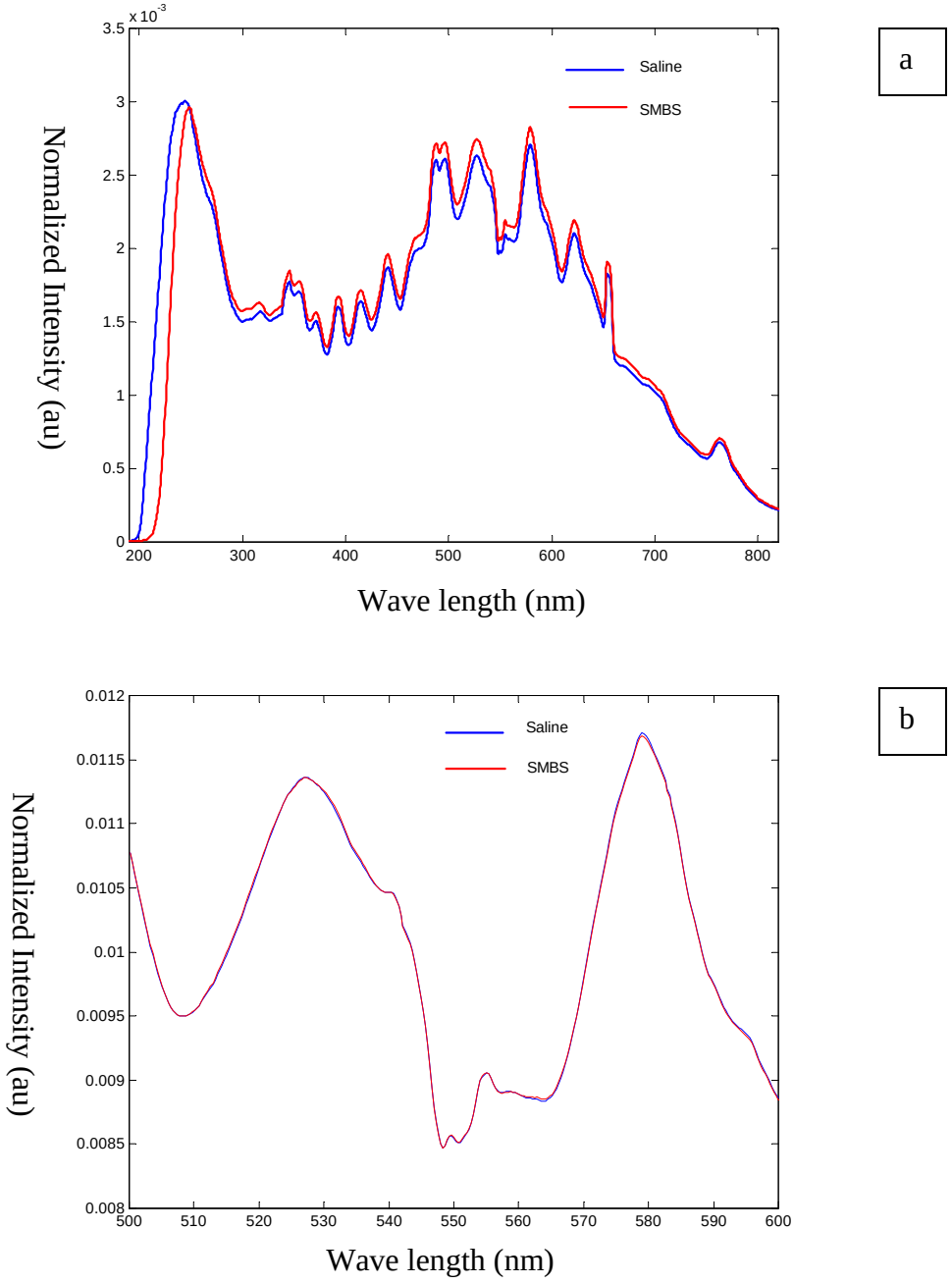

Figure 6.49. Normalized intensity profile of saline and SMBS dissolved saline solution. a) Plotted for the range of 190 nm to 820 nm. b) Expanded plot from 500nm to 600 nm where hemoglobin doublets are located. Note that the scope mode of OOIBase32 software was used for these measurements.

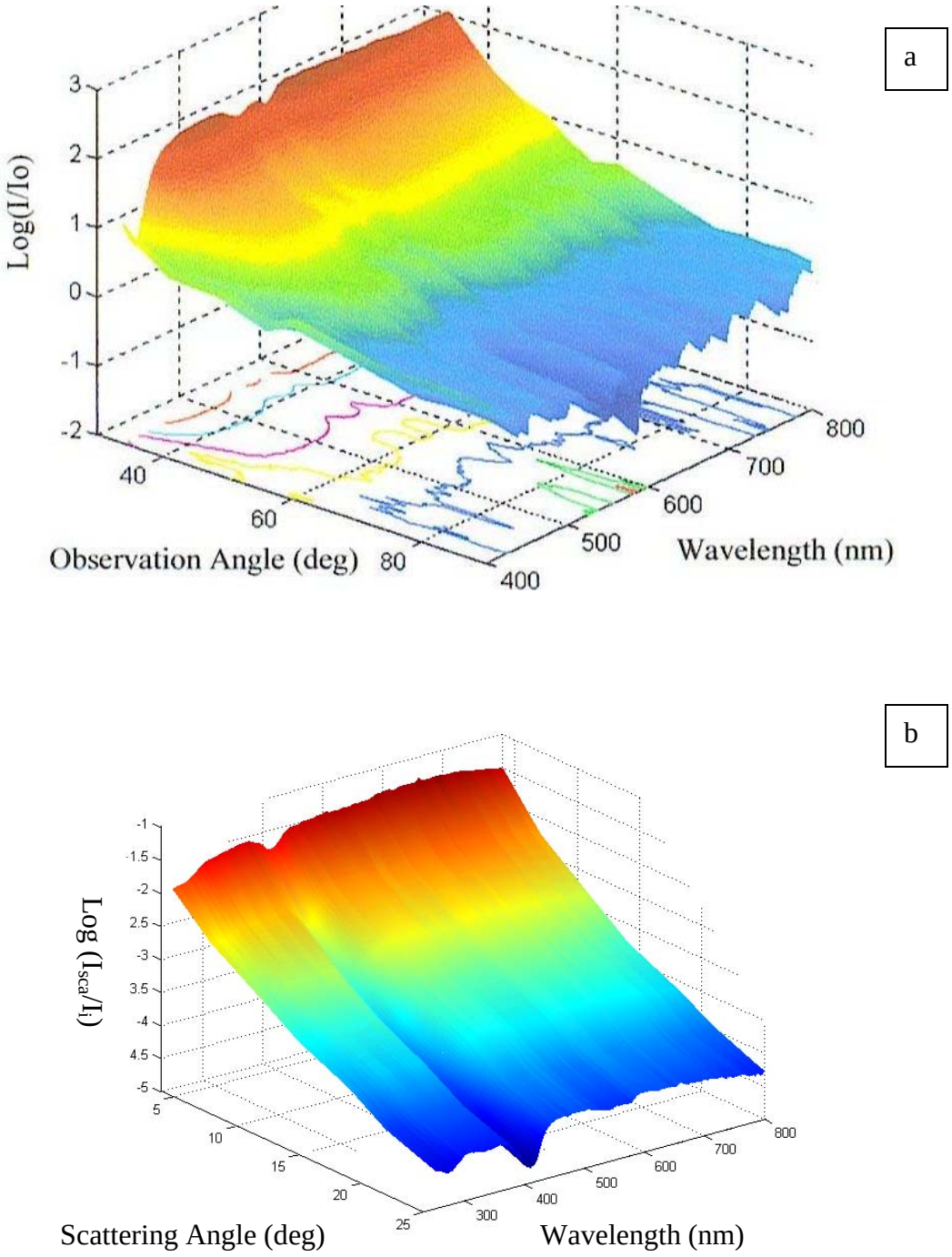

Figure 6.50. Measured MAMW response surfaces of blood samples. a) MAMW response surface of pure red blood cells in saline measured with the prototype MAMW spectrometer.[2] b) UV-VIS MAMW response surface of normal whole blood in saline measured on the day of blood sample extraction.

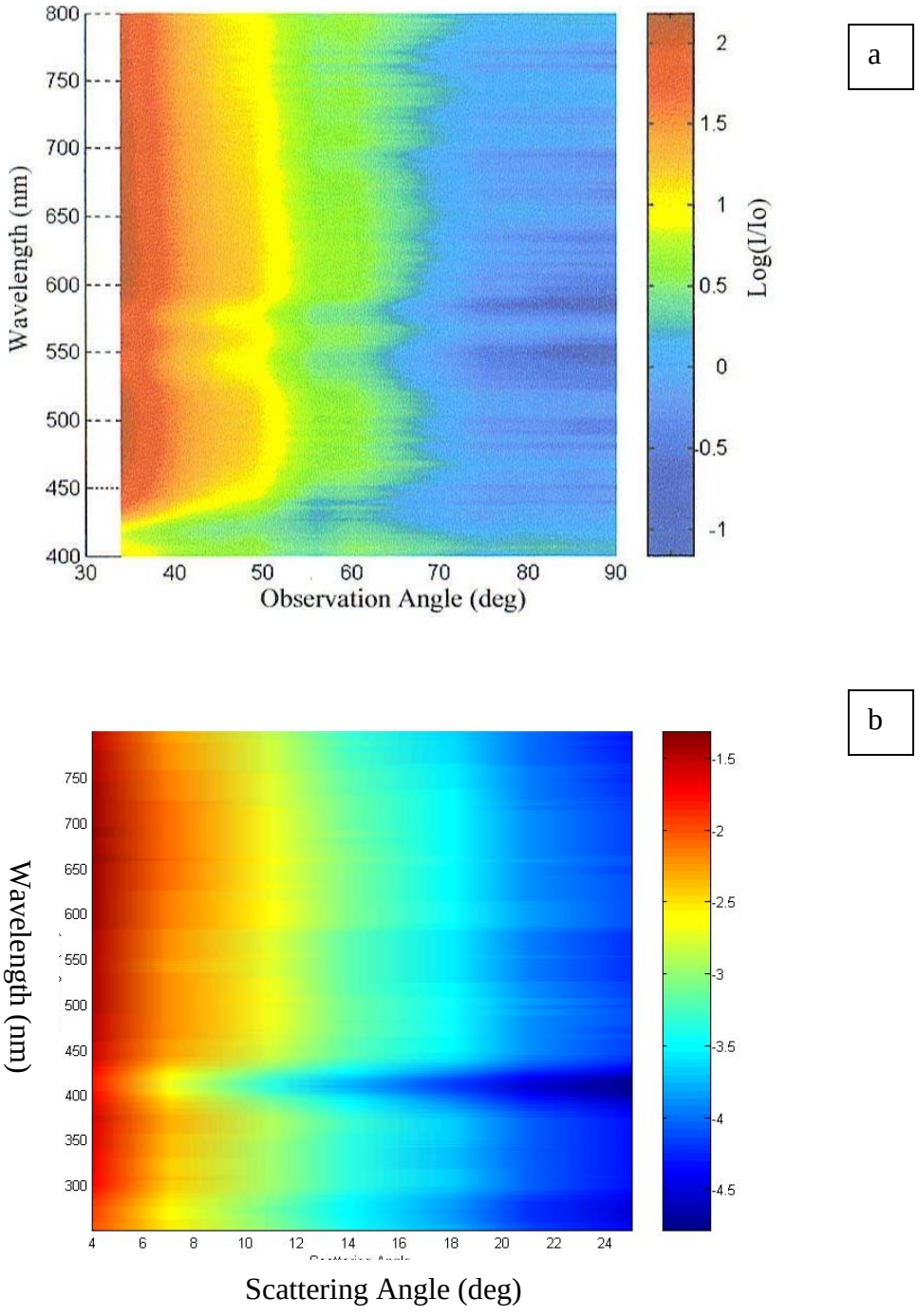

Figure 6.51. Contour plots of the measured MAMW response surfaces of blood sample. a) normal red blood (Fig 6.50.a).[2] b) normal whole blood in saline (Fig 6.50.b).

Therefore, it can be concluded that the incorporation of UV light into the MAMW spectrometer enhanced the capability of biological particle characterization by providing biologically important UV absorption or fluorescence spectra originating from biologically relevant chromophores (DNA, RNA, and proteins, etc).

6.4.3. Measured UV-VIS MAMW Spectra of Sickle Cells

Fig 6.52.a, Fig 6.53.a, and Fig 6.54.a represent the UV-VIS MAMW response surface of normal whole blood in saline measured with the Integrated UV-VIS MAMW spectrometer on the second day of blood sample extraction, the contour plot of Fig 6.52.a, and the wavelength-view plot of Fig 6.52.a, respectively. Fig 6.52.b, Fig 6.53.b, and Fig 6.54.b show the UV-VIS MAMW response surface of sickled blood in SMBS saline solution taken with the Integrated UV-VIS MAMW spectrometer on the second day of blood sample extraction, the contour plot of Fig 6.52.b, and the wavelength-view plot of Fig 6.52.b, respectively.

Compared to the normal blood response surface Fig. 6.52.a, the sickle cell response surface Fig. 6.52.b shows a round profile at low angles, widened log intensity ratio, reduced protein (280nm) and hemoglobin (415 nm) absorption band intensities, and the disappearance of hemoglobin doublets at around 570nm. This can also be confirmed from the corresponding contour plots of Fig. 6.53.a and Fig. 6.53.b or from the wavelength-view plots of Fig. 6.54.a and Fig. 6.54.b. Particularly, the wavelength-view plots provide a clear distinction of the spectral differences.

a

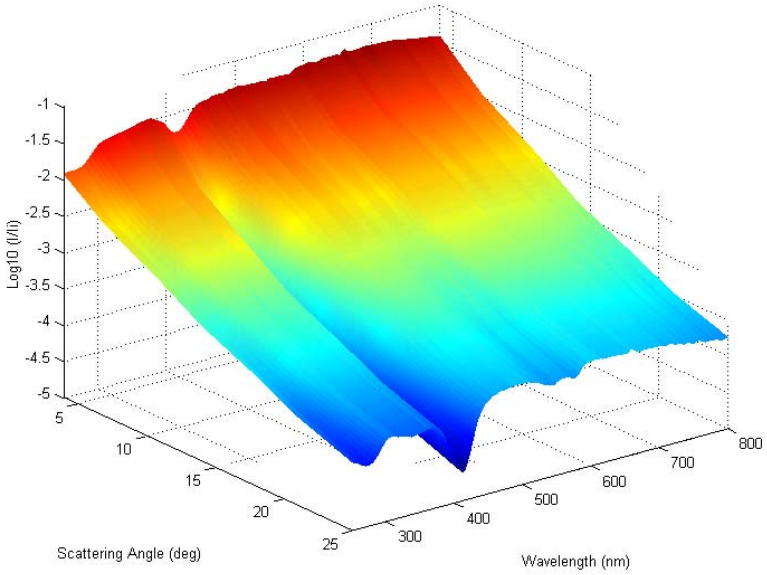

b

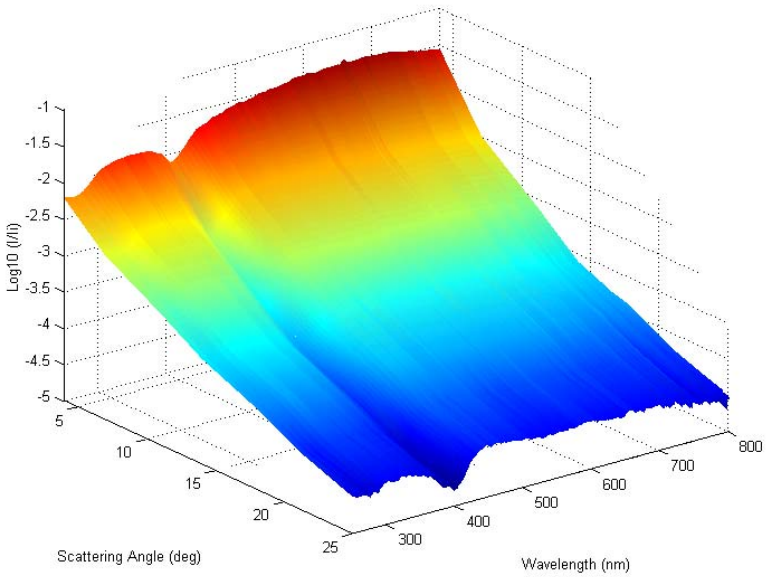

Figure. 6.52. UV-VIS MAMW response surface of normal and sickled blood samples. a) UV-VIS MAMW response surface of normal whole blood in saline measured on the second day of blood sample extraction. b) UV-VIS MAMW response surface of sickled blood in SMBS dissolved saline taken on the second day of blood sample extraction.

a

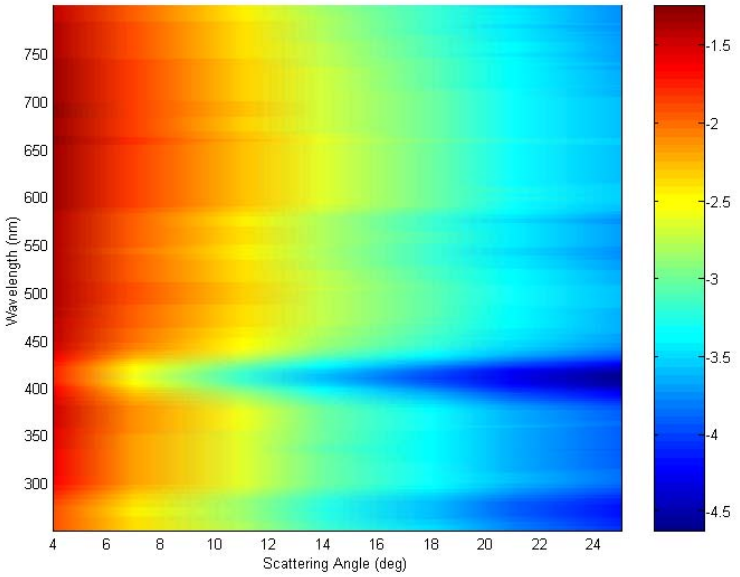

b

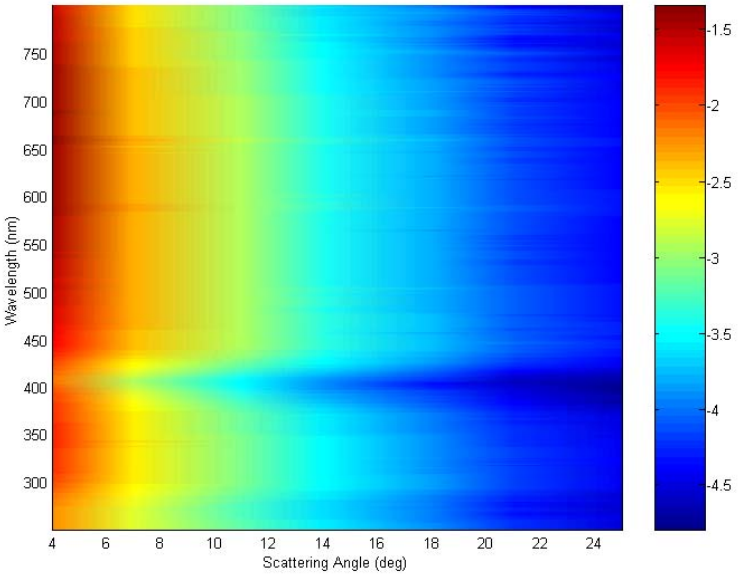

Figure 6.53. Contour plots of the UV-VIS MAMW response surface of blood sample. a) normal whole blood sample response surface (Fig 6.52.a). b) sickled blood sample response surface (Fig 6.52.b).

a

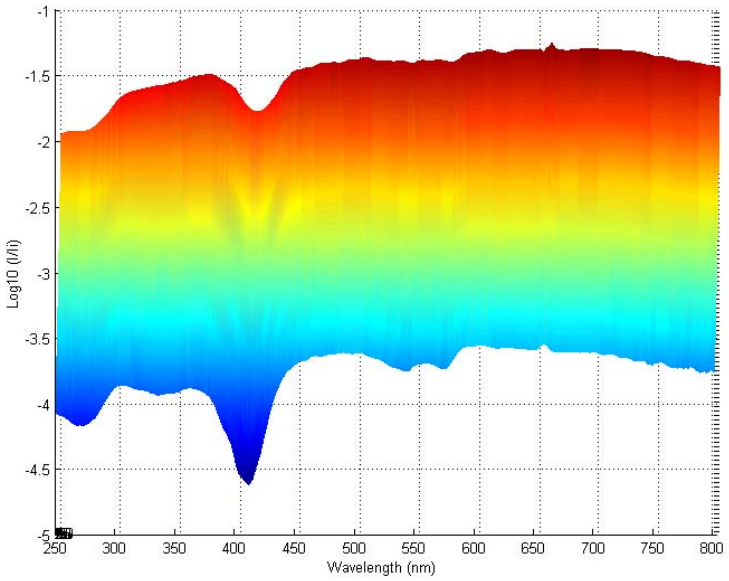

b

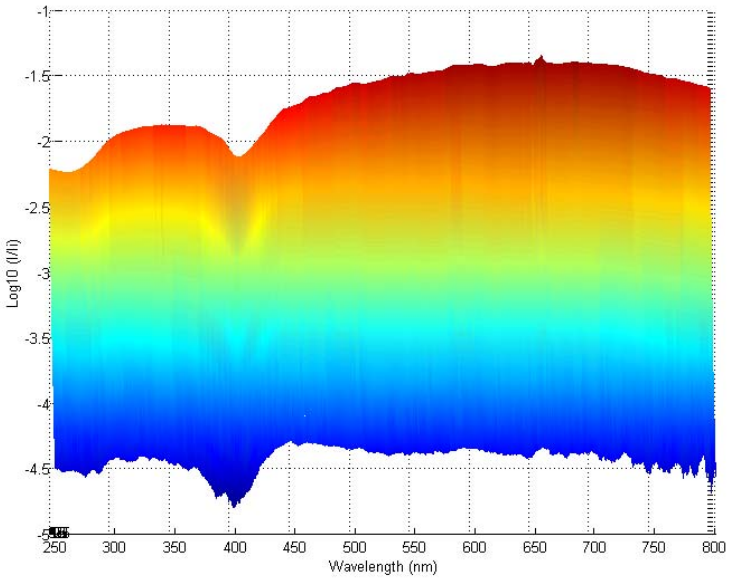

Figure 6.54. Wavelength-view plots of the UV-VIS MAMW response surface of blood sample. a) normal whole blood sample response surface (Fig 6.52.a). b) sickled blood sample response surface (Fig 6.52.b).

The round profile at low angle and the widened log intensity ratio of the sickled blood samples seem to be due to particle morphology changes from ellipsoid into holly-leaf or crest shape. The disappearance of the hemoglobin doublets at around 570 nm in the sickled blood sample can be attributed to the deoxygenation of hemoglobin.[47] Fig.6.55 shows the measured optical density spectra of oxy-hemoglobin, de-oxyhemoglobin and met-hemoglobin, respectively.[42] De-oxyhemoglobin has reduced oxygen and met-hemoglobin has no bound oxygen.[42] Sickled blood cell hemoglobin changes show the features of met-hemoglobin rather than de-oxyhemoglobin. In the wavelength-view plot of sickle cells, Fig. 6.54.b, hemoglobin doublets at around 570 nm totally disappeared and the hemoglobin absorption band at 415 nm is shifted toward shorter wavelength region compared to Fig. 6.54.a. However, in the case of met-hemoglobin, the absorption peak at 415 nm is enhanced while that of sickled blood samples is decreased. This implies that the mechanism of de-oxygenation in the hemoglobin of the sickled blood samples may not be the same as that of de-oxyhemoglobin or met-hemoglobin. Additional study to clarify the decrease of hemoglobin absorption band at 415 nm in sickled blood samples is recommended.

Comparison of the UV-VIS MAMW response surfaces of normal blood sample Fig. 6.50.b and Fig. 6.52.a shows the enhanced hemoglobin absorption band at 415 nm and hemoglobin doublets at around 570 nm in Fig. 6.52.a. This suggests that the sample was oxygenated further through storage.

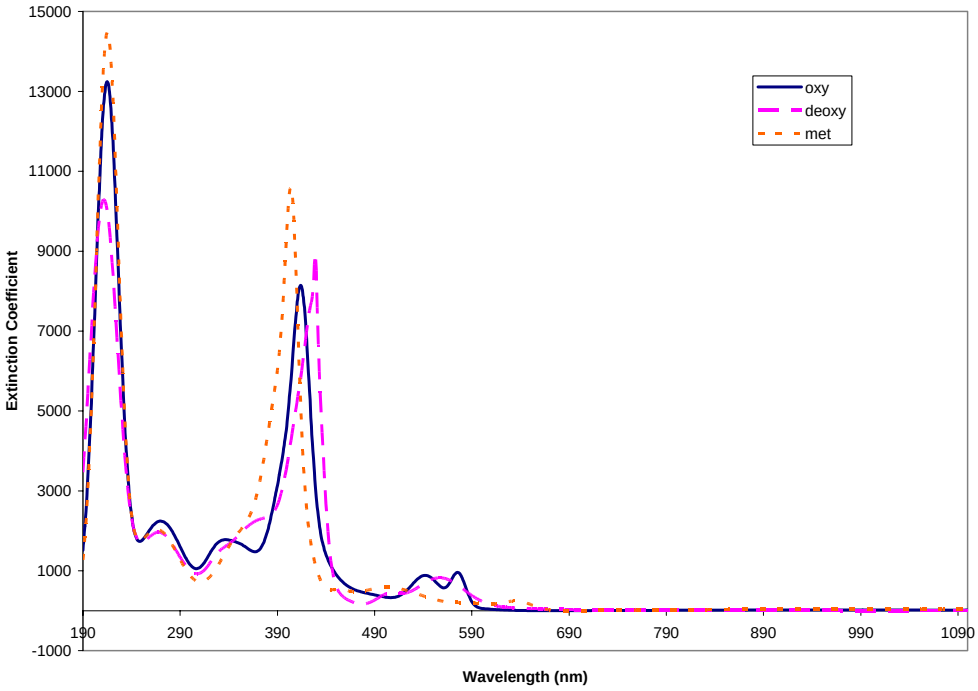

Figure.6.55. Measured optical density spectra of oxy-hemoglobin (oxy), de-oxyhemoglobin (deoxy) and met-hemoglobin (met).[42]

The UV-VIS MAMW spectra of normal blood in saline and sickled blood in SMBS saline solution were measured. The results show spectral differences due to RBC shape and compositional changes. This confirms the capability of the Integrated UV-VIS MAMW spectrometer to detect particle shape and compositional changes simultaneously. Potential applications in the area of biology and medicine are clearly important.

6.5. Discussion

The capability of the Integrated UV-VIS MAMW spectrometer to characterize micron and sub-micron size particles by the simultaneous detection of the JPPD, especially particle size, shape, and composition, has been proved by the measurement of UV-VIS MAMW spectra of different standards including polystyrene spheres with sizes from 20 nm to 10 μm, peanut-shaped particles, green fluorescent polystyrene spheres, normal whole blood sample, and sickled whole blood sample. As of Nov.14, 2004, INSPEC (physics reference search engine) search results show no report of particle size, shape, and composition information detection by single angular light scattering measurement. All the UV-VIS MAMW spectra measurement results show strong application possibilities in micron and sub-micron size industrial particle characterization, biological particle characterization including bacteria and viruses, medical diagnostics (reduce the number of unnecessary biopsies), nano-technology, etc. In addition, it can provide a tool to test the light scattering theories that predict particle shape and composition, a map to direct research direction (for example, UV laser light scattering for nano-particle study and NIR laser light scattering for large size particle characterization),

and a method of extracting information necessary for particle characterization (for instance, the derivation of the refractive indices of particles by comparing measured and simulated UV-VIS MAMW response surfaces). Moreover, transmission and frequency domain fluorescence spectra were able to be measured with the Integrated UV-VIS MAMW spectrometer. This opens the possibility of 3-dimensional MAMW spectroscopy (angular scattering, transmission, and fluorescence) for particle characterization with single instrument. In addition, the Integrated UV-VIS MAMW spectrometer is inexpensive to build and the governing technology is very simple. It can also be portable and thus, possible to use in the fields. Data measured in remote places can be transferred and interpreted in real time online. No significant problems hinder the commercial production of the Integrated UV-VIS MAMW spectrometer.

However, the research is just in the beginning stage considering the immense possibilities of the MAMW spectrometer. There is room to innovate the current Integrated UV-VIS MAMW spectrometer prototype and to develop new multidimensional MAMW spectrometers. Methods of upgrading the Integrated UV-VIS MAMW spectrometer as well as developing a new multi-dimensional MAMW spectrometer are discussed in the following section.

6.5.1. The Upgraded Integrated UV-VIS MAMW Spectrometer

The capabilities of the Integrated UV-VIS MAMW spectrometer can be upgraded by incorporating:

1. Strong light source,

2. UV-VIS achromatic lenses,
3. CCD detector with better sensitivity and grating efficiency,
4. Motorized goniometer rotation,
5. Polarization optics and
6. Modular optics.

The use of strong light source, UV-VIS achromatic lenses**,** and upgraded CCD detector will increase the overall sensitivity of the Integrated UV-VIS MAMW spectrometer drastically and widen the analyzable wavelength ranges. Computer-controlled motorized goniometer rotation will reduce measurement time and the adoption of polarization optics will amplify the dimension of the UV-VIS MAMW scattering from current 1- dimension to 16-dimension via the Mueller-matrix measurement. Modular optics will secure the optimum use of the Integrated UV-VIS MAMW spectrometer capabilities because it allows prompt change of optics while retaining the optical alignment. Currently, the UV-VIS MAMW spectra can display up to 6840 data points per sample, 570 wavelengths from 230 nm to 800 nm range with 1 nm resolution and 12 angles from 5^o to 60^o range with 5^o resolution. If this number is compared to the data points that can be typically obtained from a single wavelength scattering experiment for the measured angular range from 5^o to 170^o with 2^o resolution, the UV-VIS MAMW scattering yields about 80 times or more data points. However, if the listed upgrading is implemented, the UV-VIS MAMW spectra can display approximately 74,000 data points per sample (5^o to 170^o with 2^o resolution and 200 nm to 1100 nm with 1 nm resolution) for unpolarized incident

light and more than 1 million data points per sample with the use of polarization optics. Besides, modulation optics will allow the prompt measurement of transmission spectra including dichroism and fluorescence spectra including anisotropy. Consequently, the available information that will be obtained from the upgraded Integrated UV-VIS MAMW spectrometer will make this technology an ideal candidate for empirical particle characterization. Even nowadays, exact calculation of light scattering by particles with complicated shape or composition is virtually impossible. Therefore, for practical applications, especially for complicated biological particle characterization or medical diagnostics, methods of comparing the measured spectra to those stored in the spectral data base are actively sought. The upgraded UV-VIS MAMW integrated spectrometer is ideal methodology for this purpose because of its capacity to produce ample available information. Technologies that will be used for the construction of the upgraded UV-VIS MAMW integrated spectrometer are not far away. They already exist or will be available in the near future primarily due to drive for the commercial applications of optics products. Therefore, the construction of the upgraded Integrated UV-VIS MAMW spectrometer is not unrealistic.

6.5.2. Development of the Multidimensional MAMW Spectrometer

The Integrated UV-VIS MAMW spectrometer has been developed for the simultaneous detection of the JPPD of micron and sub-micron size particles. Single UV-VIS MAMW scattering measurement yields particle size, shape, and composition

information. However, it uses goniometer for the rotation of CCD detector and thus, true meaning of simultaneous detection of the JPPD is not accomplished. In addition, the capability of fluorescence and transmission spectra measurement was proven but these measurements were performed in serial due to the use of single CCD detector and the need to change the optics. Because of the temporal changes of particle characteristics, like settling or biological cell multiplication, simultaneous measurement of the JPPD is indispensable for particle characterization.

Ways to accomplish the simultaneous detection of the JPPD and to optimize the use of existing spectroscopic techniques are described in the concept of the multidimensional (MD) MAMW spectrometer. Unlike the upgraded Integrated UV-VIS MAMW spectrometer, the MD MAMW spectrometer will employ technologies of the future. Consequently, the description is more conceptual than specific.

Fig. 6.56 shows a schematic of the proposed MD MAMW spectrometer. It consists of a light source, a sample cell, a transmission and diffraction detector, a fluorescence detector, and multiple numbers of multiangle (MA) scattering detectors. The details of the instrumentation will be determined based on the available state of the art technology at the time of construction. To be a multidimensional spectrometer, the MD MAMW spectrometer will be able to measure the following features simultaneously:

1. Clockwise and counter-clockwise multiangle scattering-multiple number of detectors will be installed. Each detection optics will have the capability of performing the measurement of the 16-element Mueller matrix.

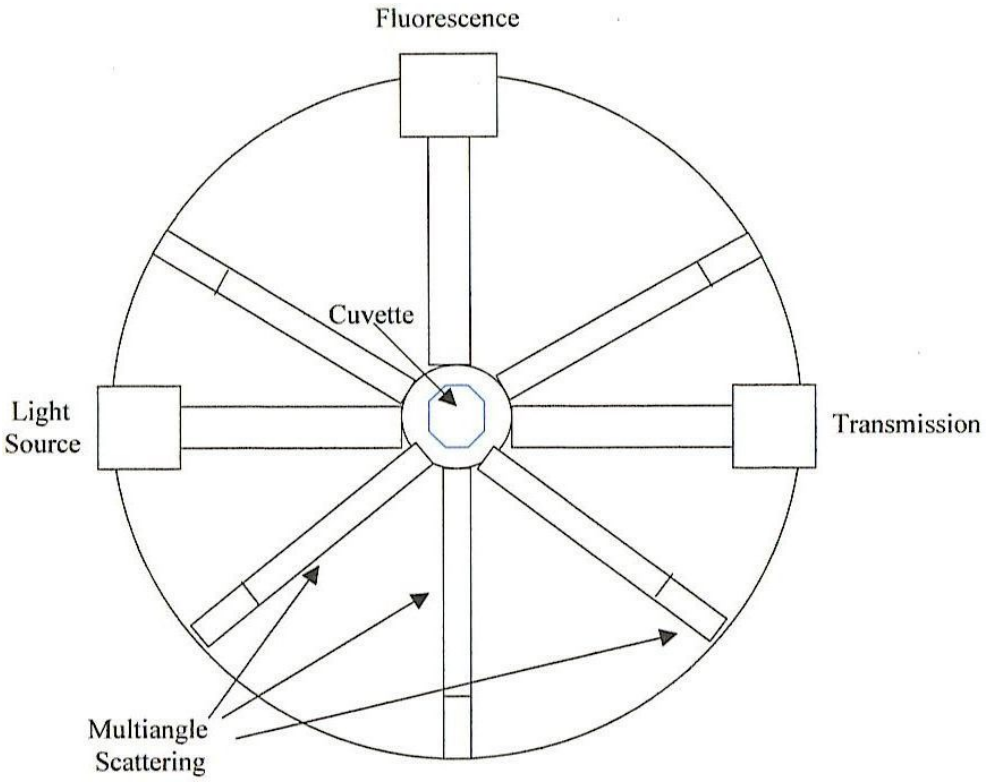

Figure 6.56. Schematic of a proposed MD MAMW spectrometer.

2. Forward scattering and/or diffraction,
3. Backscattering,
4. Transmission including dichroism and
5. Fluorescence including anisotropy.

The MD MAMW spectrometer will employ both multiwavelength light source and laser depending on applications. In addition, it will also perform the time-domain spectroscopy. Lastly, proper fields (electric, magnetic) will be applied to the sample cell to enhance the characterization capabilities. Once the MD MAMW spectrometer is developed, the limitation of its application will be determined by our imagination alone.

CHAPTER 7. CONCLUSIONS

This chapter describes the summary of the research, list of contributions and recommended work. The description of the instruments, which are required for the upgrading of the Integrated UV-VIS MAMW spectrometer and described in Section 6.5.1, is recapitulated in the section related to the recommended work.

7.1. Summary of Research

The Integrated UV-VIS MAMWspectrometer has been developed to overcome the drawbacks of the prototype MAMW spectrometer and enhance the JPPD detection capabilities. The development of the Integrated UV-VIS MAMW spectrometer becomes possible through the use of fused silica UV lenses and integration time multiplexing (ITM).

The adoption of UV lenses allows the use of a broadband UV light source, intensifies the incident light to the sample cell, and together with the use of narrow width slits and ITM, enhances the low-angle scattering capabilities. The incorporation of ITM avoids detector saturation within the linearity of the CCD detector. By overcoming the limitations of the prototype MAMW spectrometer, measurements of fluorescence, transmission, and low-angle scattered light become possible. The Integrated UV-VIS

MAMW spectrometer can perform angular scattering measurements starting at 4^{o} with the simultaneous detection of multiwavelength light from 200 nm to 820 nm, UV-VIS transmission spectroscopy with wavelengths for analysis ranging from 200 nm to 820 nm, and frequency domain UV-VIS fluorescence spectroscopy.

After the development of the current prototype Integrated UV-VIS MAMW spectrometer, possible sources of error were analyzed to ensure the reproducibility of the results. In addition, data correction and calibration procedures have been established to ensure the credibility of the experimental results. Refraction correction, scattering volume correction, and data normalization are the necessary correction factors for the quantitative analysis of the Integrated UV-VIS MAMW spectrometer results.

The capabilities of the Integrated UV-VIS MAMW spectrometer were tested by measuring: the optical density, UV-VIS MAMW spectra, and the fluorescence spectra of polystyrene standards. The measured optical density spectra show features of interference, reddening, ripple structures, and diffraction**,** as well as absorption due to electronic transitions. The results were validated by comparing to measured spectra recorded with a reference spectrometer (HP 8453 diode array spectrometer). The measured UV-VIS MAMW spectra proved that the JPPD can provide spectroscopic fingerprints of particles. The use of a broadband UV light source enabled the measurement of polystyrene standards as small as 20 nm**,** and the incorporation of low-angle scattering measurements made it possible to distinguish polystyrene 8 μm spheres and polystyrene 10 μm spheres clearly. The possibility of the Integrated UV-VIS MAMW spectrometer to infer spherical particles and non-spherical particles from the

measured UV-VIS MAMW spectra was tested using 1.85 μm peanut-shaped polystyrene latex and 1.87 μm polystyrene sphere particles. The resulting response surfaces showed a clear distinction in the UV region. Differences in the absorption of UV light and destructive interference due to differences in the beam path length resulting from particle orientation appear to manifest in differences in the measured spectra. This demonstrated the feasibility of the Integrated UV-VIS MAMW spectrometer to infer particle shape. Methods to measure the Mueller matrix and backscattering have been described to improve the identification of particle shape and orientation. The capabilities of the Integrated UV-VIS MAMW spectrometer to measure particle composition were tested by measuring the UV-VIS MAMW spectra of polystyrene 3.0 μm spheres and green fluorescent polystyrene 3.0 μm spheres. The resulting UV-VIS MAMW spectra show differences due to particle composition. A single UV-VIS MAMW scattering measurement provides information on the particle size and composition simultaneously. Fluorescence spectra of green fluorescent polystyrene 3 μm spheres were measured. The measured spectra have the features shown in the manufacturer-provided data.

As an application to biological particle systems, the UV-VIS MAMW spectra of normal whole blood sample and sickled whole blood sample were measured. The resulting spectra showed spectral changes in the low angle region, probably due to changes in the morphology of the RBC's, the blueshift of hemoglobin absorption band at 415 nm, the reduction of protein and hemoglobin absorption bands**,** and the disappearance of the hemoglobin doublet at around 570 nm in the sickled blood sample.

These clearly demonstrated that particle shape and compositional changes can be detected simultaneously with the Integrated UV-VIS MAMW spectrometer.

Ways of upgrading the Integrated UV-VIS MAMW spectrometer and developing a new multidimensional MAMW spectrometer concept are provided to enhance the particle characterization capabilities. The upgrade of the Integrated UV-VIS MAMW spectrometer is based on the currently available technologies while the development of a new multidimensional MAMW spectrometer implies the incorporation of future technologies. The upgraded Integrated UV-VIS MAMW spectrometer will generate more than one million data points per sample per measurement.

In conclusion, the simultaneous measurement of the JPPD, particularly, size, shape, and composition using the Integrated UV-VIS MAMW spectrometer has a bright prospect for the characterization of micron and sub-micron size particles. It has potential applications in the areas of industrial particle characterization, biological particle characterization, medical diagnostics, nano-technology, etc. The possibility of readily upgrading the current Integrated UV-VIS MAMW spectrometer and the new MD MAMW spectrometer make this prospect even brighter.

7.2. Contributions

The contributions of this dissertation research include

1. Development of the Integrated UV-VIS MAMW spectrometer that can perform static light scattering, transmission, and frequency domain fluorescence spectroscopy using single light source and single detector only.

2. Development of data correction procedures for the Integrated UV-VIS MAMW spectrometer.
3. Improved performance of the UV-VIS MAMW scattering experiments with starting wavelength from 200 nm and starting angle from 4^{o}.
4. Improved performance of the UV-VIS transmission spectroscopy.
5. Improved performance of the frequency domain fluorescence spectroscopy.
6. The JPPD measurements of polystyrene standards.
7. Inference of particle shape by light scattering.
8. Observation of particle composition by light scattering.
9. Measurement of the UV-VIS MAMW spectra of normal whole blood sample and sickled whole blood sample.
10. Demonstrated that changes in particle shape and composition can be detected simultaneously.
11. Suggestions: how to measure the Mueller matrix and backscattering.
12. Suggestions: how to upgrade the Integrated UV-VIS MAMW spectrometer.
13. Suggestions: concept of a new multidimensional MAMW spectrometer.
14. Recommendations: how to build the Integrated UV-VIS MAMW spectrophotometer.
15. Recommendations: use multiwavelength UV-VIS light spectroscopy for micron and sub-micron size particle characterization.

7.3. Recommendations for Future Work

To improve the capabilities of and/or to extend the application areas of the Integrated UV-VIS MAMW spectrometer, the following theoretical, instrumental, and experimental studies are recommended.

1. **Recommendations for theoretical work:**
    a. Develop a simulation program that can provide results consistent with measured data, especially for sub-micron size particles, are necessary for the establishment of quantitative calibration and validation procedures.
    b. Use the T-Matrix approach to develop a generalized particle shape characterization software.
    c. Statistical validation of the measured multidimensional spectra using the above programs is recommended. By comparing the measured and the simulated results at all the angles and the wavelengths, it will improve the sensitivity and specificity of the characterization results.
    d. Investigation of light scattering theory that can yield better interpretation of experimental results, especially related to particle shape and compositional changes, is recommended.

2. Recommendations for hardware implementations:

a. Computer controlled rotation of the goniometer arm is recommended.

b. Ensuring the mechanical stability of the optical bench is strongly recommended. Currently, the optical components are installed on the mini optical rails and reproducible precision alignment requires considerable amount of time and effort.

c. Modular design of optics is recommended, so that, depending on experiment, proper optics can be substituted and/or added without the loss of alignment and reproducibility.

d. Use of achromatic lenses that can cover a broad UV-VIS wavelength range is recommended. The use of achromatic lens may enhance the intensity of the detected light more than 10 times. In addition, the quality of the optics alignment can be improved by using achromatic lenses.

e. Use of stronger light source with long lifetime is recommended. Current tungsten-halogen bulb power is only 6.5 W. Hence, it does not provide adequate light intensities for measurement of the scattered light at large angles. The lifetime of the bulb is less than 80 hrs. Therefore, the bulb has to be changed at 80 hours and this may be a potential to lose optics alignment.

f. Upgrading of the CCD detector grating is recommended. Current grating covers UV-VIS region only. By employing a grating that can be used from

UV to NIR, large particle characterization capability of the Integrated UV-VIS MAMW spectrometer can be enhanced further.

g. Improvement of the CCD detector sensitivity is recommended. The current detector has sensitivity of 12 bits only. The use of 16-bit detector will enlarge measurable scattering angle and reduce overall measurement time.

h. Installation of polarization optics is recommended. This will enable the measurement of the Mueller matrix, dichroism, and fluorescence anisotropy simultaneously.

3. Recommended experiments:

Measurement of the UV-VIS MAMW spectra of several synthetics and biological particles that can further demonstrate the potential of this technology for particle characterization is recommended. For the systems discussed below the sample preparation and measurement protocols have to be developed.

a. Measurement of the JPPD of microorganisms is recommended. Some microorganisms have similar sizes and compositions; as a result their characterization through extinction or fluorescence measurements alone may not be sufficient. Comparative studies using the UV-VIS MAMW spectrometer are desirable.

b. Measurements of the UV-VIS MAMW spectra of polystyrene spheres larger than 10 μm are recommended.

c. Measurement of the UV-VIS MAMW spectra of TiO_2 samples are recommended to obtain the information pertinent to particle shape changes.

d. Fluorescence measurements using various samples are recommended.

REFERENCES

1. C. E. Alupoaei. Modeling of the Transmission Spectra of Microorganisms. M.S. Thesis, University of South Florida, Tampa, FL, December 2001.

2. C. P. Bacon. Simultaneous Characterization of Particle Properties (Size, Shape, and Composition) from the Development of the Multiangle-Multiwavelength Spectrometer System. Ph.D. Thesis, University of South Florida, Tampa, FL, August 1999.

3. C. Bacon and L. H. Garcia-Rubio, "Multiangle-Multiwavelength detection for particle characterization," *Particle Size Distribution III: Assessment and Characterization,* T. Provder, Ed., ACS Symposium Series **693**, 30-38 (American Chemical Society, Washington DC, 1998).

4. W. S. Bickel and W. M. Bailey, "Stokes vectors, Mueller matrices, and polarized light scattering," *Am. J. Phys.* **53**, 468-478 (1985).

5. W. S. Bickel, J. F. Davidson, D. R. Huffman, and R. Kilkson, "Application of polarization effects in light scattering: A new biophysical tool," *Proc. Nat. Acad. Sci. USA* **73**, 486-490 (1976).

6. W. S. Bickel and M. E. Stafford, "Biological particles as irregularly shaped scatterers," *Light Scattering by Irregularly Shaped Particles,* D. W. Schuerman, Ed., 299-305 (Plenum Press, New York, NY, 1980).

7. C. F. Bohren and D. R. Huffman, *Absorption and Scattering of Light by Small Particles* (John Wiley & Sons, New York, NY, 1983).

8. B. A. Brice, M. Halwer, and R. Speiser, "Photoelectric light-scattering photometer for determining high molecular weights," *Journal of the Optical Society of America* **40**, 768-778 (1950).

9. F. V. Bright, "Modern molecular fluorescence spectroscopy," *Focus on Analytical Spectrometry: A Compendium of Applied Spectroscopy Focal Point Articles (1994-1997)*, J. A. Holcombe, G. M. Hieftje, and V. Majidi, Ed., 104-109 (Society for Applied Spectroscopy, Frederick, MD, 1998).

10. Coulter Corporation, "Particle Characterization LS Short Course Note" (1997).

11. G. A. Daland and W. B. Castle, "A simple and rapid method for demonstrating sickling of the red blood cells: the use of reducing agents," *J. Lab. Clin. Med.* **33**, 1082-1088 (1948).

12. N. Damaschke, G. Gouesbet, G. Grehan and C Tropea, “Optical techniques for the characterization of non-spherical and non-homogeneous particles,” *Meas. Sci. Technol*, **9**, 137-140 (1998).

13. http://www.dukescientific.com.

14. C.E. Dungey and C.F. Bohren, “Light scattering by nonspherical particles: a refinement to the coupled-dipole method,” *Journal of the Optical Society of America A*. **8,** 81-87 (1991).

15. G. E. Elicabe and L. H. Garcia-Rubio, “Latex particle size distribution from turbidimetry using inversion techniques,” *J. Coll. Int. Sci.* **129**, 192-200 (1989).

16. G. E. Elicabe and L. H. Garcia-Rubio, “Latex particle size distribution from turbidimetric measurements,” *Adv. Chem. Ser.* **227**, 83-104 (1990).

17. X. Fu, Detection and Identification of Microorganisms using a combined Flow Field-Flow Fractionation Spectroscopy. Ph.D. Thesis, University of South Florida, Tampa, FL, October 2003.

18. L. H. Garcia-Rubio, “The effect of molecular size on the absorption spectra of macromolecules,” *Macromolecules* **20**, 3070-3075 (1987).

19. L. H. Garcia-Rubio at University of South Florida, Private Communication.

20. P. C. Gray, I. R. Shokair, S. E. Rosenthal, G. C. Tisone, J. S. Wagner, L. D. Rigdon, G. R. Siragusa, and R. J. Heinen, “Distinguishability of biological material by use of ultraviolet multispectral fluorescence,” *Appl. Opt.* **37,** 6037-6041 (1998).

21. J. M. Greenberg, “Focusing in on particle shape,” *Light Scattering by Irregularly Shaped Particles*, D. W. Schuerman, Ed., 7-24 (Plenum Press, New York, NY, 1980).

22. R. O. Gumprecht and C. M. Sliepcevich, “Scattering of light by large spherical particles,” J. Phys. Chem. **57**, 90-95 (1953).

23. F. S. Harris, G. C. Sherman, and F. L. Morse, “Experimental comparison of scattering of coherent and incoherent light,” *IEEE Transactions on Antennas and Propagation* **AP-15**, 141-147 (1967).

24. L. Hespel, A. Delfour, and B. Guillame, “Mie light-scattering granulometer with an adaptive numerical filtering method. II. Experiments,” *Appl. Opt.* **40**, 974-985 (2001).

25. A. H. Hielscher, A. A. Eick, J. R. Mourant, D. Shen, J. P. Freyer, and I. J. Bigio, "Diffuse backscattering Mueller matrices of highly scattering media," *Opt. Express.* **1**, 441-453 (1997).

26. T. Inagaki, E. T. Arakawa, R. N. Hamm, and M. W. Williams, "Optical properties of polystyrene from the near-infrared to the x-ray region and convergence of optical sum rules," *Phy. Rev. B* **15**, 3243-3253 (1977).

27. J. D. Jackson, *Classical Electrodynamics*, 2nd ed., Chapter 7 (John Wiley & Sons, New York, NY, 1975).

28. B. R. Jennings and H. Plummer, "Light-scattering photometer calibration," *Brit. J. Appl. Phys. (J. Phys. D)* **1**, 1201-1209 (1968).

29. H. Jiang, J. Pierce, J. Kao, and E. Sevick-muraca, "Measurement of particle-size distribution and volume fraction in concentrated suspensions with photon migration techniques," *Appl. Opt.* **36**, 3310-3318 (1997).

30. A. R. Jones, "Light scattering for particle characterization," *Progress in Energy and Combustion Science* **25**, 1-53 (1999).

31. M. Kerker, *The Scattering of Light and Other Electromagnetic Radiation* (Academic Press, New York, NY, 1969).

32. J. R. Lakowicz, *Principles of Fluorescence Spectroscopy*, 2nd ed. (Kluwer Academic / Plenum Publishers, New York, NY, 1999).

33. P. Latimer and P. Barber, "Scattering by ellipsoids of revolution. A comparison of theoretical methods," *J. Coll. Int. Sci.* **63**, 310-316 (1978).

34. The Mathworks Inc., "MATLAB 5.3." (1999).

35. Y. D. Mattley. An Investigation of the Spectroscopic Properties of Platelets During Activation and Storage: Implementation of a New Interpretation Model. Ph.D. Thesis, University of South Florida, Tampa, FL, December 2000.

36. M. P. Menguc and S. Manickavasagam, "Characterization of size and structure of agglomerates and inhomogeneous particles via polarized light," *International J. of Engineering Science.* **36,** 1569-1593 (1998).

37. Microsoft Corporation, "Microsoft ® Encarta ® Encyclopedia 2002" (2002).

38. M. I. Mishchenko, “Light scattering by size-shape distributions of randomly oriented axially symmetric particles of a size comparable to a wavelength,” *Appl. Opt.* **32,** 4652-4666 (1993).

39. Newport Corporation, “The Newport Resource 2003” (2003).

40. http://www.newrise-llc.com/fused-silica.html.

41. A. Nonoyama. Using multiwavelength UV-visible spectroscopy for the characterization of red blood cells: An investigation of hypochromism. Ph.D. Thesis, University of South Florida, Tampa, FL, November 2004.

42. A. Nonoyama at University of South Florida, Private Communication.

43. Ocean Optics, Inc., “2002 Product Catalog” (2002).

44. *Biomedical Topical Meetings*, OSA Technical Digest (Optical Society of America, Washington DC, 2000).

45. F. L. Pedrotti and L. S. Pedrotti, *Introduction to Optics*, Chapter 27 (Prentice-Hall International, Englewood Cliffs, NJ, 1993).

46. http://www. Photocor.com.

47. *UV Atlas of Organic Compounds, Volume II.* (Plenum Press, New York, NY, 1966).

48. Polysciences Inc., Private Communication.

49. A. Quirantes, “Light scattering properties of spheroidal coated random orientation,” *J. Quant. Spectrosc. Radiat. Transfer***. 63,** 263-275 (1999).

50. B.E.A. Salek and M.C. Teich, *Fundamentals of Photonics* (John Wiley & Sons, New York, NY, 1991).

51. H. Schnablegger and O. Glatter, “Sizing of colloidal particles with light scattering: corrections for beginning multiple scattering,” *Applied Optics* **34**, 3489-3501 (1995).

52. P. R. Smith, O. Kusmartseva, and R. Naimimohasses, “Evidence for particle-shape sensitivity in the correlation between polarization states of light scattering,” *Opt. Lett.* **26**, 1289-1291 (2001).

53. K. A. Stacey, *Light Scattering in Physical Chemistry*, Chapter 3 (Butterworths Scientific Publications, London, 1956).

54. Starna Cells Inc., Private Communication.

55. G. L. Stephens, "Scattering of plane waves by soft obstacles: anomalous diffraction theory for circular cylinders," *Appl. Opt.* **23**, 954-959 (1984).

56. http://www.thermo-oriel.com.

57. Y. Tomimatsu and K. J. Palmer, "Reflection corrections for light-scattering measurements for various cells with the Brice-type photometer," *J. Phys. Chem.* **67**, 1720-1722 (1963).

58. H. Utiyama, "Light scattering instruments," *Light Scattering From Polymer Solutions*, M. B. Huglin, Ed., 41-60 (Academic Press, London, 1972).

59. H. Utiyama, "Calibration and correction factors," *Light Scattering From Polymer Solutions*, M. B. Huglin, Ed., 61-88 (Academic Press, London, 1972).

60. H. C. van de Hulst, *Light Scattering by Small Particles* (Dover, New York, NY, 1981).

61. P. Walstra, "Discussion of errors in turbidimetry," *Brit. J. Appl. Phys.* **16**, 1187-1192 (1965).

62. R. Walters, "2000 Series OEM GUIDE," Ocean Optics, Inc. (2000).

63. R. Walters at Ocean Optics, Inc., Private Communication.

64. J. Wang and F. R. Hallett, "Spherical particle size determination by analytical inversion of the UV-visible-NIR extinction spectrum," *Appl. Opt.* **35**, 193-197 (1996).

65. L. S. Wright, A. Chowdhury, and P. Russo, "Static light scattering instrument for rapid and time-resolved particle sizing in polymer and colloid solutions," *Rev. Sci. Instrum.* **67**, 3645-3648 (1996).

66. P. J. Wyatt, "Review: Light scattering and the absolute characterization of macromolecules," *Analytica Chimica Acta* **272**, 1-40 (1993).

67. R. Xu, “Particle size distribution analysis using light scattering,” *Liquid and Surface-Borne Particle Measurement Handbook,* J. Z. Knapp, T. A. Barber, and A. Lieberman, Ed., 745-777 (Marcel Dekker, New York, NY, 1996).

68. E. Zurek at University of South Florida, Private Communication.

APPENDICES

APPENDIX A: MATLAB Program for UV-VIS MAMW Spectra Plot of the Measured Results

```
% UV-VIS MAMW
% Yong-Rae Kim
% The following program performs UV-VIS MAMW spectra plots

clear;
clc;


% Load data files for sample
% Sample v case
% up - incident beam spectrum, ur - reference beam spectrum
% vs- sample spectrum measured at 0^o, va- OD spectrum
% vr – reference scattering, vs- sample scattering

 load up.txt;load ur.txt;
 load va.txt;load vs.txt;
 load vr05.txt;load vr10.txt;load vr15.txt;load vr20.txt;
 load vr25.txt;load vr30.txt;load vr35.txt;
 load vs05.txt;load vs10.txt;load vs15.txt;load vs20.txt;
 load vs25.txt;load vs30.txt;load vs35.txt;


% Use the wavelength interval that is designated by S2000 production spectrometer.

 wavelength = up(:,1);


% Define the wavelength interval for plot.

 ind1 = (wavelength>=230) & (wavelength<=800);
 x = wavelength(ind1);


 % Use refraction corrected angles as scattering angles.

y = [4;7;11;14;18;21;25];
```

APPENDIX A: (Continued)

```
% Define the normalization standard file

 ur = ur(ind1,2);
 rm = ur;


% Define reference scattering files

 vr05 = vr05(ind1,2); vr10 = vr10(ind1,2); vr15 = vr15(ind1,2);
 vr20 = vr20(ind1,2); vr25 = vr25(ind1,2); vr30 = vr30(ind1,2);
 vr35 = vr35(ind1,2);

 kr05 = vr05; kr10 = vr10; kr15 = vr15;
 kr20 = vr20; kr25 = vr25; kr30 = vr30;
 kr35 = vr35;


% Define sample scattering files

 vs05 = vs05(ind1,2); vs10 = vs10(ind1,2); vs15 = vs15(ind1,2);
 vs20 = vs20(ind1,2); vs25 = vs25(ind1,2); vs30 = vs30(ind1,2);
 vs35 = vs35(ind1,2);

 ks05 = vs05; ks10 = vs10; ks15 = vs15;
 ks20 = vs20; ks25 = vs25; ks30 = vs30;
 ks35 = vs35;


% Define the UV-VIS MAMW scattering intensities

  s5 = ks05 - kr05; s10 = ks10 - kr10; s15 = ks15 - kr15;
  s20 = ks20 - kr20; s25 = ks25 - kr25; s30 = ks30 - kr30;
  s35 = ks35 - kr35;


% Multiply volume correction factors
% 3mm width slit case

  s5 = (1.0).*s5; s10 = (1.08).*s10; s15 = (1.12).*s15;
  s20 = (1.17).*s20; s25 = (1.24).*s25; s30 = (1.40).*s30;
  s35 = (1.51).*s35;
```

APPENDIX A: (Continued)

```
 % Multiply integration time ratio
 % The ratio shown here is example of sample v case. Each sample has its own ratio.

  rm = (5000/8).*rm ;
  s5 = 2.*s5 ; s10 =2.*s10;
  s15 = 2.*s15 ;s20 = 2.*s20 ; s25 = 1.*s25 ;
  s30 = 1.*s30 ; s35 = 1.*s35 ;


% Normalize the scattering intensity with the reference beam spectrum rm
% Check matrix dimension

  sm = [s5'./rm';s10'./rm';s15'./rm';s20'./rm';
          s25'./rm';s30'./rm'; s35'./rm'];

% UV-VIS MAMW response surface plot

  [x_grid, y_grid] = meshgrid(x,y);
  z=log10(sm);
  surf(x_grid, y_grid, z);
  xlabel('Wavelength (nm)'), ylabel('Observation Angle (deg)');
  zlabel('Intensity -  log10 (I/Ii)');

% To make smooth plot, use interpolation

 shading interp;


% Contour plot of the UV-VIS MAMW response surface

  contour(y_grid, x_grid, z);
  pcolor(y_grid, x_grid, z);
  xlabel('Wavelength (nm)'), ylabel('Observation Angle (deg)');
  shading interp;
  colorbar;
```

APPENDIX B: Method of Correcting the Measured UV-VIS MAMW Spectra for the Continuously Varying Refractive Indices of Spectrosil® Quartz

The refractive indices of Spectrosil® quartz for the whole wavelength range of the incident light can be derived using a polynomial that can fit the known refractive indices of Spectrosil® quartz at selected wavelengths. MATLAB or other mathematical software can be used to find this polynomial. Once the sought-for polynomial is acquired, the refractive indices of Spectrosil®quartz at any wavelengths can be calculated using this polynomial.

Spectrosil® quartz is a kind of synthetic fused silica. As a result, the refractive indices of fused silica can be used to figure out the sought-for polynomial. Table B.1 lists the known refractive indices of fused silica.[40] DATDEMO nonlinear data fitting code of the MATLAB version 5.3 was used to process this information to acquire the sought-for polynomial.[34] The resulting polynomial p_{ri}^{sq} is

$$p_{ri}^{sq} = c_1 e^{-\alpha_1 x} \quad + \quad c_2 e^{-\alpha_2 x} \tag{B.1}$$

where c_1 and c_2 are linear parameters and α_1 and α_2 are nonlinear parameters. There are several methods to calculate the parameters c_1, c_2, α_1 and α_2. Among them, Broyden-Fletcher-Golfarb-Shanno method was chosen to perform the data fitting and Mixed Polynomial Interpolation method was selected for line search.[34] The results are

APPENDIX B: (Continued)

Table B.1. The refractive indices of fused silica.[40]

Wavelength (nm)	Refractive index
200	1.55051
220	1.52845
250	1.50745
300	1.48779
320	1.48274
360	1.47529
400	1.47012
450	1.46557
488	1.46302
500	1.46233
550	1.46008
588	1.45860
600	1.45804
633	1.45702
650	1.45653
700	1.45529
750	1.45424
800	1.45332
850	1.45250
900	1.45175

APPENDIX B: (Continued)

$$c_1 = 1.12806683482085, \qquad c_2 = 1.47368681934608 \qquad \text{(B.2)}$$

and

$$\alpha_1 = -0.01319698325957, \qquad \alpha_2 = -0.0000174875432 \qquad \text{(B.3)}$$

The accuracy of the acquired refractive indices using the above polynomial was examined by comparing them with the manufacturer-provided data. The results that are summarized in Table B.2 show excellent agreement between the calculated and the known refractive indices of Spectrosil® quartz. The maximum error is only 0.14 % at 1000 nm. Fig.B.1 shows that the known refractive indices of Spectrosil® quartz and fused silica accurately fit for the curve obtained by plotting this polynomial Eq. (B.1). This further confirms the validity of the method of acquiring the unknown refractive indices of Spectrosil® quartz using a proper polynomial. Therefore, the calculated refractive indices can be used for the correction of the measured UV-VIS MAMW spectra for the whole wavelength range of the incident light.

After finding the unknown refractive indices of Spectrosil® quartz, the refraction correction and the scattering volume correction were performed again to elucidate whether the corrections using the continuously changing refractive indices are necessary

or not. The manufacturer-provided refractive index of 1.551 at 200 nm and the calculated refractive index of 1.4532 at 800 nm were used. The results are summarized in Table B.3 and Table B.4 for the refraction (scattering angle) correction and Table B.5 through Table B.8 for the scattering volume correction. These results are compared with the results shown in Table 5.2, Table 5.3, and Table 5.4 that are acquired using the median value of the manufacturer-provided refractive index of Spectrosil® quartz, 1.504 at 254 nm. For refraction correction, the maximum error is 2.8% if the refractive index for 200 nm is used and 4.2 % if the refractive index for 800 nm is used. For the scattering volume correction the results are consistent if the refractive index for 200 nm is used and the maximum error is 4.0 % if the refractive index for 800 nm is used.

In summary, if the median value of the continuously varying refractive indices of Spectrosil® quartz is chosen for the correction of the measured UV-VIS MAMW spectra, the errors due to differences in the refractive indices of Spectrosil® quartz for the wavelength range from 200 nm to 800 nm is smaller than 5 %. Therefore, it can be concluded that the correction of the measured UV-VIS MAMW spectra for the continuously varying refractive indices of Spectrosil® quartz is unnecessary.

APPENDIX B: (Continued)

Table B.2. The refractive indices of Spectrosil® quartz.[54]

Wavelength (nm)	Manufacturer-provided Refractive index	Calculated Refractive Index	Error (%)
200	1.551	1.549	0.13
254	1.506	1.507	0.07
300	1.488	1.487	0.07
400	1.470	1.469	0.07
600	1.458	1.459	0.07
1000	1.450	1.448	0.14

APPENDIX B: (Continued)

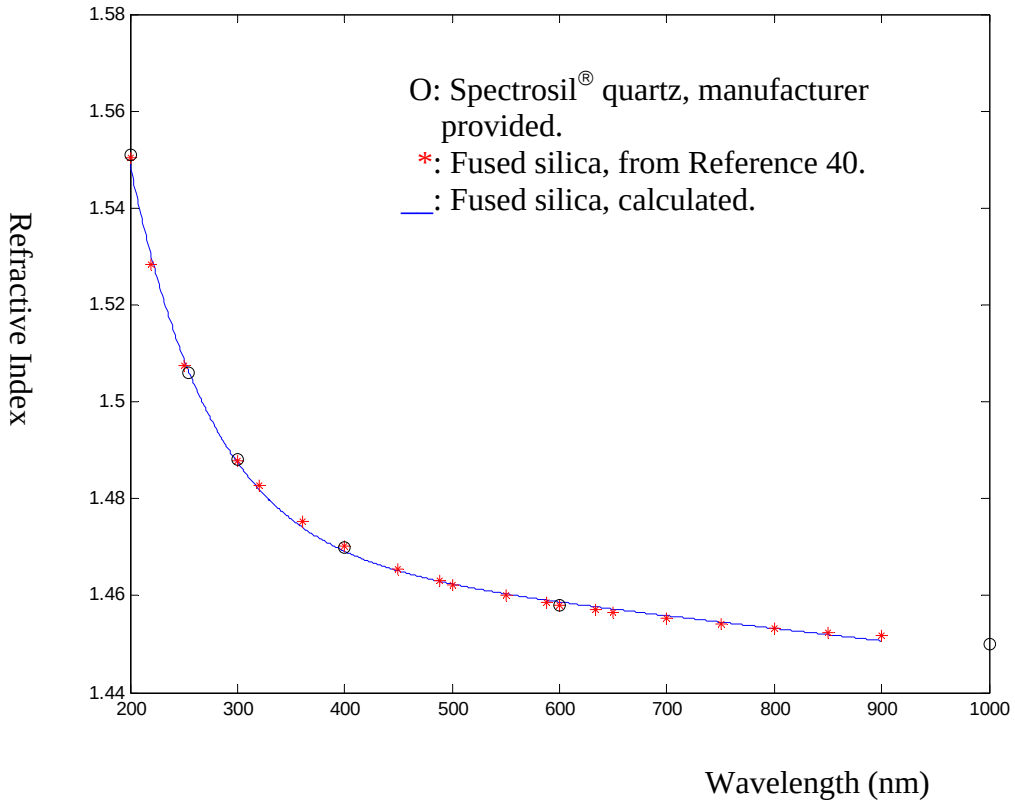

Figure B.1. Refractive indices of fused silica (*, __) and Spectrosil® quartz (O). The data in Reference 54, Reference 40, and the calculated result of Eq. (B.1) were used for plotting.

APPENDIX B: (Continued)

Table B.3. Differences in observation angle and the refractive-index-corrected actual scattering angle. The manufacturer- provided refractive index of 1.551 at 200 nm was used for the correction. The results are compared with the data shown in Table 5.2.

Observation angle θ_a (deg)	Refracted angle by cuvette wall θ_q (deg)	Corrected scattering angle θ (deg)	Error (%)
5	3.2	3.5	2.8
10	6.4	7.1	1.4
15	9.6	10.6	2.8
20	12.7	14.1	2.1
25	15.8	17.6	1.7
30	18.8	20.9	2.3
35	21.7	24.2	2.0

Table B.4. Differences in observation angle and the refractive-index-corrected actual scattering angle. The calculated refractive index of 1.4532 at 800 nm was used for the correction. The results are compared with the data shown in Table 5.2.

Observation angle θ_a (deg)	Refracted angle by cuvette wall θ_q (deg)	Corrected scattering angle θ (deg)	Error (%)
5	3.4	3.7	2.8
10	6.9	7.5	4.2
15	10.3	11.3	3.7
20	13.6	14.9	3.5
25	16.9	18.5	3.4
30	20.1	22.1	3.3
35	23.2	25.5	3.2

APPENDIX B: (Continued)

Table B.5. Calculated scattering volume for 3 mm width slit. The manufacturer-provided refractive index of 1.551 at 200 nm was used. The results are compared with the data shown in Table 5.3.

Observation Angle θ_a (deg)	Scattering Angle θ (deg)	Scattering volume (mm^3)	Error (%)
5	4	560	0
10	7	520	0
15	11	500	0
20	14	480	0
25	18	450	0
30	21	400	0
35	24	370	0

Table B.6. Calculated scattering volume for 6 mm width slit. The manufacturer-provided refractive index of 1.551 at 200 nm was used. The results are compared with the data shown in Table 5.4.

Observation Angle θ_a (deg)	Scattering Angle θ (deg)	Scattering volume (mm^3)	Error (%)
5	4	1150	0
10	7	1120	0
15	11	1070	0
20	14	1030	0
25	18	1020	0
30	21	1010	0
35	24	970	0

APPENDIX B: (Continued)

Table B.7. Calculated scattering volume for 3 mm width slit. The manufacturer-provided refractive index of 1.4532 at 800 nm was used. The results are compared with the data shown in Table 5.3.

Observation Angle θ_a (deg)	Scattering Angle θ (deg)	Scattering volume (mm^3)	Error (%)
5	4	560	0
10	8	520	0
15	11	500	0
20	15	470	2.1
25	19	460	2.2
30	22	410	2.5
35	26	385	4.0

Table B.8. Calculated scattering volume for 6 mm width slit. The manufacturer-provided refractive index of 1.4532 at 800 nm was used. The results are compared with the data shown in Table 5.4.

Observation Angle θ_a (deg)	Scattering Angle θ (deg)	Scattering volume (mm^3)	Error (%)
5	4	1150	0
10	8	1130	0.9
15	11	1070	0
20	15	1050	1.9
25	19	1030	1.0
30	22	1000	1.0
35	26	970	0

ABOUT THE AUTHOR

Yong-Rae Kim received a Bachelor of Science Degree in Physics from Kyung Hee University at Seoul, South KOREA in 1984. Then he continued his research in the area of Nuclear Physics and got a Master of Science Degree in Physics from Kyung Hee University in 1986. After working a few years as a Graduate Assistant at Kyung Hee University, he entered the Master of Science program at the University of South Florida in 1994. He majored Laser Spectroscopy and received a Master of Science Degree in Physics from the University of South Florida in 1996. He continued his study for a Ph.D. Degree in Applied Physics and engaged in the research of Biomedical Spectroscopy.